UNIVERSITY OF GLASGOW

A sensitive device for SThM quantification

By Zarina Umatova

A thesis submitted in partial fulfilment for the degree of Doctor of Philosophy

in the School of Engineering
Electronics and Nanoscale Engineering Research Division
April 2018

“It always seems impossible until it’s done”

Nelson Mandela

Acknowledgments

Doing Ph.D was the most difficult task of my life. This would have never been achieved without support of people who encouraged me a lot on doing research and writing this thesis.

Firstly, I would like to express my sincere gratitude to my supervisor **Prof. Jonathan Weaver,** for the continuous support from first time meeting at the Edinburgh airport and during all my Ph.D study, for his patience, motivation, and immense knowledge. His guidance helped me in all the times of research and writing of this thesis.

I'm not less grateful to my second supervisor, **Dr. Phil Dobson,** for his wise and brilliant suggestions and advice for his support and help during these unforgettable years of my Ph.D.
I could not have imagined having a better supervisors for my Ph.D study.

I'm very thankful to **Dr. Yuan Zhang** for her kind support and knowledgeable encouragement of my research, for her brilliant advice on fabrication and measurements. I think she believed in my abilities and skills more than I did from very first days.

I really appreciate the help and support of members of AFM and Hyperlithography research group **Lesley Donaldson**, **Dr. Ravish Kumar, Dr. Yunfei Ge, Rory Lambert, Francesca Toffani, Lukas Avilovas, Christopher Mordue** who became a second family for me.

My big acknowledgment to kind and friendly **James Watt Nanofabrication Centre and Kelvin Nanotechnology** staff who are high professionals and experts in their fields.

Special thanks to my PhD friends, **Dr. Olesya Ignatova** and **Elmira Mynbayeva,** who inspired and supported me during my Ph.D study.

Last but not the least, I would like to thank my family: my husband **Kuanysh** and daughter **Kamila,** for supporting me spiritually throughout my PhD and my life in general.

List of variables and abbreviations

l- mean free path

λ - thermal conductivity

q- heat flux

g- thermal conductance

g_{0rt}- thermal conductance quantum at room temperature

$g_{t\text{-}s}/g_{0rt}$ – tip-sample thermal conductance at room temperature

r-electrical resistance

i-electrical current

V-electrical voltage

R_{th}- thermal resistance

$V_{3\omega}$ -3 ω voltage

T-temperature

σ is Stephen – Boltzmann constant for phonons

α- TCR

P- power

STM- Scanning tunneling microscope

AFM-Atomic Force Microscopy

SThM- Scanning Thermal Microscopy

EBL- Electron beam lithography

FDTR- Frequency domain thermal reflectance

TDTR - Time domain thermal reflectance

List of tables

List of figures

Abstract

This thesis describes an experimental study of the heat transport between the tip of a Scanning Thermal Microscope –Atomic Force Microscope (SThM-AFM) and nanofabricated sample.

SThM is one of the most flexible tools available for measuring thermal transport at the nanoscale. However, heat transfer between the probe and sample has a complicated nature as it depends on different parameters such as the nature of the surrounding gas (pressure, temperature, degree of humidity), and that of the mechanical contact between probe tip and sample (surface roughness and topography, mechanical properties of the tip surface and sample surface and the force applied). So understanding the heat flow between tip and sample requires careful study of all of these parameters. Thus quantification of tip and sample thermal contact is a key problem in the interpretation of SThM measurements.

In this work the fabrication of devices to quantify SThM tip and sample surface thermal resistance in one single contact are presented. The fabrication was performed using lithographic nanofabrication and MEMS technology. Thermally grown silicon dioxide was chosen as a membrane material for all devices due to its low thermal and electrical conductivity and ease of fabrication.

An "active" device was fabricated, consisting of a Silicon dioxide membrane with integrated thermal sensors (Pt heater / thermometer and Pt / Au thermocouple). This was studied in passive SThM mode (heated sample) with different SThM and AFM probes. The different types of tip which were examined to investigate the nature of the contact included Si_3N_4, metal coated Si_3N_4 and silicon tips. The device was constructed on the top of a 10×10 um square of 50 nm thick silicon dioxide membrane for thermal isolation from the substrate. The fabrication process for the devices was new, combining some standard processes with the use of new processes such as Pt wire definition by subtractive processing of a Pt-Au metal stack and ICP Plasma etch of a 50 nm membrane all combined in a novel process flow. The techniques used for fabrication were electron-beam nanolithography, lift-off processing and a combination of aqueous and plasma etching to define the free-standing membrane. High thermal isolation of the sample and the high sensitivity of the sensors used allowed the detection of thermal conduction between tip and sample with high precision. The measured temperature range of Pt resistor was 293-643K. The measured thermal resistance of the membrane was 3×10^5 K/W in air and 1.44×10^6 K/W in vacuum and the sensitivity of thermocouple was 3.3μV/K. The tip contact resistance was measured with a noise level of $0.3g_{0rt}$ at room temperature, where g_0 is the thermal resistance quantum.

A novel device consisting of a set of membranes with 12 different geometries and metallisation monolithically fabricated on a single die is proposed as a possible calibration sample for measuring thermal conduction between tip and sample with “active” SThM probes. Such probes, in which the tip is significantly heated, are used in investigations of thermal conduction and other thermal properties of samples. This sample was fabricated using the same methods as the “active” sample above to give a range of values of sample thermal conduction of $15\ g_{ort}$ -$85 g_{ort}$ which corresponds to value of bulk silicon.

Introduction.

In the early 18th century accuracy and precision in thermometry was established when Fahrenheit invented a mercury in a glass thermometer which consists of bulb with mercury inside connected to a glass tube. The volume of the mercury varied sensitively and reproducibly with temperature change. Such a thermometer needs to be in close contact with an object or medium in order to quantify a temperature. [1] However, measuring a temperature by that technique was limited by the size of the thermometer and the objects measured.

Later when considering a smaller object (typically micrometre scale) heat was defined by the first law of thermodynamics such that "Energy is conserved if heat is taken into account". [2] When temperature gradient exists in a body, there is an energy transfer from the high - temperature region to low- temperature region. Energy is transferred by conduction, convection and radiation. [3].

The heat transport in dielectric materials is dominated by phonons.[4] When the size of an object is much larger then phonon mean free path, heat transport is purely diffusive and is accurately modelled by Fourier's law. (Figure 1) [5]

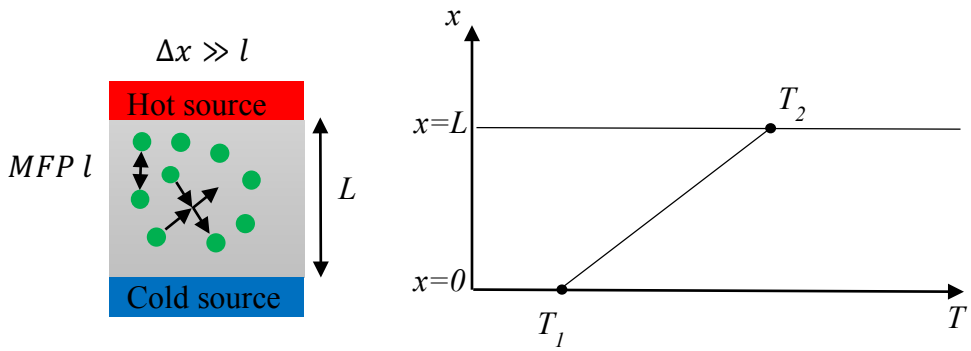

Figure 1 Diffusive transport after [6]

In the experiment Fourier showed that heat transfer through plane layer is proportional to temperature gradient across the layer and heat transfer area.(Eq. 1)

$$\boldsymbol{q = -kA\frac{\partial T}{\partial t}}, \qquad \textbf{Eq. 1}$$

where q is a heat flux, k is thermal conductivity, A is the area perpendicular to the direction of heat flow and $\frac{\partial T}{\partial t}$ is temperature gradient.

According to kinetic theory, thermal conductivity in the diffusive regime can be found as,

$$\boldsymbol{k = c\frac{1}{3}cvl}, \qquad \textbf{Eq. 2}$$

where in Eq. 2 c is specific heat capacity of the solid per unit volume, v is the average speed sound, l is mean free path. [5]

However, Fourier's law cannot characterize heat conduction process at small scales where the size of objects is much smaller than mean-free path. The reason is that thermal conductivity depends on the existing temperature gradient within a material and heat scattering will only occur at boundaries. Since the temperature at a point can be defined only under local thermodynamic equilibrium, meaningful temperature can be defined only at points separated on an average by the mean free path. This is because local thermal equilibrium is restored by phonon scattering due to lattice defects and other phonons. So in the limit of small dimensions when the size of the object is much smaller than phonon mean free path there is no temperature gradient and process is purely ballistic. Thus when Mean Free Path (MFP) l is less than size of medium and the process called ballistic thermal transport, as shown on Figure 2

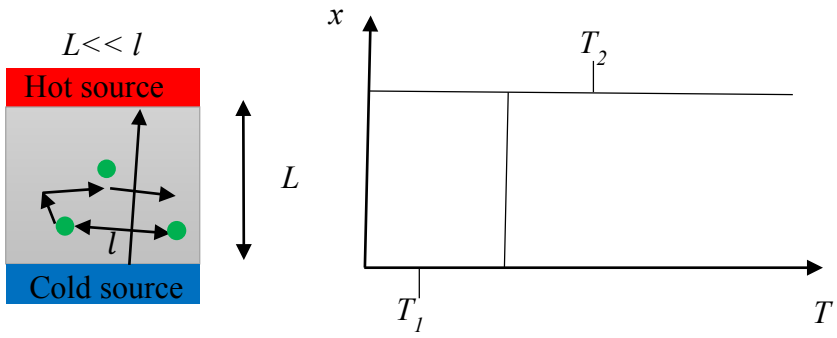

Figure 2 Ballistic transport

Thus, heat conduction in nanostructures is different, because it is difficult to reach local thermal equilibrium. A phonon ballistic transport regime has been described from radiative transfer in [7]. The assumption made when considering analogue of blackbody radiation is shown in Figure 3. The idea is that two "blackbody" cavities with a different temperature T_1 and T_2 are connected by a ballistic tube via small hole (aperture) with area A. The temperature within the tube is measured with 2 thermometers separately. Thermometers were placed inside the cavities as well as within the tube. All phonons incident on the aperture transmit across the hole. The energy flux across the aperture is finite and given by

$$q = 4A\sigma T^3 \Delta T, \qquad \textbf{Eq. 3}$$

the temperature difference in Eq.3 is given by $\Delta T = T_2 - T_1$,

where σ is the Stephen Boltzmann constant and A is the area of aperture.

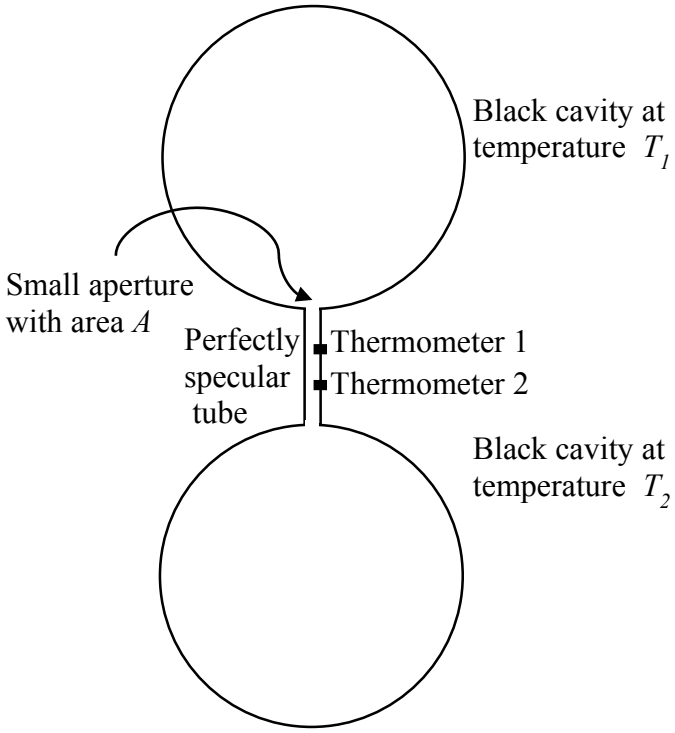

Figure 3 Blackbody picture for ballistic transport. After [7]

Assuming that the heat transport between the two solids only depends on the transmission probability which depends on the side from which phonon hits the interface and temperature of both sides of interfaces, the heat transport can be written as

$$Q = A(\sigma_2 T_2^4 \alpha_{2\to1} - \sigma_1 T_1^4 \alpha_{1\to2}) \qquad \textbf{Eq. 4}$$

where $\alpha_{2\to1}$ and $\alpha_{1\to2}$ in Eq.4 is a transmission probability from side 2 to side 1 and from side 1 to side 2 respectively. In the case of dynamic thermal equilibrium, when second law of thermodynamics is kept, the number of phonons leaving one side is the same to the number of phonons returning. This is also a statement of the principle of detailed balance. Two thermometers in the channel measure the same temperature which is in-between T_1 and T_2.

Using this principle, by recognizing a temperature at boundaries as corresponding to that of the cavities, a heat flux for ballistic regime can be found as

$$q = \sigma(T_1^4 - T_2^4). \text{ [7]} \qquad \textbf{Eq. 5}$$

Where in Eq.5 σ is Stephen – Boltzmann constant for phonons, T_1 and T_2 are temperature at boundaries.

The phonon transport in a one dimensional channel at low temperature was studied by Schwab et.al. [8] where the thermal conductance approaches a minimum value, which called the

universal quantum of thermal conductance g_0. This represents the value of energy transported per phonon mode in ideal coupling between a ballistic thermal conductor and a reservoir, so that the modal transmission coefficients, α_m, are equal to unity. This assumption leads to a fundamental relation for the quantum of thermal conductance [8] which can be represented by

$$g_0 = \pi^2 k_B^2 T/(3h), \qquad \textbf{Eq. 6}$$

So that it can be found from as $g_0 = (9.45 \cdot 10^{-13} W/K^2)T$.

From the discussion above we see that heat transport at the nanoscale is different. We are going to measure the heat conductance between SThM tip and sample. Measuring these small conductances requires the sensible numbers for scaling and expressing these values. By expressing the heat conductance in terms of thermal conductance the obtained values will be expected to be a small multiple of conductance quantum g_0. Another reason for using that scaling is to investigate whether the contact is quantized. In some experiments, these contacts have been found to be quantized [9], and in some there is no evidence of strong quantization[10] In this work there was no obvious quantization observed.

From a practical point of view heat transport can be characterized by different methods such as Time Domain Thermal Reflectance [11], Frequency domain thermal reflectance (FDTR), the 3ω method [12], [13] microfabricated test structures [14], [15], [16] and Scanning Thermal Microscopy[17]. These methods are discussed briefly below.

Time Domain Thermal Reflectance (TDTR) is a method to measure the thermal conductivity of nanomaterials. The method is based on a pump – probe optical method and mode-locked laser oscillators [18]. Once a material is heated up, the change in the reflectance of the surface can be utilized to derive the thermal properties. The mechanism of this method is based on monitoring of acoustic waves which are generated with a pulsed laser [19]. (Figure 4)

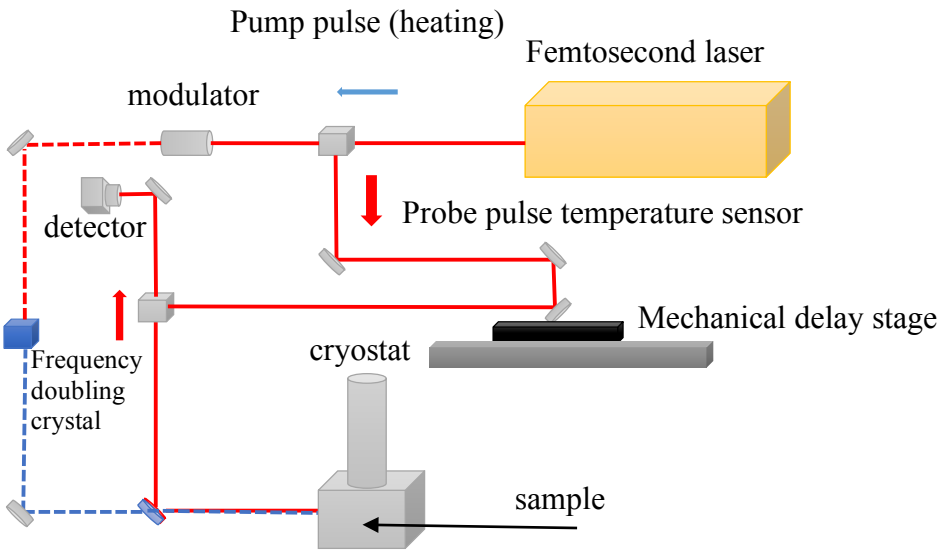

Figure 4 time domain thermal reflectance

In TDTR measurements, the output of a mode- locked laser oscillator is split into a pump beam and probe beam, with the relative delay time between the pump and probe pulses being adjusted by mechanical stage. The sample surface temperature is determined by the probe beam. TDTR is a flexible and accurate tool for measuring the thermal conductivity of a bulk and thin film materials in the range starting from the lowest thermal conductivities of fully dense solids [20] to the high thermal conductivities of pure metals, diamond [21]. However, it requires that the surface of the sample is smooth enough to avoid undesired modulation of diffuse scattering. [22] Also due to the complexity of the equipment and the small changes in reflectance which are being measured small errors can cause significantly wrong results.

Another method is **Frequency Domain Thermal Reflectance (FDTR)** which includes the advantages of TDTR with the relative experimental simplicity of modulated photothermal methods. Frequency-domain thermoreflectance (FDTR) is a non-contact optical technique capable of a wide range of thermal conductivity measurements for solid materials. FDTR measures the phase lag between a periodic surface heat flux and surface temperature over a range of heating frequencies (100 kHz-200 MHz). The unknown thermal parameters (most commonly thermal conductivity and thermal boundary resistance) are extracted by fitting experimental data to an analytical model. In order to make a measurement, a thin metal layer is deposited on the sample surface. This metal layer, referred to as the transducer, undergoes a temperature-induced change in reflectance due to the periodic heat flux. Similarly to TDTR, frequency domain thermal reflectance is only applicable for measuring the thermal properties of homogenous materials and submicron thin films and is inappropriate for rough or structured samples such as electronic devices.[23]

The use of microfabricated test structures is another technique employed for the study of heat transport. [24],[25],[26],[16]. For example, a microfabricated test structure to illustrate a

new gas sensor detection principle was presented and fabricated out of SOI wafer.[27] Fabrication of a heated reference sample with localized resistive temperature sensors made of platinum heaters suspended on a silicon nitride membrane on micro-scale was performed by Lemare et.al.[16] A device thermal resistance of $2.3 \cdot 10^4 K/W$ was determined. SThM measurements were performed on the heated membrane and was demonstrated that the influence of the probe/surface contact can be evaluated using this calibrated chip with some limit of sensitivity due to the probe –surface contact area of several micrometres.

A commonly used technique for studying thermal transport is the 3ω method.[28]. The 3ω method is one of the most widely used because of its low cost, simplicity, and high accuracy. The method requires a thin metallic strip to be deposited onto the dielectric sample surface [12] which can be used as heater and thermometer at the same time. The technique will be discussed in more detail in Chapter 3.

SThM has the highest spatial resolution of any thermal measurement technique which does not require special specimen preparation techniques but these measurements are hard to quantify because the thermal coupling between tip and sample is variable. [9] Measuring the exact properties of this contact is hard because it is a tiny area (typically 90-100 nm in size) [29] and hence has small thermal conductivity. [28], [12], [30] A scanning thermal microscope (SThM) operates by bringing a sharp temperature-sensing tip close to the sample surface. Tip-sample heat transfer information can be mapped out by scanning the tip across the sample. The technique will be discussed in more detail in Chapter 1.

Nanoscale thermal property measurements are hard to make. SThM has good resolution and is much simpler than making a device, but it is hard to quantify because the tip-sample contact is poorly understood and variable. The subject of the thesis is solving the SThM tip-sample quantification by fabricating sensitive samples and measuring tip-sample thermal conductance by 3ω method. Another issue to be solved is fabrication a set of calibration samples in order to calibrate the SThM method.

Chapter 1. Scanning thermal microscopy

1.1 SThM technique development

The Scanning Tunnelling Microscope (STM) was the first technique giving atomic resolution on normal bulk samples.[31] STM is a technique based on vacuum tunnelling, and yields topographies in real space and work function profiles on an atomic scale.

Surface microscopy using vacuum tunnelling was demonstrated by Binning et. al. for the first time to obtain topographic images on an atomic scale using a Scanning Tunnelling Microscope [32]. STM was originally invented as a microscope technique for measuring the superconducting energy gap of thin films. The atomic resolution was an accidental discovery.[33] On imaging semiconductors, it was found that the STM was very sensitive to topography but also to density of states. [34] The ability to image band gap is a major application of STM. The STM can also image ballistic electron transport and measure surface potential which led to the use of STM to measure the Seebeck coefficient of molecules [35].

Nevertheless, STM is limited by the need for the sample to be a conductor.[36] This led to the development of other Scanned Probe microscopies such as Atomic Force Microscopy (AFM) and Scanning thermal microscopy (SThM). In 1986, Binning, Quate and Gerber demonstrated for the first time the idea of the Atomic Force Microscope, which used an ultra – small probe tip at the end of a cantilever. Similarly to STM, in AFM a sharp tip is raster-scanned over a surface. Instead of using the quantum mechanical effect of electron tunnelling, in AFM atomic forces are used to map the tip-sample interaction [37].[38] AFM works by bringing the very fine tip close to the surface, so that the two interact. Since the tip is located at the end of a cantilever, which is just a simple form of spring, the force exerted between the tip and surface causes a deflection which can be measured and used to control the force between tip and sample. Originally this deflection was measured using an STM. Nowadays the use of optical methods is almost universal [39], In particular, the use of an optical deflectometer based on a laser and split photodiode is very common [40] The AFM was originally designed to determine the topography of surfaces, [37] however an image of the attractive forces between tip and sample in different locations of the sample is obtained by scanning the tip above the surface allowing measurement of electrical, magnetic and capillary forces. [39], [41], [42] For example, Scanning Capacitance Microscopy (SCM)[43] which simultaneously maps relative changes of majority carrier concentrations and sample topography. Another example is Tunneling AFM / Conductive AFM which simultaneously map the electrical characteristic of the sample and its topography.

Placing different sensors in the end of the tip allows topography and unknown characteristics to measured simultaneously. By placing a Hall sensor at the end of an AFM tip it

is possible to make a scanning Hall probe microscope which may be used to image magnetic field [44]. For the study of thermal properties Scanning Thermal microscopy is used in order to get information about topography and material thermal characteristics.

This last technique is based on the thermal interaction between a heated tip and surface and was first demonstrated by C.C. Williams and H.K. Wickramasinghe in 1992 [45] who are the inventors of the Scanning Thermal Microscope. They fabricated a thermocouple probe, which is a junction of two metals, located at the end of a sharp tip shown in Figure 5. The measurement was obtained by scanning the heated thermocouple junction across a sample surface. When the tip was brought close to the sample the thermocouple measured a change the rate of heat transfer into the specimen through the air and this was used to obtain a topographic image of the sample.

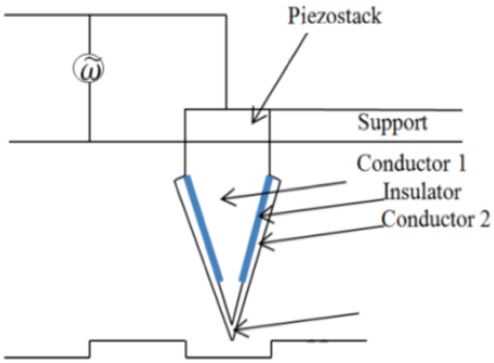

Figure 5 Schematic diagram of thermocouple probe supported by piezoelectric element. after[45]

Soon after M. Nonnenmacher and H. K. Wickramasinghe developed a new probe technique for mapping the thermal conductivity variations of surfaces on the nanometre scale [46]. The basic technique is shown in Figure 6 where a heated pointed probe tip is brought within close contact to a sample surface. The point contact with the sample provides a conduction path away from the heated tip into the sample. The temperature at the top of the tip is maintained about 365 K. The (near) point contact with the sample provides a conduction path away from the heated tip. The temperature at the junction *Tj* then typically decreases to a few degrees above ambient.

Based on that model, there is a presence of air gap *d* between tip and sample, and it is assumed that $d \sim a$, where a is the contact area, also it is assumed that sample thermal conductivity k_s is much higher than thermal conductivity of air k_a. The thermal conductivity of the sample was calculated based on measurements of junction temperature *Tj* and heat power with known dimension of the contact *a.*[46], [47]

$$k_s = \frac{2P}{\pi T_j a} \qquad \textbf{Eq. 7}$$

Temperature measurements were performed successfully by this method in order to map thermal conductivity variations of samples. However, this method will not work for samples with thermal conductivities lower than thermal conductivity within the air gap and for nanometre size contacts as the size of the gap is considered similar to the size of the contact being made.

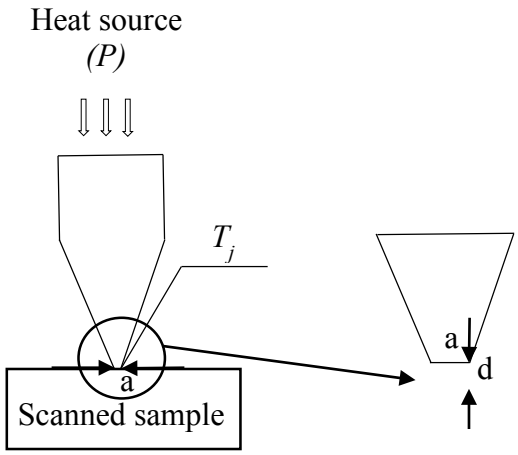

Figure 6 Schematic of scanning thermal conduction microscope. After [46]

SThM Sensors

Different SThM probe types are used to study thermal properties using electrical method. All of these methods can be categorised according to the sensor temperature dependence which is used. There are two main methods which are widely used. Firstly, thermovoltage based measurements which involve probes using passive thermal sensors such as tunnelling thermometry [10] and thermocouples [17], [48] [46]. Secondly, electrical resistance based measurements using resistive metallic or silicon probes [49] such as Wollaston wire probes [50],[51] and resistive Si probes. [52], [53], [54] Examples of these sensor types are compared below.

Thermovoltage based measurements

Thermovoltage based methods exploit the thermoelectric voltage generated at the junction between two electrodes to carry out thermometry. Measurements can be performed either in non-contact or contact modes with junction located at the end of the tip, using either STM or AFM systems to control the state of contact. Thermovoltage – based methods include tunnelling thermometry and, most commonly, the point – contact thermocouple method. These methods use the sample as one side of the thermocouple, in contrast to the ones in which both elements are part of the probe, as discussed later. [55]

Tunnelling thermometry is an uncommon technique based on the principles of a tunneling thermocouple and uses the temperature dependence of the tunneling electronic current between two dissimilar electrodes without contact. The technique was first proposed by Weaver

et.al. [56]in 1989 based on STM that is capable of recording optical absorption spectra with nanometre resolution. The tunnelling thermometer provides direct optical absorption maps of sample, it could be very powerful in chemical analysis. However, it has a limitation as it is requires only conducting samples.

Later, Nonnenmacher and Wickramasinghe developed a technique of thermal microscopy based on measurement of contact potential between a metallic tip and a thin metal film on the sample surface in 1992. [46]. The AFM system was adapted in to contact potential measurements system.(Figure 7)

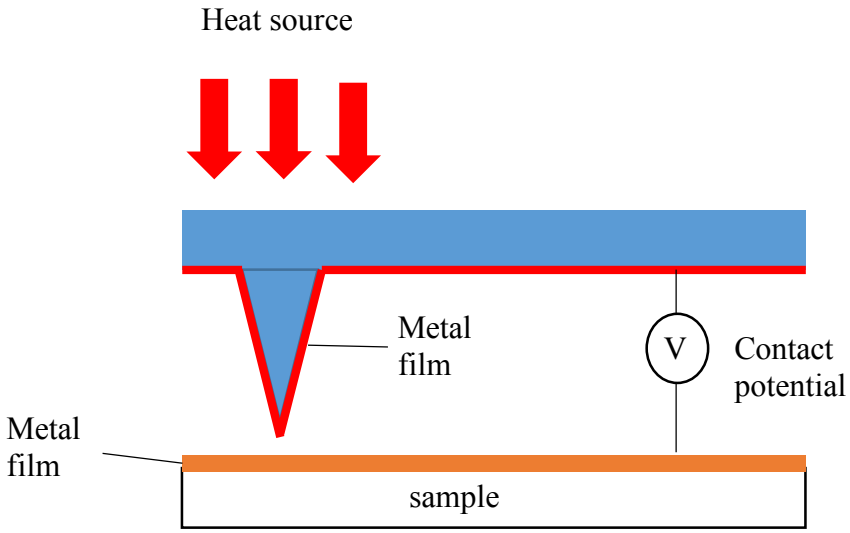

Figure 7 Contact potential method

Two techniques described above such as the tunnelling thermocouple and contact potential measurements require the sample to be coated by a metal film. This is often not desirable when probing electronic devices and integrated circuits where a thin metal film may alter the heat conduction in the device or may cause the devices to electrically short.

Later Progress in thermal imaging was made by Majumdar et al [57], [48]. They introduced a technique based on the AFM in which the topographic feedback used the tip-sample force, which was decoupled from the process of temperature measurement. This allowed the operation of the SThM on any material. Three types of thermocouple probe were designed. These were bare wire probes[57], diamond – tip wire [48] and thin film probes. (Figure 8)

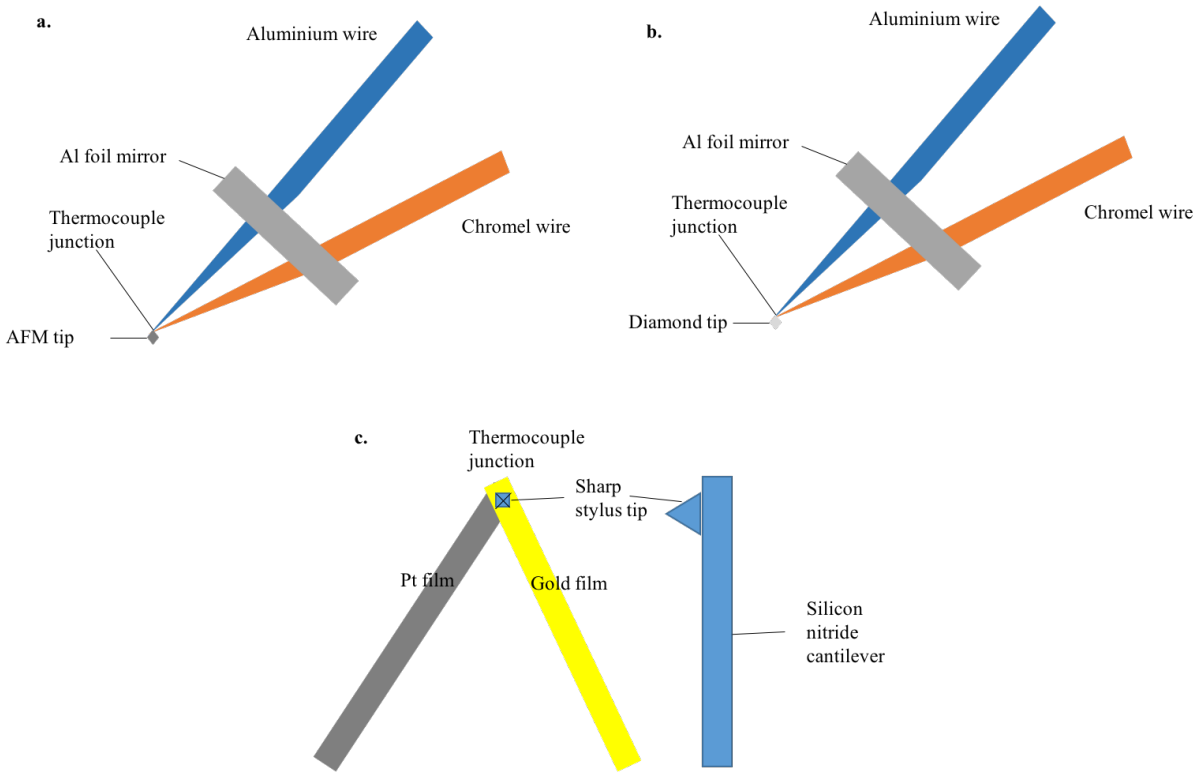

Figure 8 Three types of thermocouple probes. a. Bare wire probe. b. Diamond tip wire probe. c. Thin film probes

The bare thermocouple probe consists of cantilever with two wires of type K thermocouple made of chromel and alumel. Using this probe thin water layer on the surface had no influence on sample-probe thermal conduction, solid-solid contact was also not significant. Gas conduction dominated sample – probe heat conduction. However, the metals used in the wire thermocouple were soft and so after using it they will be deformed and unusable. Another problem was that probes were handmade and thus not reproducible.

Another improved design in order to get harder and sharper tips and reduce thermal resistance between tip and sample was the diamond –tip thermocouple probe wire probe. A small single crystal piece of diamond was stuck using epoxy glue to the end of the thermocouple wire probe. However, although solving some problems of the bare thermocouple wire probes with the diamond tip thermocouple probe, reproducibility of the probes is still problem and spatial resolution of about 0.05 um was not possible to be achieved.

To improve the reproducibility problem thin –film thermocouple probes were designed and batch fabricated on commercially available Si_3N_4 AFM probe.[48]

More generally used are sensors based on AFM probes with built-in microfabricated thermocouple sensors. Here AFM provides a mechanism for topographic feedback independent of the function of the temperature sensor.

A method for batch fabrication of SThM probes with attached Au/Pd thermocouples by conventional electron-beam lithography, using PMMA resist and pattern transfer technique such

as float coating and lift-off was developed by Zhou et.al.[58] The thermocouple junction is formed by two nanofabricated wires, one of 25 nm thick Gold and one of 50 nm thick Palladium as shown in Figure 9.

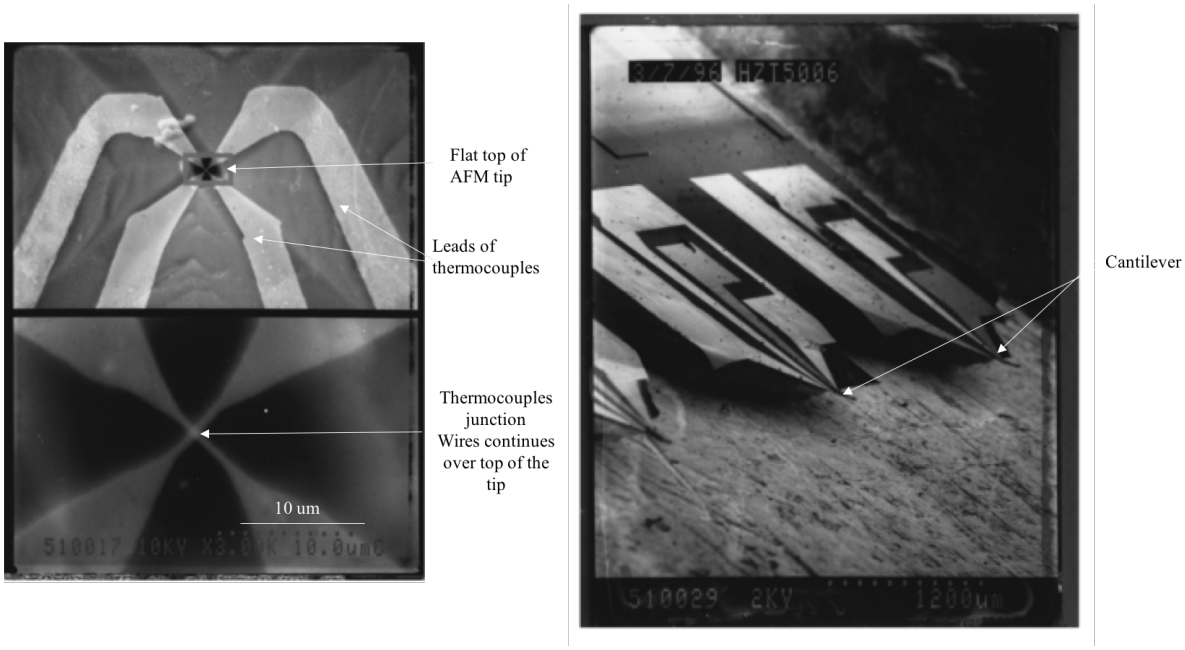

Figure 9 Thermocouple junction **Reproduced with permission** [58]

By heating the probe with a laser spot, the measured Seebeck coefficient differed from the expected bulk value of *15 uV/K* by a factor of 2. The error was reported as being due to uncertainty of laser spot size but was found subsequently to be due to the use of thin-films. The main problem with the flat ended probes is that the thermal contact to the sample was at the corner of the flat. The thermal resolution was not dependent on the thermocouple size, just on the tip shape (which was badly defined) and so another type of thermocouple probes was fabricated. These probes are also probes with Au/Pd thermocouples situated at the end of Si_3N_4 cantilevers. The tip definition is the main difference with previous probe design. The probes were batch fabricated by G. Mills et. al. using electron beam lithography and silicon micromachining tools in 1999 (Figure 10). Two wires, one 25 nm thick gold and another 50nm thick palladium, where patterned in separate level of ebeam lithography. The wires overlap the edge of the cantilever to define one of the edges of the wire. The thermocouple junction is therefore self-aligned to the end of the cantilever. More recently thermocouples based on self alignment to a hole have been demonstrated in manufactured tips [44], [59], [49]. The metals used in other designs are gold and chromium[60] which gives a much bigger Seebeck coefficient.

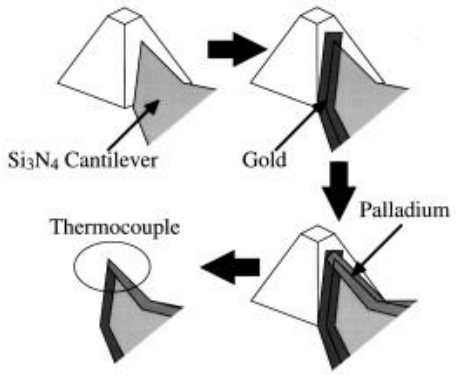

Figure 10 Fabrication stages of the thermocouple probe process. Reproduced with permission [61]**.**

However, all thermocouple probes need to be heated by a separate heater and the thermocouple can normally only be used a thermometer [60].

Resistive probes

Another class of thermal sensor is the resistive probe. Different types of SThM resistive probes such as doped silicon probes and metallic probes have been developed using the temperature dependence of the electrical resistivity *R(T)* of doped silicon and pure metal films. The resistive probes can be used both as a thermometer and as a heat source which is an advantage over the thermocouple probes for measurements of materials properties. The most common resistive probes widely used may be divided into resistive Si probes, Wollaston wire probes and batch fabricated "KNT" probes.

SThM doped silicon resistive probes are based on Si probes developed for Ultrahigh Density Atomic force microscopy for data storage applications by IBM [62]. The heated AFM tip enables a nanomechanical data storage concept in which the heated AFM cantilever tip can melt small indentation data bits into a thin polymer film. The use of multiple parallel tips gave a fast data rate. [63] The technology was never made commercially available but the probes have proven to be very useful for materials characterisation and fabrication. [1]

The cantilevers are U-shaped and consist of a heater element at the end, placed above a sharp silicon tip. The electric current flowing through the resistive element causes resistive heating and a temperature rise of the tip. Single probes of this type are now extensively used for microthermal analysis.[64]

Silicon cantilevers have advantages over metal cantilevers, since they allow higher operating temperatures. [52] Si is most typical material for cantilevers with doped heaters [54][53]. However the tip wear and fouling are the main limitation of Si tip, also they are not

[1] SwissLitho AG, Technoparkstrasse 1, 8005, Zurich

well suited for an electrical and electrothermal microscopy, since the tip voltage is coupled to the cantilever temperature as they made of the same material.

In 1994 the first metallic SThM probes “Wollaston wire probes” were introduced by Dinwiddie and Pylkkie and the capability of the probe to provide contrast based on the thermal conductivity of the sample was demonstrated.[59] The Wollaston wire probe design is based on the Wollaston process wire [65]. The Wollaston wire probe is relatively massive structure compared to other probes and mostly used for microthermal analysis because of its mechanical and thermal strength [66], [50]. From the standpoint of spatial resolution the probe is poor at mapping thermal properties, such as thermal conductivity but it is excellent for local thermal-mechanical measurements [67].

Wollaston wire usually consists of a platinum or platinum-rhodium core surrounded by a thick silver sheath. Once the wire is properly oriented the silver in the end of loop is etched away. The basic diagram of the Wollaston wire probe is shown in Figure 11.

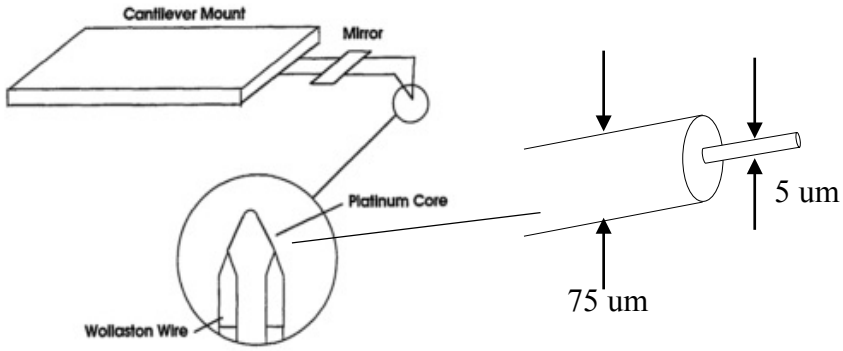

Figure 11 Schematic diagram of the resistive Wollaston wire probe after [68]

Later Wollaston wire probes were used by Hammiche et.al. [69] who further developed this method and made it possible to perform localized thermal and mid infra-red photothermal analysis of surfaces.

Another type of the batch microfabricated SThM probe is presented in [70] by Phillip S. Dobson and others. The probe (Figure 12) combines a Pd resistor in close proximity to a sharp tip at the end of a thin Si3N4 cantilever. The tip is designed to be tall (14 μm) to maximize the cantilever – sample separation, minimizing heating of the cantilever by the hot sample. [71] Initially they were designed as thermometers, but then also used as a heaters, something they are not optimised for.

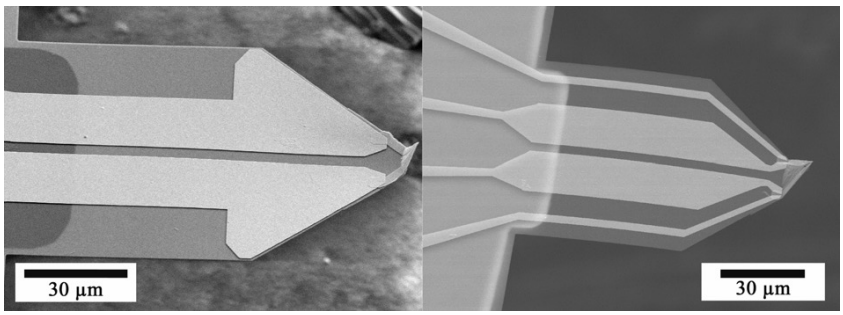

Figure 12 Completed 2 and 4 terminal resistance probes [70]

The resistive metallic SThM probes fabricated and commercialised by Kelvin Nanotechnology ("KNT probe")[2] are batch fabricated AFM probes which are commercially available and well-suited to temperature and thermal conductivity mapping. The probe consists of tip manufactured by the e-beam lithography technique pioneered by Mills et. al. which initially used a thermocouple sensor, with gold pads and tracks which are connected to a palladium sensor and heater positioned at the sharp tip apex and with a trimming resistor on the probe base to adjust the total resistance. With current available SThM probes sub-100 nm topographic and thermal resolution and a temperature resolution of 0.1 K are achieved

A dual cantilever resistive probe for scanning thermal microscopy has been fabricated by Y.Zhang, P Dobson and J.M.R.Weaver. [72]. The batch fabrication for dual cantilever resistive probes is based on the fabrication process for single cantilevers. In dual probe measurements, one is used as a local heater and directly excited by the oscillator of lock-in amplifier. The second nearby sensor detects the thermal diffusivity at a microscopic scale. The main difference from the Dobson probe is that there are two sensor/heater elements. [72]. (Figure 13)

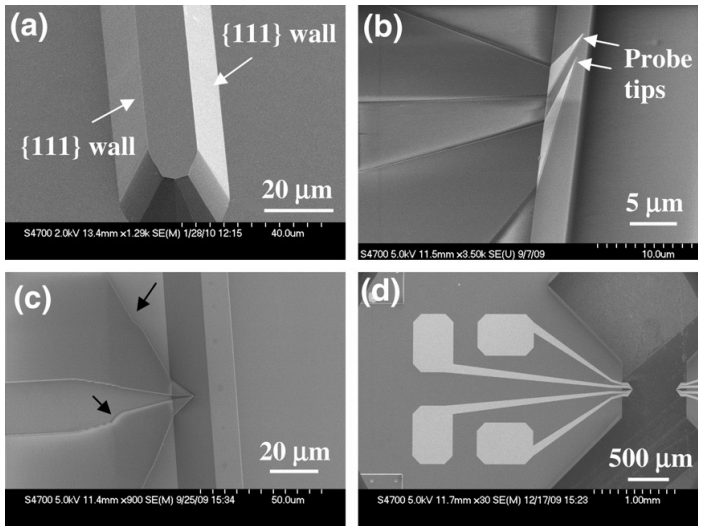

Figure 13 SEM images of (a) a long silicon bar with {1 1 1} walls; (b) dual tips defined on a {1 1 1} wall; (c) dual cantilevers defined; and (d) a dual cantilever resistive probe [72]

[2] Kelvin Nanotechnology, 70 Oakfield avenue, Glasgow, UK, G12 8LS, KNT-SThM-01-an.

Instrumentation

An example of the connection of a resistive probe to an SThM system is shown in Figure 14

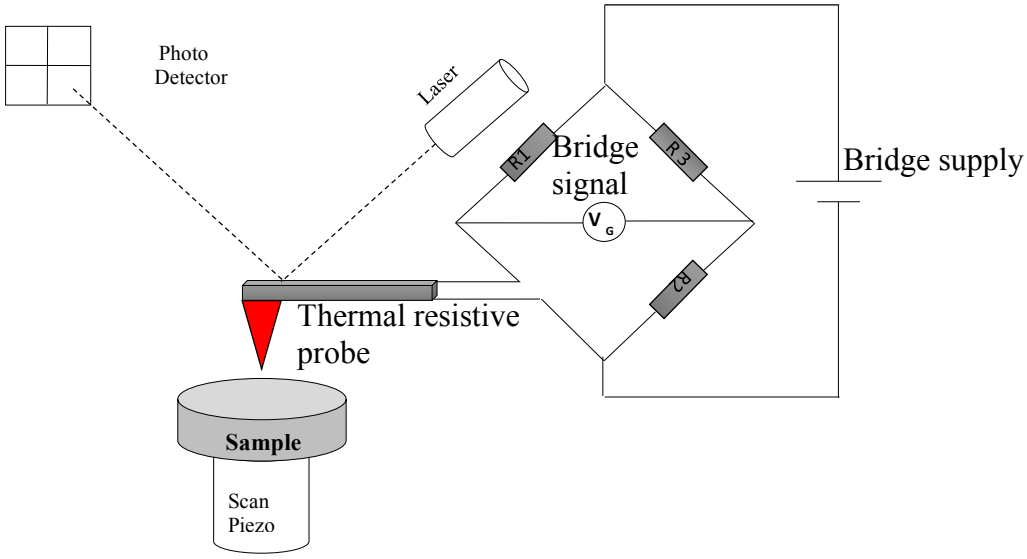

Figure 14 Schematic diagram of SThM system [73]

Figure 14 shows the schematic diagram of a SThM system using a resistive thermal sensor. [74] A resistance thermometer is mounted at the end of the AFM cantilever. While the distance between the probe tip and sample surface is controlled by the usual AFM method, the thermal probe forms one leg of a Wheatstone bridge, which enable the measurements of probe resistance. This provides a very accurate measurement of probe resistance and is suitable for very sensitive devices. The use of a bridge removes sensitivity to the large constant resistance of the probe allowing measurements of the temperature variation which might not be possible by measuring resistance directly with a voltmeter. [75]

A topographic AFM image can be generated from changes in the cantilever's deflection which is determined by laser beam. Thus, topographic information can be separated from local variations in the sample's thermal properties, and the two types of images can be collected simultaneously. However, moving the laser changes the temperature calibration causing drift and additional heating from laser and making a new calibration necessary each time the microscope is used even with the same probe. Noise in the laser can also cause noise in the thermal measurement. [76]

1.2 SThM measurement quantification

In order to measure thermal characteristics using SThM is important to understand the temperature distribution within cantilever and tip when brought into contact with sample surface.

As shown in Figure 15 the heat from a heated SThM tip goes through the cantilever, surrounding gas, through solid-solid mechanical contact and the water meniscus. [77], [78], [79].

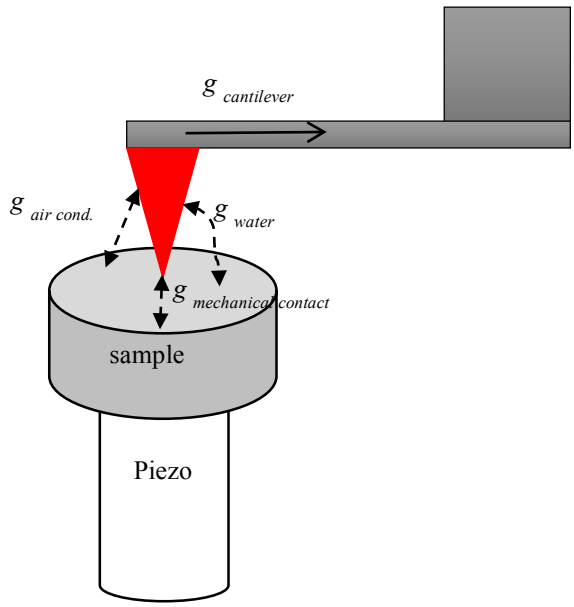

Figure 15 Thermal contact between tip sample and through cantilever

As was shown by P.O. Chapius et al. [80] a very significant part of the heat transfer between the tip and sample is due to the air heat conduction. Experiments were done in ambient air where the interaction of the hot tip of a Wollaston wire probe and sample surface were studied for thermal analysis. Also, as was shown by Shi and Majumdar, when there is a large heated region on the sample, air conduction is the dominant tip – sample heat transfer mechanism. [29]

Gomes suggested that the water meniscus might be the dominant source of heat transfer, depending on the sample thermal conductivity [81]. The water meniscus at the nano-contact between a heated atomic force microscopy probe and a hydrophilic sample was described by A. Assy and others.

Another type of heat conduction channel between tip and sample is by mechanical solid to solid contact. As shown by Shi et. al.,[29] at about 90 nm diameter contact area between sample and SThM probe tip mechanical conduction increases linearly when contact force increases due to elastic – plastic contact between the sample and an asperity at the tip end. [29].

Heat conduction between tip and sample through the possible channels discussed above can be studied when either SThM probe tip is heated or sample is heated based on the principle of detailed balance.

When the heated probe touches the sample surface this method is called “active mode”. When a cold (unheated) probe is brought into contact with heated sample this is called “passive mode” SThM.(Figure 16)

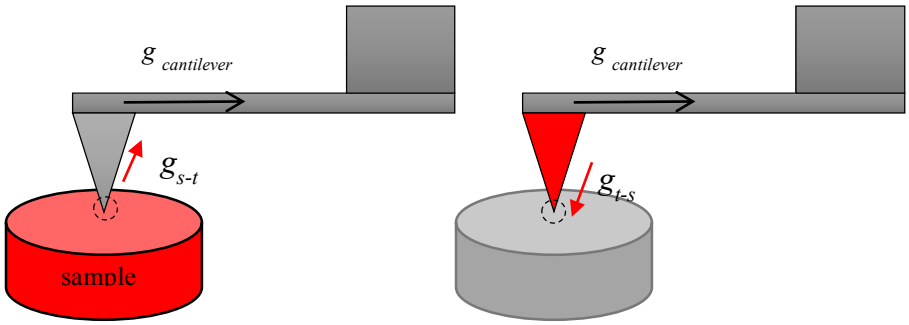

Figure 16 Heat distribution in Passive and Active modes

In **active mode** a heated probe used to measure the characteristics of an unheated sample.

Active mode is used to measure thermophysical properties of materials such as thermal conductivity. Active mode can also be used to locally heat the sample in order to induce and study thermally-dependent phenomena such as the glass transition thermometry of polymers.[82] In active mode the tip can be heated directly or indirectly. The direct method utilizes current flowing through the tip and so the tip needs to be a resistive element [43], [83]. A large current is passed through the probe, resulting in significant Joule heating. Probe temperature is controlled by changing the current and is observed by measuring the probe resistance. The indirect method for heating the tip can be performed by using a separate heater to affect the temperature of a tip made of a high thermal conductivity material.[84] In both cases a thermoresistive or thermocouple tip is expected to be used. However, there is a possibility to use a laser - beam – heated thermocouple probe in active mode or to operate a Joule heated thermocouple probe. [84] There is a problem of trying to separate the thermovoltage and resistive voltages in this case. [60] Thermoresistive probes discussed are suitable for passive and active modes.[85], [86]. To calibrate the SThM probe for thermal conductivity measurements various reference sample such as ZnO [87], Bismuth telluride [88] , Au [89], Si and Ge[90] with known thermal properties are required.

However, there are problems with using different materials for calibration purposes due to difficulties of keeping the same microscope calibration parameter and tip interfacial thermal resistance. Thus there is a requirement in developing a set of sample for SThM calibration in active mode which will be discussed in Chapter 4.

The thermal conductance from heated object to cold object is equal to

$$g = \frac{\Delta T}{P}, \qquad \textbf{Eq. 8}$$

In active mode the rate of the transferred heat from heated tip to sample can be written as a function of thermal power used for the heating of the probe and measured probe temperature.

$$\boldsymbol{Q = P - \frac{(T_p - T_a)}{R_{cant}} - \frac{(T_p - T_a)}{R_s + R_c}}\text{, or} \qquad \textbf{Eq. 9}$$

$$Q = P - \Big((T_p - T_a) g_{cant}\Big) - ((T_p - T_a)(g_c + g_s))$$

where in Eq. 9 P is the same as in Eq. 9 T_a is ambient temperature, T_p is probe temperature, $T_{t,s}$ is tip-sample temperature, $R_{th,s}$- sample thermal resistance, $R_{th,cant}$ is cantilever thermal resistance, $R_{th,c}$ is the thermal resistance of contact. Based on the nature of sample probe tip contact this can be written as

$$\boldsymbol{g_{t-s} = g_{rad} + g_{gas} + g_w + g_{mc}} \qquad \textbf{Eq. 10}$$

Where g_{rad}, g_{gas}, g_w, g_{mc} are heat transfer through radiation, gas conduction, water meniscus, and mechanical contact respectively.

An example showing that the tip sample thermal conductance is complicated as tip doesn't travel to the sample directly and spreads through several channels such as radiation, water meniscus and mechanical contact is shown in Figure 17 where the topographic image and temperature maps were obtained simultaneously [73]. Topography resolution is very high and the signal is clearly very different from the thermal. The centre of hot region is not in the centre of the NiCr resistor because the tip sample thermal conduction is complicated as shown in **Figure 17** The topographic image corresponds only to mechanical tip-sample contact. The thermal image incorporates all of the different thermal conduction paths which have different spatial variation. The thermal image is shifted towards the cantilever side of the tip as heat doesn't travel directly to the sample, there are more channels for heat flows as shown in Figure 15. A lot of the heat travels directly into the cantilever by the air. (Figure 16)

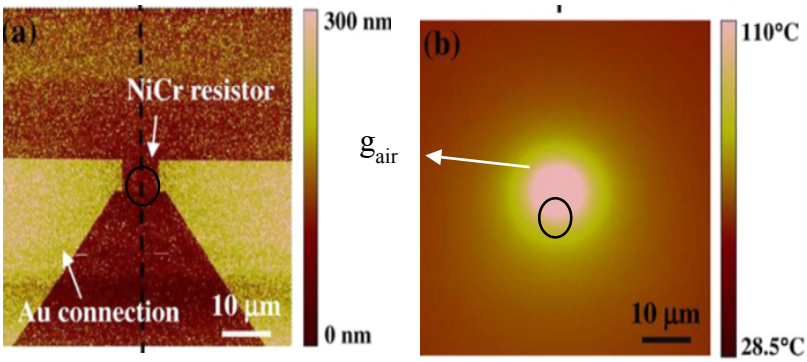

Figure 17 Topography and thermal mapping [73] **reproduced with permission**

In **passive mode** an unheated tip scans along the heated active sample. A very small current (for example, about *I = 1-2 mA* for Wollaston wire probe[91] and *0.1 mA* for a KNT

probe[71], [26]) is passed through the probe, in order to minimize minimal Joule heating whilst it is still possible to measure the electrical resistance.

Various self-heated samples have been fabricated in order to quantify heat transfer between probe and tip in passive SThM mode. [70], [71] Some of these self-heated samples have been designed and fabricated specifically for absolute temperature measurements on the micrometre scale. One which was fabricated for calibration of a nano-thermometer (SThM probe) with accuracy better than 1K on the scale of one micron was based on the use of the measurement of Johnson noise (P. S. Dobson et.al [26].) The instrument used conventional monolithic amplifiers and a custom sensor fabricated by bulk micromachining and electron-beam lithography.

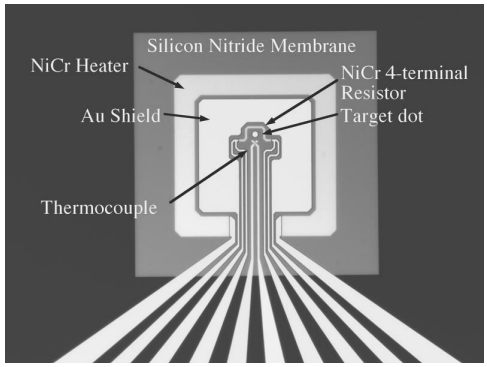

Figure 18 Showing the heated end of the sensor device. [26] **[reproduced with permission]**

The device was constructed so that the temperature of a thermally and electrically isolated metal disc ("dot") was determined by measuring simultaneously the voltage generated by a thin film thermocouple and the Johnson noise in an adjacent resistor (Figure 18).

Johnson noise is a primary standard of temperature. [92] The Johnson noise device was demonstrated as an accurate calibration device, however it suffered from some thermal nonuniformity due to its asymmetric wiring onto the silicon substrate. An improved device having a more symmetric configuration which offered maximum temperature uniformity at the device centre was fabricated by Ge et.al. [71] The device was designed, fabricated and characterised using SThM to provide an accurate and spatially variable temperature distribution that could be used as a temperature reference (Figure 19.) Thermal conductance between the SThM tip and active sample was determined as $1.2 \cdot 10^{-6}$ W/K in air.

By the model proposed in [71] g_{ts} is a value attributed to multiple heat paths. The tip-sample thermal resistance includes thermal resistance due to solid-solid contact, R_{int}, the resistance of the tip Rtip, and sample Rs, water meniscus Rw, and the surrounding air.

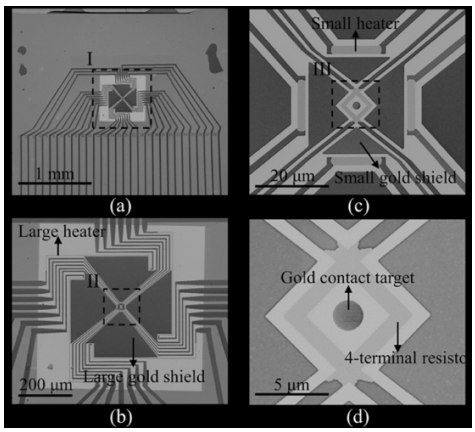

Figure 19 SEM image of the Johnson noise device [71]

For the Nulling probe used in that work it was assumed that thermal conductance through the water meniscus is 1-6 % of the total and so neglected. The temperature on sample surfaces measured was equal, thus spreading resistance was not considered and contact simplified as single contact instead of multi-asperity contact by increasing the pressure as suggested by [76]

In terms of a resistance network [93] the quantity of heat flowing between the tip and sample, $Q_{s\text{-}t,}$ can be written by following equation representing the model shown in Figure 20:

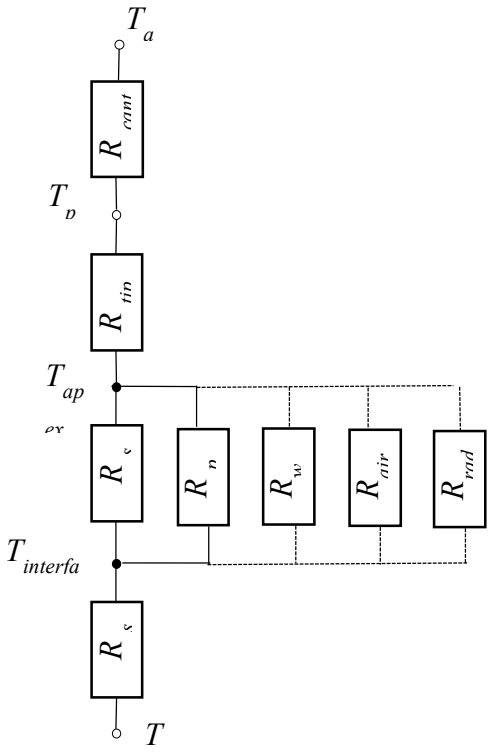

Figure 20 SThM Resistance network in Passive mode

The sample surface which is to be thermally characterised needs to be in contact or very close to the thermal sensor, so $Q_{s\text{-}t}$ is written as

$$Q = \frac{(T_s - T_p)}{(R_{th,s} + R_{th,c})} = \frac{(T_p - T_a)}{R_{th,cant}} \qquad \textbf{Eq. 11}$$

where T_s is the sample temperature, T_p is the probe temperature which needs to be measured. $T_{s,c}$ is sample tip contact temperature and $T_{t,c}$ is temperature at the tip apex.

Tip-sample heat transfer depends on several factors such as sample temperature, tip temperature, cantilever temperature and surrounding medium.

A detailed description of the different heat transfer mechanisms contributing to the probe-sample thermal interaction is important.[90] In order to study probe tip and sample heat transfer we need to understand its nature. Under ambient conditions most of the heat is conducted to the cantilever and through the air gap to the sample surface and only fraction of the heat travels through tip and sample. Therefore, it is necessary to operate SThM in vacuum to avoid heat conduction through gas or liquid meniscus at tip-sample contact. [77], [94](Figure 21)

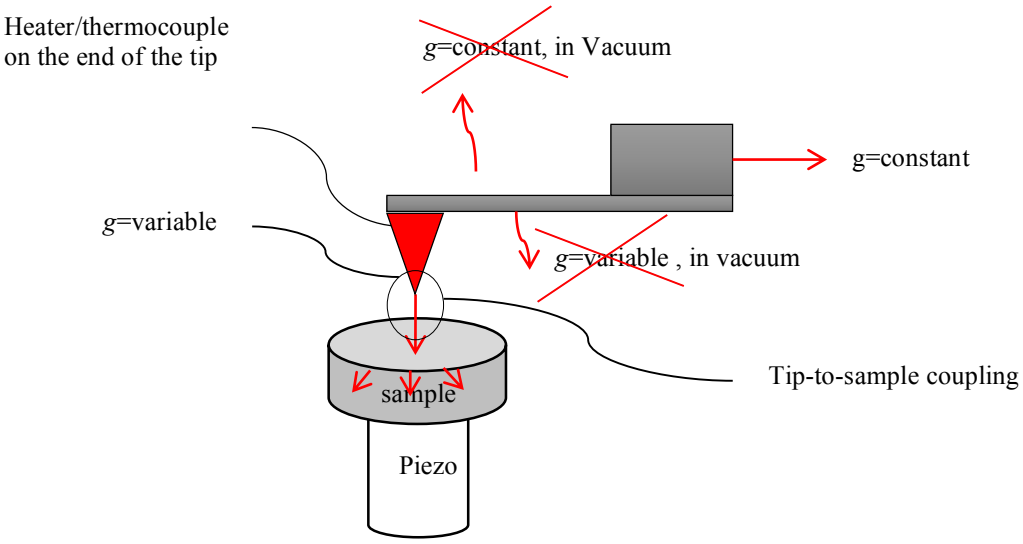

Figure 21 Heat transfer mechanism in vacuum

Thus, when considering heat flow between the tip-sample or sample – tip in vacuum (Figure 21) can be written as,

$$g_{t-s} = \frac{(T_p - T_{cont})}{(R_{th,s} + R_{th,cont})} = \frac{\Delta T}{R_{th,s} + R_{th,cont}}, \qquad \textbf{Eq. 12}$$

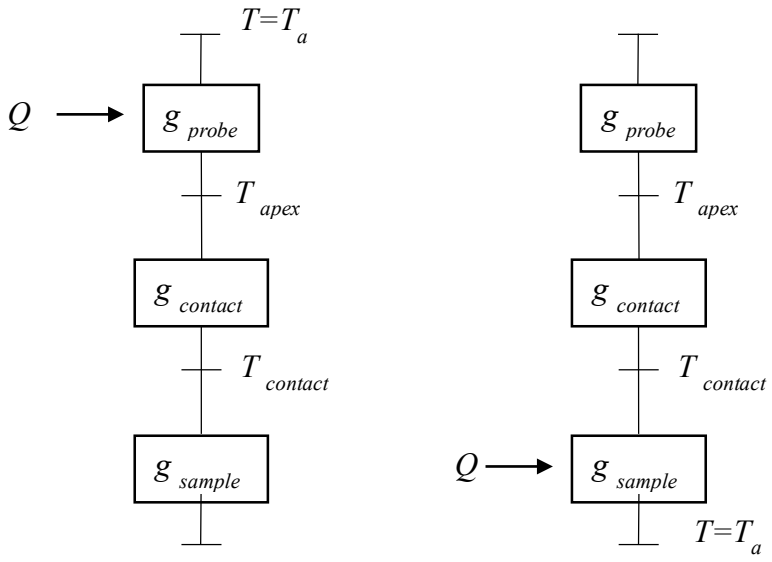

Figure 22 Probe - sample heat transfer

One of the most accurate attempts at Temperature quantification by the self-heating of silicon nanowires in vacuum was performed by Menges et.al. [78] The thermal resistance of the tip-surface contact was measured at DC and then the local temperature was determined from the AC heat flow. The capability of scanning thermal microscope to determine the temperature distribution quantitatively on nanometre scale with a resolution on the order of 20-30 K at approximately 25 nm lateral resolution was shown. However, there are some limitations on the method demonstrated. The sensitivity of the temperature measurements is limited by the resistance measurements of the heater with when scanning in contact mode.[78] The thermal-spatial resolution of that experiment was also limited by the temperature gradient of the sample itself and also by the wear robustness of the SThM tip sliding on silicon oxide during the scan. [78].

Another issue which needs to be considered in sample- probe tip contact is surface roughness at the nanoscale because the effective value of the contact radius can change depending on that factor. As described by Bernd Gotsmann [9] heat transport across multiple nanoscale contacts between an SThM tip and sample was seen as a pressure dependence of thermal transport across a polished nanoscale contact. Also the effect of different materials on the interfacial resistance is important factor to consider. Various sample resistances with the same material surface and roughness and can be fabricated. This effect will be discussed later in Chapter 4 and 5.

It was therefore decided to make measurements of thermal conduction between tip and sample in vacuum during this work. [77]

Chapter 2 Fabrication

2.1 Fabrication background

Before discussing in detail the whole fabrication process, the fabrication facilities which are required for the process and exist in Glasgow will be introduced.

2.1.1 Film deposition

Thermally grown silicon dioxide and Low Pressure Chemical Vapour Deposited silicon nitride are the most commonly used dielectric materials for the membranes due to their low thermal conductivity, high dielectric and mechanical strength and chemical resistance.

There are two common ways of depositing the silicon nitride which was considered within that work: [95] The methods are Low Pressure and Plasma Enhanced Chemical Vapour Deposition (LPCVD and PECVD). The Low Pressure Chemical Vapour Deposition technique was chosen due to desired properties of materials such as a high chemical resistance for the release etch and good thermal and electrical resistivity. These films were deposited at the MC2 Laboratory [3]. [96] LPCVD is used to deposit a wide range of possible film compositions with good conformal step coverage and including those with low stress. The deposition is made on both sides of wafer at a temperature of about 900^0C. [96]

Some semiconductors can be oxidized by various methods. These include thermal oxidation, electrochemical anodization, and plasma reaction. Among these methods thermal oxidation is by far is the most important for silicon devices. [97]

The thermal oxidation kinetics of silicon was examined by B.E. Deal and A.S. Grove.[98] The oxidation of silicon is a key process throughout modern integrated circuit fabrication process. [98] The chemical reactions describing the thermal oxidation of silicon in oxygen or water vapour are given in following equation.

$$Si\ (solid) + O_2 \rightarrow SiO_2\ (solid)\ (dry\ oxidation)$$
$$Si\ (solid) + 2H_2O \rightarrow SiO_2\ (solid) + 2H_2\ (wet\ oxidation)$$

Oxidation is diffusion limited, so hotter means faster growth and thick films take much longer than thin ones. Dry oxidation is slower than oxidation in water vapour, but gives a denser,

[3] MC2 Nanofabrication Laboratory, Chalmers University of Technology
Department of Microtechnology and Nanoscience - MC2
Nanofabrication Laboratory
SE-412 96 Göteborg
Sweden

more chemically resistant film because fast oxidation leaves more dangling bonds at the silicon surface.[99]

This results in a dense chemically resistant SiO_2 film in a convenient time which is still sufficiently long to allow good control of film thickness by varying the diffusion time. Thermal oxidation was performed in furnace by dry oxidation in an Oxidation furnace available Rankine building cleanroom, University of Glasgow. [4]

The general oxidation equation for thickness and time kinetics is given by

$$\boldsymbol{x_0^2 + Ax_0 = B(t + \tau)} \qquad \text{Eq. 13}$$

A, B and τ coefficient can be taken from [98]. The coefficient for 975^0C was also calculated.

$$975^0\ \mathrm{A} = 5.16\mu; \mathrm{B} = 0.000841\frac{\mu^2}{\mathrm{h}}; \frac{\mathrm{B}}{\mathrm{A}} = 0.0434\ \mu/\mathrm{h}$$

The relevant properties of thermally grown silicon dioxide and LPCVD nitride are shown in Table 1. At the temperature of 975° and above no stress was observed for the dry thermal oxidation process. [100]

Table 1 List of thermal oxide and LPCVD nitride properties taken from [98],[101],[102]

	Value	
Property (units)	SiO_2	Si_3N_4
Thermal conductivity (W/m-K)	1.3	15-30
Specific heat (kJ/kg-K)	1.0	0.7
Young's modulus(GPa)	66	290
Film stress at 25^0 C (dynes/cm^2)		2-4X10^9

2.1.2 EBL and photolithography

The word lithography came from the Greek words *lithos* meaning "stones" and *graphia* meaning "writing". [103]There are three types of lithography available at Glagow: photolithography, electron beam lithography and nanoimprint lithography[5]

Photolithography is a process which is mostly used in microfabrication to generate patterned thin film or bulk materials. [104] Photolithography uses UV light to transfer patterns

[4] Rankine building cleanroom, University of Glasgow, Oakfield Avenue, G12 8LT, Glasgow, UK

[5] EV Group, Germany, EVG 6200 Nano imrinter

through a glass chromium photomask which is an opaque plate with holes that allow UV light to shine through defined features. This allows photolithography to be highly efficient and cost effective while writing patterns. However, photolithography requires a completely flat surface in order to produce effective patterns. Contact photolithography is limited to pattern features just less than 1 um. [105], [104] The equipment used for the photolithography exposure in the James Watt Nanofabrication centre is either MA6 or MA8 [6].

Photolithography includes several important steps in order to write the features. The first step is substrate cleaning. The substrate needs to be properly cleaned from contamination prior to photoresist coating. Typical types of contamination which need to be removed are dust from scribing or cleaving, atmospheric dust, abrasive particles, lint from wipers, resist residue etc. The most common way to clean the substrate is the solvent cleaning which involves soaking in Acetone, Methanol, IPA with ultrasonic agitation for 2-5 minutes each and finishing with DI water cleaning and blow drying with N_2. Another option to clean the substrate is "pirhana" cleaning which can be done either with Sulphuric Acid/ Hydrogen peroxide or commercially available MDS20/water with 1:1 proportion. To assist better resist coating adhesion promoters/primer can be used before resist spinning.

This step is followed by photoresist application. The wafer or sample is held on a spinner chuck by vacuum to get uniform resist thickness by spinner coating. Typically, it will be spun at 3000-6000 rpm for 15-30 sec. The first baking stage called also soft bake follows after the resist has been spun. Resist can be soft baked either in an oven or on a hot plate.

After the resist has been baked it is ready to be exposed with UV light through the photomask. There are two type of exposure: Top side and bottom side exposure. This is useful when some of the features, for example, cleave lines, need to be patterned on the back side of the wafer. It is essential to align the bottom side of the wafer to the top side and the photomask to the sample before exposure. The photomask is a master pattern which is transferred to the wafer. After being exposed the sample needs to be soaked in a wet chemical development solution to develop the required features. To stabilize and harden the developed photoresist prior to processing a hard bake is required. This post exposure bake is essential for dry etch process however it is not needed for a processes in which a soft resist is desired, for example lift off. After the resist pattern is transferred into a useful material the photoresist can be removed.

Electron beam lithography Electron beam lithography (EBL) is a powerful technique for creating nanostructures with very high resolution that are too small to fabricate with conventional photolithography. [104], [106], [107] The technique works by moving a highly

[6] MA6/MA8 Part number: Rev.01182427 07-03. SUSS Micro Tec SE, Schleissheimer Str.90, 85748 Garching, Germany.

focussed electron beam over a sample to write out a pattern designed with suitable CAD tools. Electron beam lithography consists of writing of very small patterns in a radiation sensitive film called a resist. These patterns are then developed in chemicals which selectively remove either exposed or unexposed resist (positive or negative tone respectively). There are different developers for different resist. The developers used will be listed later in Table 2. Typically nano-lithography is carried out using a vector scan Gaussian beam tool[108], which is the tool available in Glasgow. The overall e-beam lithography process is shown in Figure 23.

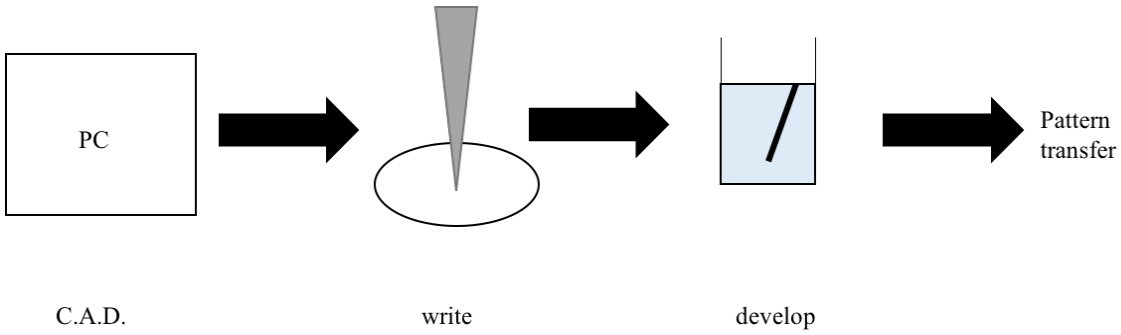

Figure 23 The overall e-beam lithography process

Unlike photolithography, no mask is required. The pattern data is held only in software in the computer. Therefore CAD forms a significant part of the e-beam lithography process.[109] The pattern on the micro and nanometre scale was drawn and designed in Layout editor Tanner L-edit software [7] which is the CAD package used in Glasgow. Once a pattern is designed it needs to be saved in GDSII format and sent through the computer network to the lithography tool via pattern fracturing software. The job to be written on the e-beam lithography tool is created by Beamer software which runs on "scotty", a linux server.

Exposure is followed by the development stage which is a simple dip in a developer solution for the required duration of time, then rinse and blow dry.

An EBL system consists of a chamber, an electron gun and a column[110]. E-beam lithography usually uses 50-100 kV electron beams with diameters in the range 3-400 nm depending on the feature size required.

The advantages of ebeam lithography over conventional phtolithography are following: better resolution about 20 nm [110], gives better layer to layer alignment, is more flexible as no mask required to write a pattern. However, it is slower and more expensive. E-beam resist (PMMA) has worse etch resistance compared to photoresist.

[7] Tanner Research, 825 South Myrtle Avenue, Monrovia, CA 91016. Tanner L-Edit

The tools used for EBL in JWNC are VB6 UHR EWF[8] and Nanobeam nB5[9].

List of photoresists and e-beam resists are placed in Table 2.

Table 2 Photo- an e-beam- resist [10] available in JWNC

Ebeam resist type				**Photoresist**			
Positive		Negative		Positive		Negative	
Resist name	Developer used	Resist name	Developer used	Resist name	Developer used	Resist name	Developer used
Polymethyl methacrylate (PMMA) [111], [112]	MIBK	Hydrogen silsesquioxane (HSQ) [113]	CD26, TMAH	S1800 series	MF319 MF321/10	SU-8 [114]	
ZEP[115]				UVIII [116]	CD26		
UVIII[117], [118],[112]	CD26			LOR [119]	CD26		
CSAR 62[11] [120]				AZ4562 [121]	AZ-400 developer		

As mentioned before, depending on desired features the photoresist and ebeam resist used can either be negative or positive tone. After exposure through the mask window the uncovered area will remain and covered area will be removed for negative resist. The remaining resist after exposure will be for the covered area for positive resist as shown in **Figure 24**

[8] Vistec Electron Beam GmbH, Ilmstrasse 4, 07743 Jena Germany. VB6 UHR EWF.
[9] Nanobeam LTD, Unit 4, College Business Park, Colhams Lane, Cambridge, CB1 3HD
[10] MicroChem Corp. 200 Flanders Road, Westborough, MA 01581 USA, MICROPOSIT™
[11] ALLRESIST GmbH, Am Biotop 14, 15344 Strausberg, Germany

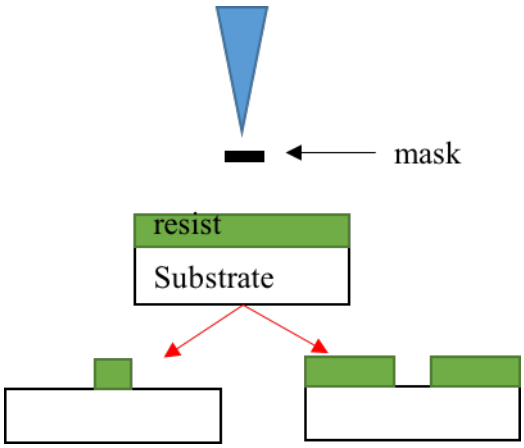

Figure 24 Resist processing for positive resist (left) and negative resist (right)

Alignment markers for ebeam and photolithography

Alignment markers are important when doing multilayer lithography. It is important to label each alignment mark in order to identify them because marks are damaged during the exposure process when being used. One alignment mark is sufficient to align the mask and wafer in x and y but it requires two alignment marks to correct for rotatory offsets.

In photolithography there are 3 methods for aligning a sample: contact, proximity, and projection. In the contact method a resist coated sample is brought into physical contact with a wafer and held by vacuum. The advantage of this method that it gives a possibility of high resolution, however due to very close contact, resist from the sample can cause contamination and damage to the mask. The proximity method is similar to the contact method with the presence of small gap of 10-25 um between sample and mask during the exposure. This gap will minimize the damage to the mask however it gives poorer image. In the projection method mask damage can be avoided entirely. An image of the pattern on the mask is projected onto the resist-coated wafer which is several centimetres away. To achieve a high resolution image only a small part of the mask is imaged. All alignment procedures are performed by user in photolithography.

In ebeam lithography at Glasgow there are three common markers used: Cross marker, Global markers, and Cell markers. The whole structure (wafer/small sample) consists of number of individual cells with four markers patterned in each corner positioned with the same distance one to the other.

First of all a cross marker, defined by the offset distance from (0;0) position region to the cross, will be located. In ebeam the starting point (0;0) for the wafer is considered a center of the wafer and for a small sample is bottom left corner. For each level fresh markers need to be used, so patterning number of cross markers and number of cell/global markers is essential [122], [123].

The alignment takes place in two stages: global alignment and cell alignment. Each stage

requires four markers known as a marker group. The global alignment is carried out once, near the start of the job, whereas cell alignment can take place many times. After finding a global markers the ebeam job will start to be written and will be attempt to find each cell and expose it.

The global markers should be large enough, so they can be found quickly even with large initial error and need to be well separated from other features. Cell markers can be smaller as their position is well known after the global marker search. However the same markers could be used for global and cell alignment.

The photolithography and ebeam markers used for device fabrication are described in table 3 below.

Table 3 Alignment markers

Marker type	Image	Description
Alignment stripes	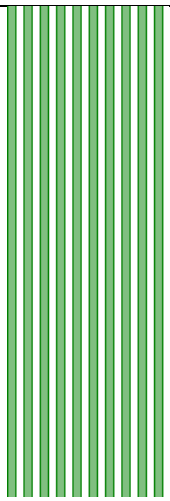	As there are no alignment marks on the wafer before the first pattern transfer an alignment is typically done referring to the wafer flat. Thus Markers used in first level of photolithography are several stripes to align wafer flat. This is an important alignment part in the first level of lithography in order to accurately pattern features for wet etching of (100) orientation of Si wafer.
MA6 circles		Circles with various diameters can be used in photolithography for back side alignment as well as accurately aligning in X and Y directions. After being patterning on the back side of the wafer in previous level of photolithography and after being wet etched, this type of marker can be used to align the back side of the wafer to the top side of the wafer
Cross markers	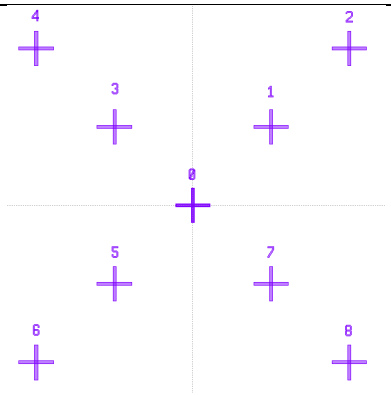	The cross marker is an ebeam marker used to find the starting position to be able to find the global markers on loading the wafer into the exposure tool. Starting from (0:0) position the first step in an ebeam job is finding a cross before defining the actual coordinates and position of features. It is essential to have fresh not exposed cross markers for new level of ebeam lithography as they will be damaged after exposure.
	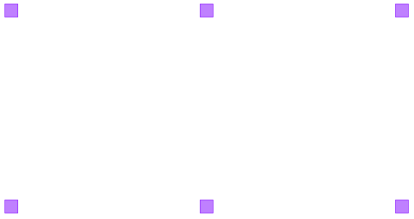	Pit markers – Square alignment markers are used as a global position reference to align the whole wafer and cell markers are used to align each individual cell.

2.1.3 Evaporation. Lift off

Evaporation is common technique to deposit a thin film of metal in vacuum [124]. The vacuum allows vapour particles to move directly to the substrate surface, where they condense back to a solid state. One technique used for patterning desired metal features is called the lift off technique, which is known as a method for making a metallic patterns on a substrate especially for noble metals such as platinum, gold and other metals such as nickel, tantalum etc. [125] The process (Figure 25) includes firstly, defining a pattern by lithography using a bilayer of resist for ebeam lithography or just layer of resist with undercut for photolithography. The undercut allows removing of unwanted metal easier. This is only true for an evaporated film, as it is deposited with a well-defined direction Then the metal film is evaporated on top of the substrate, including resist and substrate where resist was cleared by developer, and finally the photoresist under the film is removed with solvent, taking the film with it, and leaving only the film which was deposited directly on the substrate. Metallic structures can be patterned by photoresist[119] or ebeam resist [126] or ebeam/photoresist [126]. The metal deposition tool used in Glasgow are Plassys Sputter tool, Plassys electron beam evaporators, Manual Thermal Evaporator and Plassys Confocal Sputter Tool. [12]

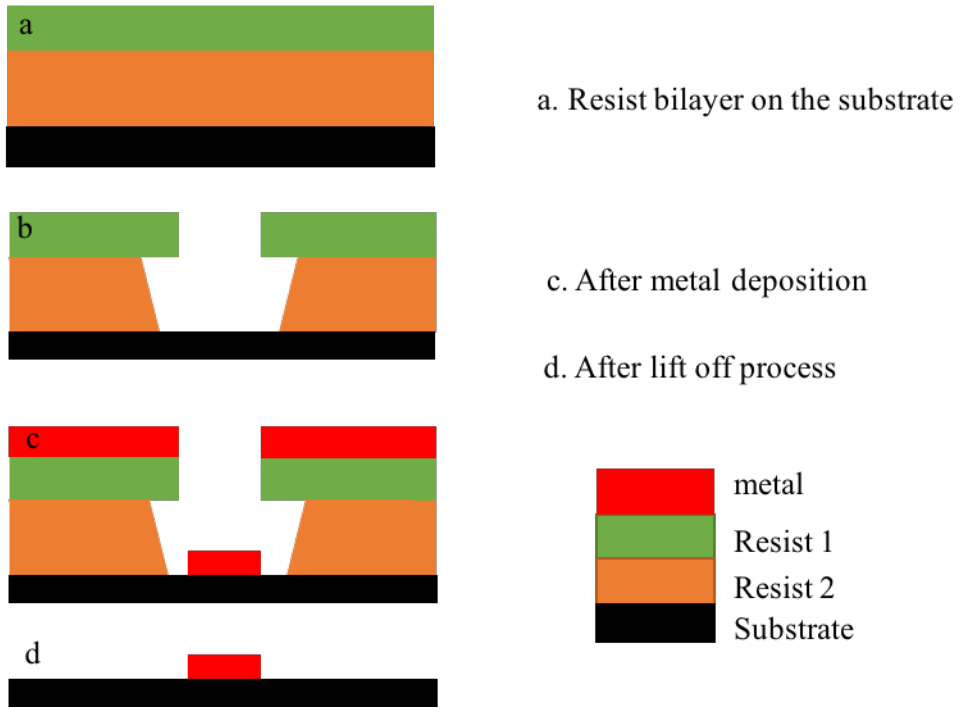

Figure 25 Lift off process

[12] Plassys Bestec, 14 rue de la gare, 91630, France, MP 900S, MEB 400S, 550S, 400, MP 600S.

2.1.4 Etching

One of the major parts of the device fabrication process is micromachining. Micromachining is the fabrication of micromechanical structures with the aid of etching techniques to remove part of the substrate or deposition techniques to add a thin film.[127] The type of micromachining used in the membrane fabrication is called “Bulk micromachining”[128] which encompasses techniques that remove significant amounts of Substrate (bulk) material and in which the bulk is part of the micro - machined structure. (Figure 26)

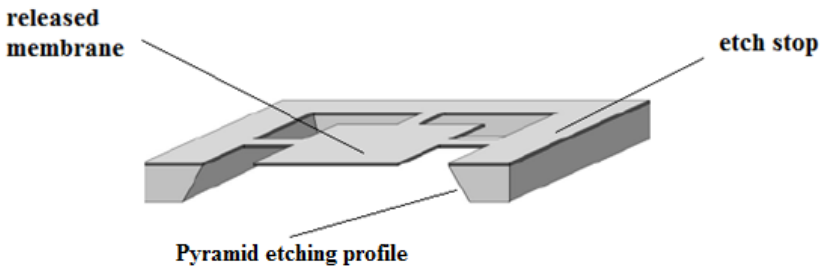

Figure 26 Typical bulk micro - machined structure of membrane

Substrate removal can be performed using variety of techniques and methods which may be derived into either “wet etch”, when the phase of the reactants is liquid, almost exclusively relying on aqueous chemistries, or “dry etch”, when reactants are in the plasma phase. Also depending on the requirements the etching there are two types of etching which may be chosen: anisotropic or isotropic.

The wet etching process involves multiple chemical and physical processes. Firstly, the etchant species is transported to the surface of the wafer. This step includes diffusion of the etchant towards the surface and absorption of the etchant. This is then followed by the chemical reaction between etchant and exposed surface. Finally, the products of the reaction will desorb and move away from the surface by diffusion.

When a material is attacked by wet etchant with uniformity in all direction it causes an isotropic etch. Typically wet etching is isotropic. However, on crystalline materials, for example Si, the etching rate is typically lower on the more densely packed surface than on a loosely packed surface. This effect can allow very high anisotropy. Etching a (100) silicon wafer with KOH results in a pyramid shaped etch pit as shown in Figure 27. The etched wall will be flat and angled. The angle to the surface of the wafer is 54.7°.

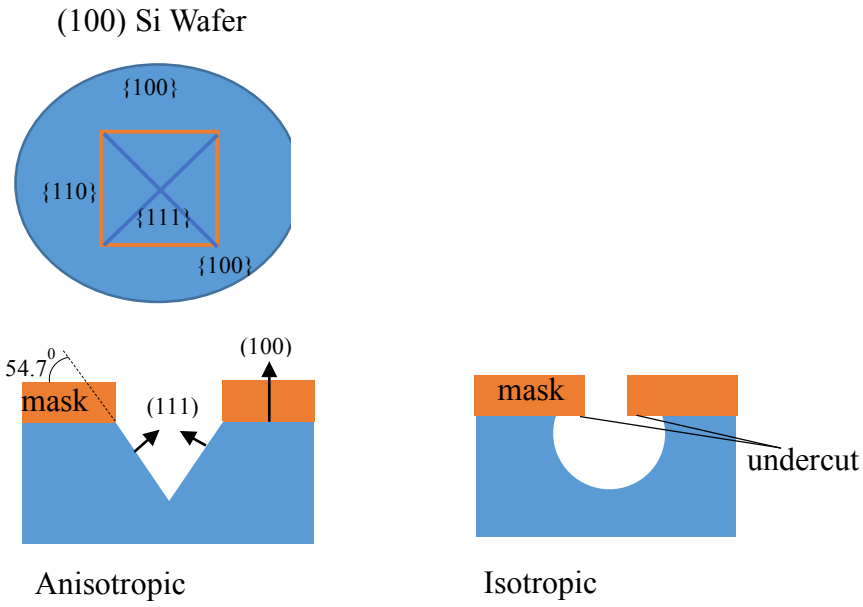

Figure 27 Wet etching technique

Some wet etches are classified as anisotropic because different crystal planes etch at different speeds. The most commonly used anisotropic etchants for silicon are (EDP) [129], KOH [130], [131] and (TMAH) [132]. KOH and TMAH are anisotropic silicon etches, used to make V-grooves, membranes and holes through wafers, as well as other devices. When Isopropyl alcohol is added to the KOH better surface roughness can be achieved [133]. Ethilendiamine-pyrocatechol-water (EDP) also gives a smoother surface than pure KOH [129]. TMAH is an organic hydroxide with slightly lower etch rate compare to KOH and with more surface roughness left after the etch [134].

In the case of crystalline silicon, isotropic wet etching can be done using a solution containing a mixture of hydrofluoric acid (HF) and nitric acid (HNO_3) with an etch rate which depends on HF concentration[135].

Dry etching is one of the widely used processes in MEMS because is easier to control and is capable to defining feature sizes smaller than 100 nm due to lower etch rate and selectivity. However, dry etch requires expensive machinery. In general, it is better for smaller features (nm size) and also suitable for a fragile structure where wet etch is not working because of surface tension.

The mechanism of dry etching is based on a controllable combination of ion bombardment (anisotropic) and radical chemical (isotropic) etching which offers a tunable etch rate, profile and selectivity. Assuming the same, suitable gases are employed, a low pressure and large electric field favors ion bombardment resulting in a more anisotropic profile; whereas higher pressure plasma with lower electric field gives a less isotropic profile.

The general dry etching classification is shown in Figure 28.

Isotropic	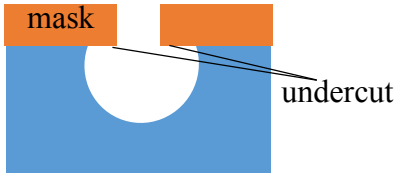	$anisotropy = \frac{v_{horizontal}}{v_{vertical}} = 1$
Anisotropic	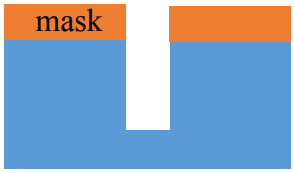	$anisotropy = \frac{v_{horizontal}}{v_{vertical}} = 0$

Figure 28 Etching technique diagram

There are two type of plasma etching in JWNC: Reactive Ion Etching (RIE) and Inductively Coupled Plasma (ICP). RIE combines physical processes with chemical reactions. It uses a chemically reactive plasma generated under a low pressure (20-200mTorrr) to consume materials deposited on the wafer, along with non-reactive ionic bombardment. The ICP employs radio frequency generated by the electromagnetic induction coil to create plasma of ionized atoms and radicals. (Figure 29)

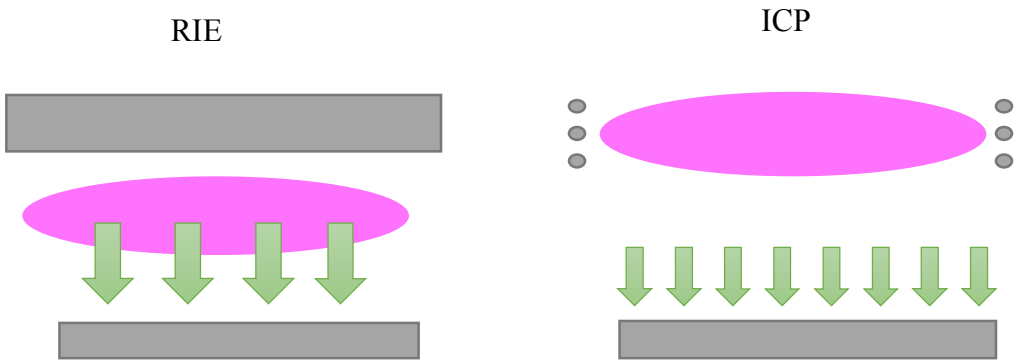

Figure 29 RIE and ICP principles

In RIE one power controls ion density and ion energy. In ICP ICP and bias power control ion density and ion energy separately. The substrate is part of plasma generation region in RIE and in ICP it is not. RIE has a higher probability to move etchants in the direction of electric filed and produces a more anisotropic etch profile. ICP often provides better performance because of lower ion bombardment to substrate, lower plasma damage, higher ionization degree 10^{-4}-10^{-1} (RIE - 10^{-6}-10^{-3}) and higher plasma density 10^{11}-10^{12} cm^{-3} (RIE-10^{9}-10^{10} cm^{-3})

2.2 Device fabrication

2.2.1 Passive device

Quantification of thermal conductivity measurements by SThM is also achieved [51] by calibration of the thermal loading of the tip using a range of samples of contact resistance/conductance. This is inconvenient in that it requires many samples to be scanned to acquire a calibration and may lead to problems of contamination or reproducibility of surface preparation between different samples such as the embedding of polishing paste in the surface of a metal during polishing.

The passive devices rely on strong thermal isolation from the underlying substrate, achieved through a suspended membrane. The temperature rise depends on the material, the width of the supported arms and number of supporting arms rather than a change in material.

The fabrication of the passive device includes 3 main stages. The first stage defines individual chips by fabricating alignment structures and cleave grooves. The second stage is lithographically patterning the gold markers for device layer alignment and gold structures to modulate thermal conductivity for different thermal contrast. The final stage is isolating the silicon dioxide membrane from the Silicon substrate using an isotropic dry etch to avoid damage to the membrane.

To fabricate the device a 3-inch (100) Si wafer coated by 40/60 nm of SiO_2/Si_3N_4 deposited from both side was used as the starting material. Due to the better selectivity of Si_3N_4 to alkaline anisotropic etches the thin Si_3N_4 layer was better able to withstand an etch through 320 nm of Silicon than a much thicker film of oxide alone. The use of a thin oxide layer close to the surface of the silicon provided better adhesion and stress control of the nitride film. These films were deposited at MC2 Laboratory [13].

The first stage diagram is shown in Figure 30.

[13] Nanofabrication Laboratory, MC2 Chalmers, SE-412 96 GOTHENBURG, SWEDEN

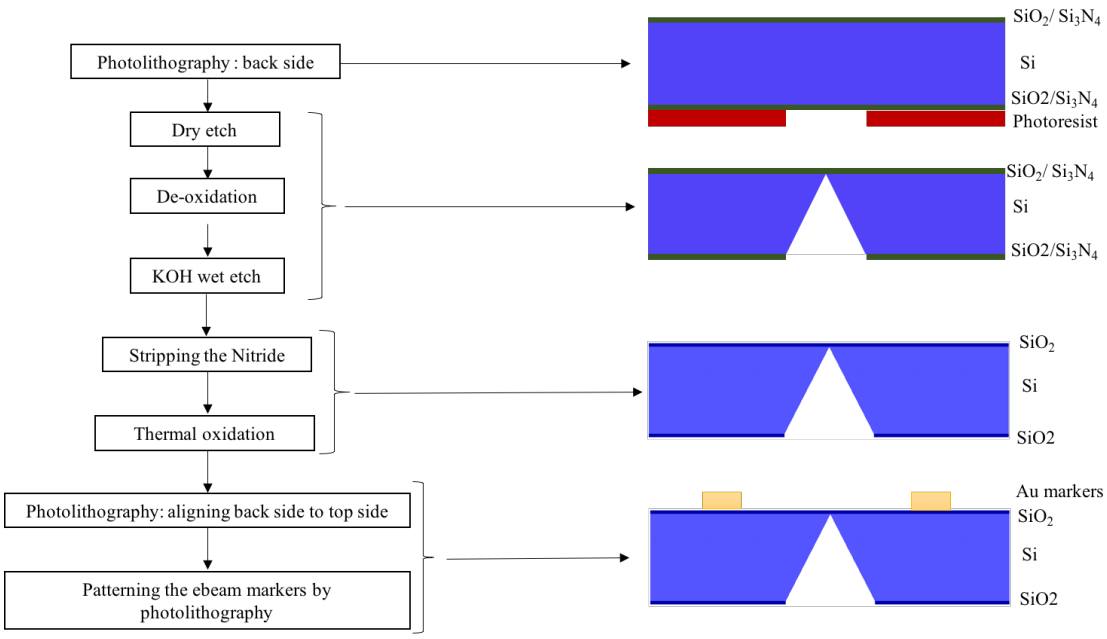

Figure 30 Defining individual chips

To define the Nitride, the back side of the wafer was covered with S1818 photoresist and then was exposed by UV light using a mask by photolithography. Next a dry etch process using an RIE etch in BP80 tool in C_2F_2 gas was used to remove the Nitride from defined windows. Following a deoxidation of the surface, the Si was etched by anisotropic wet etching with 5% KOH solution at 105 ^{0}C in order to get V-shaped grooves.

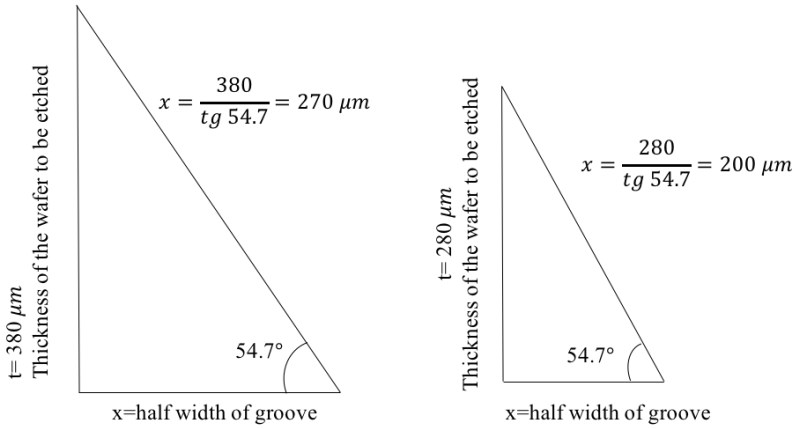

Figure 31 Definition of width of grooves for wet etch.

The sizes of the grooves were calculated to be 400 and 540 μm to etch all the way trough until etch stop and also leave some Si by wet etch principle discussed in section 2.1.4 Etching (Figure 31).

The circle photolithography markers were used as a marker for aligning the back side to the front side of the wafer after being wet etched. The thin film of oxinitride was then stripped after being used as an etch stop for the wet etch process. The detail of the back side wafer processes can seen from the Table 22 in Apendicies A.

After stripping the oxinitride from the wafer there is a requirement to grow the film for the thin film membrane. A 50 nm membrane was grown by dry thermal oxidation. Dry oxidation was chosen as it gives a denser, more chemically resistant film.

After oxidation there is a need to align the back side of the wafer to the top side. The principle of back to top side alignment is shown in Figure 32. The features patterned in previous level of photolithography after being anisotropically wet etched can be used as a marker. Markers on the back side of the wafer are projected and monitored on the screen allowing alignment to the front side of the wafer and patterning ebeam markers for future ebeam lithography levels. The front and back microscopes are aligned to each other and the images combined to show the back and front sides in registration with one another

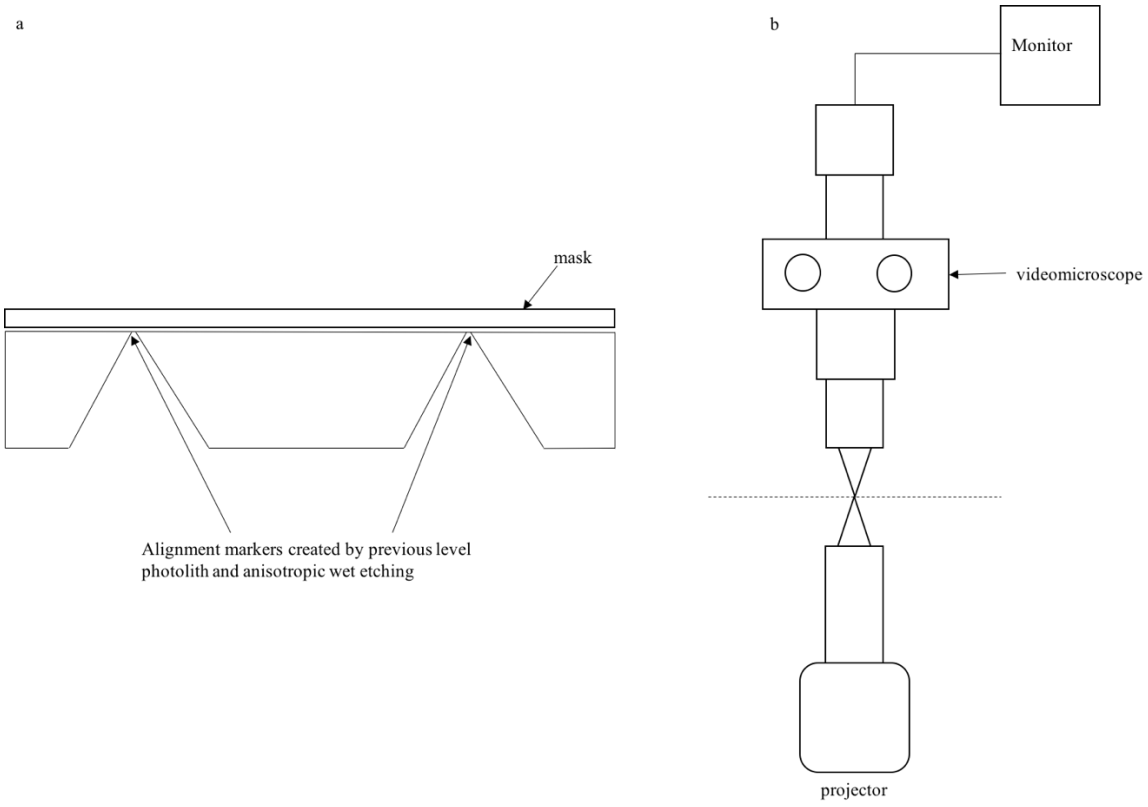

Figure 32 a. Schematic overview of front to back side alignment. b. Alignment principle uses two optical microscopes which are aligned to have a common optical axis to image the back side of the wafer and the mask position on the other side of the wafer. The use of photolithography is necessary as the wafer is opaque to electrons

There are two types of photolithography mask designed for the process. The first is used for patterning cleave lines, as described above. The second one is used for aligning the back side

of the wafer to the top side by patterning 20 μm rectangular e-beam markers and cross markers for aligning next levels of e-beam lithography (Figure 33). Gold e-beam markers were patterned by photolithography using bilayer of LOR 3A and S1818 photoresists. Metal markers should be Au or some other dense, high atomic number metal with a thickness at least 40 nm need to provide significant contrast in back-scattered electron imaging mode. [136]

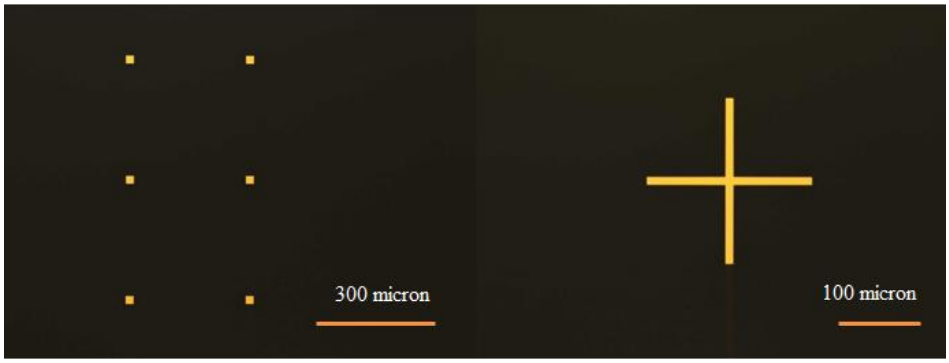

Figure 33 E-beam markers with a cross shape to define the centre of the wafer and 20µm squares to align to the pattern. Multiple square markers are defined as the process of imaging causes subsequent processing to damage the marker. The cross marker is found manually and the operator easily ignores visible changes due to processing damage

The next stage is patterning a metal structures on top of the membrane by ebeam lithography, metallization and lift-off. The detailed description of the process can be seen from the Apendicies B.

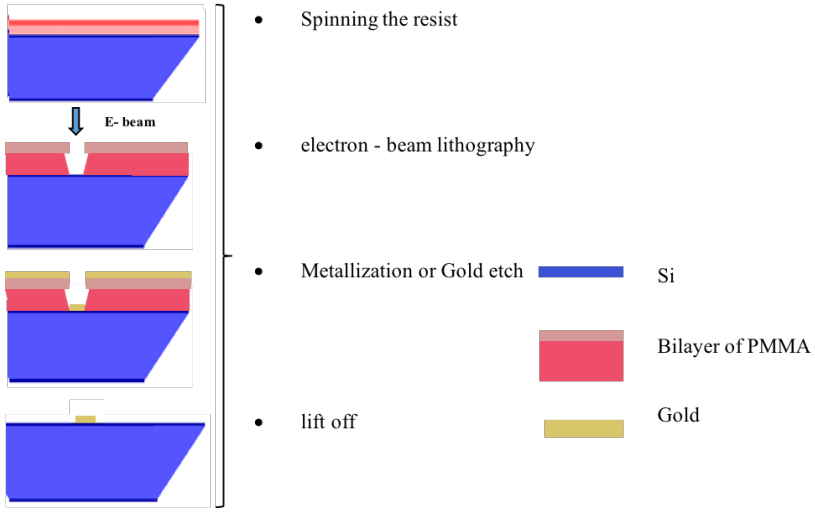

Figure 34 Patterning the metal structures using a bilayer of PMMA resists of different molecular weights to give an undercut resist profile

Small and big gold squares, as well as fully covering the membrane with gold were patterned in the second stage of device fabrication (Figure 35). In order to get the required range of thermal resistance values, a number of different membrane geometries were fabricated by varying number of supported legs, their width, and the presence or absence of evaporated Au on

the centre of the membrane, corresponding to the modelled designs (Figure 35) which will be discussed in result part.

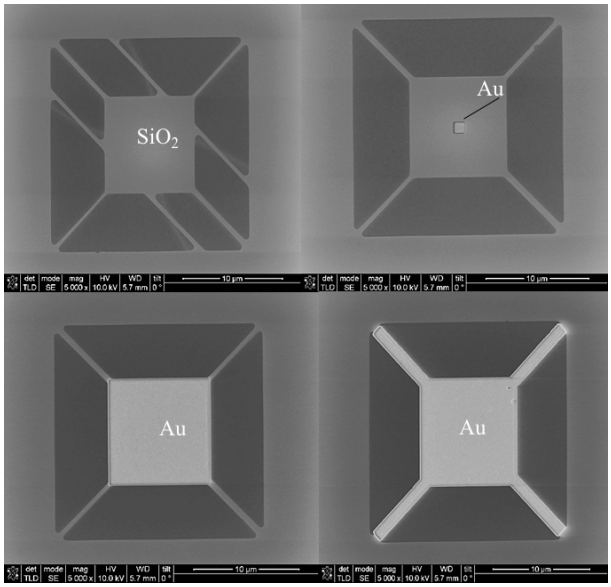

Figure 35 Changing a geometry and adding an extra material to the membrane gives different degrees of thermal isolation using the same set of process steps

The last process stage is the thermal isolation the device from the silicon heat sink which was done by e-beam lithography and dry etch. The process diagram of final third stage is shown in Appendices D.

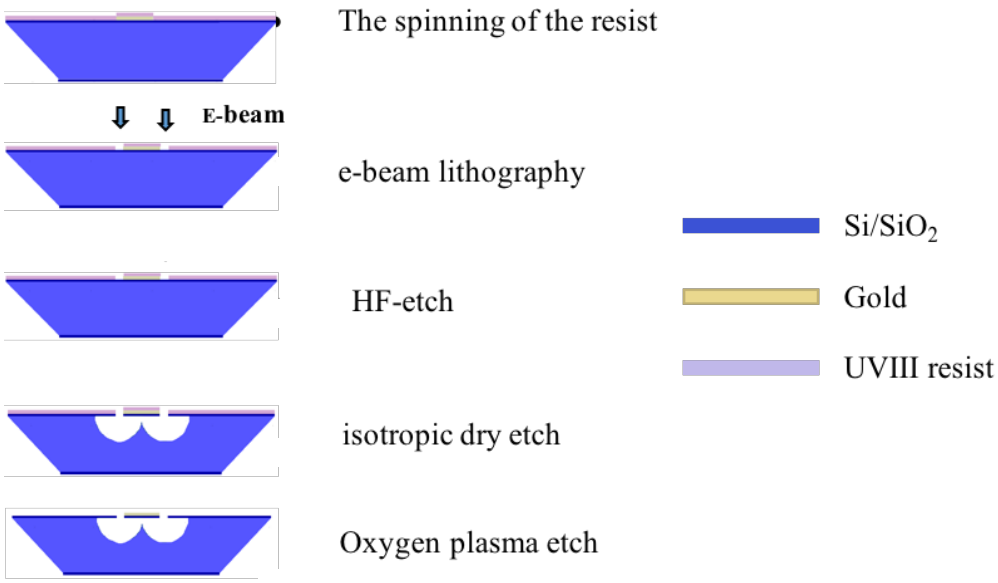

Figure 36 Thermal isolation of the membrane. The membrane shape is defined by a wet HF etch, then the same mask is used to define the extent of the isotropic silicon dry etch which removes the silicon below the membrane. The mask is eliminated by an oxygen etch because the use of a solvent would cause the membrane to collapse due to surface tension

From a device design point of view, making the supporting arms as narrow as possible will make the membrane more thermally isolated from a heat sink, minimizing the thermal conduction through it. This requires using electron beam lithography instead of photolithography due to the small minimum feature size required for thermal isolation and high aspect ratio of resist thickness to width required due to the etch selectivity of the UVIII resist. Therefore, e-beam lithography was used to pattern supporting arms leading to the membrane. Firstly, the SiO_2 was etched by buffered 5:1 HF. The HF etch is safe because the membrane is still supported by silicon and so is not damaged by capillary forces.

Due to surface tension and the fragility of the membrane anisotropic wet etching for membrane release as used in [30], [16] is not applicable. [137] Thus thermal isolation of the membrane from the Si substrate was performed by an isotropic dry etch. There were a choice of two dry etch tools available in JWNC for isotropic dry etching. The dry etch test was done using an STS RIE [14] etching tool and ICP plasma etching with an ESTRELAS [15] [138] tool in order to find the etch rate and a suitable resist as a mask material.

As described in [139] a mixture of SF_6 and S_4F_8 was required for getting a sloped sidewall profile to fully release the membrane from the Si heat sink. [140] The process requires $1\mu m$ thick e-beam resist to protect the metal from etching. The etch developed in reference [19] was used to release structures of greater than 50μm width which had been defined using thick AZ4562 photoresist. So several tests were done with AZ4562 photoresist (Figure 37)

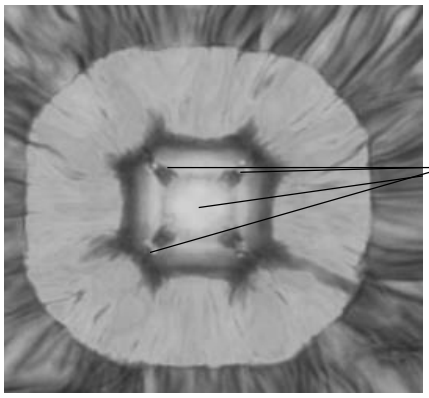

Figure 37 Failing process with photoresist showing absence of narrow membrane supports

The AZ4562 photoresist didn't work due to the high aspect ratio and small size of the supported arms, about $5\ \mu m\ resist$ thickness and $1\mu m$ width, as the all resist from membrane area was washed away during the developing. It was impossible to pattern the suspended arms of the membrane with widths of $1\mu m$ and below. The need to maximize the thermal isolation of the

[14] STS ICP RIE

[15] Oxford instruments, Tubney Woods Abingdon, Oxfordshire OX13 5QX United Kingdom, PlasmaPro 100 Estrelas Deep Silicon Etch System.

membrane by making the arms as narrow as possible necessitated the use of e-beam lithography and a different resist. [141]

Using e-beam lithography instead of photolithography solved the problem. The most common e-beam resist is positive PMMA resist. However, the PMMA resist cannot be used due to the high etch rate of the resist in the plasma. As described in [142] the selectivity of PMMA/Si etch rate is about 1:1 when RF power is 200 W. The increase of the RF power needed in order to release the membrane would be expected to make selectivity worse.

Another option is the positive photoresist UVIII which can also be used as a positive e-beam resist. The advantage of this resist is good selectivity and resolution, but the disadvantage is that resist suffers from delay effects, which is a change in sensitivity with the time delay between the exposure and post exposure bake process.[143] The solution is to bake it after being exposed and develop immediately.

A dose test was required to avoid membrane failure.

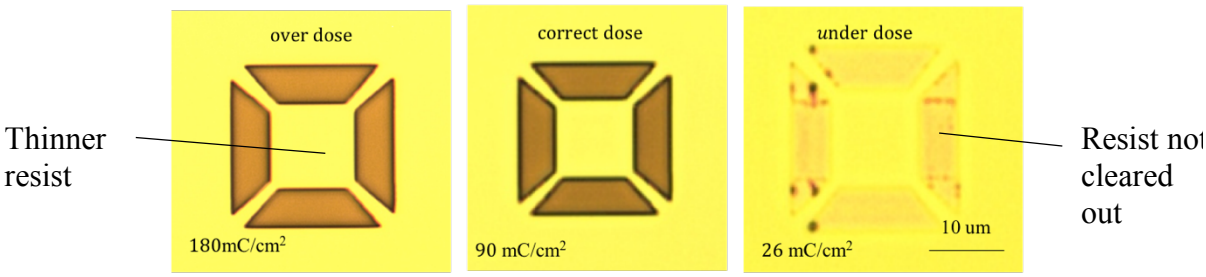

Figure 38 Dose test showing the effect of over and underexposure on the resist structure

A dose test was performed for UVIII from 25-180 mC/cm^2 and optimal dose of 90 mC/cm^2 was found for the process as shown in **Figure 38**. [144]

UVIII resist is suitable for the process. As was discussed in section 2.1.4 Etching dry etch is a good choice for an isotropic etch . The STS ICP tool was chosen as it provides better performance than RIE. Halogen based SF_6 gas was chosen as it attacks Si and the metal structures will be protected by resist. By increasing the Coil power to 650 W the etch rate increased to approximately 7.6 um/min in vertical direction and 3.6 um/m in lateral direction with selectivity resist/Si about 1/230.

The $\mathbf{1}\ \boldsymbol{\mu m}$ thick bilayer of UVIII used as a mask material for 2 processes: Etching of the oxide membrane and release of the membrane by plasma etch of the underlying silicon. A bilayer of resist was spun in order to get a thicker resist layer. One layer after the other followed by soft bake between.

After exposure of positive resist almost all resist will be cleared out from the exposed area. However, there is a presence of very thin layer of some resist residues that was hardened

after the exposure and was not cleared out during development. After patterning the desired features, HF etch of SiO_2 layer was performed immediately which caused undesired effect because HF was not able to etch the resist residue (Figure 39) In order to solve that problem, it required 'ashing' of the surface in dry plasma to clean the developed area from positive UVIII resist residue. The resist residue was cleaned by an Oxygen plasma etch on 80 Watts.

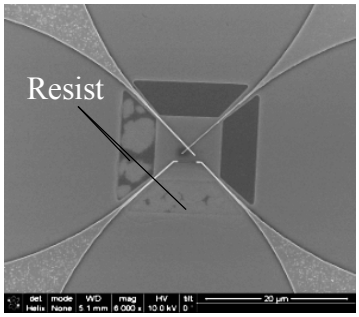

Figure 39 Resist residue after exposure and development resulting in masking of the SiO_2 layer from the HF etchant

SF_6 gas silicon etch at high power is exothermic as there is a chemical reaction that releases heat and the wafer is also heated by the plasma. Therefore, the back of the sample is cooled using helium gas during etching to prevent the wafer getting hot and melting the resist. So the back side of the wafer needs to be protected. The wafer size of the starting material is 3" and the etcher is designed for use with 4" wafers so it is required to mount sample on a carrier wafer in such a way that wafer makes good thermal contact. This involves the use of a glue. Hence "Crystal bond" [16] was used for wafer bonding. It is vacuum compatible and may be removed by dissolving in water, being careful not to get water on the front of the wafer which would destroy the membrane by capillary force. Adhesive 555 crystal bond [145] was chosen to stick the sample on carrier wafer for the dry etch process. The carrier wafer can easily removed by heating it on the hot plate up to 60°C. To strip the resist after the Si isotropic etch process a dry etch is also required. As the membrane after being isotropically etched became extremely fragile and due to the need to avoid capilary forces the resist was stripped in dry Oxygen plasma using an RIE tool.

The fully released SiO_2 membrane is shown in Figure 40

[16] Agar Scientific Ltd, Unit 7, M11 Business Link, Parsonage Lane, Stansted, Essex CM24 8GF UK, Part number: AGB7311

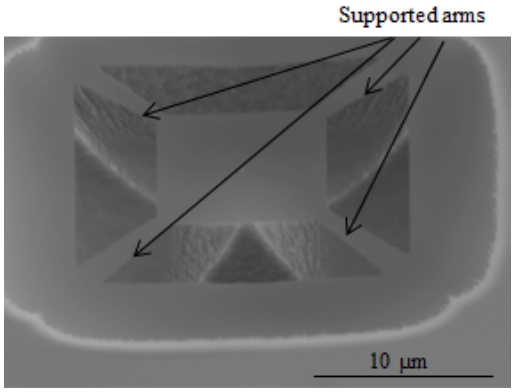

Figure 40 fully released 10X10 micron SiO2 membrane showing suspended membrane and undercut produced by the isotropic plasma etch

2.2.2 Active device

One of the advantages of working in the James Watt Nanofabrication Centre is that a sample specifically designed to study low dimensional heat transport between SThM tip and sample surface can be made using nanofabrication and MEMS technology. The whole process for active device fabrication is presented in the diagram shown in Figure 41

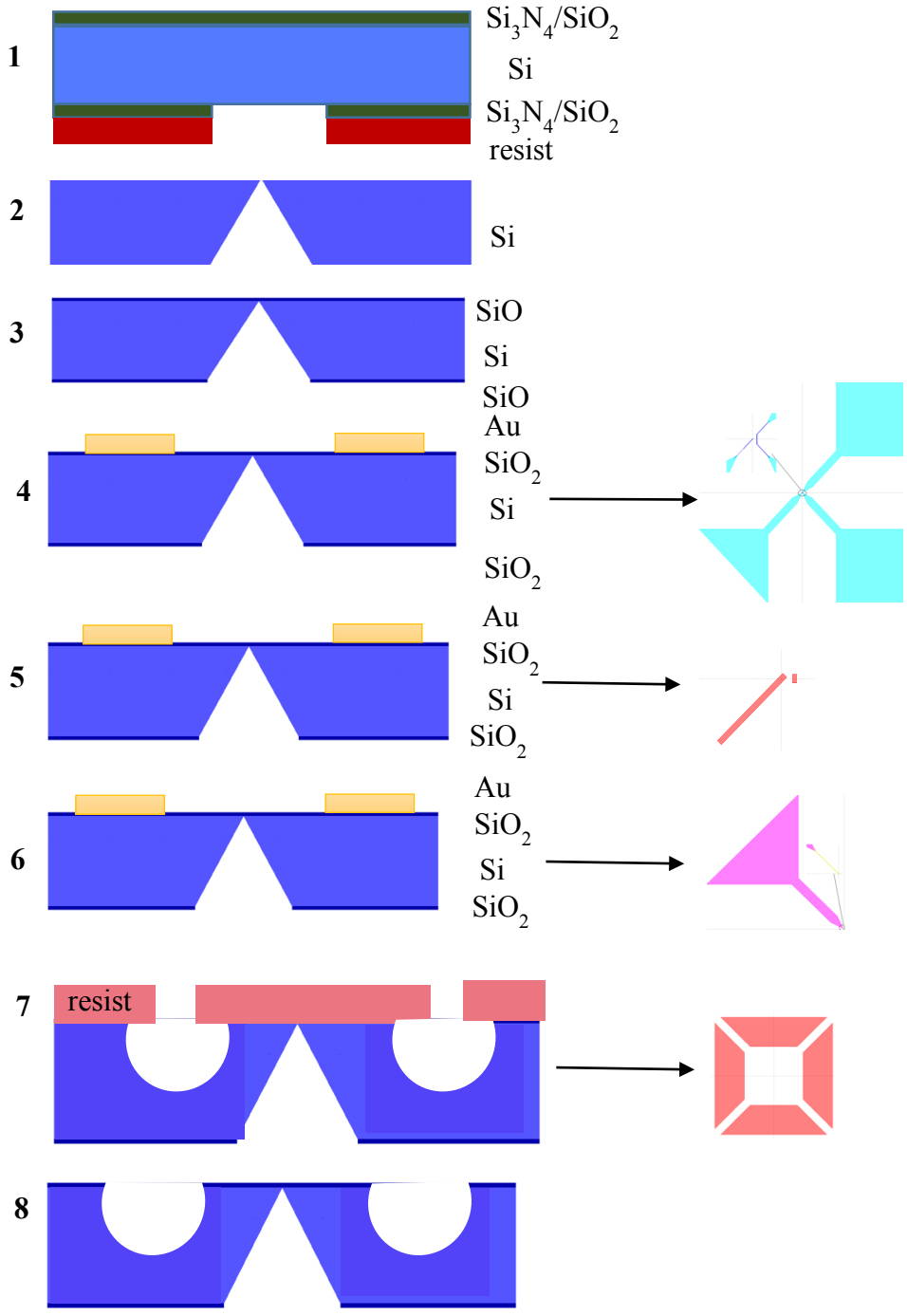

Figure 41 The fabrication process of active device.

1. Photolithography I (back side) for defining cleaved lines. Dry etch for etching oxinitride 2 Wet etch (anisotropic etch of Si then stripping the resist and oxinitride. 3 Dry thermal oxidation. 4.Photolithography (back side) for aligning back side to top side of the wafer. Ebeam lithography: 4a.one lead of thermocouple, 2 leads and pads connected to heater; 4b. Gold etch to define Pt heater/thermometer; 4c. Second lead of thermocouple; 4d. Windows to define membrane. 5. HF etch of SiO_2 and isotropic Si dry etch. 6. Stripping the resist.

The geometry of the membrane and device were drawn in Tanner L-edit [146] software for fabrication as shown in Figure 42. Sixty-four devices were patterned on the 3-inch size wafer circle. 1 mm rectangular and triangular pad shapes were chosen in order to distinguish heater and thermocouple when bonding to the PCB during measurement.

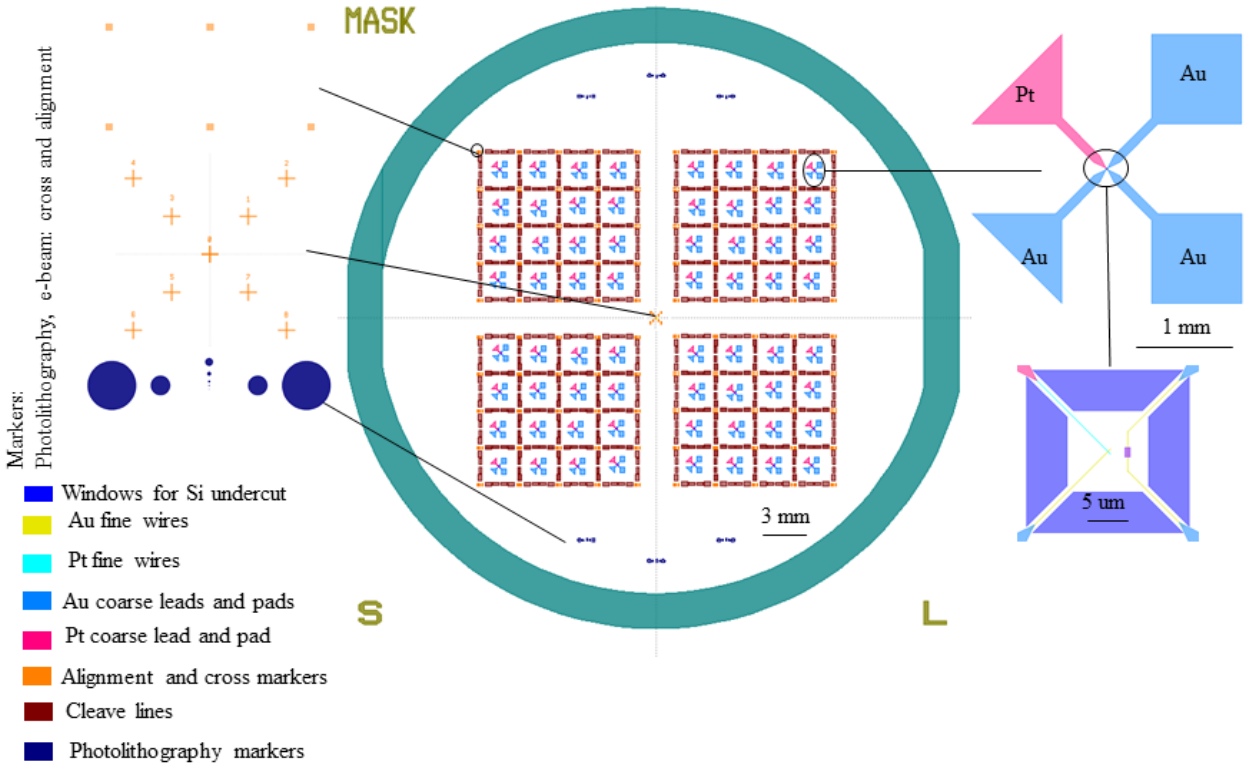

Figure 42 Tanner L-edit design for active device showing the hierarchy of alignment and device structures

A process was devised for the fabrication of the sensitive nanodevice using bulk micromachining using both wet and dry etching processes, electron beam and photolithography.

The process was developed taking into account the required properties of the device and the processes available at Glasgow.

The same as for the passive device fabrication, the whole process includes 3 stages: defining the individual chips, active device fabrication and thermal isolation of membrane from a heat sink. Fabrication of the thermally isolated membrane itself has no difference between active and passive device. However, the second stage needs to be discussed separately.

The second stage is fabrication of the electrical components of the nanodevice itself. Three e-beam lithography levels were patterned on the wafer to construct the device. The first three levels as shown in the scheme in Figure 43 belong to the second stage and the 4th level of

e-beam lithography is part of the third stage in which the membrane is released. Due to the resolution limitation of photolithography [105], when the pattern size is less than $1\mu m$ electron beam lithography (EBL) is more suitable for device fabrication. The tool used for the EBL was a wide area e-beam Writer, VB6 UHR EWF.

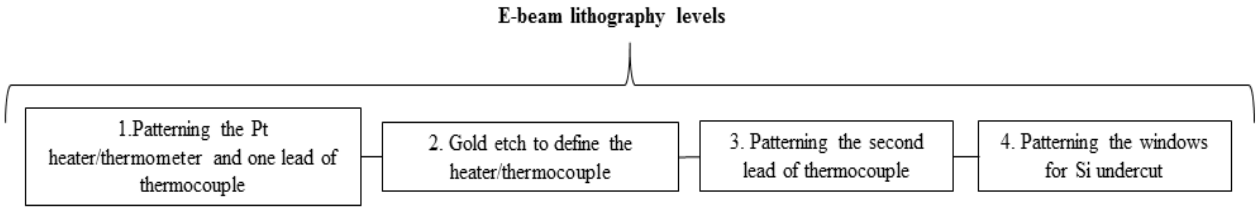

Figure 43 Sequence of the E-beam lithography levels used to fabricate the device

The first, second and third levels of e-beam lithography consists of the steps shown in Figure 43. These are resist spinning, e-beam lithography, metallization and lift off for the 1st and 3rd levels and Gold etch for 2nd level. Each level was aligned using gold markers as shown in Figure 34

In order to minimize the access resistance of the device elements initially metal leads were designed with a distance less than one μm between each other to have end of the lead as narrow as possible on the device and wider on the membrane supported arms as shown in Figure 44.

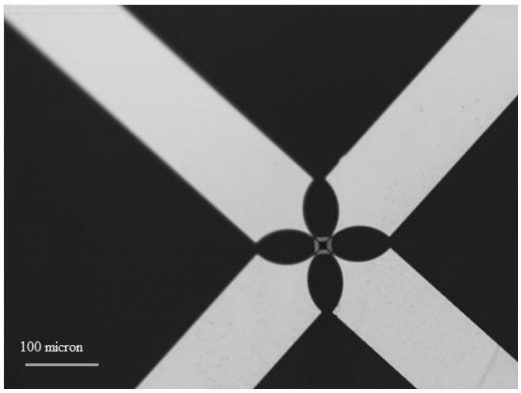

Figure 44 Initial design of device showing successful fabrication

However, it was hard to lift – off all of the metal from the device area, because of the shape of the end of the metal leads, which were too close one to another. (Figure 45)As this retention of metal is one for the most common faults in lift off processes, it is very likely to happen in smaller enclosed areas. The metal part supposed to be lifted off will remain on the wafer because metal adhered so well and cannot be removed after drying.

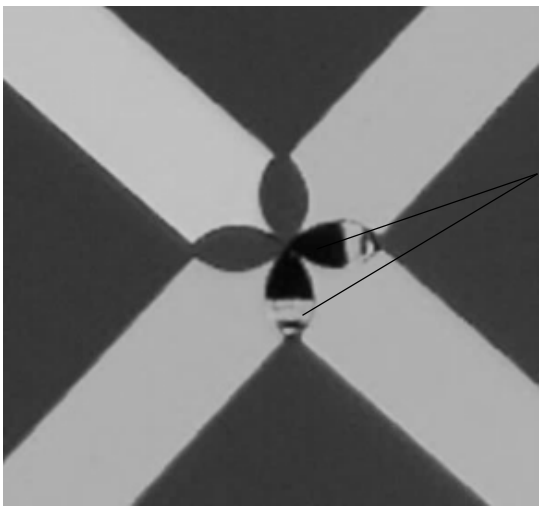

Figure 45 lift –off issue for closely spaced large metallic structures leading to unsupported metal shorting adjacent leads

The design of the Au/Pt thermocouple and Pt heater/thermometer leads was changed to have a shallower taper in to the device and therefore to allow easier lift off from the device area whilst still avoiding sharp corners in the membrane suspension which could lead to stress concentration and fracture. As shown in Figure 46 the taper of the metal leads was changed to be narrower for better lift-off.

After changes to the design were made, three layers of metal were deposited in a single deposition. Firstly, 5nm of NiCr as a sticky layer. The adhesion of the metal is necessary as some noble metals, for example gold, suffer from easy peeling from substrate surface thus an adhesion film is needed to promote adhesion of the noble metal device layer to the membrane. For example NiCr layers tested in [147] shown very high adhesion strength. Then 45nm of Pt which will be used as metal for heater/thermometer and one lead of the thermocouple wire, and finally 90 nm of Au on the top of the other two metals was deposited in order to act as the pad metal, but by depositing at the same time as the Pt you avoid the need for a second sticky layer by having gold deposited on top of clean Pt. The wires on the membrane are very narrow to minimize heat conduction from the device to the silicon substrate but the wires on the silicon are wide to minimize electrical resistance

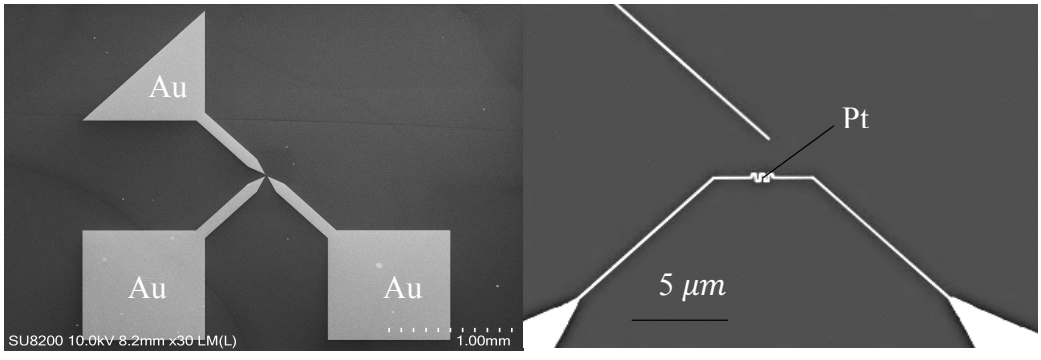

Figure 46 1st level of E-beam lithography showing triangular pad identifying the gold thermocouple lead and

relationship between heater and thermocouple

The gold layer on the top of heater and one lead of the thermocouple can be removed selectively from the NiCr/Pt using a solution of 0.15 M I_2 in molar KI solution with a PMMA mask protecting other metal as described in [26] where similar standard process was used to define a standard NiCr resistor. By depositing both metals at the same time and then removing the gold layer problems of contact between different metals are avoided, as both are deposited at the same time without breaking vacuum. The gold etch was done from one of the lead of thermocouple in order to save one e-beam level and as well as to fabricate a Pt heater / thermometer. The gold etched from the metal can be seen in **Figure 47**. As shown in the figure there is an undercut which is due to the resist mask is becoming partly detached from the underlying film resulting in enhanced lateral etching.[148]

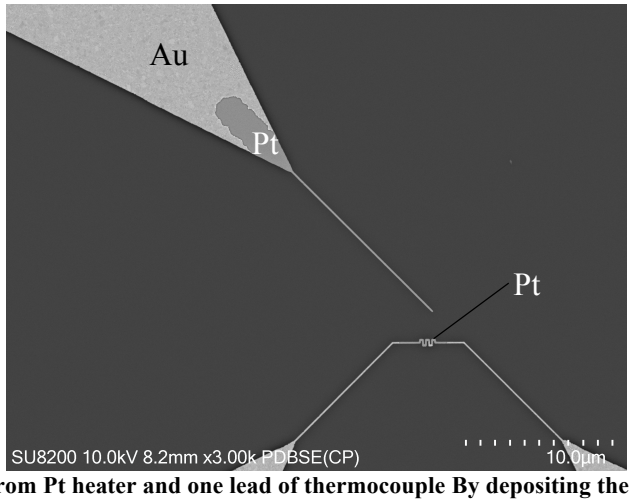

Figure 47 Gold etch from Pt heater and one lead of thermocouple By depositing the Pt andAu in the same evaporation step the gold lead and pad metal forms an excellent metallic contact with the platinum sensor metal. A low resolution gold etch defines the extent of the platinum-only region.

Devices having fixed resistance NiCr heaters or Pt (which has a strongly variable resistance with temperature) were made. In the second case the Pt resistor formed an additional type of thermometer in addition to the thermocouple. This was better suited to calibration using a heat bath than the thermocouple where the “cold junction” is at the same temperature as the substrate

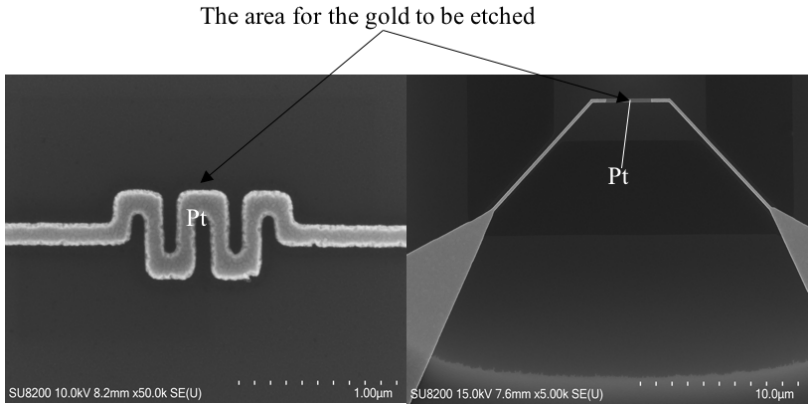

Figure 48 Pt resistors/heaters shapes The serpentine resistor is more compact allowing larger heating powers for

a given area but is more difficult to fabricate using the lift-off technique

Various resistors as shown in Figure 48 with different widths and shapes were designed to have different thermal sensitivity of the device heater. The values of the electrical resistance in the devices are measured to be 165-320 Ohm.

The second lead of thermocouple was patterned in the next level of e-beam lithography by bilayer of PMMA and metallization with 5nm NiCr and 90 nm of Au which is two times thicker than the first Pt wire to ensure that the thermocouple doesn't break[136] so that the second line is continuous when it crosses first one. (Figure 49)

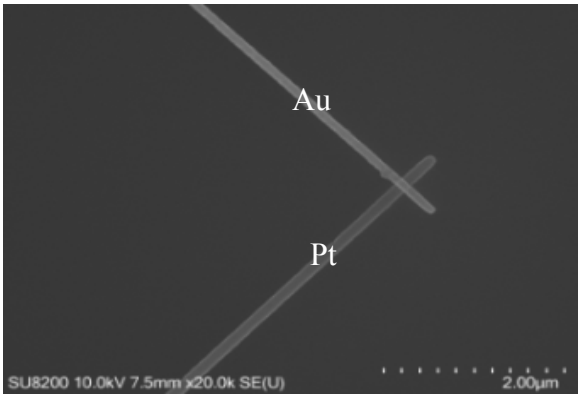

Figure 49 Patterning of Gold lead of thermocouple showing good coverage of the thinner Pt electrode and good layer to layer alignment

The device fabrication process details can be seen from Appendices C.

The thermal isolation of the membrane was achieved using the same technique as already discussed in Passive device section. A tilted SEM image of the final device is shown in **Figure 50**. It is clear from the image that membrane is fully released from the Silicon substrate.

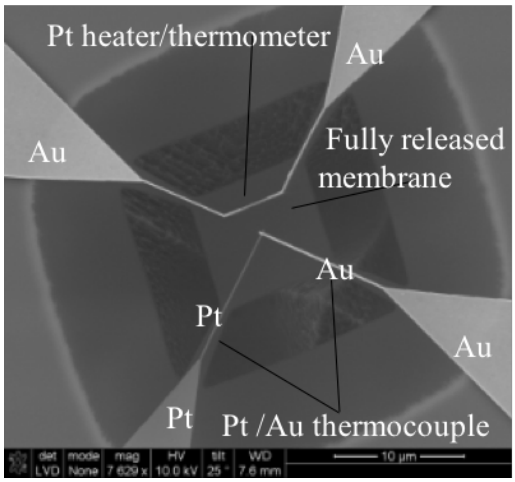

Figure 50 Final device showing platinum resistance and thermocouple sensors fabricated on the 50nm thick free standing SiO_2 membrane. Undercut of the SiO_2 membrane by the isotropic SF_6 plasma etch is visible near the edge of the image

Chapter 3. Methodology

3.1 Active Device calibration

Before connecting the active device to the SThM system it needed to be calibrated. In order to do that measurement, the set up needed to be assembled and the device electronic characteristics needed to be measured.

3.1.1 Assembly of the measurement system

For the device described in [16] the RTD heats up to $200°$ C when 40 mW power is applied, a sensitivity of $5 \cdot 10^3 K \cdot W^{-1}$. Modelling the device with higher sensitivity shows that it is possible to heat up to 425 K when 89 μW power applied. The finished fabricated device has a very large thermal resistance of $1.5 \cdot 10^6 K \cdot W^{-1}$ due to its geometry as predicted by modeling (section

4.1 Passive device modelling.) This sensitivity, which is a deliberate feature of the design, makes the device extremely susceptible to electrical damage and necessitated the development of a custom measurement system and delicate inspection methods. As well as the thermally isolated membrane, the device also consists of a small electrical heater/thermometer as well as a thermocouple that acts as a second thermometer. This gives the flexibility to work with a heated sample and a cool probe or heated probe with a cool sample and to perform an absolute calibration of thermal conduction using the self-heating of the resistance thermometer. The device was fabricated on top of the silicon dioxide thin film and isolated from a Si heat sink.

This means that even the small heat flow between it and the SThM probe will cause it to have a large change in temperature, making the measurement as sensitive as possible.

Before connecting the device to the electrical circuit, a number of initial inspections were performed. Firstly, the device was scanned in the FEI scanning electron microscope.

Unfortunately, the device was blown up and membrane destroyed while scanning in the SEM due to charging effects as shown in Figure 51. When the SEM contrast of a non-conductive specimen is interpreted, a charging effect arises from electron/ion irradiation. The charging effect is caused by the accumulation of static electric charges on the specimen surface, which results in many problems. [149]

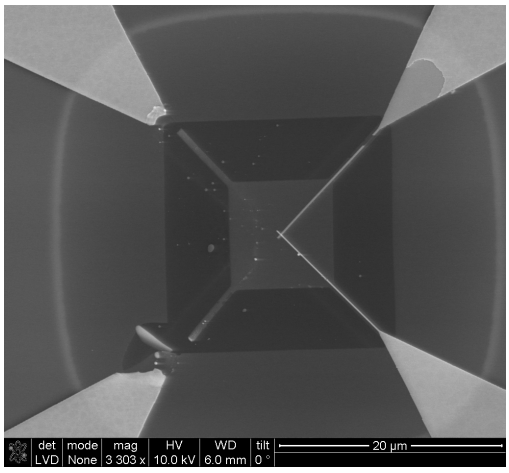

Figure 51 Blown up device after SEM attributed to the discharge of charge accumulated in the capacitance formed by the device bond pads and the substrate on exposure to a 10kV electron microscope probe in high vacuum

To avoid this problem in future, it was necessary to use SEM detectors with reduced charging effects. As explained in [150] by Thiel et. al., when using a Helix or Low Vacuum Detector, the charging of insulating specimens is stabilized by positive ions produced in the Nitrogen gas ionization cascade. Gas gain measurements were made using nitrogen and a polished, grounded aluminium stub as the specimen. [150]

As shown in Figure 52 this allows high resolution images to be taken without damage to the device using water as a gas.

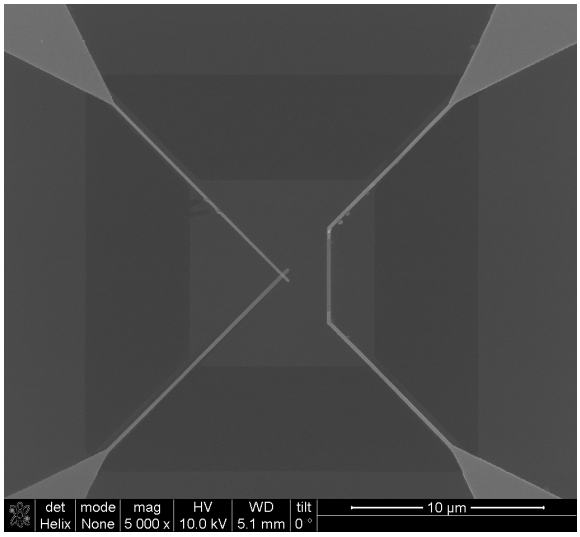

Figure 52 Device after Inspection with Helix detector showing no evidence of damage due to the electron microscope exposure under 0.3mBar water vapour environment

The device was so sensitive that a conventional semiconductor probe station [17] was found to blow it up due to ESD [151] which is one of the most frequent causes of failure of wires in our device. As the device is well thermally isolated from a Si heat sink, current applied to the device cause its failure due to electromigration. The electromigration in metal wires is due to high current densities and high Joule heating in thinner and narrower wires as shown in **Figure 53**. Orange blobs of gold dots on the membrane surface can be seen from the image which were formed from vaporized metal due to electrostatic discharge. In this image the secondary electron signal is used to form the green channel of the colour image and backscattered electrons are used to form the red channel. Thus the Silicon and SiO_2 structures are seen as green and the device metallization as orange. Due to the fragility of the device the development of a different electrical measurement system was required.

[17] Cascade microtech Inc, via Ronchi, 18D, 20025 Legnano, Italy

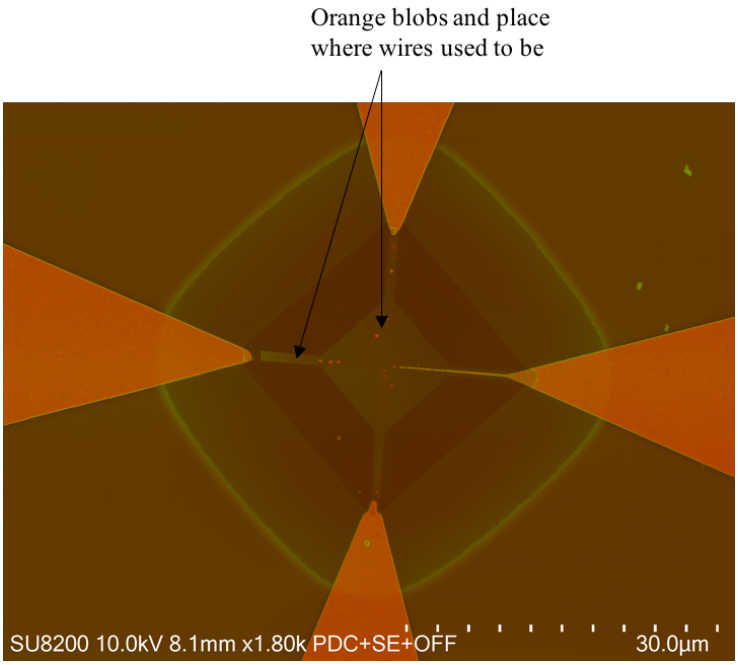

Figure 53 Blown up device after probe station measurement showing discontinuous conductors and small spherical metal blobs resulting from transient melting of the device leads

To measure the thermal resistance of the membrane directly a measurement set up was made. The measurement set-up allows more sensitive measurement than a probe station because the resistance bridge is amplified using a local low-noise instrumentation amplifier, minimizing amplifier noise and interference in the measurement.

The circuit consists of a power supply, an ADC board/lock-in amplifier[18] to replace the multimeters and for data collection to the PC, PCB to the bridge with a Wheatstone bridge, PCB for the device for wiring it to the system, Peltier module and a PT100. The device is placed in an isolated box on the top of a cooling aggregate and Peltier thermoelectric cooler module for accurate temperature calibration and uses a Wheatstone bridge to measure and bias the resistance thermometer. The reference resistance in the bridge can easily be changed to compensate for the small changes in sensor resistance by placing a large resistance with known value in parallel with the precise reference resistor which has a value of 300 ohms, slightly larger than that of the sensor. (Figure 54)

[18] Made by Prof. Johnathan Weaver

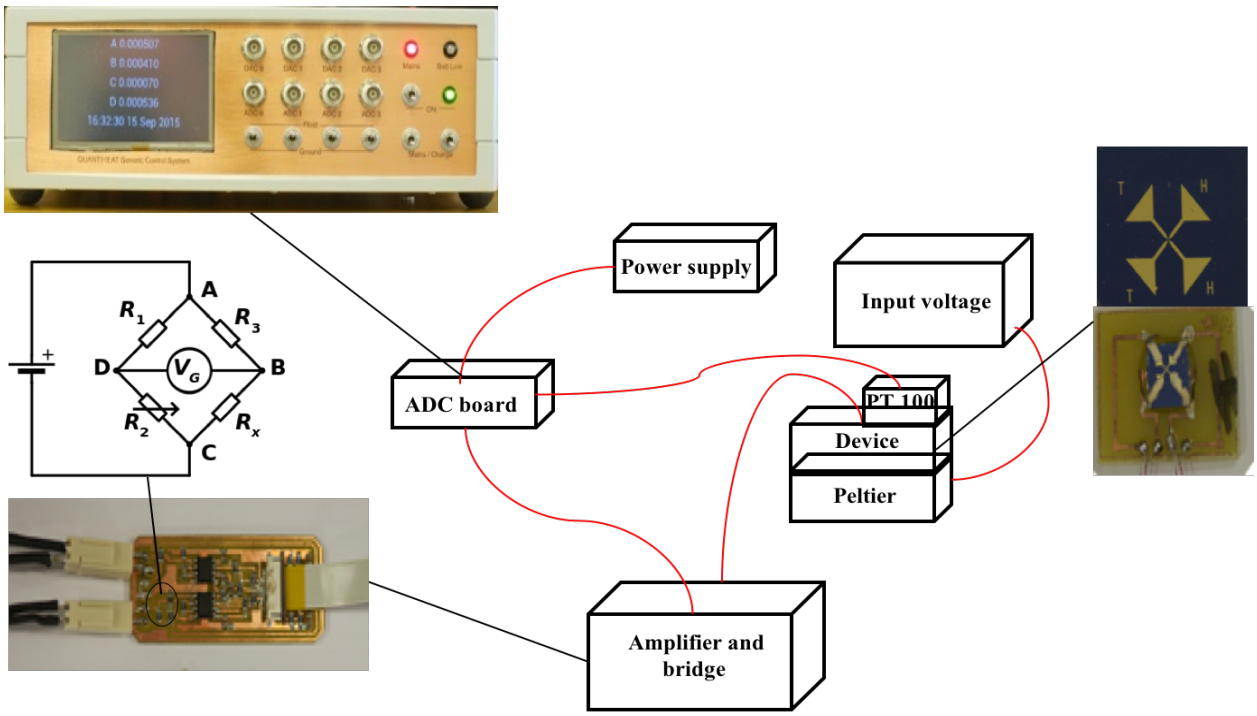

Figure 54 Measurement set up used for calibration of the platinum resistance sensor. The temperature is varied by means of a Peltier thermoelectric element and the resistance change measured using a DC Wheatstone bridge

3.1.2 Temperature coefficient of resistance

The temperature coefficient of resistance (TCR) of device was calculated by the following equation:

$$TCR = \frac{\Delta R}{R_0 \Delta T} \qquad \textbf{Eq. 14}$$

Where R_0 is the resistance value at room temperature, ΔR is the resistance change with respect to T_0 resistance, and ΔT is the change in temperature.

Two different environments were used in order to calibrate temperature change. Liquid is easier to measure the temperature but air cannot damage the membrane. Flutec is known as chemical with high dielectric strength and resistivity with low values of permittivity and dielectric loss. Flutec (FLUTEC pp3, Chemicals Ltd)[19] was chosen because of the ability to define a homogeneous temperature distribution and because of its low surface tension it doesn't damage the membrane. However, it can cause residue on the surface of the metal.

[19] F2 Chemicals Ltd, Lea Lane, Lea Town, Nr. Preston, Lancashire, PR4 0RZ (UK), FLUTEC pp3

By heating the Peltier the temperature coefficient of resistance (TCR) of value 0.00233 ± 0.00018 K^{-1} and 0.0018111 ± 0.0000008 K^{-1} in air and fluorocarbon liquid respectively was measured. The error was calculated by repeating the measurements several times. Also there is the accuracy of the type A PT100 sensor which is only 0.15°C at 0°C with an additional scale error of ±0.2% which would correspond to 0.00181±0.00004 K^{-1}.

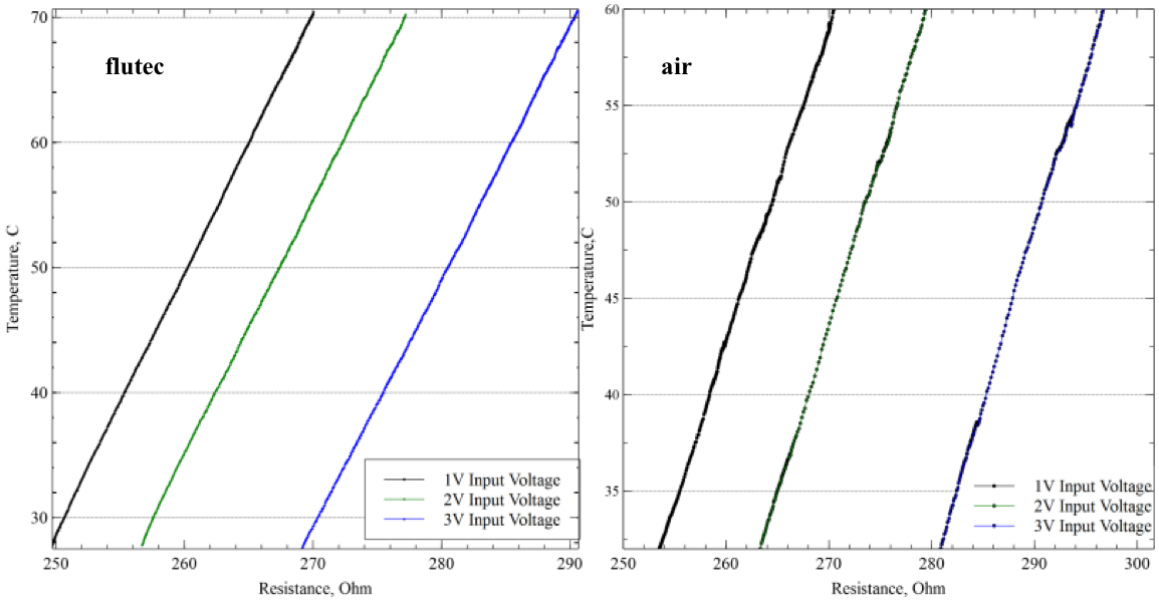

Figure 55 Variation of resistance with ambient temperature and self heating for air and liquid ambients. Note the increased noise in the air measurements due to imperfect thermal contact and air currents and the difference in measured self-heating.

In order to obtain more precise data, every measurement was carried out more than 10 times, and the average value was then used in each case. This result was used to find the temperature change by heating the Pt heater with input power to the Wheatstone bridge from 1 to 3V. (**Figure 55**). It can be noticed from the temperature calibration plots that there is obvious self heating which can be measured with the same set up as a lateral shift in the curve as a function of bias voltage. This is discussed next.

3.1.3 Self heating measurements

Temperature sensors can demonstrate a phenomenon known as self- heating. When a temperature sensor is self-heated, the operation of the sensor itself provides heat to raise its own temperature. In the case of a resistance thermometer the heating arises from the current used to measure the resistance. Internal heat generation in semiconductor devices is usually due to the Joule heating. Joule heating is a positive power generation as charge carriers move along the structure under the influence of the electric field, giving up energy to the lattice. [152]

A platinum resistor was chosen as the metal for the temperature sensor. In the current measurements it was used as a heater and thermometer at the same time.

Self-heating measurements allowed us to test how much power was required to heat the membrane. A heater was connected in balance to the Wheatstone bridge with balance resistance of 250 Ohm as shown in **Figure 56**.

According to Wheatstone bridge equation the heater resistance can be calculated.

$$\boldsymbol{V_{out} = (\frac{R_2}{R_1+R_2} - \frac{R_x}{R_x+R_3})V_{in}} \qquad \textbf{Eq. 15}$$

After rewriting the bridge equation knowing the values of R_1 =5110 Ohm, R_2 =5110, R_3 = 250 Ohm, output voltage from Pt heater/thermometer V_{out} and Input voltage to the bridge V_{in} , the heater resistance can be found

$$\boldsymbol{R_{heater} = 5110 * [\frac{1}{(\frac{V_{out}}{V_{in}*100+0.9535})} - 1]} \qquad \textbf{Eq. 16}$$

The difference between two media can be seen from the plot which shows different conduction through air and Flutec.

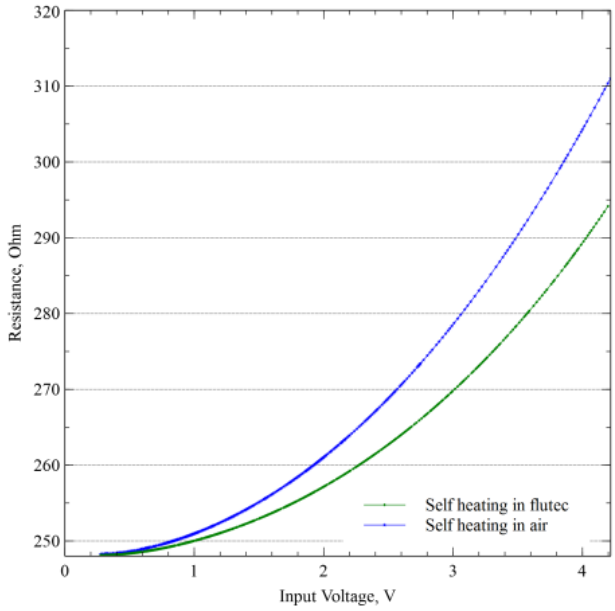

Figure 56 Self heating when input voltage was applied to the bridge

The heater was heated by changing the bridge input voltage from 1-4 V. This heated the membrane by up to *331 uW* giving 53-degree temperature change. From equation of thermal

resistance $R_{th} = \frac{\Delta T}{P}$ a thermal resistance of 3X10^5 $\pm 1.2 \cdot 10^3$ K/W of device in air. The error is taking into account is standard deviation of repeating of measurements and covering the box holding the device.

The thermocouple sensitivity is 3.3 μV/K. The thermocouple is a device for measuring temperature, which consists of two wires made of different metals connected at two points. The second connection is through voltmeter. One point is called cold junction. The thermocouple sensitivity cannot be measured using a Peltier to heat the sample as its heats the whole surface, and thermocouple requires a cold junction.

The measurement of device thermal resistance in air and Flutec is of low precision and lower than that predicted due to conduction through the environment and due to thermal transport by motion of the environmental fluid which varies with air flow across the device or bulk motion of the Flutec. In order to get a more accurate value, the same measurements need to be carried out in vacuum. More importantly, the reason to use vacuum is to achieve the maximum thermal resistance for measuring the heat exchange between tip and sample. Since the device is going to be used in vacuum to measure thermal conduction, it is necessary to measure its thermal conduction in vacuum. The Flutec and air measurements were mostly used to get the temperature coefficient of resistance of the sensor. The self heating in air and Flutec was interesting as it varies with the medium, but the important thing is self heating in vacuum

To heat the membrane in vacuum much less Input Voltage was required to get a big temperature change. Heating the Pt heater by 0.4 V the membrane was heated by 450 K.

According to measurements in vacuum, the thermal resistance value of 1.44*10^6 $\pm 3 * 10\ K/W$ compares well with the modelled value of 1.49±0.04*10^{6}K/W. (Figure 57)

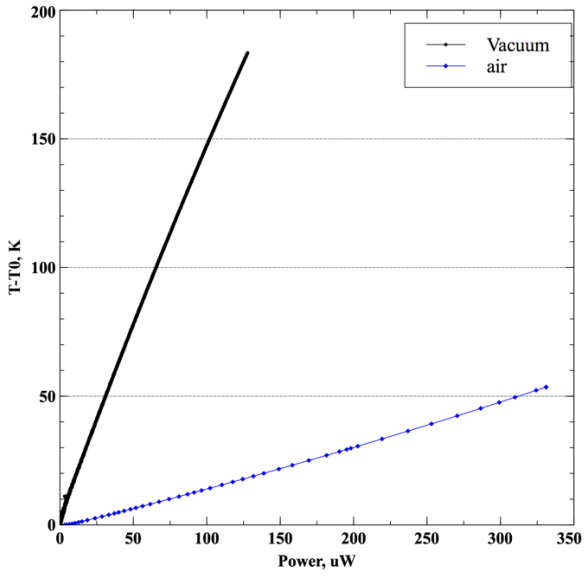

Figure 57 Self heating in vacuum and air

It is obvious from Figure 57 that the self heating in vacuum is much higher than in air.

The voltage was swept from 0V to a high voltage repeatedly with a higher maximum voltage each time. The device characteristics were initially found to be stable (black and green curves) up to 320K rise, but on heating to 500K the resistance of the sensor was permanently changed. The measured temperature rise is taken from the initial Flutec / Air measurements of resistance, so once the sensor has changed the rise in temperature from resistance is no longer calibrated.

Heating the Pt sensor with higher Power will change the device electrical properties due to phenomena such as recrystallization of the gold leads. As explained in [153] gold deposited at room temperature can be recrystallized when heated from 300-900 ^{0} C. (Figure 58) Heating the membrane with higher input voltage will therefore change the electrical properties of the device. Assuming that the thermal resistance of the device is constant it is possible to estimate the temperature of the device from the input power, as is shown in the right hand side of Figure 58, confirming that thermal degradation is a plausible mechanism for the change in response seen in the left hand side.

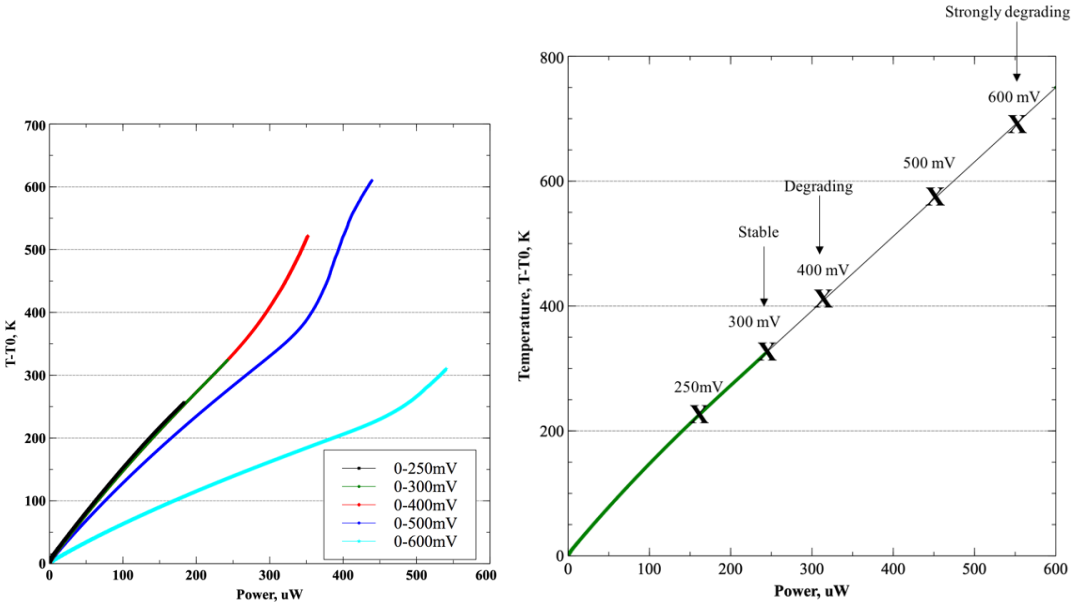

Figure 58 Successive self heating measurements with increasing the input voltage/Power showing irreversible resistance changes at high power

The device is still working but not stable and is not a good sensor for thermal measurements when subjected to an input power of more than about 200µW. This defined the range of powers used during experiments.

3.2 Passive and Active modes measurement set up

The passive and active mode measurements in were performed by implementing a 3ω technique within Nanonics vacuum AFM/SThM system[20].

3.2.1 3ω techique

The 3ω technique, which was described for the first time by D.Cahill [154] is used in order to implement SThM in active and passive modes measurements. This is an AC Technique closely related to the hot – wire and hot strip [155] method. In 3 ω measurements, a narrow metal line is patterned on the sample. Electrical current i of frequency ω is applied to the metal line with electrical resistance r, generating Joule heating of i^2r within the metal line with a frequency component at 2ω. As a result of this oscillating heat source, temperature oscillation and a corresponding resistance oscillation at frequency 2ω are induced in the metal line. The heating produces a temperature oscillation at the same frequency. The resistance is a function of temperature. The resistance oscillation at 2ω multiplied by the excitation current at ω produces a voltage oscilation at 3ω which can be measured by a lock-in amplifier.

Using this technique, the thermal conductance of the sample to the tip $g_{t\text{-}s}$ can be found as a fraction of the known conductance of the device to ambient. This can be quantified by calibrating the heater as a thermometer. The self heating and the 3ω change on contact with a Probe in vacuum can be measured.

The measurement is limited by thermal noise in the sensor and bridge resistors. The minimum voltage noise in the bridge can be calculated from the thermal noise equation

$$\Delta V = \sqrt{4k_B T r}, \qquad \textbf{Eq. 17}$$

For the 250Ω Pt sensor this is equal to

$$\Delta V = \sqrt{4 \cdot 1.38\times10^{-23}}\,\frac{J}{K} \cdot 250\Omega = 2.03 nV/\sqrt{Hz} \qquad \textbf{Eq. 18}$$

Other possible errors adding to the measuring limit are thermal noise in the sensor and bridge resistors and amplifier noise. The error in $R = \frac{\Delta V}{I} = \Delta R$ in practice is found from the 3ω measurement noise limit when the probe is out of contact defining the $noise\ limit = \frac{\Delta V_{3\omega}}{V_{3\omega}}$. The

[20] Nanonics imaging Ltd,

noise limit is stable and found to be $0.27 \pm 0.02 g_0$. Values higher than that number therefore correspond to real changes in thermal conduction.

The 3ω voltage is measured in order to calculate the value of thermal conductance between heated sample and cold probe tip. The 1ω voltage is substantially balanced with a Wheatstone bridge.

An RTD determines the equilibrium temperature of sample by measuring the change in resistance of a pure metal sensor in thermal contact with the sample. The resistance of the sensor is assumed to be linearly related to temperature as

$$\boldsymbol{r_{sensor} = r(1 + \alpha \Delta T)}, \qquad \textbf{Eq. 19}$$

where α is the temperature coefficient of resistance (TCR), ΔT- temperature change T-T_0 with T_0 as a reference temperature where resistance is R_0, eg. 0°C for a PT100. As described in Chapter 2 Fabrication, a Wheatstone bridge may be used to measure the resistance change by passing a current through the Pt heater/ RTD. When an AC current is passed to the Pt heater/thermometer the Power dissipated by it due to Joule heating is defined as

$$\boldsymbol{P = i_h^2 r_h}, \qquad \textbf{Eq. 20}$$

where I_h and R_h are the heater current and resistance respectively. The AC current passing through the heater is given as

$$\boldsymbol{i_h(t) = i_{h,0} \cos(\omega t)}, \qquad \textbf{Eq. 21}$$

$$i^2 = \frac{i}{2}(1 + cos2\omega t)$$

where $I_{h,0}$ is the peak amplitude of the nominal heater current at frequency ω. If I_h is given by $I_{h,0}$ cosω then

$$\boldsymbol{P(t) = \frac{1}{2} i_{h,0}^2 r_0 (1 + cos2\omega t)}, \qquad \textbf{Eq. 22}$$

The temperature change measured can be written as

$$\Delta T = \frac{P}{g_{device}}, \text{ or}$$

$$\Delta T = \frac{\frac{Ri_0}{2}(1+cos2\omega t)}{g_{device}} \quad \textbf{Eq. 23}$$

where g_{device} is thermal conductance of the device.

The resulting voltage across the sensor is

$$V_h(3\omega) = \frac{ir_{h,0}^2\alpha}{2g_{device}} \frac{cos3\omega t}{2} \quad \textbf{Eq. 24}$$

When probe is out of contact the 3ω voltage is

$$V_{3\omega}(out\ of\ contact) = \frac{const}{g_{device}} \quad \textbf{Eq. 25}$$

And in contact with sample surface

$V_{3\omega}(in\ contact) = const\left[\frac{1}{g_{device}+g_{s-t}}\right]$ since $g_{s-t} << g_{device}$ by the binomial expansion, then $V_{3\omega}$ is equal to $\frac{const}{g_{device}}(1-\frac{g_{s-t}}{g_{device}})$

The ratio of $V_{3\omega}$ in and out of contact is equal to

$$\frac{V_{3\omega}(out\ of\ contact)}{V_{3\omega}(in\ contact)} = 1 + \frac{g_{s-t}}{g_{device}}$$

The thermal conductance for sample-tip contact is then equal to:

$g_{s-t} = \frac{\Delta V_{3\omega}}{V_{3\omega}(in\ contact)R_{cantilever}}$, for active mode or

$g_{s-t} = \frac{\Delta V_{3\omega}}{V_{3\omega}(in\ contact)R_{device}}$, for passive mode

then

$$G_{Th} = \frac{g_{s-t}}{g_{0rt}} \quad \textbf{Eq. 26}$$

where g_{0rt} is thermal conductance quantum at room temperature

The conductance can be described in general terms by scaling it to the conductance quantum, allowing easy comparison and helping in the recognition of any evidence of quantized thermal conduction.

3.2.2 Nanonics

Thermal quantification measurements in vacuum were obtained by Nanonics AFM/SThM system.

The experimental set up for active and passive mode measurements is shown in Figure 59. Measurement set up is made by Prof. John Weaver. It consists of a Nanonics Vacuum SThM system, an ADC board which is connected to the PC for data acquisition. The fabricated device was placed inside the vacuum chamber with the SThM/AFM probe and bridge amplifier to minimize electrical interface. The driving frequency is 135 Hz. The thermal probe has a time constant 300 us [21].

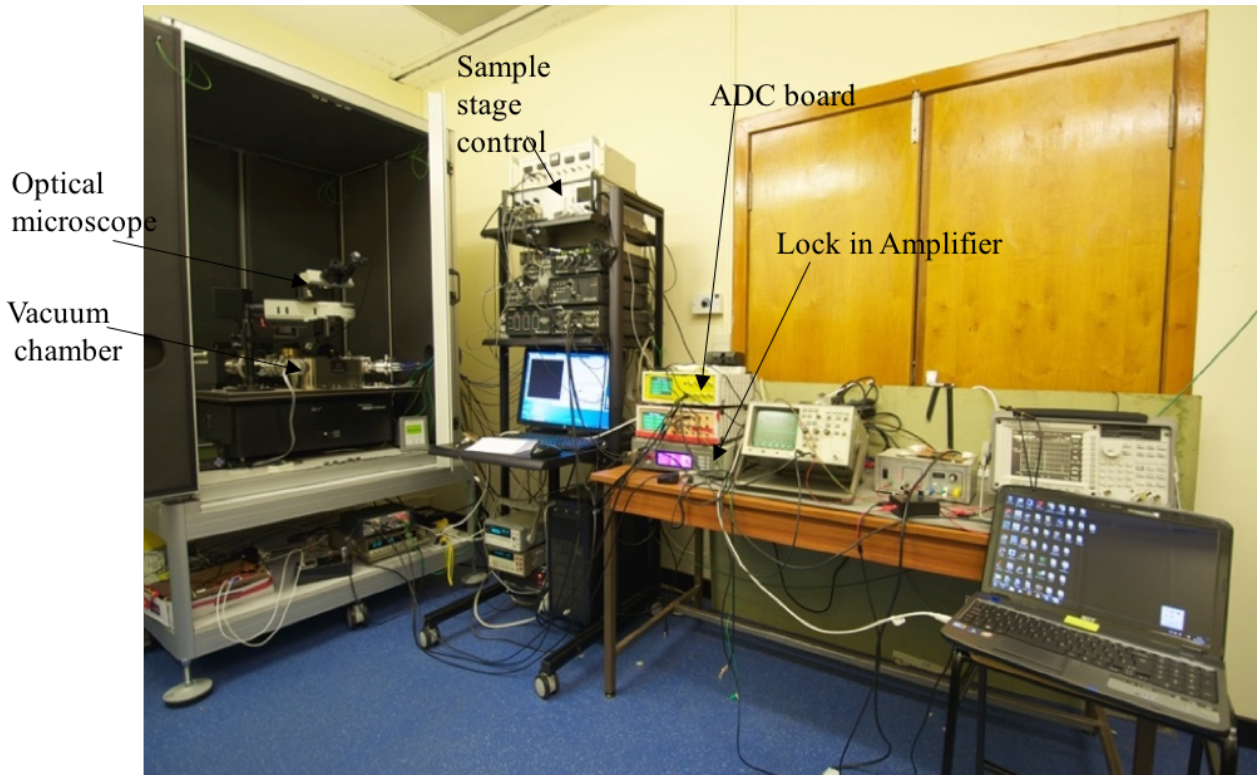

Figure 59 Experiment set up

Approaching and retracting the tip to the sample is done without using a laser. The tip-sample contact was detected by step change in thermal conduction. Optical microscope was used to get the probe near to the surface. In order to bring the probe tip into contact with the device on

[21] Yunfei Ge PhD thesis.

the sample the optical microscope is used to control the stage position during experiments. The stage is a closed loop three axis piezo flexure with a range of 80 μm and uses a stick-slip coarse adjust for larger motions in the plane of the sample. The optical microscope has a long working distance. For a magnification of 10X, NA is 0.3 so the resolution is equal to approximately 1 um, although in practice the smallest thing you can see is several μm because the pixel size of the camera is 2.3 μm. By using the Z-piezo the AFM/SThM tip can be made to approach the heated membrane. A diagram of the geometry of tip and sample contact shown in Figure 60. The diagram explains the coordinate system used and shows how the sample and probe tip are mounted inside the chamber for contact.

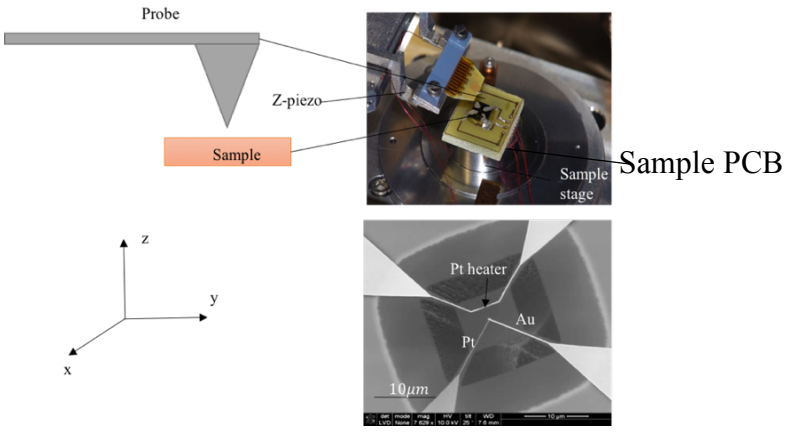

Figure 60 Diagram of geometry of tip and sample defining coordinate system used

The probe was driven by a piezo actuator in the *z*-direction. The probe approaches and is retracted from the sample surface using a triangular movement from 0 to 256 counts corresponding to a *z*-motion of 2µm range. At each count a measure of the 3ω component is made and the *z*-DAC is incremented. The probe starts furthest away (count = 0) then approaches until it is at its closest (count = 128) then retracts to the same distance away as at the start (256).

As shown in Figure 61 at count = 0 the tip is 1.2µm above the surface. It makes contact at count = 76 at which point *z* is 0. The tip continued to be pushed in to the sample for a *z*-piezo motion of 0.8µm at count = 128, after which the *z*-piezo motion is reversed.

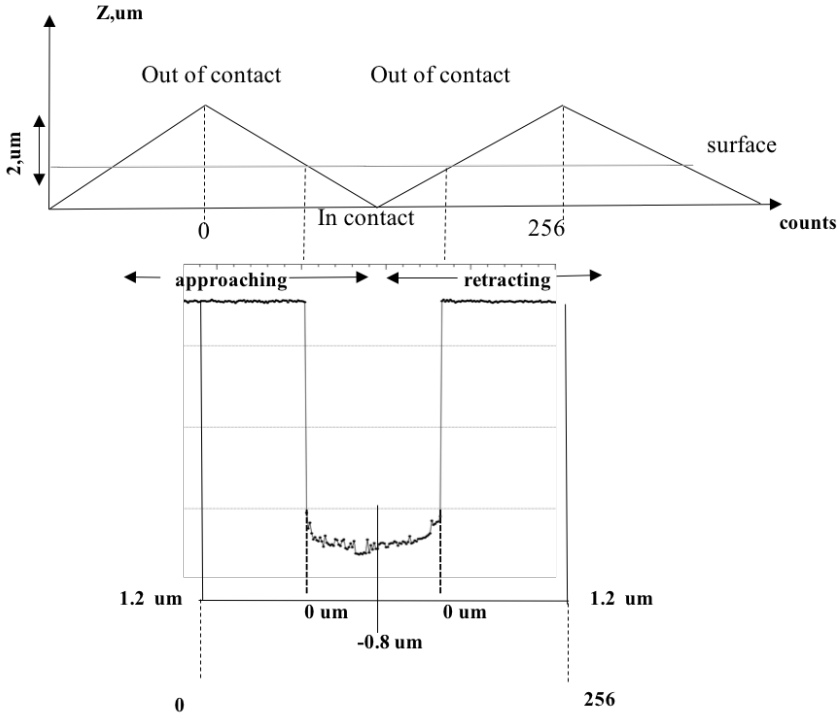

Figure 61. 3-omega signal as a function of z- piezo movement showing constant, low noise value out of contact, abrupt jump on first contact and significant in-contact changes with pressure due to changes in the nature of the tip-sample contact

The expected variation in $3\boldsymbol{\omega}$ signal on the tip and sample position and force applied is shown schematically in Figure 62 which may be compared with the experimental trace shown in **Figure 61**. The initial position is when probe tip is out of contact and furthest away from the sample (1), the next position is when tip is just touches the sample surface (2) causing an abrupt increase in thermal conduction corresponding to $\boldsymbol{g_{s-t}}$. As the stage continues to approach the sample the force starts to increase and the sample surface is slightly bent (3) leading to an increase in conductance. On retracting the probe from the sample the pull-off forces appear potentially leading to smaller overall force and thermal conductance than at initial contact (4) and finally the probe is separated from sample surface (5).

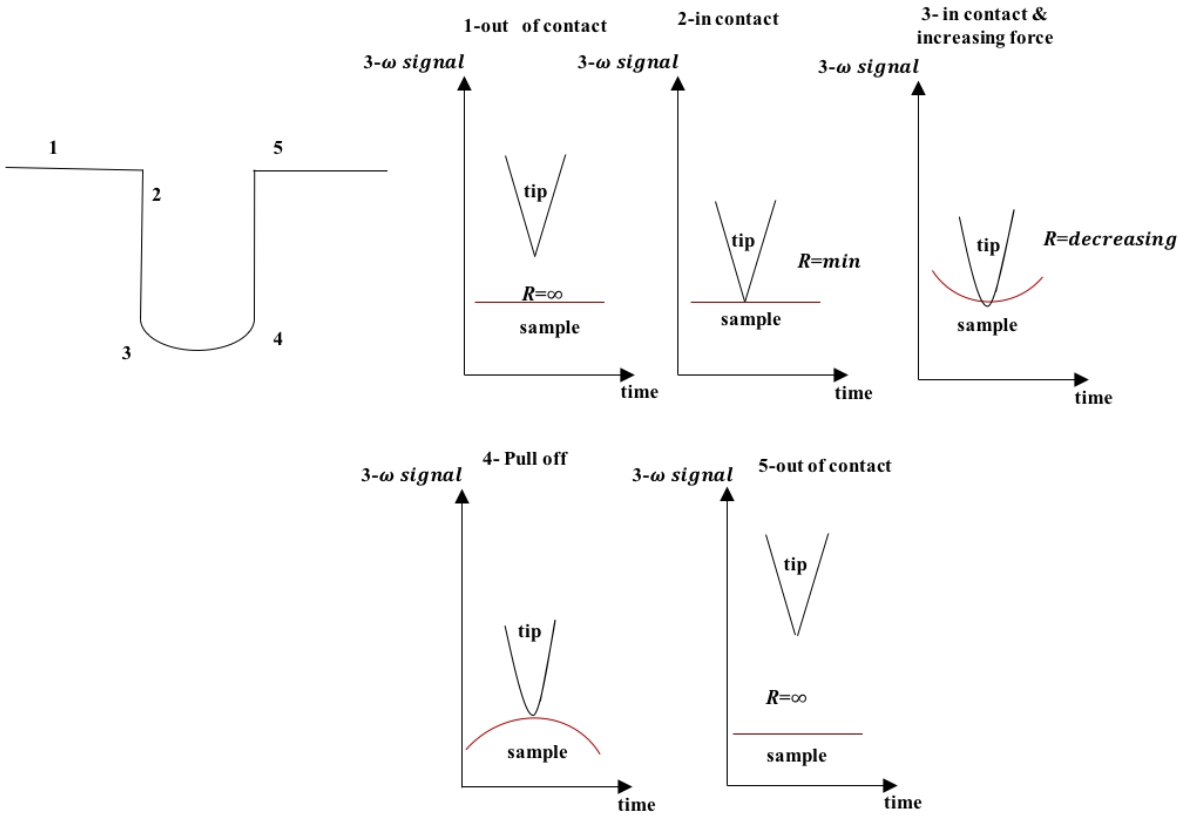

Figure 62 Schematic diagram of tip - sample contact

In order to quantify the tip-sample thermal conductance value vacuum is required.

The vacuum chamber is shown in Figure 63 has two pumps connected to the chamber via valves. There are two pumps to be used: Turbo pump and Ion Getter pump.

The turbo pump is pump used to stabilise the vacuum. [156] However, turbo pump cannot be used for SThM/AFM scan due to additional vibrations. In order to avoid vibrations using a Ion Getter Pump is required.

The Ion Getter Pump is a type of vacuum pump in which gas is exhausted by sorption

in metal layers in presence of ionizing electron stream. [157]So after the desired vacuum level is reached with the turbo and Ion Getter pumps the turbo pump can be disconnected and measurements will be performed with Ion Getter Pump. After the desired vacuum level of $2 \cdot 10^{-6}$ mbar is reached the measurements can be started.

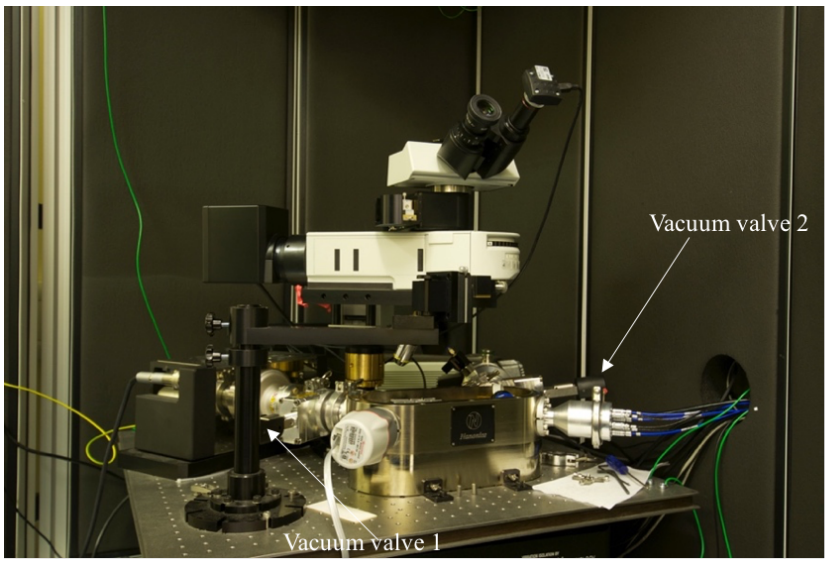

Figure 63 SThM/AFM system in chamber with optical microscope above

The output from the bridge is measured using a lock-in amplifier and sent via the ADC box to the PC. (Figure 64)

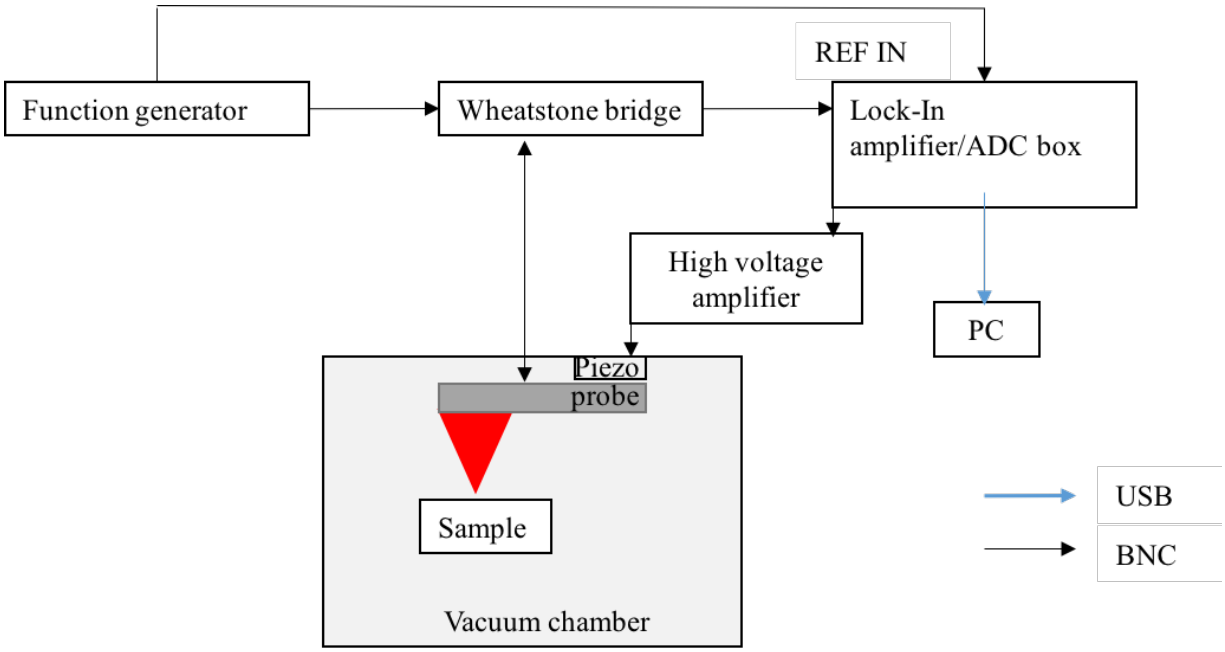

Figure 64 Schematic diagram of 3ω apparatus The high voltage amplifier is connected to an additional bimorph piezoelectric element onto which the probe holder is mounted

In order to implement the 3ω technique, a low noise sinusoidal AC signal at frequency ω is created by a function generator. The Pt heater/thermometer is connected to the Wheatstone bridge in order to detect the 3ω voltage whilst removing much of the large background signal at ω. The membrane was heated by an input of a constant alternating 2V AC Peak to Peak voltage to the Wheatstone bridge which includes the sensor, reference resistor and 5$k\Omega$ resistors. The basic circuit with Wheatstone bridge is shown in Figure 65.

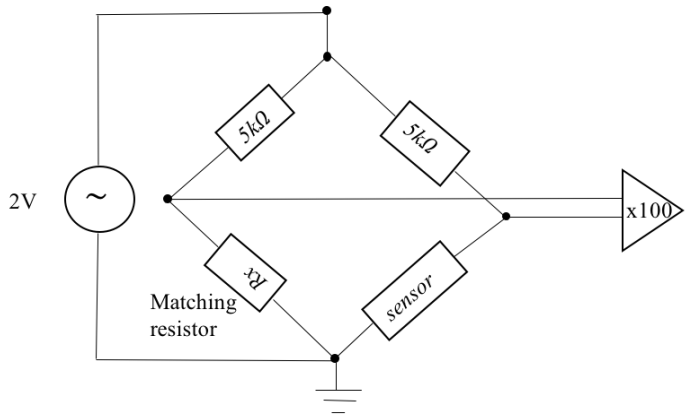

Figure 65 Schematic diagram of circuit with Wheatstone bridge

3.2.3 Self heating of the SThM probe

The sensitivity of the active device was determined by performing the self-heating measurements which were described in section 3.1.3 Self heating measurement, and that value was used for Passive mode measurements. The probe sensitivity was determined by another measurement of self-heating of the probe itself. The self heating measurements of the probe allowed an estimate of the amount of heat which goes to the cantilever when the probe is out of contact and an evaluation of the membrane thermal isolation when contacting the solid substrate and membrane.

The «Nulling probe» (Figure 66) was used for SThM probe tip and sample contact measurements and is well suitable for quantitative SThM measurement. The idea of this probe is that when operating the heat flux through the tip-sample contact of the probe is zero. It uses a separate heater to make the temperature of the cantilever the same as that of the sample[158]

The nulling probe consists of a Pt sensor and NiCr heater. The resistance of the sensor changes with temperature, giving a 3ω signal. The resistance of NiCr is stable with temperature and allows larger power to be dissipated than the sensor, which is why it is used as a heating resistor element for nulling thermometry.

A membrane was fabricated as the test sample used in order to perform self heating measurements when heating the NiCr heater with DC voltage up to 1 mV and temperature change was measured by Pt thermometer. Pt/Au thermocouple wasn’t used.

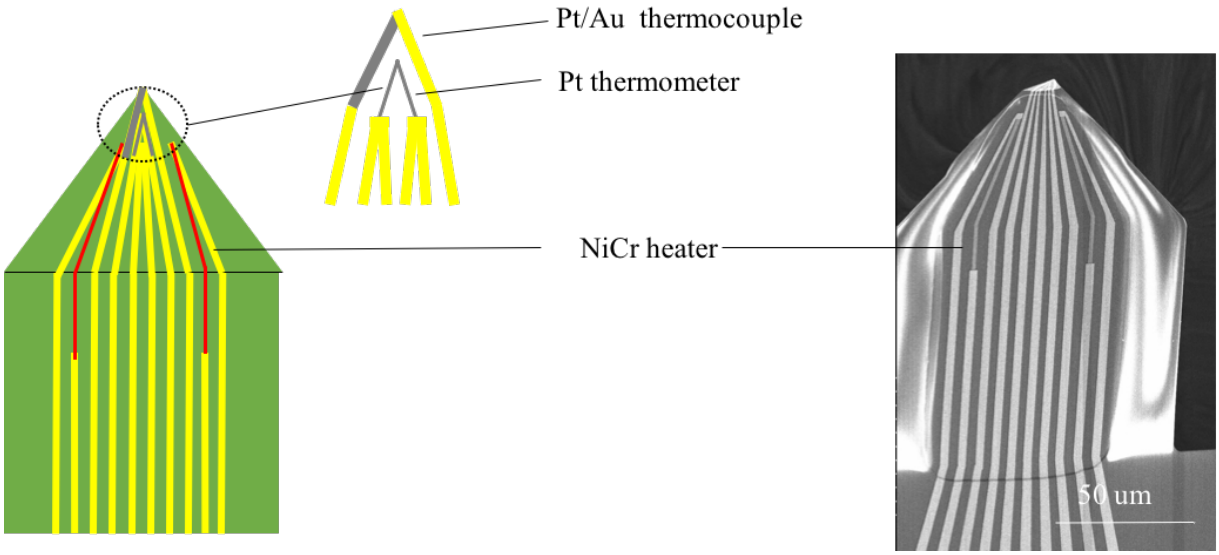

Figure 66 Nulling SThM probe schematic diagram and SEM image. [22]

The resistance of the Pt thermometer on the probe was measured by a Wheatstone bridge. The Wheatstone bridge of the probe circuit consists of two *5k* resistor, one matching resistor with value of 200 ohm, and gain of 100 amplifier as shown in Figure 67.

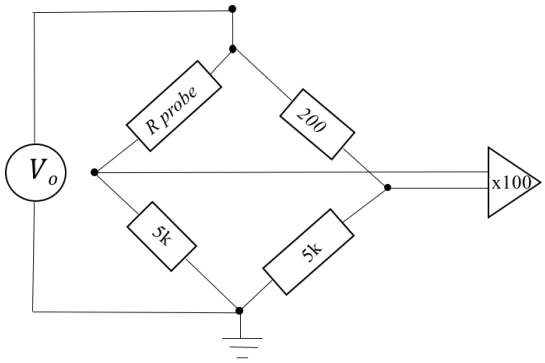

Figure 67 Nulling probe Wheatstone bridge circuit

The SThM probe was heated by heating the NiCr heater using a DC current. It was then contacted firstly to the membrane, then to the solid surface and finally held out of contact whilst the temperature changes of the tip due to self-heating was measured. The DC measurements was used to give a quantitative measure of self-heating because calibration is much more direct and simple to analysis than 3-ω method.

[22] Fabricated by Dr. Yuan Zhang

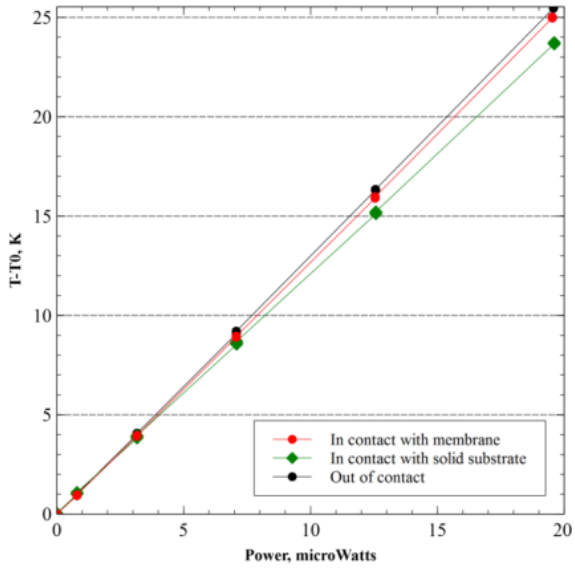

Figure 68 SThM point contact with Si substrate, membrane and out of contact signal in vacuum

The experiments were performed in vacuum. In vacuum heat only can only flow through the solid structures of the probe and sample. The plot in Figure 68 proves that the membrane is thermally isolated: it conducts much less heat than a solid Si sample where membrane was etched value of $1.23 \cdot 10^6 \pm 1.5 \cdot 10^4$ K/W. The membrane contact curve is $1.28 \cdot 10^6 \pm 2.5 \cdot 10^4$ K/W which is much closer to that of the thermally isolated probe $1.3 \cdot 10^6 \pm 10^4$ K/W. The membrane has a lower thermal conduction than the substrate but still gives a significant change in temperature rise. Thermal loading by the sample is small relative to that by the cantilever

Chapter 4. SThM measurements in active mode

A range of passive samples with different geometry and material contrast were used to determine SThM tip - sample thermal contact. As discussed earlier in this chapter, extra thermal conduction paths (e.g. gold coating or extra leads) were added to increase the thermal conduction of the sample, mimicking a wide range of materials in order to get range of thermal spreading resistance. 12 types of different SiO_2 membranes have been designed to have different thermal isolation from the environment in order to be assessed as a possible sample for calibrating measurements of the thermal conduction from a SThM tip. The heat can only go through the supporting arms in vacuum.

The potential advantages of using the set of different calibration devices in one sample is the easy access from one sample to another in one scan instead of using different samples of different materials, the lack of chemical difference between in the surfaces contacted, the intrinsic reproducibility of the samples and their economy of manufacture. In order that the design of the thermal contact measurement device should give the highest possible sensitivity to thermal transport mechanical and thermal simulations are required. Since the requirements of reliable fabrication for device strength compete with the requirements for extreme thermal isolation.

A list of the devices are shown below in order to label them for future discussion in measuremnts chapter. **(table 4)**

Table 4 Devices specifications

name	Size of supporting arms	Material added	Number of arms	
A1	700 nm	Clean SiO_2 membrane	4	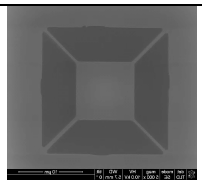
A2	700 nm	Membrane fully covered with Au	4	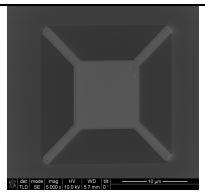
A3	700 nm	Membrane with 1X1 um Au dot	4	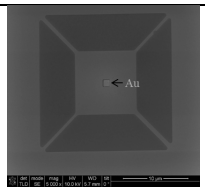
A4	700 nm	Membrane with 10X10 um Au dot	4	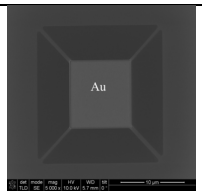
B1	700 nm	Clean SiO_2 membrane	8	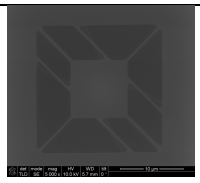
B2	700 nm	Membrane fully covered with Au	8	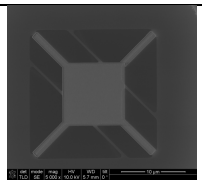
B3	700 nm	1X1 um Au dot	8	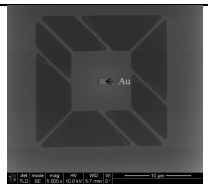
B4	700 nm	Membrane with 10X10 um Au dot	8	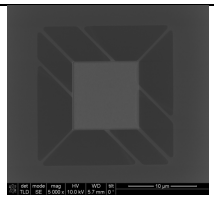
C1	1.4 um	Clean SiO_2 membrane	4	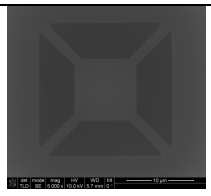

C2	1.4 um	Fully covered with Au	4	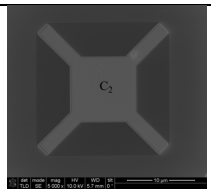
C3	1.4 um	1X1 um Au dot	4	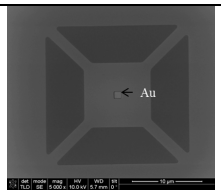
C4	1.4 um	10X10 um Au dot	4	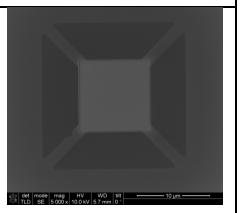

4.1 Passive device modelling

The modelling prior to experiments was simplified by looking at the heat spreading within the membrane, as it gives an idea of tip positioning and heat distribution for both active and passive SThM modes; as well as modelling of the sensitivity of active device for Passive SThM mode measurements in order to get maximum sensitivity and electrically and mechanically stable device.

The geometry of the membrane was designed and simulated using finite element analysis (FEA) software packages ABAQUS [159]. The device mechanical strength and spring constant were simulated on ABAQUS. Boundary conditions for displacement as can be seen from Figure 69 made to be stable from the edges as it was set up with 0 displacement at the edges. The boundary conditions were chosen on the edge of the membrane where the clean SiO_2 is touching the bulk Si. Mesh element type is a hexagonal 20-node quadratic brick

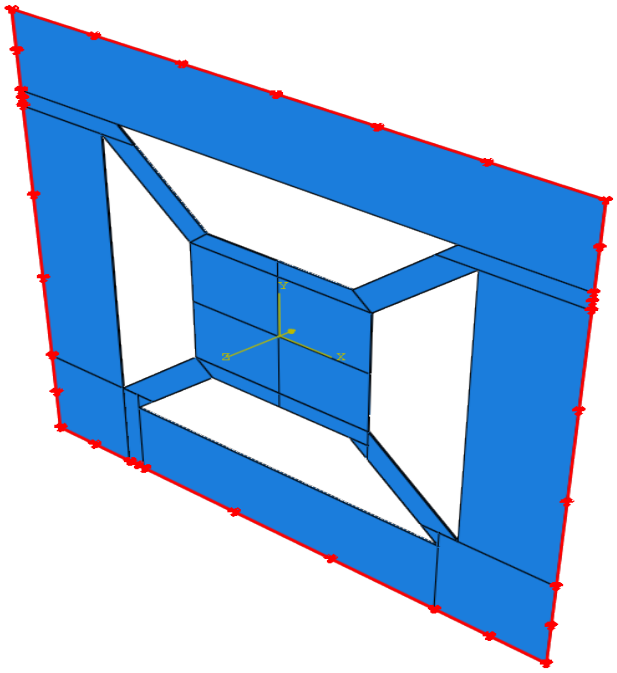

Figure 69 ABAQUS boundary conditions

SiO_2 is chosen as a material for the membrane with the thickness of 50 nm due to its low thermal conductivity properties.

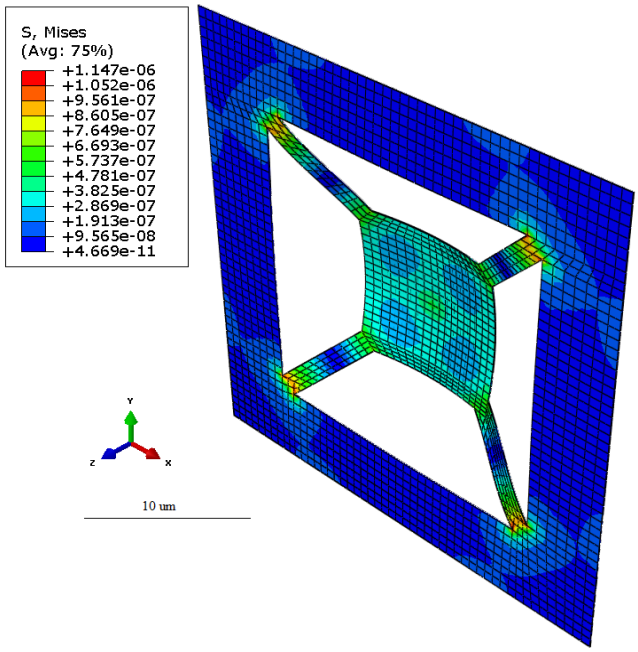

Figure 70 Stress concentration within the membrane

It can be seen in

Figure 70 that stress is mostly concentrated on the very edge of the supported arms connecting to SiO_2.

Figure 71 shows the membrane deflection of order $9.395 \cdot 10^{-9}$m, with 1 nN force to the center of the membrane applied.

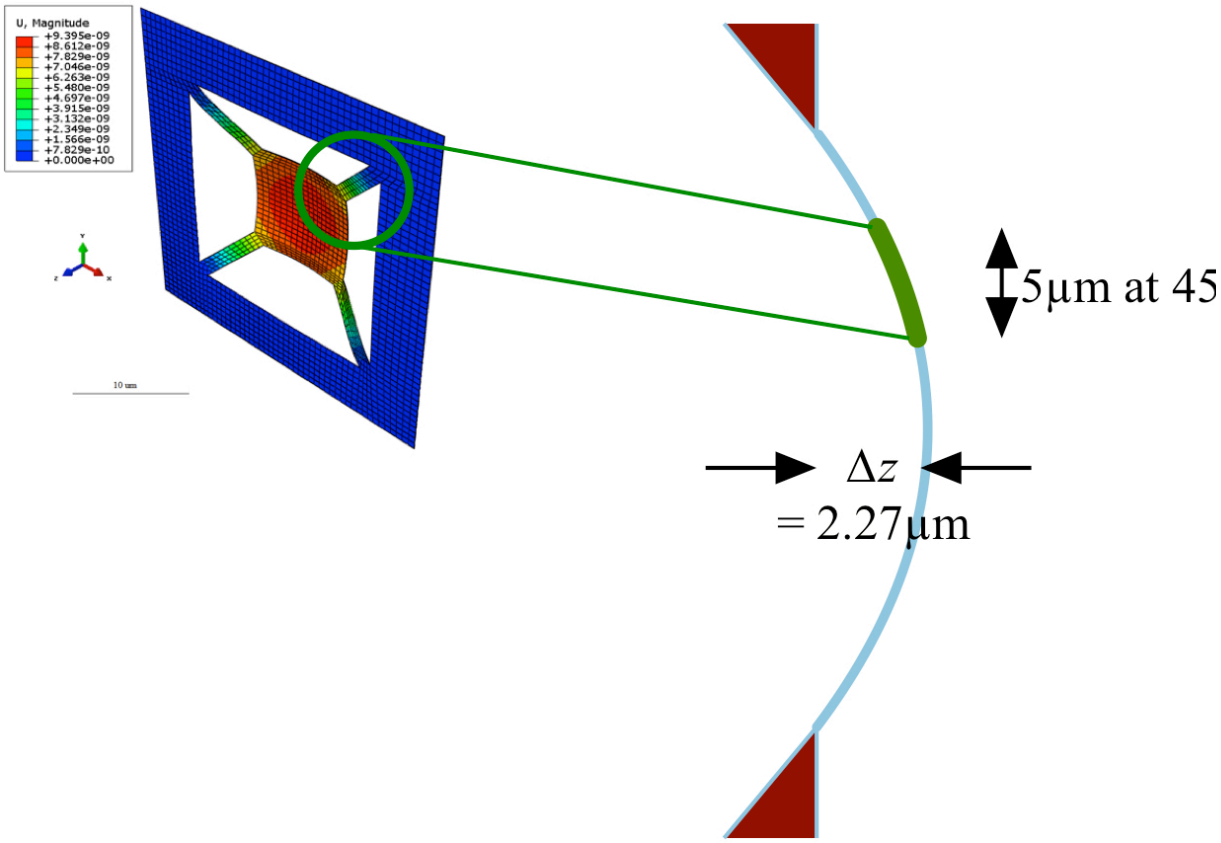

Figure 71 Deflection of the membrane

The spring constant of the membrane is therefore calculated to be about $0.106\,N/m \pm 0.005$, which is comparable to the stiffness of a SThM probe which is 0.25 *N/m*. The quoted error of $\pm 0.005 N/m$ was estimated by changing a mesh to be coarser or finer, mesh element type C3D20R which consists of quadratic bricks, C3D15 which consists of quadratic triangular prism, C3D10 which consists of quadratic tetrahedron and by changing the thickness of the membrane $\pm 10\,nm$. The estimated experimental precision of thickness control of SiO_2 film deposition by dry oxidation is about 10 nm. The film is under a compressive strain which is typically 1.5% for thermal oxide [160]. This results in the membrane bulging by approximately 2.3µm and increases the stiffness of the membrane to approximately $20 N \cdot m^{-1}$. As this is much larger than the stiffness of the cantilevers used the membrane may be regarded as a rigid surface

A number of different membrane geometries (Figure 72) were modelled in COMSOL Multiphysics software[161] with and without structured gold squares in order to manipulate thermal resistance within the membrane, with different number and width of supported arms. The aim was to produce a range of samples with different thermal conduction and control the value and nature of thermal spreading resistance within the membrane, in an attempt to mimic a set of bulk thermal conduction samples having different thermal conductivity. The metal structures were chosen to change the thermal conduction to and from the membrane so that, whilst some samples are designed to have very high thermal resistance others have low thermal

resistance. This is accomplished while using the same set of materials and processes so that all devices can be fabricated on the same chip.

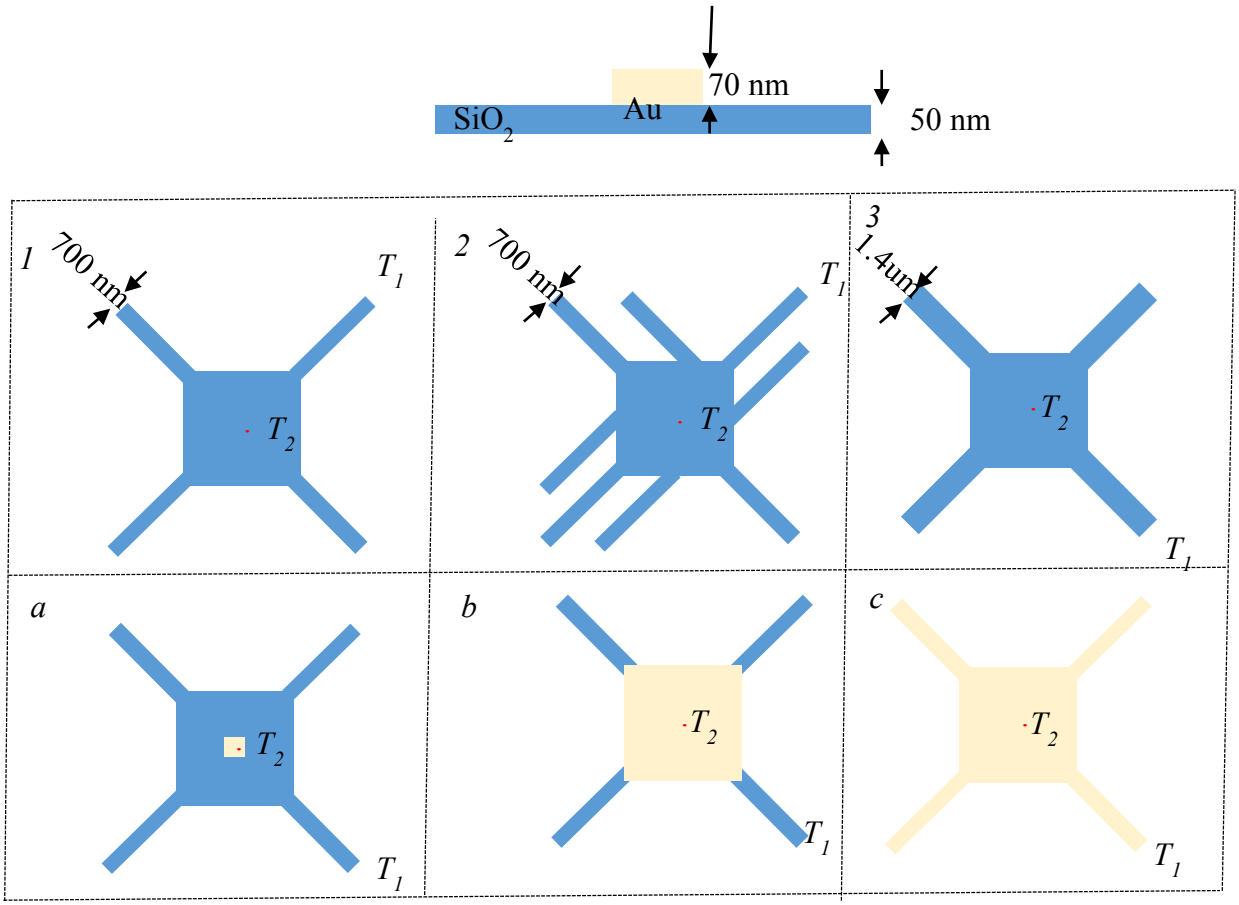

Figure 72 Geometry of passive samples

1.SiO_2 membrane with 4 supported arms 700 nm width each. 2. SiO_2 membrane with 8 supported arms 700 nm width each. 3. SiO_2 membrane with 4 supported arms 1.4 um width each. Geometry of gold structures in a,b,c will be applied all devices in 1,2 and 3.

The passive devices are adapted to use for calibration of active SThM probe. Temperature distribution within the membrane was simulated using COMSOL software with thermal boundary conditions to be set as room temperature at the edges of the supported arms. (Figure 73)

The centre of the membrane was heated to temperature T_2 when Power of 10 µW applied. The edges of the supported arms were set at room temperature T_1 as it touches the Si which is considered as a heat sink. As discussed in Introduction section the temperature gradient between T_1 and T_2 with distance *5 um* can be considered as in the diffusive regime and can be evaluated based on Fourier's law. The thermal resistance within the membrane can be found as

$$R_{th} = \frac{\Delta T}{P}$$

Type A devices include 4 different membranes with the same width of supported wires and different amounts of Gold as an extra material deposited on the top and cut line along the diagonal (**Figure 73**)

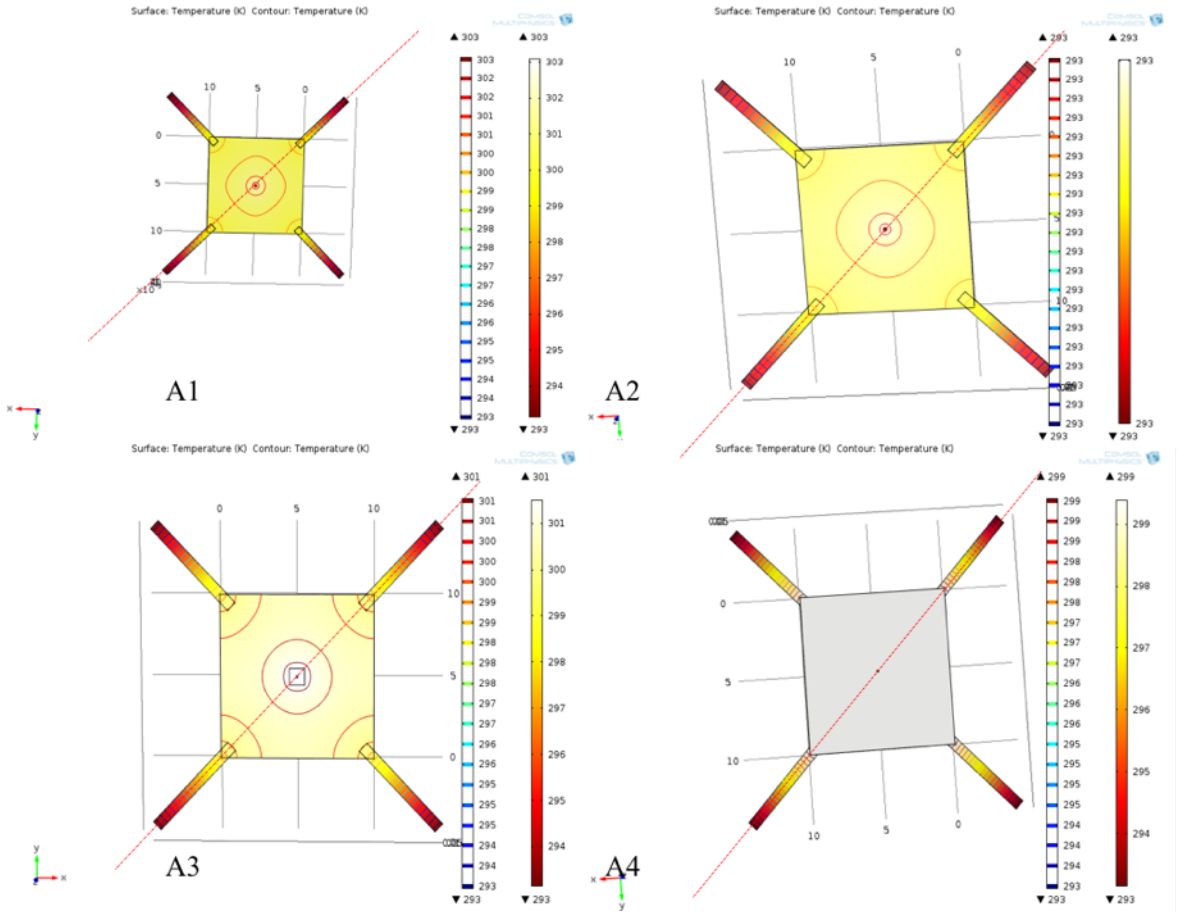

Figure 73 700 nm width membranes with 4 supported arms showing diagonal cutline used for plotting temperature in Figure 74.

The heat transfer plot of a fabricated membrane when plotting temperature versus distance can be divided in to 2 main parts: The membrane *a-area* with *log(r)* temperature dependence and supported arms *b-area* which is linear with *r*. (**Figure 74**) The areas a and b are indicated in the figure in the case of the bare membrane curve only.

The temperature distribution within the membrane (**Figure 73**) can be plotted as a temperature dependence versus distance within the membrane (Figure 74). The thermal resistance is dominated in area *b* which corresponds to supported arms and changing radially in centre of the membrane.

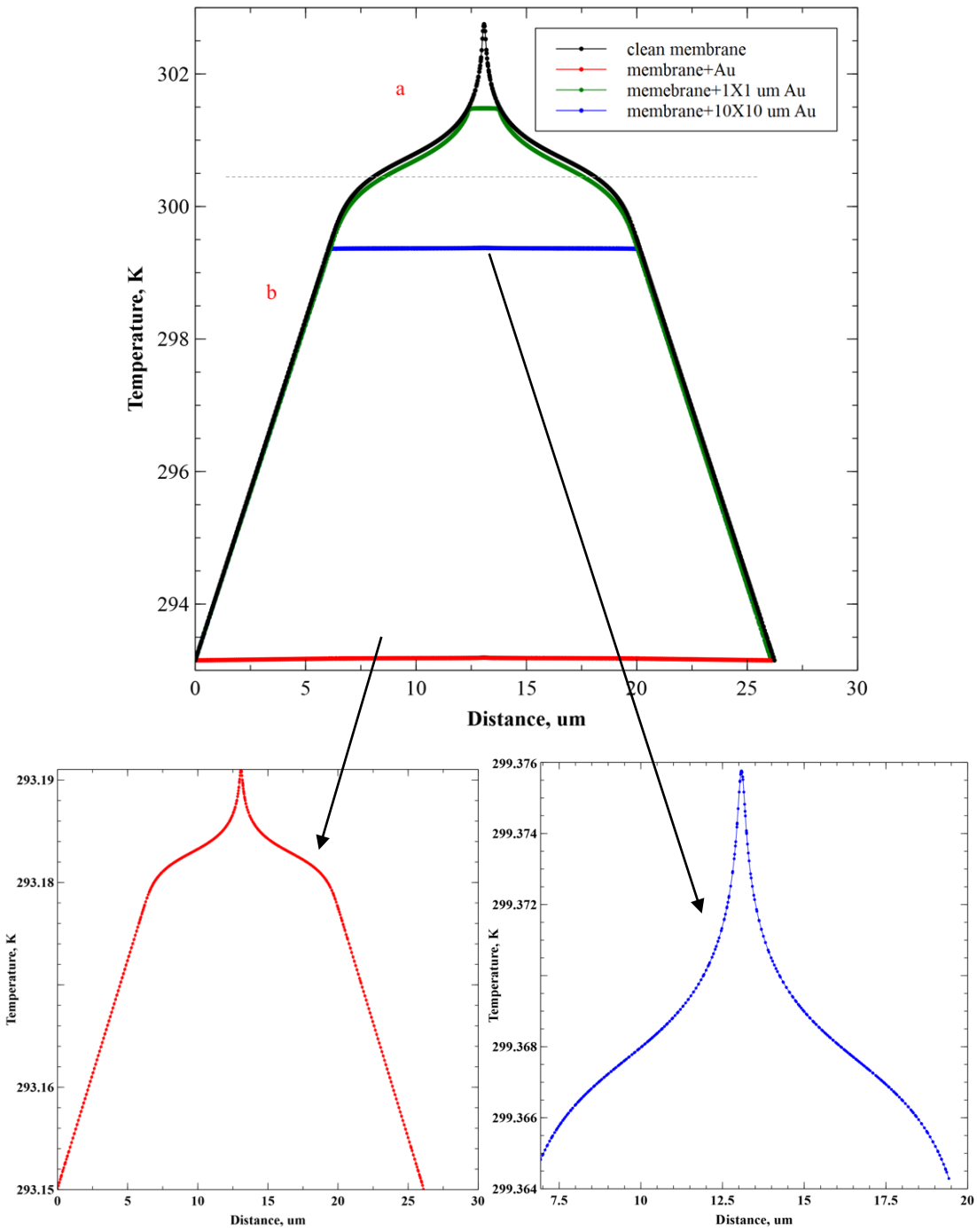

Figure 74 A devices membrane temperature distribution within the membrane and alone the supported arms.

A membrane with 0.7µm supported arms was heated for 9.60 K when 10 µW Power was applied to the centre of the membrane. The thermal resistance of passive device is $9.60*10^7$ K/W.

By fully covering the membrane and arms with thickness of 70 nm of gold, the shape of the plot (red curve) is becoming similar to the device which is free of metal which has similar number of supported arms and geometry. However, the value of thermal resistance is massively lower and so it cannot be seen when plotted at the same scale. The proportion of thermal resistance of area *b/a* is equal to *3.3* and overall thermal resistance is $4.10*10^5$ *K/W*. So by fully

covering device with gold the overall resistance dropped by a factor of "200" as the value of resistance value dropped in both parts and became dominated by the gold. Thus fully covered membrane has been plotted separately below. As can be seen from the plot that it looks similar to clean membrane (since they are geometrically identical) and temperature distribution is also uniform. However, the value of temperature change is much lower.

By placing 1X1 μm^2 Gold dots onto the middle of the membrane we can also increase the conductivity and reduce the thermal resistance (green curve). The thermal resistance is still dominated by the supported arms and remain constant after adding extra material compared to the arms in a clean membrane. However, the thermal resistance in the membrane area *a* is now reduced because contact resistance changes, so the proportion b/a is now about *6.24* and overall thermal resistance is about $8.33*10^7$ K/W. An extra material can change contact resistance without altering the overall resistance of the membrane – therefore contact resistance and overall resistance can be manipulated separately. Au could be replaced with any material.

Another option is to cover a 10X10 μm^2 membrane area with gold and to leave the supported arms free of metal (blue curve). In this case thermal resistance increases over the whole device uniformly. An interesting fact that compared to the clean membrane the effect of spreading resistance across the membrane is negligible, and all of the resistance is in the arms. Thus the membrane area is plotted separately to show that value of temperature change is very small. As spreading resistance in supported arms is dominating, the contact resistance in membrane area is becoming negligible. The overall resistance value is about $6.23*10^7$ *K/W* and the ratio of b/a is 663.

To evaluate possible error for thermal model, it essential to take into account 2 possible errors: The first is when the actual thickness of the fabricated membrane may vary slightly from the desired thickness, and second is the location of heated tip approach.

Changing the thickness of the membrane by 10 nm, the same as with the mechanical model, also has influence to thermal result and changes the heating of the membrane by 1 K for the plane membrane, which is about 10% of overall temperature change value. Changing the thickness of the silicon dioxide with membrane area covered with gold and supported arms left free of metal changed the heating of the membrane by 0.5 K less with increased thickness and 0.5 K more with thinner membrane. The same temperature change was found for the membrane with a small gold square in the centre. Changing the thickness of silicon dioxide fully covered with gold has very small affect to its temperature distribution as is fully dominated by gold contact and the possible error is about 0.01% of total value.

To estimate the possible error when the heated point moves from central location 3 cases were taken into account: membrane with small gold square in the centre, membrane covered with gold with supported arms free of metal and clean silicon dioxide membrane. (Figure 75).
When changing the position of the heated point, the overall resistance is not changing significantly for a plane silicon dioxide membrane, fully covered with gold, and membrane covered with gold. As contact area is small and overall resistance dominated by supported arms, changing the contact position does not affect the overall resistance value but has affected the uniformity of temperature distribution for the fully covered with gold and plain membranes. In region *a* the temperature drop mostly happens very close to the contact point. Changes in the distance to the edge of the membrane are not expected to have such a large effect.

In total with potential error caused with varied silicon dioxide thickness possible error will be about 5-10 %. However, for membrane 10X10 um covered with gold the temperature distribution keeps the same shape. The reason for that is that resistance is negligible within the membrane. For that purpose the membrane area was plotted separately,(blue line Figure 75.b) and is clear that the uniformity is also changed for that type of device.

The contact resistance for the membrane with a small gold dot has a dependence on the place where power is applied for overall resistance value and for uniformity. As the contact diameter is modelled as 100X100 nm and the size of the gold dot is 1 um it is important to heat the area within the gold, otherwise the contact resistance will be equal to a plain SiO_2 membrane. Thus, missing the gold square causes about a temperature change value of ΔT increasing 4 times.

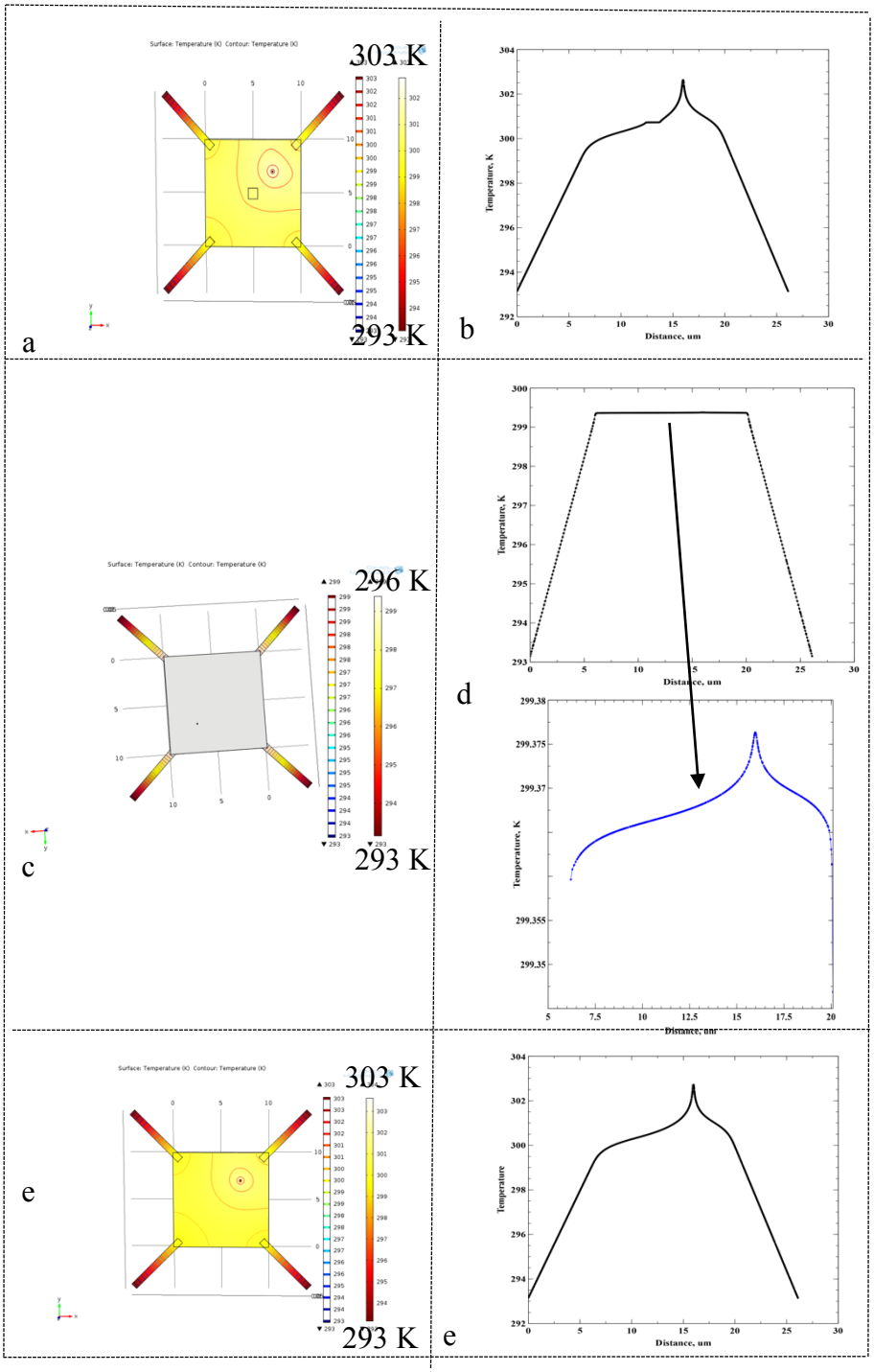

Figure 75 Temperature distribution with the membrane with changing of position of contact. ***a****. Touching the membrane with 1X1 um gold dot 2um away from center.* ***b****. Changing the temperature distribution uniformity and value of overall resistance.* ***c.*** *Touching the plain silicon dioxide membrane 2um away from center.* ***d.*** *Changing the temperature distribution uniformity.* ***e****. Touching the membrane covered with gold 2 um away from center* ***f****. Temperature distribution remains same.*

A second type of device is “type B”. These devices are similar to the above devices but with doubled number of supported wires as shown in Figure 72 number 2. Extra material is added based on the same principles as for Number 4,5, and 6. The reason increasing the number of supported arms is to reduce the thermal resistance without adding an extra material for the plane membrane and to manipulate the spreading and contact resistance as they might have

roughly similar values. The thickness and shapes of the gold films deposited on the top are also similar to previous devices. (Figure 76)

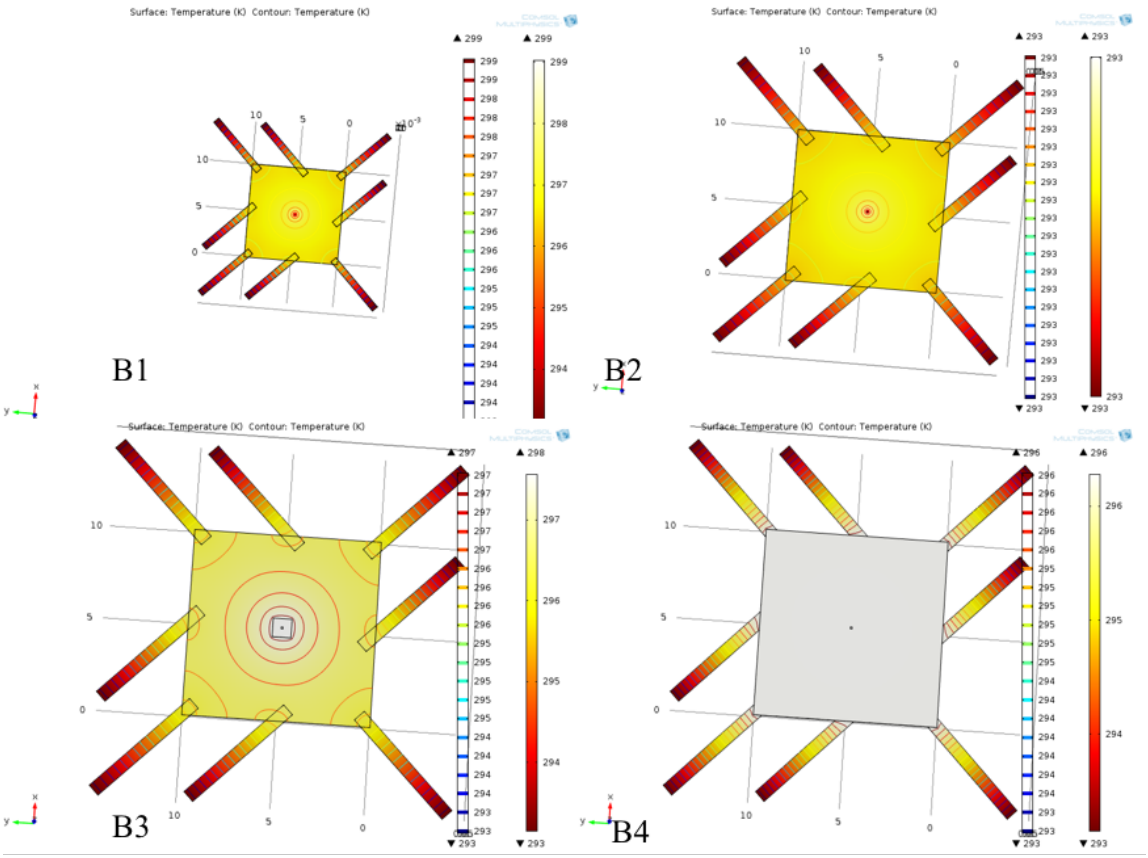

Figure 76 700 nm width membranes with 8 supported arms. Device B1 is clean membrane; device B2 is clean membrane fully covered with gold; device B3 is clean membrane with small gold square; device B4 is membrane covered with gold with supported arms left free of metal.

The temperature distribution within the membrane is again divided into 2 main parts, the membrane ***a-area*** with *log(r)* dependence and supported arms ***b-area*** with linear with *r* conduction. (**Figure 77**)

When adding 4 additional arms the temperature change decreases to 5.55 K which means that the thermal conductivity has increased and thermal resistance decreased as expected. The thermal resistance of the membrane region is the same but that of the arms is reduced so there is a nice balance between spreading resistance in the membrane and the arms and temperature distribution within the membrane is also balanced. Thus the proportion of thermal resistance in each R_{th1} /R_{th2} (or *a/b*) is about *1* and the overall thermal resistance is $5.55*10^7 K/W$. From a mechanical point of view, the doubling number of supported arms makes the membrane stronger.

By fully covering the membrane with 8 supporting arms with gold we see a nice balance between thermal resistance of membrane area and arms with overall value of $2.33*10^5$ *K/W*.

To reduce the membrane resistance and the resistance of the supporting arms a gold dot needs to be added and the number of arms needs to be increased. So the thermal resistance is

becoming dominant in the arms and reduced in the membrane. The ratio of R_{th} of part *b/a* is about 3.4 and overall thermal resistance is $4.40*10^7$ *K/W*.

The same concept of making the contact resistance negligible as with previous device, the 10X10 square membrane needs to be covered with gold to leave the supported arms free of extra material. The thermal resistance is reduced slightly more than in previous cases which makes the thermal resistance of that area negligible as can be seen. The value of overall thermal resistance is equal to $3.12*10^7$ *K/W*.

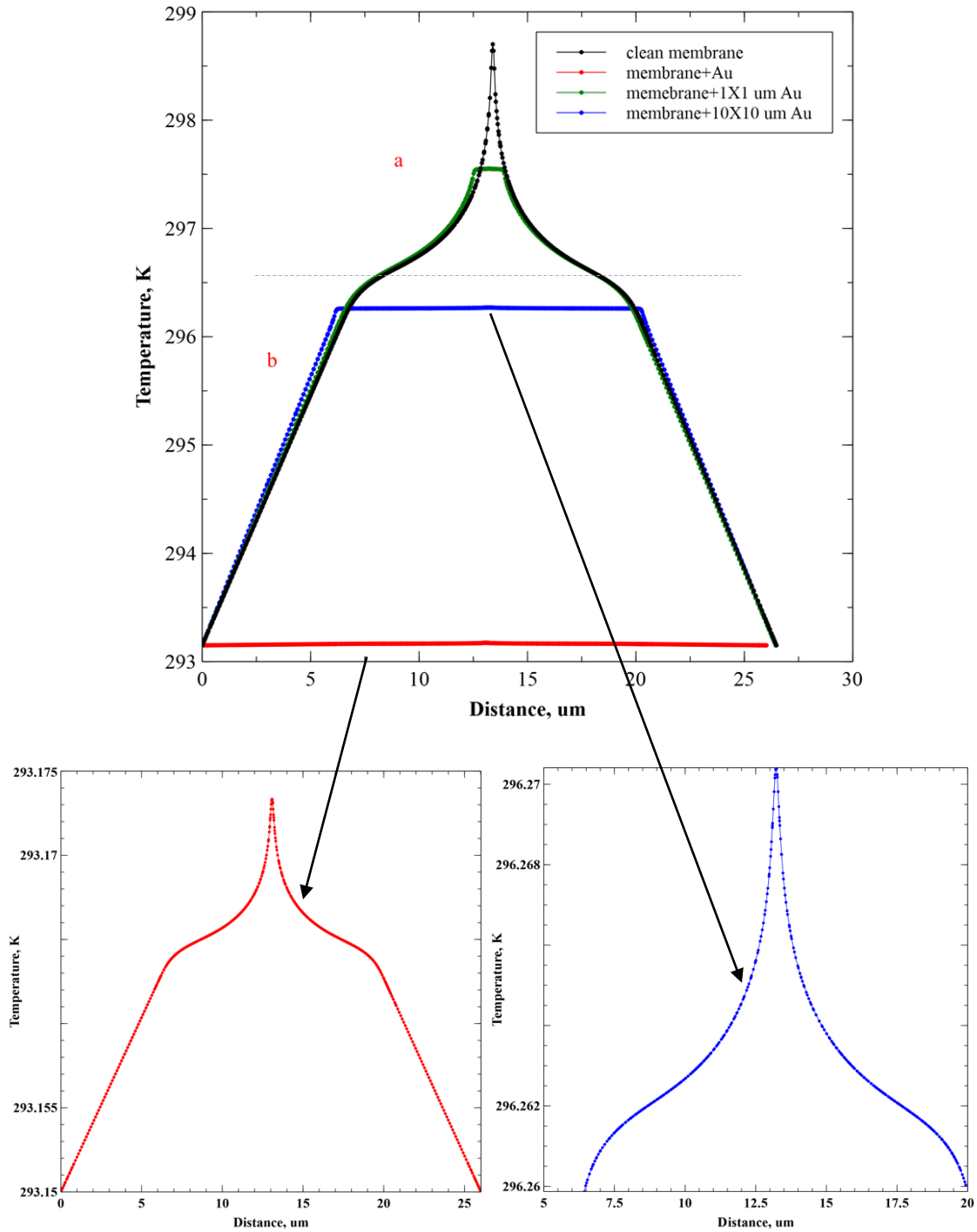

Figure 77 B devices membranes temperature distribution within the membrane and alone supported arms.

Instead of increasing the number of supported wires another option is to increase the width of them. So another set "type C" of 4 devices were designed with 4 supported wires 1.4 μm width each (Figure 78). In that case the overall thermal resistance might change, and extra mechanical strength can be achieved the same as with increasing the number of supported arms. However, the uniformity of temperature distribution might have changed. And nice balance between spreading resistance within the supported arms and within the membrane also might

stop being the case and as a result thermal resistance within the supported arms will dominate over the resistance over the membrane.

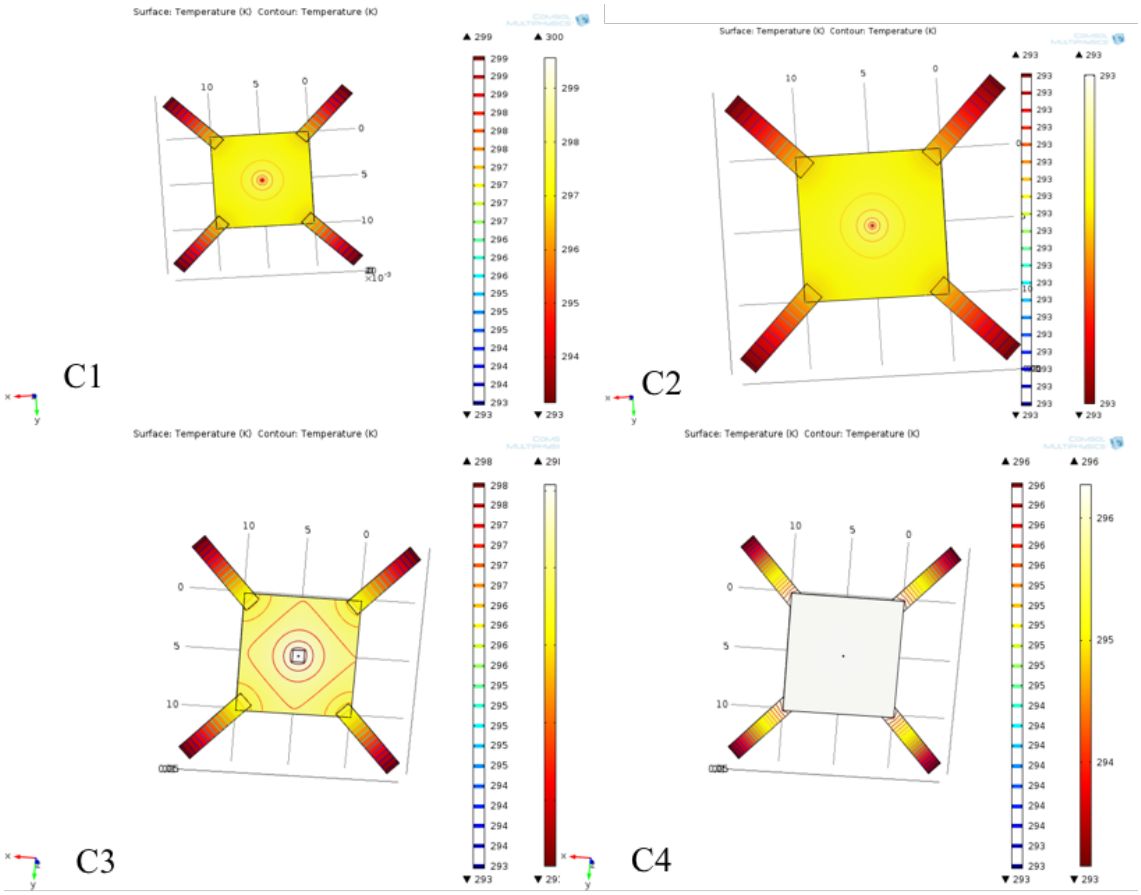

Figure 78 C Devices with 1.4 μm supported arms. Device C1 is clean membrane; device C2 is clean membrane fully covered with gold; device C3 is clean membrane with small gold square; device C4 is membrane covered with gold with supported arms left free of metal.

The temperature distribution within the membrane and supported arms in area ***a*** and ***b*** is shown in Figure 79.

The temperature of the membrane with 1.4 µm supported arms increased by 6 K when 10 µW Power was applied. The thermal resistance of device is about $6.08*10^7$ K/W which is higher then the thermal resistance of the active device as it also includes contact resistance.

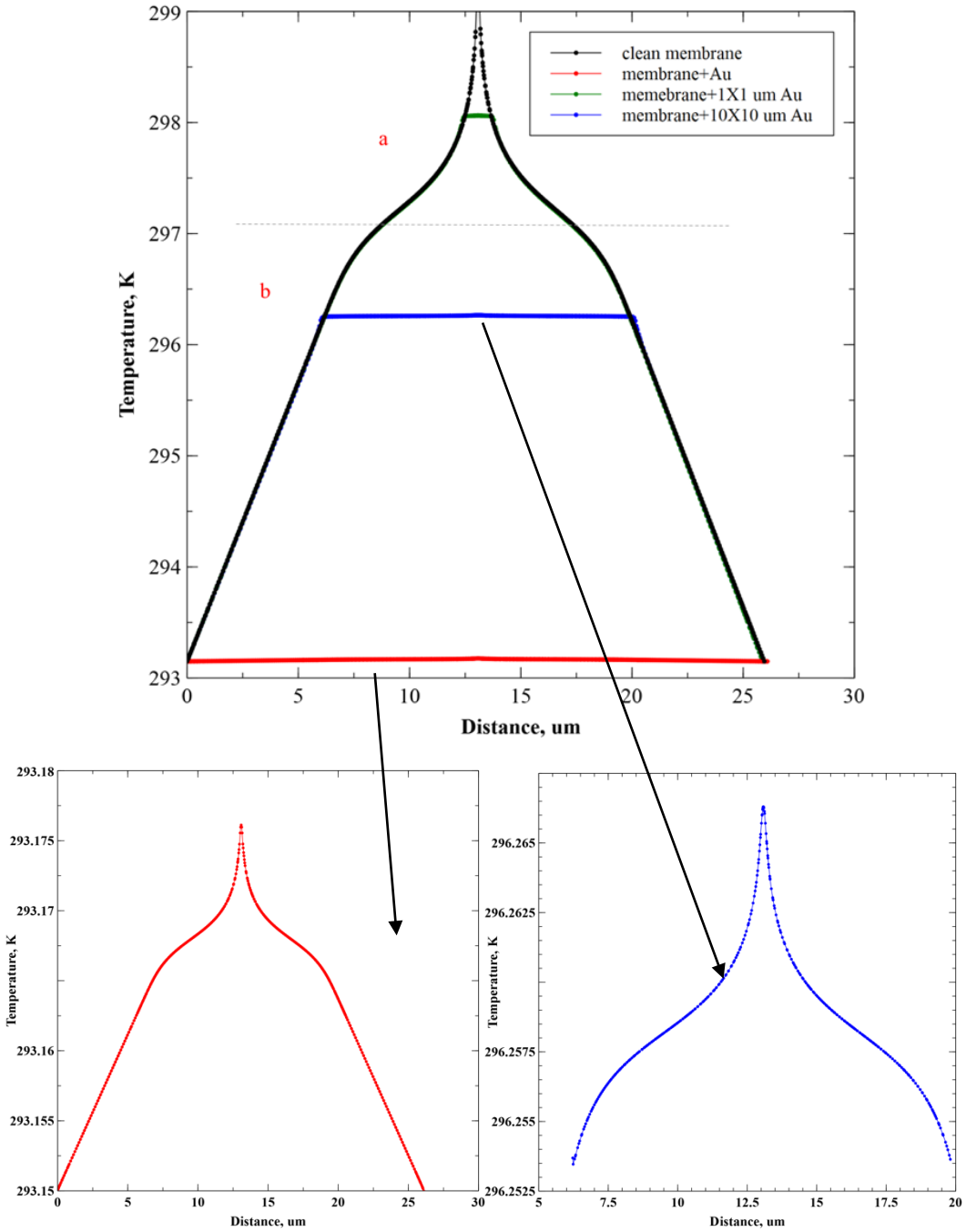

Figure 79 C devices membranes temperature distribution within the membrane and alone the supported arms

By fully covering the membrane and arms with gold the value of thermal resistance became very small, so that it cannot be seen from the overall plot on the same scale as the other curves and is equal to $2.61*10^5$ *K/W*. Thus it is also plotted separately below.

By placing 1X1 μm^2 Gold dot onto the middle of the membrane we can also increase the conductivity and reduce the thermal resistance. The thermal resistance in the membrane area *a* is now reduced so the proportion b/a is now about *3.3* and overall thermal resistance is about $4.91*10^7$ K/W.

The same as with previous geometries, covering 10X10 μm^2 membrane area with gold and leaving supported arms free of metal, the thermal resistance of the whole device is

increasing uniformly. The overall resistance value is about $3.12*10^7$ K/W and the ratio of b/a is 332.

The geometry of the passive devices was drawn in Tanner L-edit [146] software in expansion for fabrication as shown in Figure 80. A series of samples were developed on the one piece of Si.

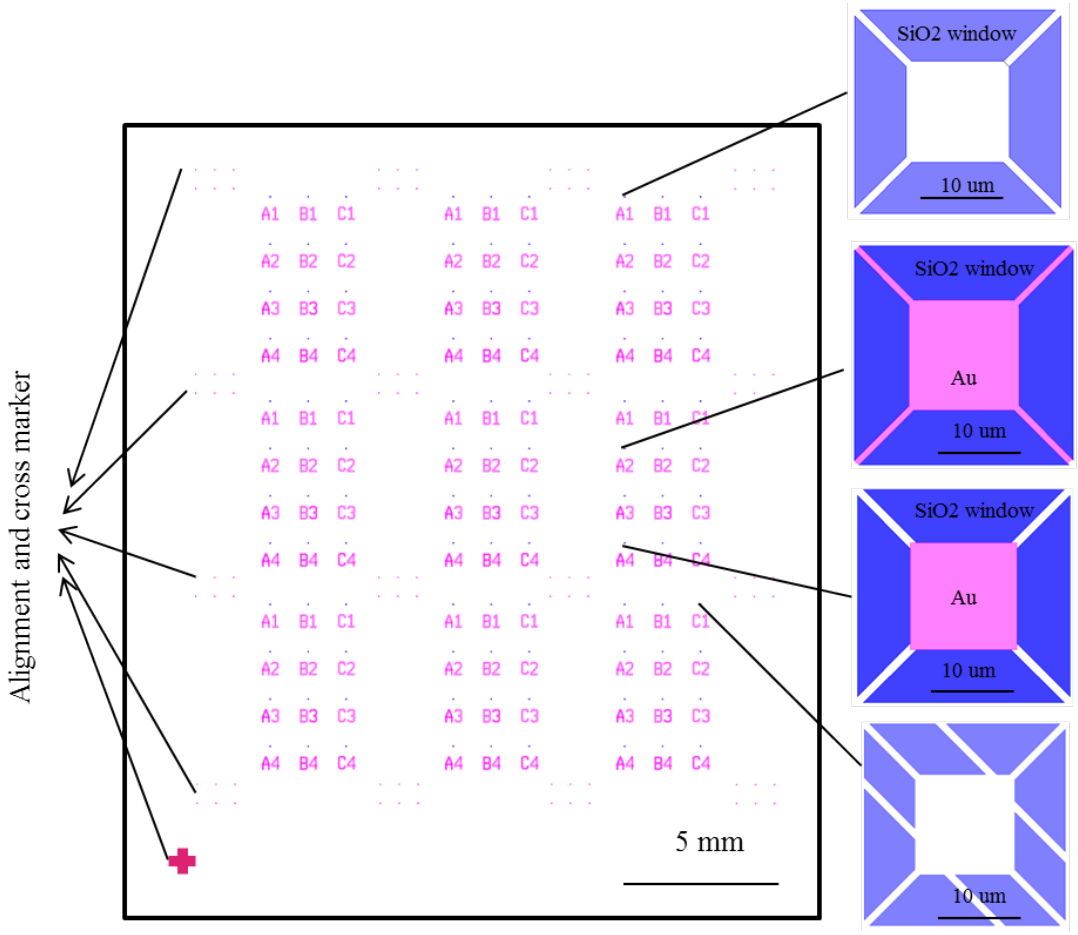

Figure 80 Passive devices L-edit design for 9 chips consisting 12 different devices.

4.2 Passive device heated by active SThM probe.

The thermal sensitivity of a Nulling SThM probe was performed by self heating with DC current and was measured as $1.25 \cdot 10^6 K/W$.

By heating the probe sensor with an AC signal the 3ω signal was measured in order to determine heated probe tip- sample thermal conductance with increased precision. The 3ω takes advantage of lock-in amplifier technology and measurement performed in frequency domain. [154] The thermal conductance equation was derived in previous chapter. In Eq.26. A diagram of the process of heated tip-sample interaction is shown in Figure 81

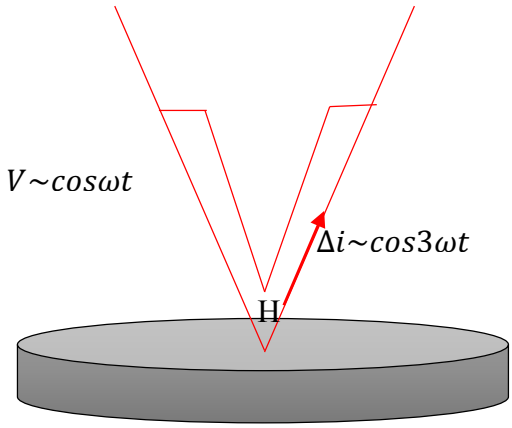

Figure 81 Heated tip-sample contact schematic diagram

Before performing measurements with fabricated devices bulk silicon was scanned first in order to get reference number to relate to future measurements. The $g_{t\text{-}s}$ and $g_{t\text{-}s}/g_{0rt}$ values for Si substrate measured to be $2.33 \cdot 10^{-8} \pm 4.5 \cdot 10^{-10} W/K$ and 83.0 ± 1.6 respectively. The values for $g_{t\text{-}s}/g_{0rt}$ changes with temperature. As a temperature change is not big, the value scaled as $g_{t\text{-}s}/g_{0rt}$ at room temperature. If the the temperature rise is 3 °, any step would be 1% bigger but we haven't seen quantization.

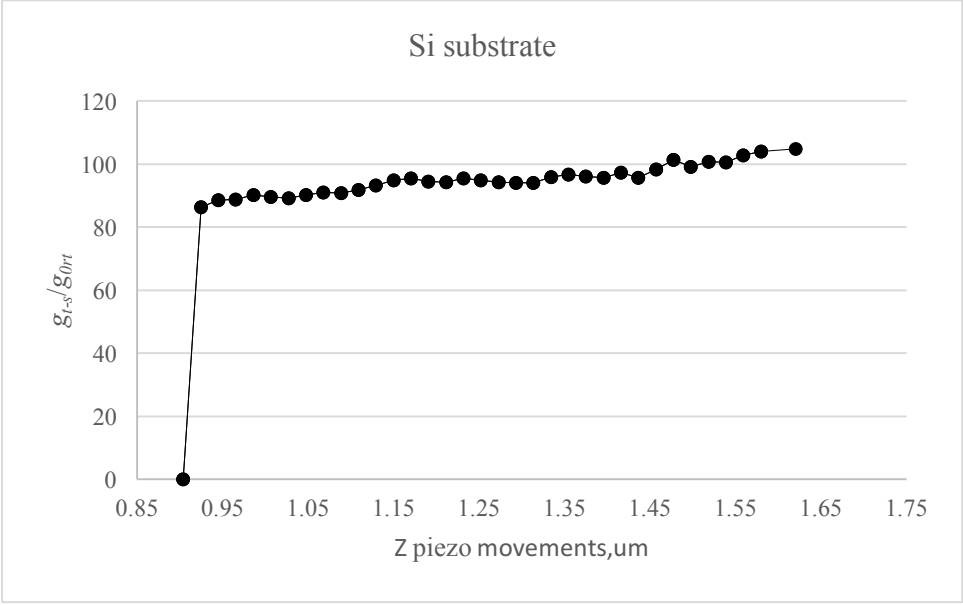

Figure 82 The step of thermal conductance signal when tip is approaching the bulk Si surface

The first measurements were done by approaching the SiO_2 membrane with four 700 nm width supported wires. As can be seen from the simulation this has a thermal resistance dominated by the supporting arms. The device A1 is shown in SEM image on Figure 83 and is a simple thermally isolated silicon dioxide membrane.

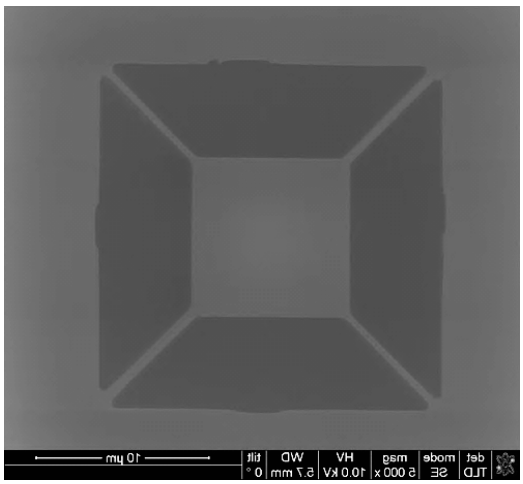

Figure 83 Device A1 clean SiO_2 membrane

The heated nulling SThM probe tip and clean SiO_2 membrane were contacted and the results are shown in Figure 84. The use of the 3-ω technique give greatly improved sensitivity of measurement compared to DC I-V measurement such as is used in Figure 68, but the use of a DC measurement avoids errors due to the frequency response of the system, and hence is preferred for absolute calibration. As shown by equation 26 the amplitude of the 3-ω signal is proportional to the total thermal resistance from the sensor to ambient. Thus the 3-ω signal amplitude out of contact (0.4876V) corresponds to the thermal resistance of the cantilever measured by the method shown in figure 68 ($1.25 \cdot 10^6$ K/W). The sudden change in 3-ω amplitude on contact corresponds to the reduction in total thermal resistance due to the parallel conduction path from the sensor to the sample At first contact the step change in thermal conduction was $16.02 \pm 0.35 g_{0rt}$. The step change for each contact is relatively similar for all contacts and there is a presence of a small pull-off force value of 34.85 ± 1.87 nN.

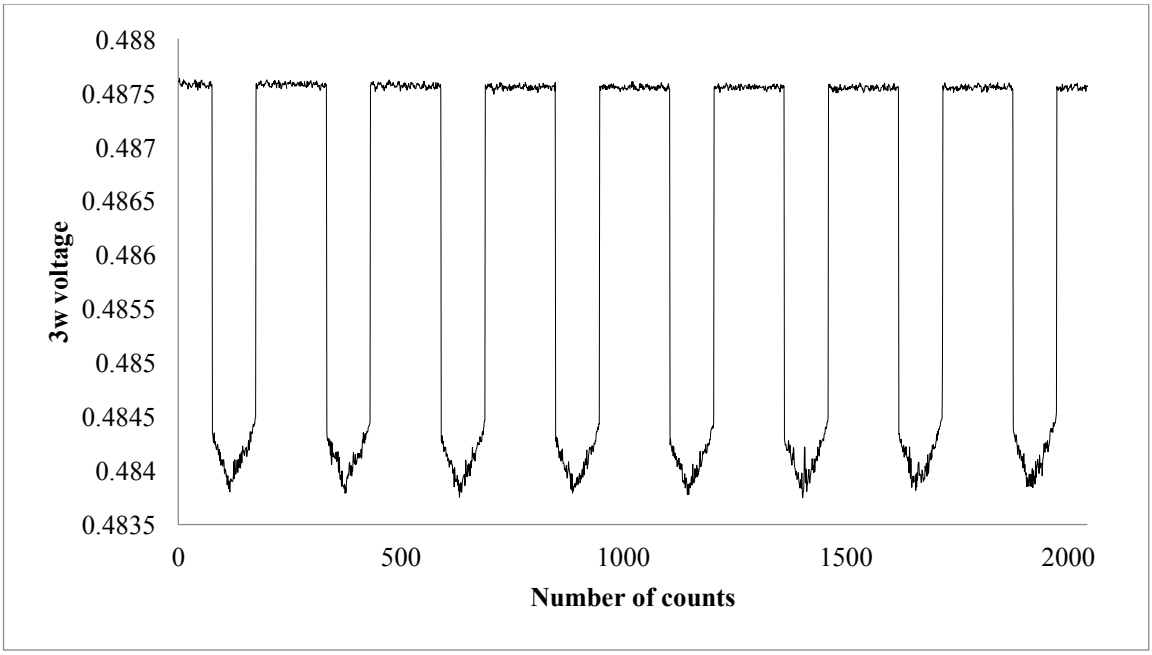

Figure 84 Device A1 in contact with SThM probe tip

A summary of probe tip- sample contact results for the clean SiO_2 membrane are shown in **Table 5**.

The error was estimated to be a standard deviation for all contacts when probe tip approached the sample at the same place 8 times. The value is the mean of these measurements

Table 5 DeviceA1 heat transport summary

g_{T-S}, W/K	$g_{t\text{-}s}/g_{0rt}$	F, pull off, nN
$4.57 \cdot 10^{-9}$	16.05	34.02
$4.54 \cdot 10^{-9}$	15.915	34.02
$4.60 \cdot 10^{-9}$	16.15	35.91
$4.69 \cdot 10^{-9}$	16.47	35.91
$4.68 \cdot 10^{-9}$	16.45	35.91
$4.62 \cdot 10^{-9}$	16.21	34.01
$4.58 \cdot 10^{-9}$	16.07	34.01
$4.43 \cdot 10^{-9}$	15.55	30.24

The thermal conductance value of g_{T-S} **in column 1** was calculated from the known value of the 3ω Voltage when probe out of contact and in contact with sample surface and the Nulling probe thermal resistance value of $1.25 \cdot 10^{6} K/W$ which was calculated from DC measurements in section 4.2. The value was converted into a value expressed as a multiple of g_{0rt} as discussed in the Introduction section **(column 2)**.

The pull-off force in **column 3** for each contact was determined from the change in *Z* Piezo movement and the known value of spring constant for probe and membrane. *Z* piezo movement was determined as discussed in chapter 3.

The measurement of electrical noise is done by quantifying the noise level of the signal when the probe is out of contact in terms of thermal conductance quantum g_{0rt} and has a value of $0.2\ g_{0rt}$. Thus all values are above the noise limit can be considered as a significant value.

The noise in contact is assumed to not have more electrical noise so the increase in noise is due to variations in thermal conduction. The value is greater than when out of contact by a factor of 2.

As discussed in [9], contact between SThM-AFM tip and sample can occur by in micro- and nanoscale single-asperity contact and multi-asperity (Figure 85). The force dependence of the thermal conduction resulting from such contacts are studied.

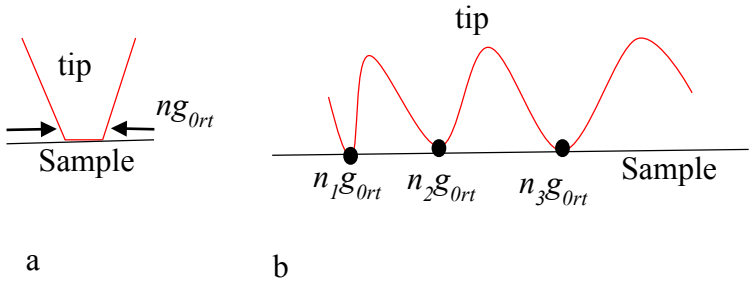

Figure 85 The nature of tip-sample contact. a. Ideally flat surface contact. b. Rough surfaces contact.

Based on Figure 84 with the thermal conductance value of $n_i\ g_{0rt}$ there is a presence of range of thermal value corresponding to noise or multi-asperity contacts. In order to evaluate the nature of tip-sample contact it is essential to zoom in the "In contact" area from the plot in Figure 84. In the case of multi-asperity contact it would be expected that the variation in thermal conduction would show discrete steps which would repeat as a function of force over subsequent contacts (Figure 86).

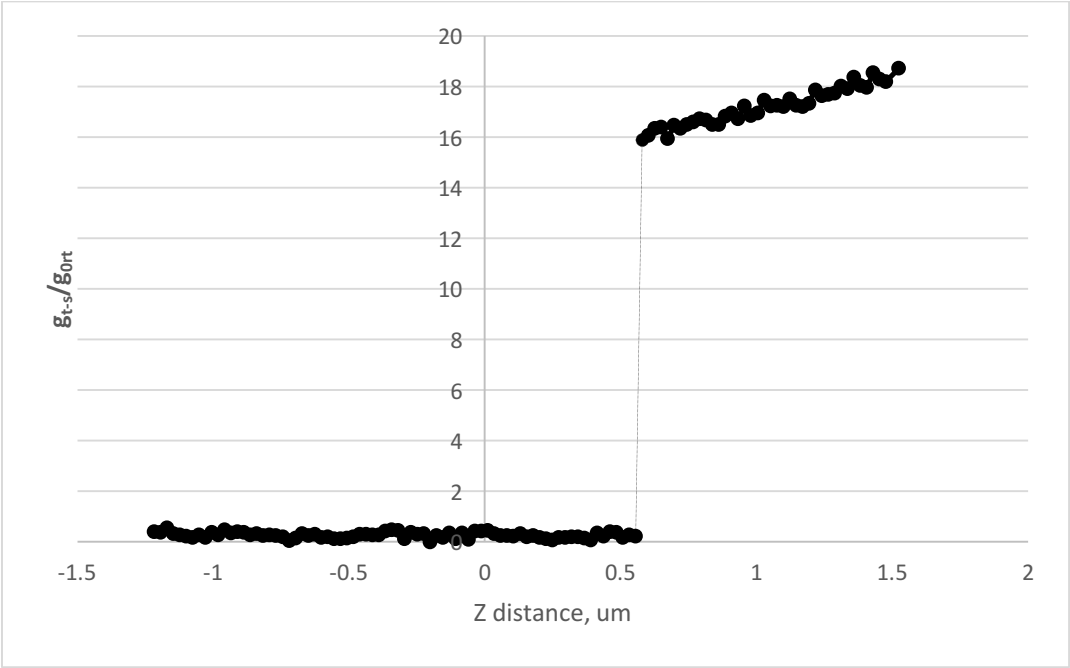

Figure 86 The step of thermal conductance signal when tip is approaching and retracting from device A1

Because the noise in contact does not repeat with multiple contacts there is no evidence of multi-asperity contact. We don't expect ballistic quantization as SiO_2 has a very small mean free path. Therefore, we attribute the noise to mechanical vibration between tip and sample modulating the thermal contact.

The straight line of 3ω Voltage values plotted versus force applied when the probe is approaching the sample surface is shown in Figure 87. The thermal conductance value is increased when force increased as was discussed in [9] and values plotted for the first 4 contacts. The force – conduction curve is similar for all contacts, so we don't think the tip is changing with time. it can be seen that probe is smooth and there is no repeat one above other. Heat flowing out of the tip to membrane is dominated by the thermal conductivity of sample and corresponds to fixed thermal extraction from the probe.

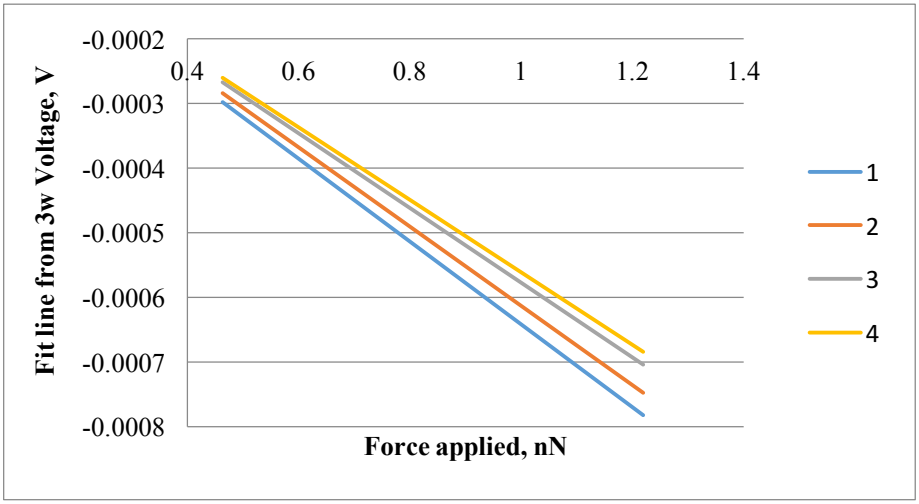

Figure 87 Thermal conductance value with force applied

As the thermal conductance was dominated by the thermal resistance of SiO_2, the contribution of the tip-sample conductance to the total thermal conduction from the tip wasn't well defined. Based on the thermal resistance network discussed in Chapter 1, when a heated SThM tip contacts a silicon dioxide membrane fully covered with gold (Figure 88) there will be a strong dependence on tip-sample thermal conductance $g_{t\text{-}s}$ as the tip and sample are both made of materials with high thermal conductivity.

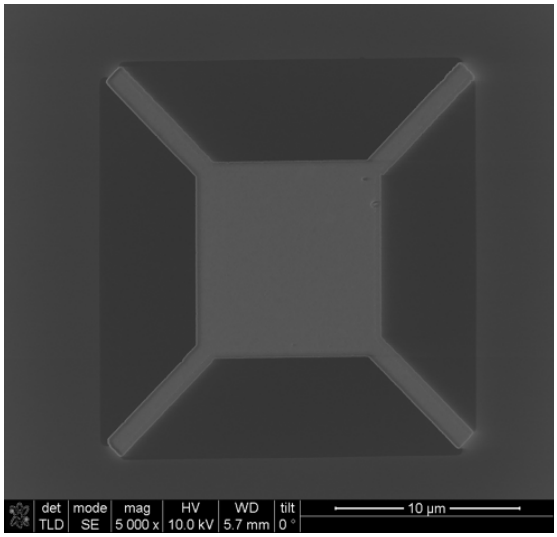

Figure 88 Device A2 fully covered with gold

The results of such a measurement are shown in **Figure 89**. Tip-sample thermal conductance $g_{t\text{-}s}$ has a high resolution in circumstances when sample thermal conductance is dominated so the large scatter in tip-sample conduction is easily seen is a lot of scatter. As can be seen from Figure 89 The noise is characterised by many big jumps suggesting multi-asperity contacts. It is much larger than that seen in the first sample. By inspection some features seem to repeat, such as the shelf 2/3 of the way up on contacts 3,4 and 5 but then they go away. This is characteristic of the tip shape changing with each contact, which would be consistent with metal flakes making the contact. Noise because of mechanical vibrations can be excluded due to high thermal signal between tip and sample. However, due to the instability of the thermal signal all measured contacts need to be measured to estimate the probability of multi-asperity contact.

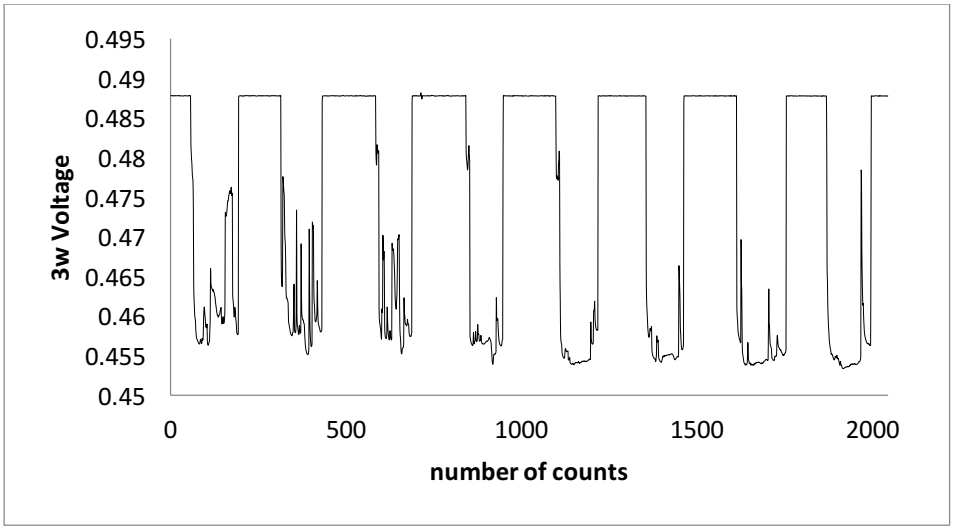

Figure 89 Device A2 in contact with SThM probe tip

In order to evaluate the value of very first contact the g_0 when tip just touched the sample surface was measured and summarized along with with values for pull-off force in

Table 6

Table 6 Device A2 heat transport summary

g_{T-S}, W/K	$g_{t\text{-}s}$ / g_{0rt}	F, pull off, nN
$9.68 \cdot 10^{-9}$	33.9	29.48
$2.73 \cdot 10^{-8}$	110.49	-1.63
$9.95 \cdot 10^{-9}$	40.22	18.02
$1.02 \cdot 10^{-8}$	41.24	22.92
$8.46 \cdot 10^{-9}$	34.21	42.58
$3.16 \cdot 10^{-8}$	127.89	21.29
$3.77 \cdot 10^{-8}$	152.38	80.25
$8.41 \cdot 10^{-9}$	34.00	54.04

According to Table 6 values of g_{0rt} for first contact can be classified into two groups which correspond to two contacts from *30-40* $g_{0\text{rt}}$ as a first and *100-150* g_{0rt} for second group.

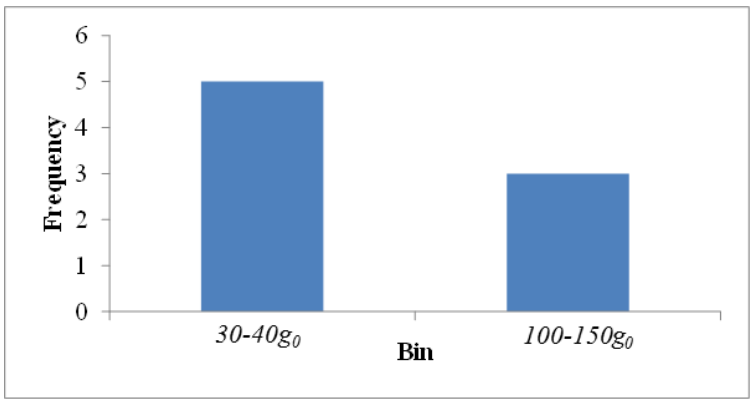

Figure 90 Two group of thermal conductance value

Looking at the distributions of thermal conduction at first contact there appear to be two distinct types of contact being made. The first possible contact is the Pt resistor with gold surface $R_{Pt:Au}$, with value of thermal resistance of supported legs in parallel, which is supposed to have the larger value. The second case is might be silicon nitride cantilever touching a surface of gold, as the metal from tip might be peeled of slightly.

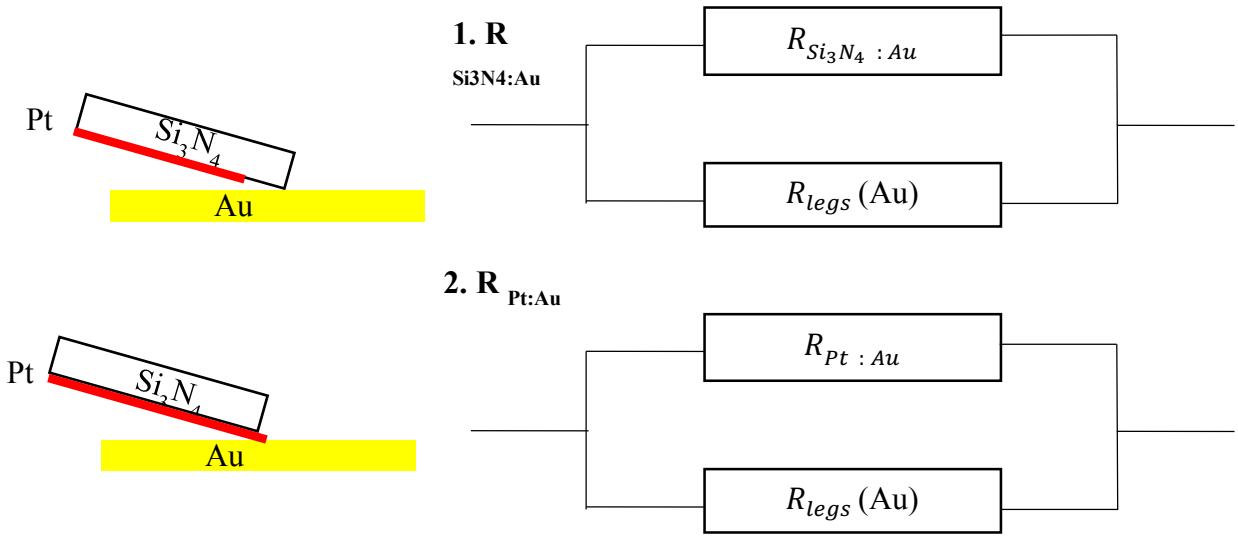

Figure 91 Possible thermal resistance affecting the thermal conductance value

This theory is supported when looking at the first contact. The value for first thermal conductance is equal to $32.17\ g_{0rt}$ which means that Si_3N_4 is making a contact with gold surface. As the tip is pushed harder the value changes to $133.93 g_{0rt}$ which more likely that Pt making a contact with gold and is consistent with the higher values seen at first contact.

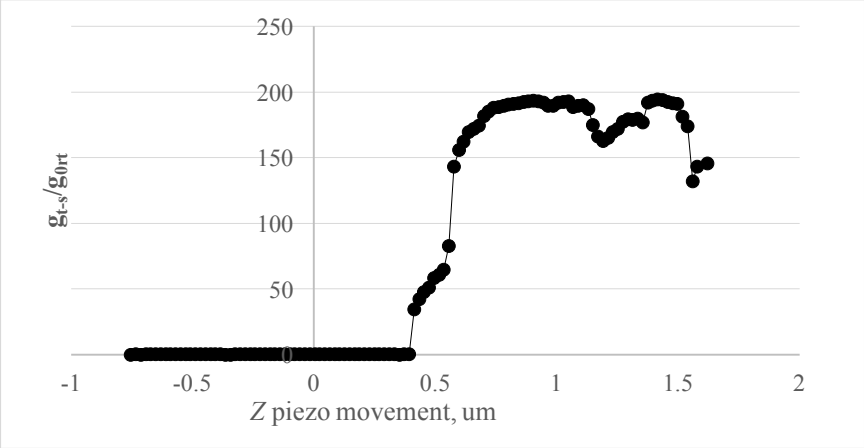

Figure 92 The step of thermal conductance signal when tip is approaching and retracting from device A2

In order to determine whether the type of the contact is multi-asperity, thermal conductance value in units of g_{0rt} when the probe is in contact for all eight approaches have been plotted. (**Figure 93**)

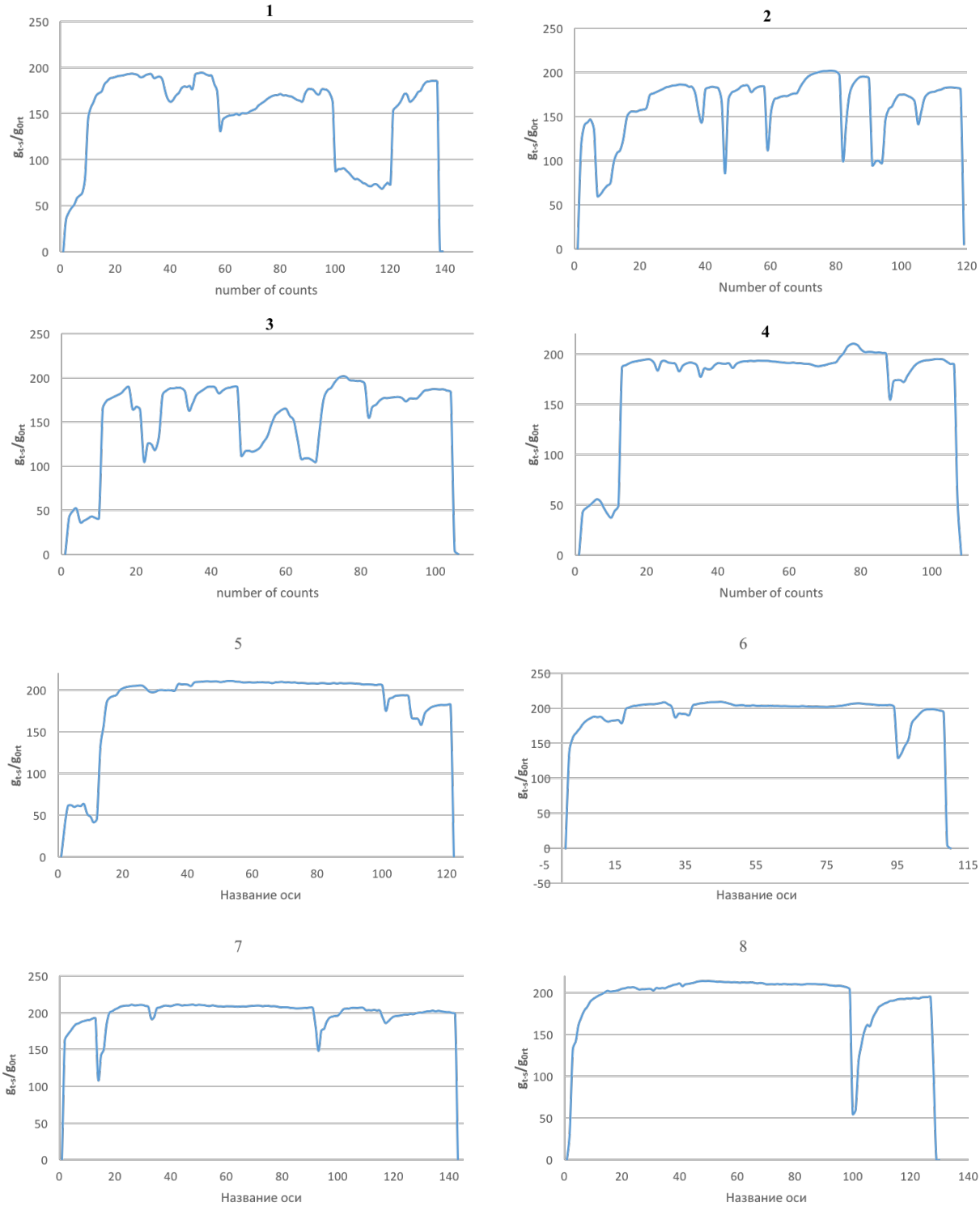

Figure 93 Multi-asperity contact values when tip in contact with Device A2

There is no real correlation between pull-off force and initial contact value and thermal signal when retracting and pulling force as can be seen in Figure 94. One possibility is that the pull off force is associated with different bits of the tip sticking to the sample than the first one to make contact, and that it is different each time.

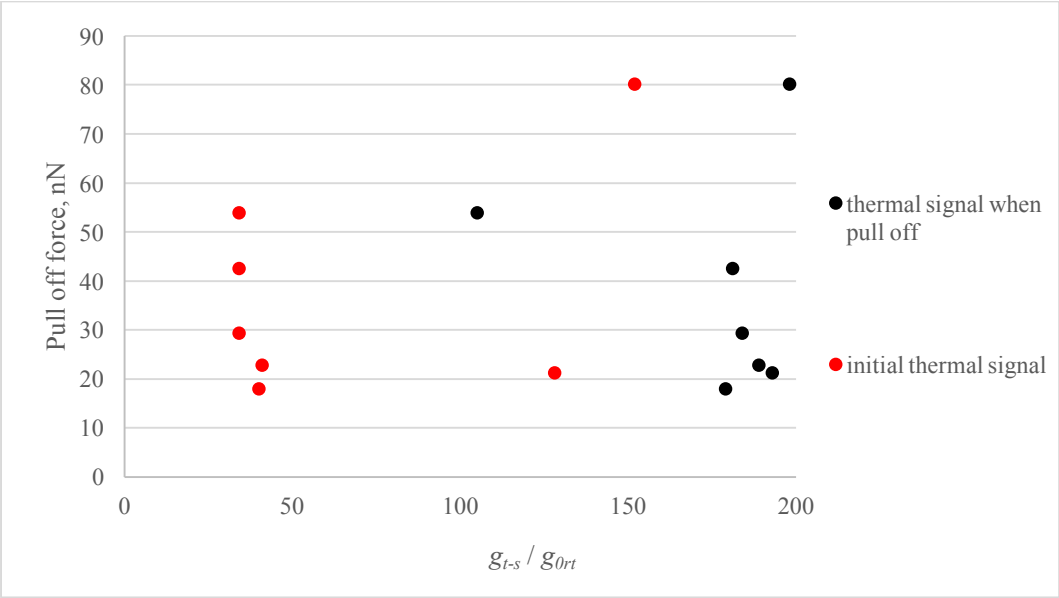

Figure 94 Pull off correlation with initial contact

The first three contacts are the noisiest compared to others. The tip may have flakes of metal flopping about. The contact with the surface may move these or rip them off, so that later contacts just take place with the more mechanically stable bits of metal. Fewer bits of metal to make contact, hence fewer jumps. In contact number four the in-contact area looks more stable. Confirmation of this behaviour is seen in the active measurement of the KNT probe later on, where a big chunk of metal is seen to be detaching from the tip. Based on the assumption made in the previous section (Figure 90), by classifying the type of contact by material touching the Au surface it appears that while the first contact may correspond to either Si_3N_4 or Pt on increasing the force the subsequent contacts add to give a relatively stable value of about 140 g_0. That is to say, in the case when possibility of silicon nitride touching the gold surface was high, it was followed by second contact corresponding to the case of platinum touching the membrane surface. It happened in contact number 1,3,4,5,8. In opposite case for contacts number 2,6,7 the value for second contact was around $30g_{0rt}$ which means that is more likely that Silicon nitride is touching the membrane. Thus it can be concluded that device type A2 (fully covered with gold) might be a case of multi-asperity contact.

The thermally isolated membrane made of dielectric material has the highest sensitivity to heat flow. For sensitivity to the heat flow between tip and sample, the membrane fully covered with metal is better. However, due to higher thermal conductivity this can lead to larger measurement errors in that number. One possible solution is to vary the size of the metal film covering the dielectric membrane and leave the supported arms free of metal.

An example, adding a gold 1X1 μm^2 square with thickness of 100 nm is shown in (Figure 95).

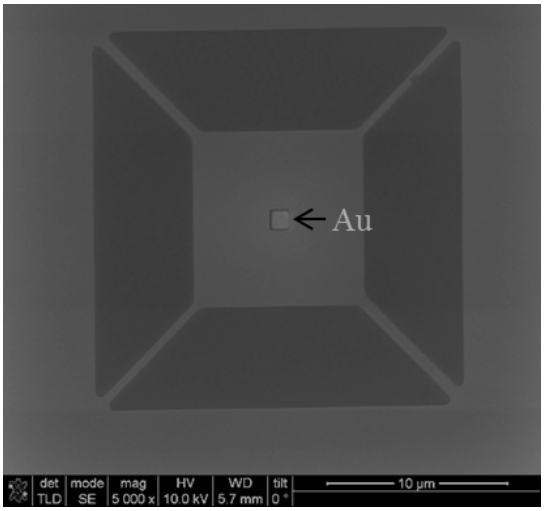

Figure 95 Device A3 with small gold dot

At first contact the step change in thermal conduction was $15.54 \pm 0.55 g_{0rt}$. The step change for each contact is relatively similar for all contacts and there is a presence of a small pull-off force value of 11.08±1.07 nN. The values of 3ω signal changing with time are plotted in Figure 96.

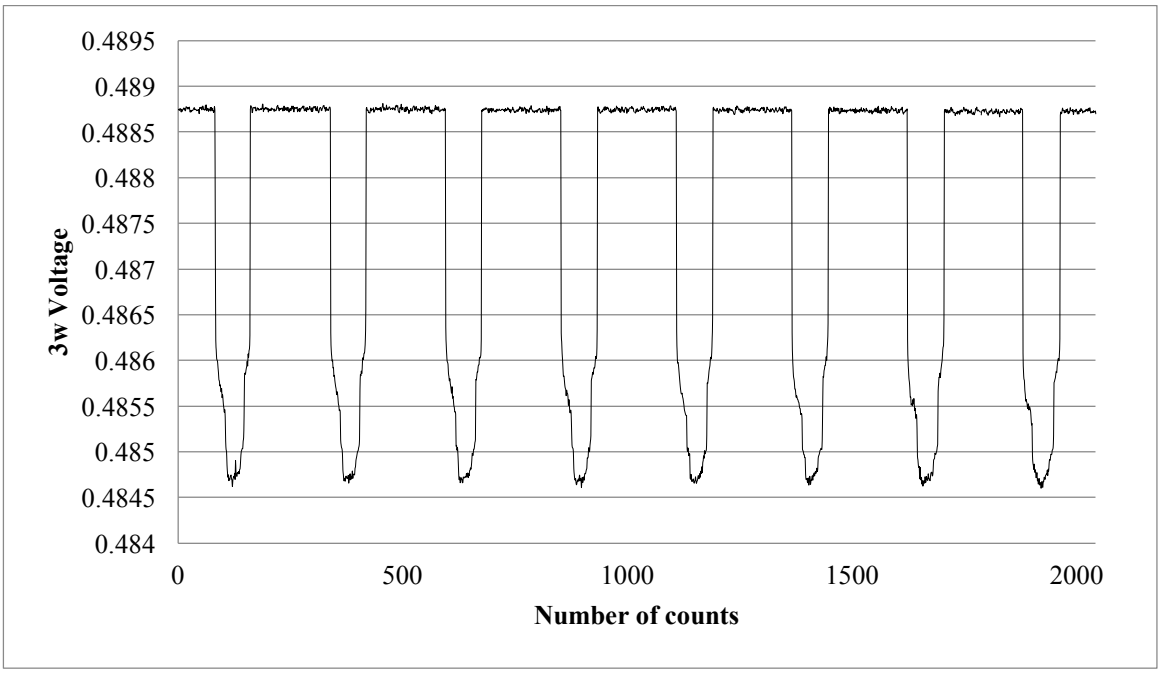

Figure 96 Device A3 in contact with SThM probe tip

The values of heat conductance in initial contact and pull of force values for each contact placed in Table 7

Table 7 Device A3 heat transport summary

g_{T-S}, W/K	$g_{t\text{-}s}$ / g_{0rt}	F, pull off, nN
$4.14 \cdot 10^{-9}$	14.53	10.07
$4.33 \cdot 10^{-9}$	15.20	10.07
$4.42 \cdot 10^{-9}$	15.50	10.08
$4.37 \cdot 10^{-9}$	15.36	11.08
$4.53 \cdot 10^{-9}$	15.90	11.08
$4.42 \cdot 10^{-9}$	15.54	11.08
$4.53 \cdot 10^{-9}$	15.90	11.08
$4.66 \cdot 10^{-9}$	16.37	12.09

From the values in Table 7 and plot in Figure 97 it might be assumed that the small size of the gold dot makes it difficult to focus on the centre of the membrane making this sample difficult to use in practice. Thus heated SThM tip possibly contacted the SiO2 surface instead of gold dot and value of first contact is close to device A1 which is shown in diagram in Figure 98.

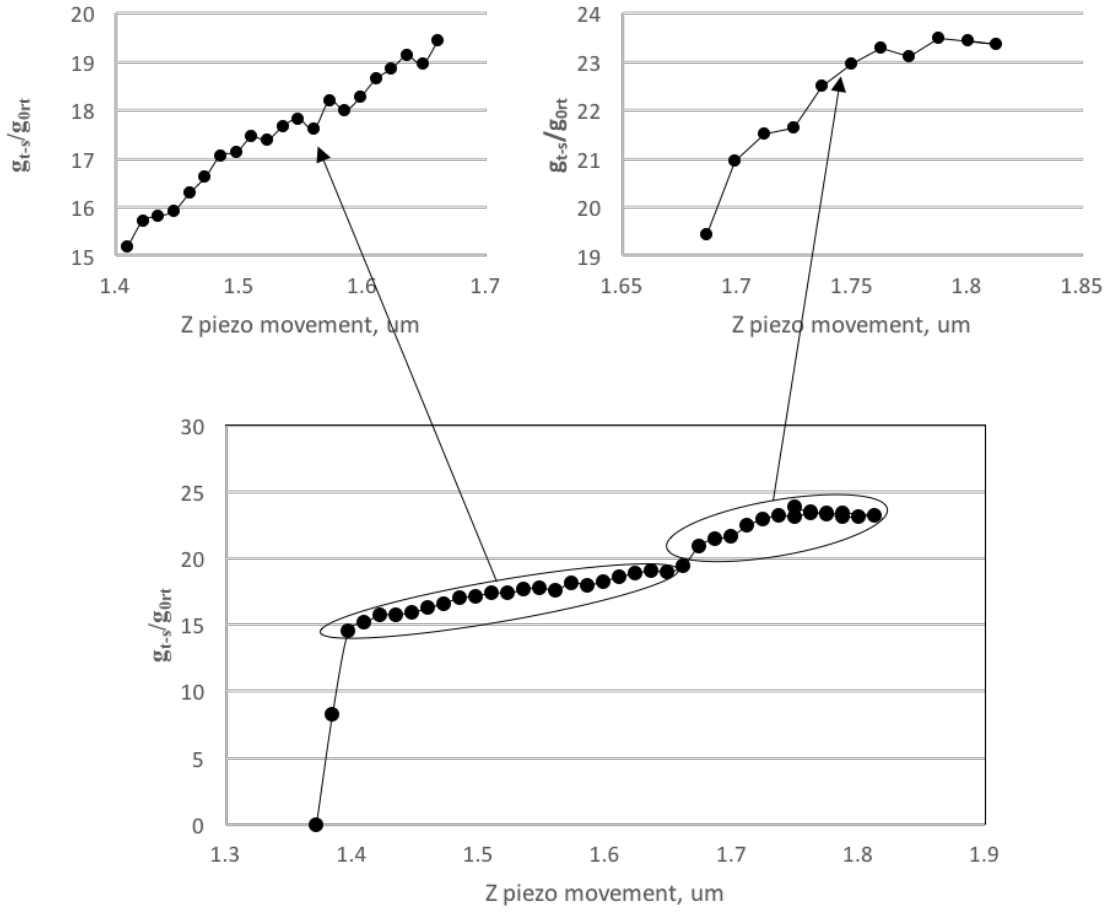

Figure 97 The step of thermal conductance signal when tip is approaching and retracting from device A3

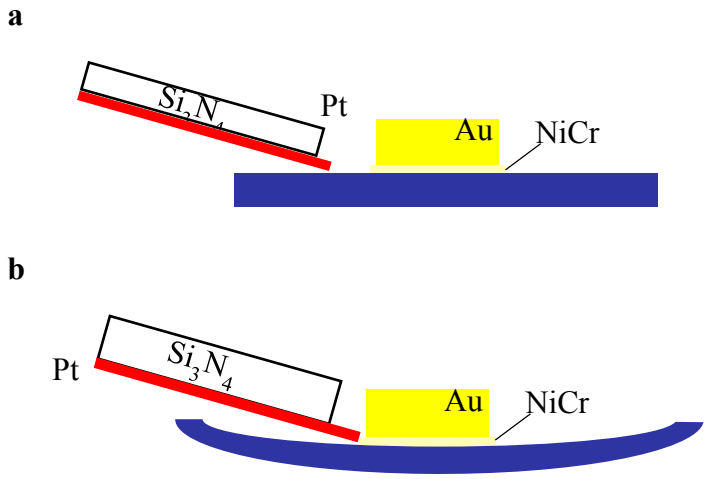

Figure 98 Possible tip-sample contact. Not in scale

a. First contact of platinum tip and sample surface on the silicon dioxide area. b. When pushing harder the membrane bended and tip sledged close to metal square.

The area when tip is approaching the sample surface might be divided into 3 sections. The first section is when tip just touched the surface and made initial contact. And based on the values of thermal conductance is possible contact of SiO_2 surface. The second stage is sliding the silicon dioxide surface when increasing the force applied. There is a small noise similar to device A1 when brought into contact with tip with value of about $0.4\ g_{0rt}$. In third stage when the force increased further, the tip possibly touched the corner of NiCr/Au:SiO_2 surface, as it only came to the edge of the 5nm of NiCr which used as sticky layer (discussed in section **Passive device**). The size of the change in conduction is smaller than for gold thus assumed as it touched NiCr.

Another option to change the value of tip-sample thermal conductance is extending the area of extra gold from 1X1 to 10X10 μm^2 square with thickness of 100 nm. (Figure 99)

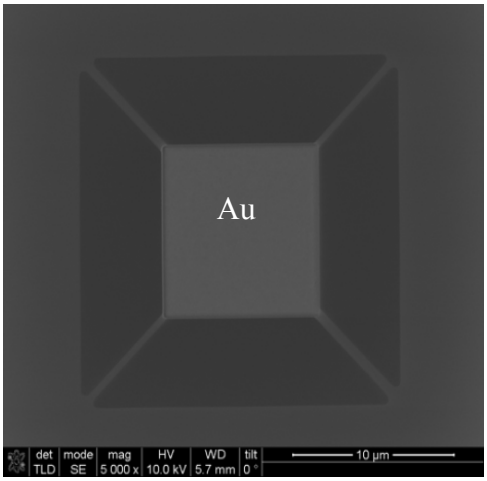

Figure 99 Device A4 membrane covered with gold and supported arms left free of metal

At first contact the step change in thermal conduction was $33.10 \pm 0.56 g_{0rt}$. The step change for each contact is relatively similar for all contacts and there is a presence of a small pull-off force value of 25.82±1.41 nN. The value of 3ω signal changing with time is plotted in Figure 100.

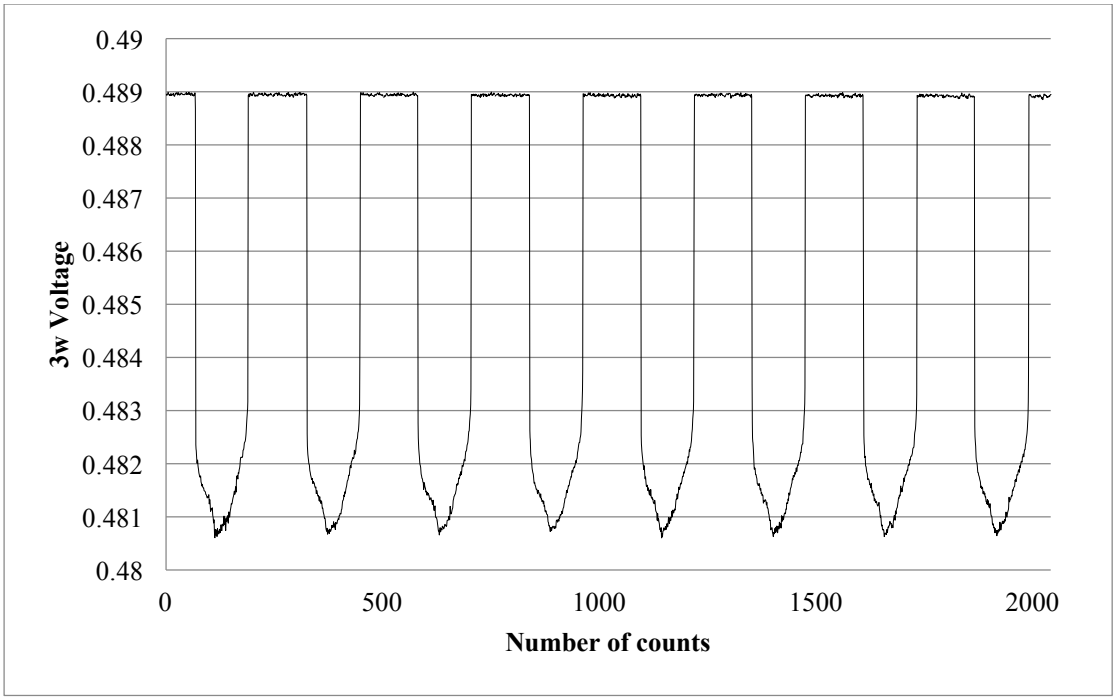

Figure 100 Device A4 in contact with SThM probe tip

The values of heat conductance in initial contact and pull of force values for each contact are placed in Table 8.

Table 8 Device A4 heat transport summary

g_{T-S}, W/K	$g_{t\text{-}s}$ / g_{0rt}	F, pull off, nN
$1.03 \cdot 8$	36.35	25.19
$1.04 \cdot 10^{-8}$	36.57	25.19
$1.01 \cdot 10^{-8}$	35.34	23.18
$1.03 \cdot 10^{-8}$	36.27	27.21
$1.04 \cdot 10^{-8}$	36.64	26.20
$8.89 \cdot 10^{-9}$	31.14	25.19
$4.80 \cdot 10^{-9}$	16.87	27.21
$1.01 \cdot 10^{-8}$	35.64	27.21

Based on the the table and figure above the following diagram explaining the tip – sample contact can drawn as shown in Figure 101.

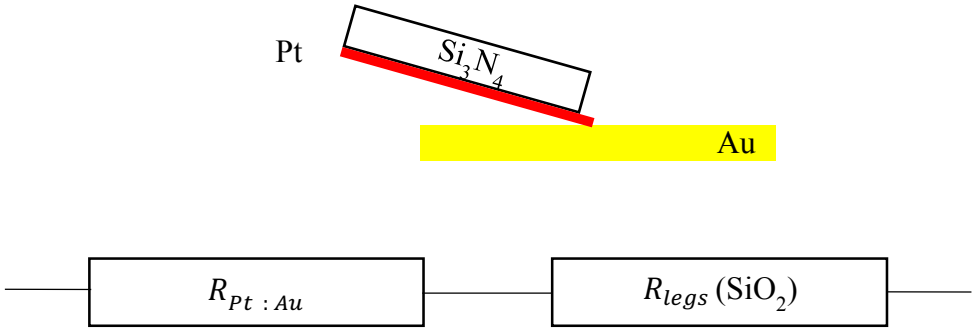

Figure 101 The diagram of tip sample contact

The probability of landing on gold surface is very high and as was discussed in previous section 4.1 missing the centre of the membrane will not change the total value of tip-sample thermal conductance just change the uniformity of temperature distribution which will not affect the heat conductance. The value of tip –sample thermal conductance is depending on two thermal resistances of $R_{Pt\text{-}Au}$ and $R_{legs}(SiO_2)$ and according to modeling in section 4.1 is still dominated by thermal resistance in the supported legs.

In order to evaluate the thermal noise level and determine the nature of contact: single point or multi-asperity, the approach to the surface of the A4 device by the probe is studied in detail. (Figure 102)

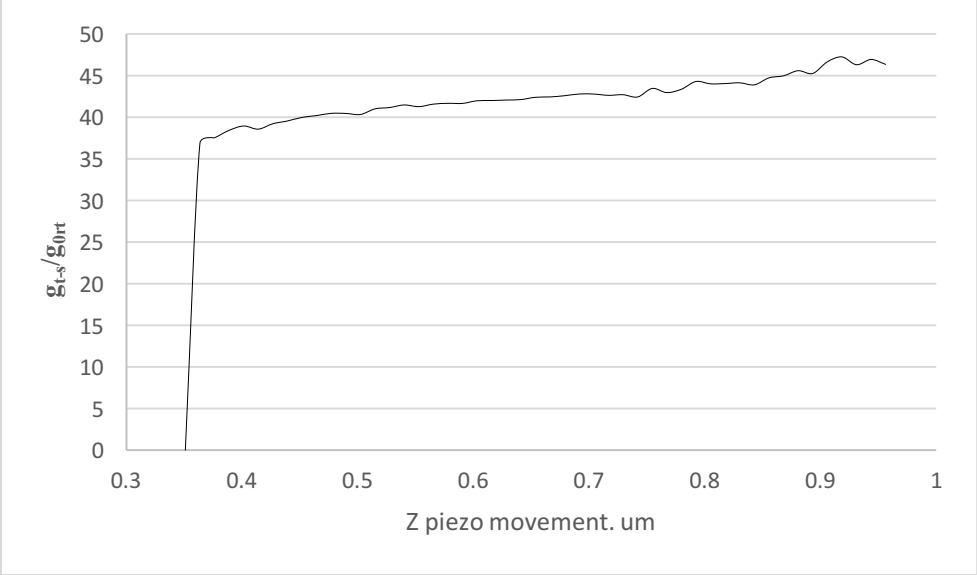

Figure 102 The step of thermal conductance signal when tip is approaching and retracting from device A4

By increasing the number of supported wires with similar width to device A1, making it 2 times more, (Figure 103) we expect some increase in the value of thermal conductance as estimated in previous section

4.1 Passive device modelling.

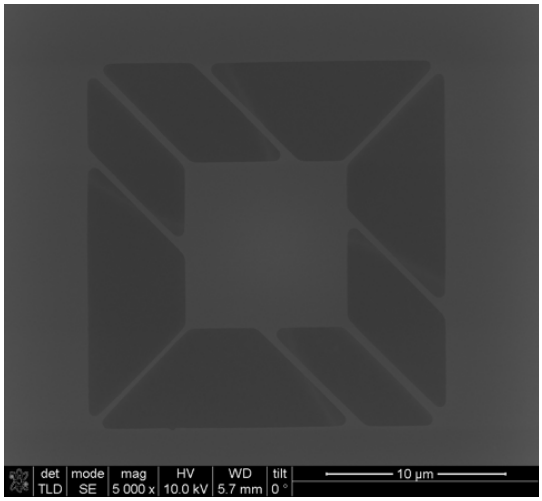

Figure 103 Device B1 SiO_2 membrane with 8 supported arms

The heated nulling SThM probe tip and clean SiO_2 membrane were contacted and the results are shown in **Figure 104** and

Table 9. The mean for first contacts in thermal conduction was about $19.50 \pm 0.64\ g_{0rt}$. The step change for each contact is relatively similar for all contacts and there is a presence of a small pull-off force value of 18.52±1.95 nN.

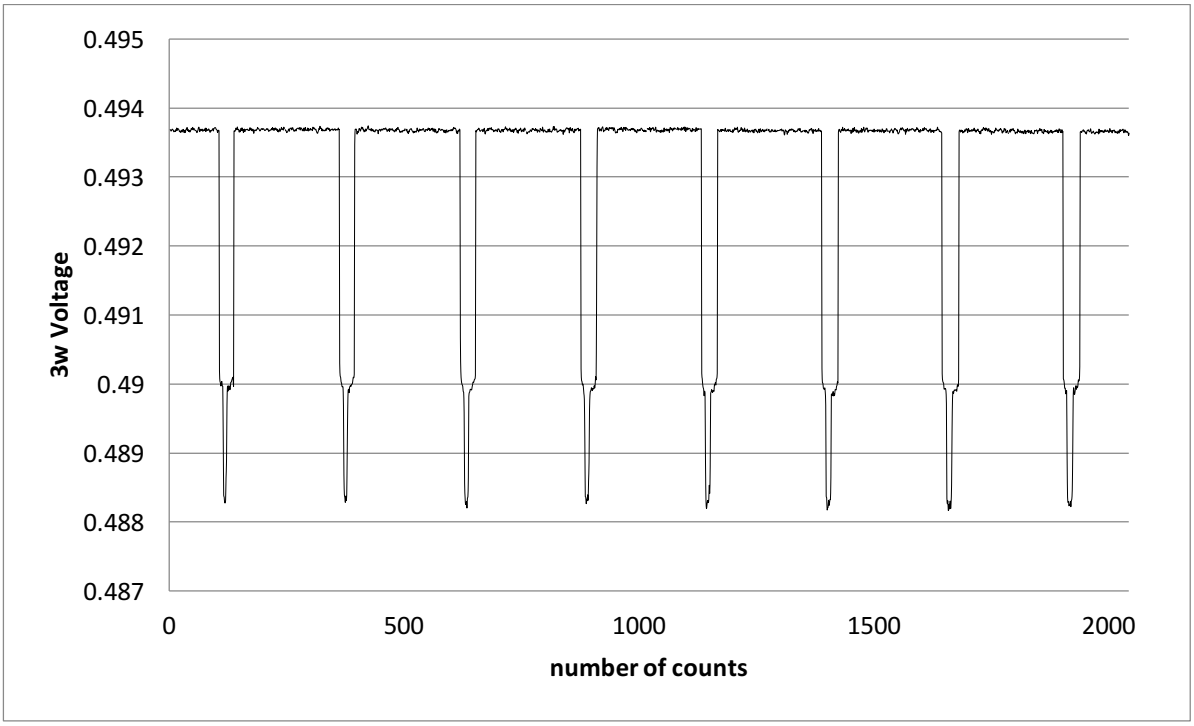

Figure 104 Device B1 in contact with SThM probe tip

Table 9 Device B1 heat transport summary

g_{T-S}, W/K	$g_{t\text{-}s}$ / g_{0rt}	F, pull off, nN
$5.64 \cdot 10^{-9}$	19.82	17.01
$5.49 \cdot 10^{-9}$	19.29	15.11
$4.89 \cdot 10^{-9}$	17.13	17.01
$5.63 \cdot 10^{-9}$	19.76	18.89
$5.74 \cdot 10^{-9}$	20.16	18.9
$5.58 \cdot 10^{-9}$	19.59	17.01
$5.65 \cdot 10^{-9}$	19.85	15.11
$5.81 \cdot 10^{-9}$	20.39	18.89

When looking at the curve in Figure 104 it is clear that the tip making a contact with 2 different materials. In order to evaluate that contact, the first approach of the sample surface is plotted separately in **Figure 105**.

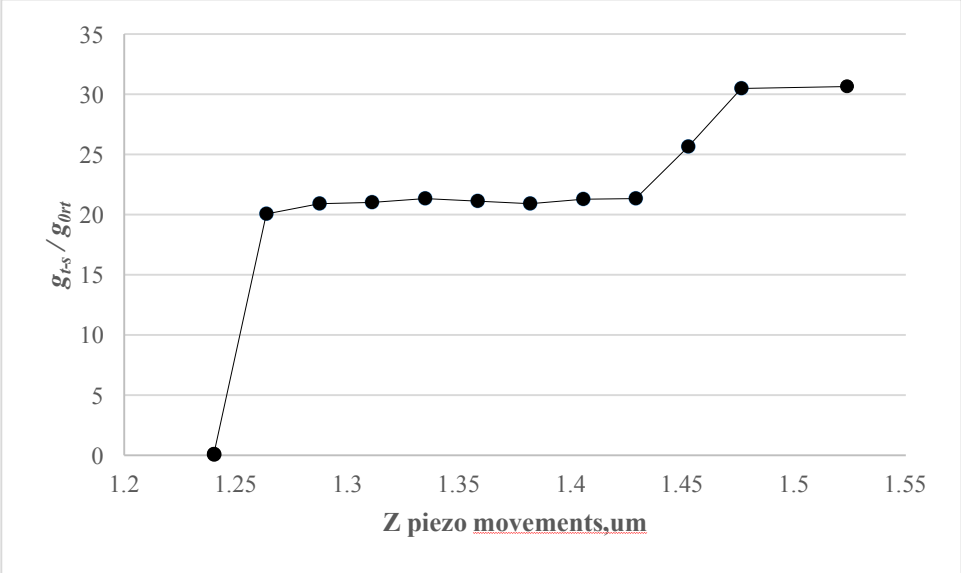

Figure 105 The step of thermal conductance signal when tip is approaching and retracting from device B1

There are 2 step contact being made between heated tip and device B1. The first contact where tip made a contact was Pt sensor and silicon dioxide surface. At second step it might be better contact with the Pt due to increasing pressure.

Covering the full membrane with gold layer and additionally the 4 supporting wires (Figure 106) led to a quite different result as the chance of heat spreading through supported legs increased 2 times compare with device A2. (Figure 106)

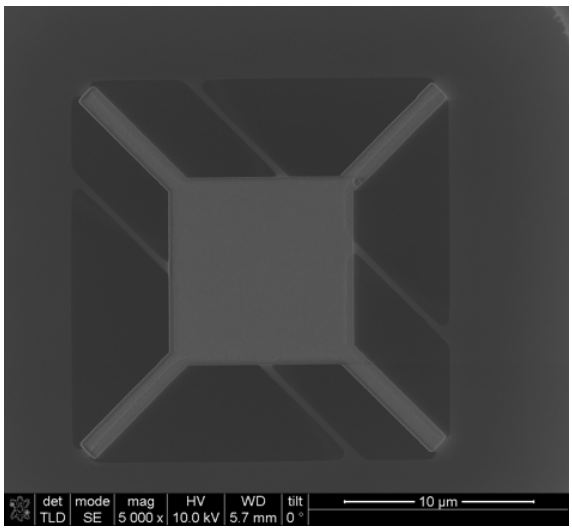

Figure 106 Device B2 membrane and 4 supported arms covered with gold and 4 supported arms left free of metal

The heated nulling SThM probe tip and membrane with four legs covered with gold and another four left free of metal were contacted and the results are shown in Figure 107 and Table 10.

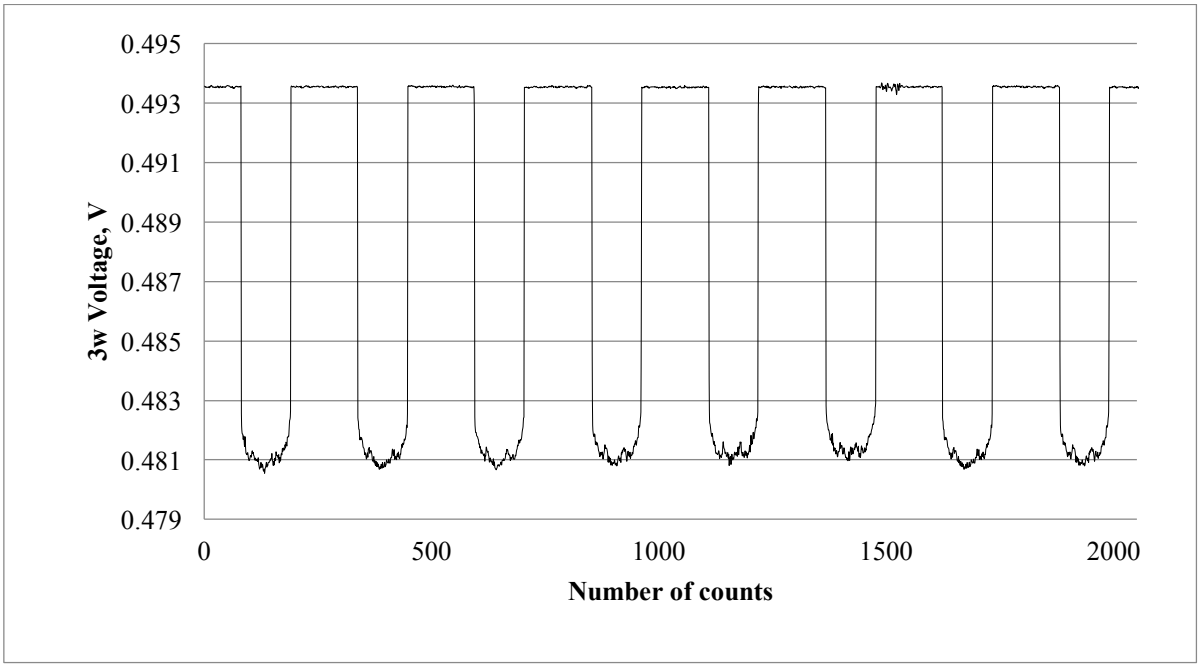

Figure 107 Device B2 in contact with SThM probe tip

At first contact the step change in thermal conduction was $58.90 \pm 5.46g$. The step change for each contact is relatively similar for all contacts and there is a presence of a pull-off force value of 27.39 ± 2.62 nN.

Table 10 Device B2 heat transport summary

g_{T-S}, W/K	$g_{t\text{-}s} / g_{0rt}$	F, pull off, nN
$1.79 \cdot 10^{-8}$	62.69	28.3
$1.80 \cdot 10^{-8}$	63.29	26.4
$1.80 \cdot 10^{-8}$	63.21	22.67
$1.45 \cdot 10^{-8}$	51.02	28.35
$1.59 \cdot 10^{-8}$	55.86	28.34
$1.73 \cdot 10^{-8}$	60.84	30.24
$1.80 \cdot 10^{-8}$	63.29	26.46
$1.45 \cdot 10^{-8}$	51.02	28.35

When looking at the first contact curve (**Figure 108**), it can be seen that there some evidence of multi-asperity contact. So will be essential on looking at this plot zoomed in Figure 109. Moreover, increasing the number of supported arms making a device stronger from mechanical point of view.

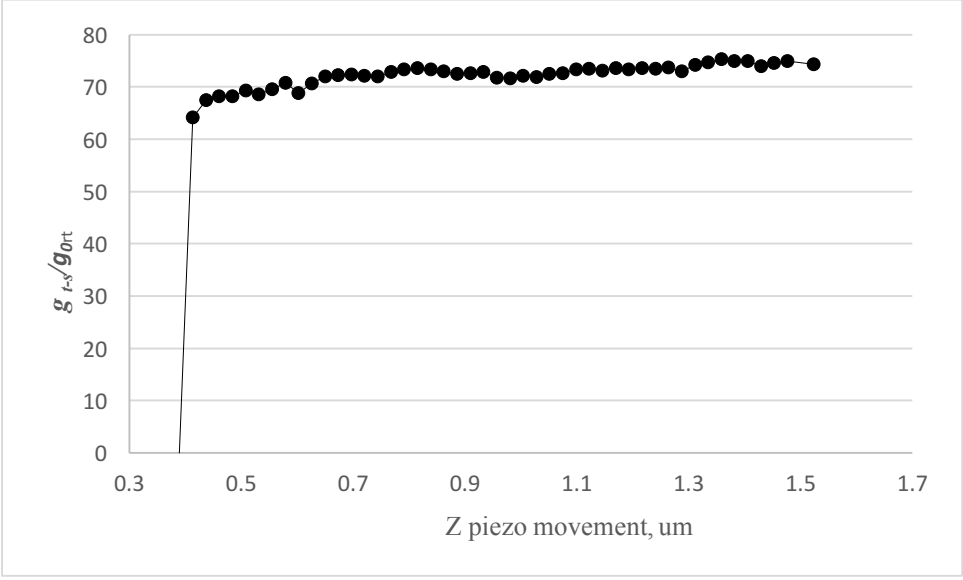

Figure 108 The step of thermal conductance signal when tip is approaching and retracting from device B2

As can be seen from Figure 109 there is a repetition of the shape of the curve in the colour plot and a weak change in contact. It might be because of two bits of metal close together touching.

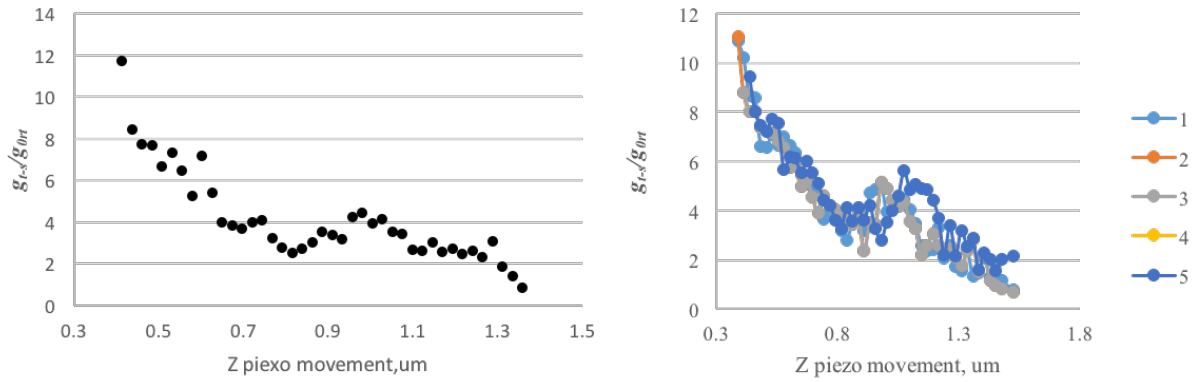

Figure 109 In contact area of thermal signal for device B2

To investigate the reason of jumps happening while in contact the correlation of pull off force with thermal signal was plotted. (Figure 110).

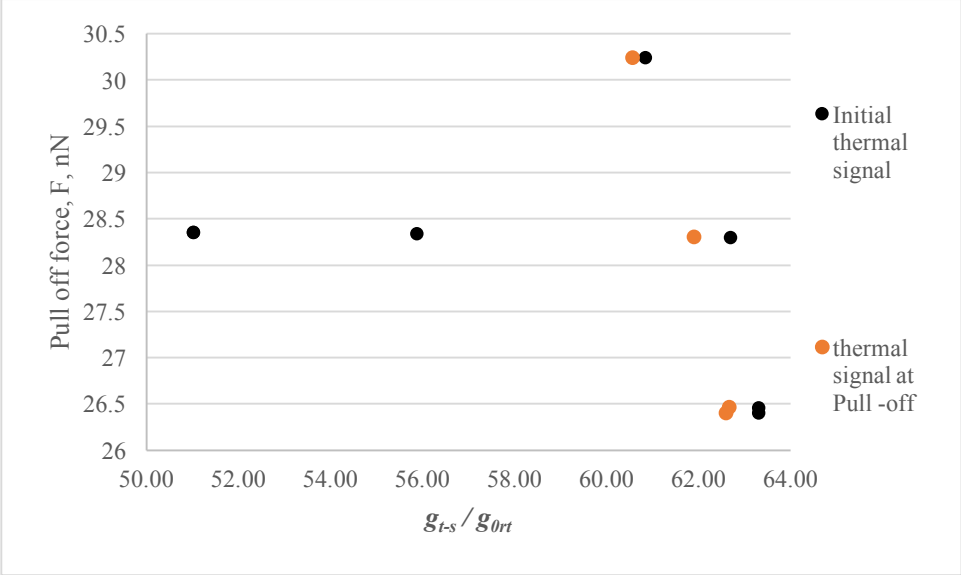

Figure 110 Correlation of pull of force with thermal signal

The value of first contact is lower than device A2 as both devices have the same width of Au covering the supported legs. Since the gold increases the conductance by a factor of 200 the additional SiO_2 legs will not have a significant effect on conductivity. The jump when Si_3N_4 contacted the gold surface has not happened so a stable contact is being made with Pt to Au surface.

Similar value of small jumps in thermal signal suggested that it might be multi-asperity contact. A multi-asperity contact of magnitude $3g_{0rt}$ on top of mechanical vibrations of similar amplitude to those seen before. It can be seen from Figure 110 that there no correlation between pull off force and thermal conductance at pull off and in initial contact.

The device B1 was modified by placing a 1X1 μm^2 square of Gold layer in the centre of the membrane. (Figure 111) The signal change by depositing additional metal was expected to give a different thermal conductance value compared to a plain membrane as was suggested by modeling in Comsol. As the thermal conductance by modelling should be dominated by supported arms hence slightly higher than device B1.

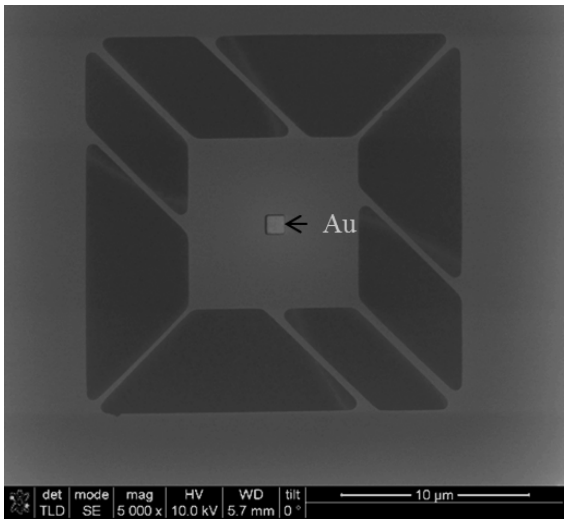

Figure 111 Device B3 with small gold dot

The heated nulling SThM probe tip and device B3 were contacted and the results are shown in Figure 112 and Table 11

At first contact the step change in thermal conduction was $24.06 \pm 0.82\ g_{0rt}$. The step change for each contact is relatively similar for all contacts. There is a presence of a small pull-off force value of 30.48±0.83 nN.

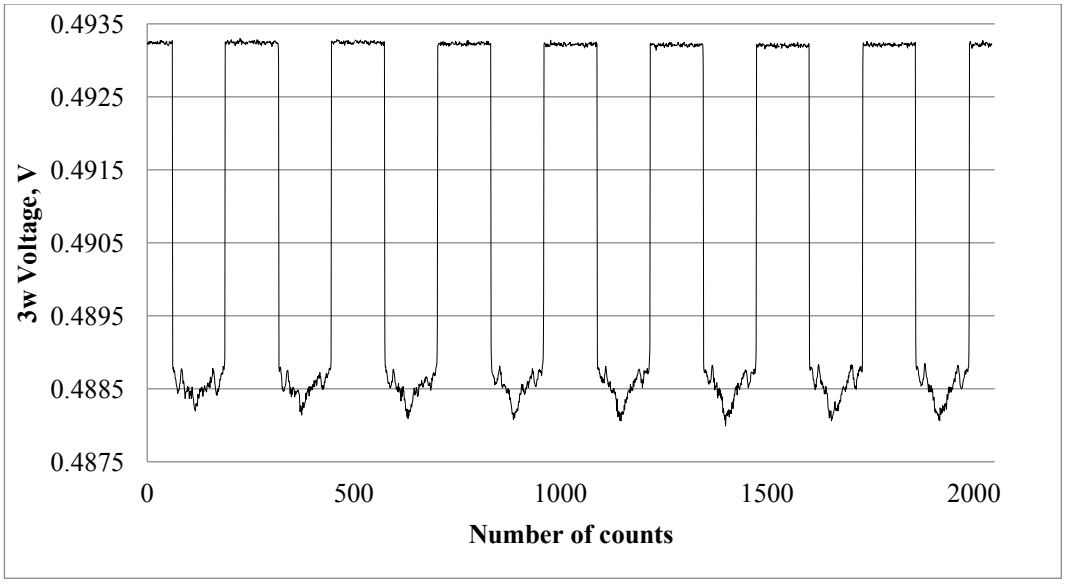

Figure 112 Device B3 in contact with SThM probe tip

Table 11 Device B3 heat transport summary

g_{T-S}, W/K	$g_{t\text{-}s}$ / g_{0rt}	F, pull off, nN
$7.21 \cdot 10^{-9}$	25.31	32.13
$6.83 \cdot 10^{-9}$	23.95	32.13
$6.59 \cdot 10^{-9}$	23.13	30.24
$6.64 \cdot 10^{-9}$	23.31	30.24
$7.92 \cdot 10^{-9}$	24.29	30.24
$6.93 \cdot 10^{-9}$	24.31	28.35
$7.12 \cdot 10^{-9}$	25.01	30.24
$6.61 \cdot 10^{-9}$	23.21	30.23

As can be seen in **Figure 113** the change of g_{0rt} is higher compared with B1. Which means that it might be due to the contact of the heated tip and gold dot. As was suggested by modelling **Figure 77** that adding extra material will change the spreading resistance by small amount compared to plain membrane. There is a presence multi-asperity contact of magnitude *1.5* which might be again two bits of metal close together touching the surface.

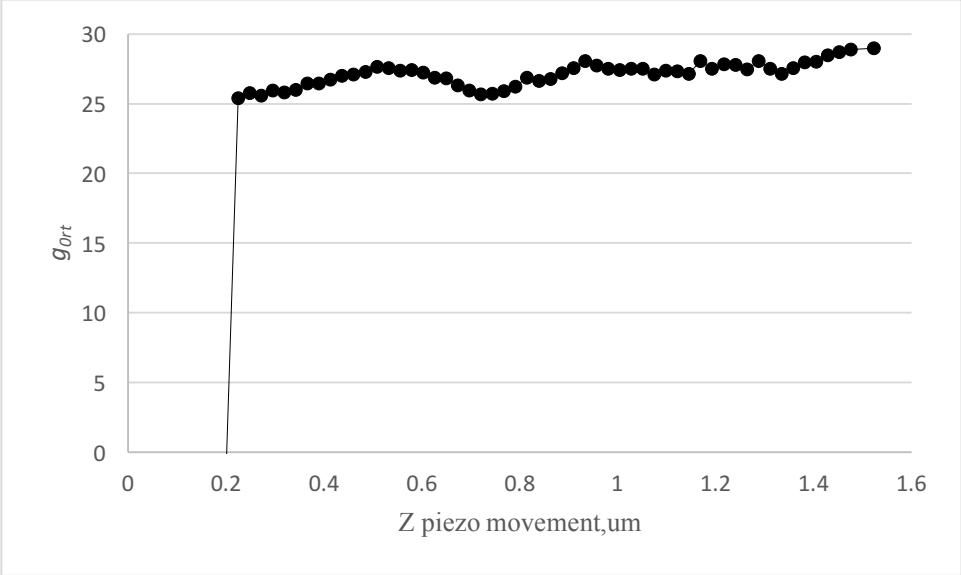

Figure 113 The step of thermal conductance signal when tip is approaching and retracting from device B3

The same as with all previous devices there is no correlation of pull off force with initial thermal signal and thermal conductance at pull off. (Figure 114). The change of thermal signal when in contact was only due to the mechanical vibrations. The value of initial thermal signal was higher than device with less number of supported arms as the heat traveling through the supported legs is increasing.

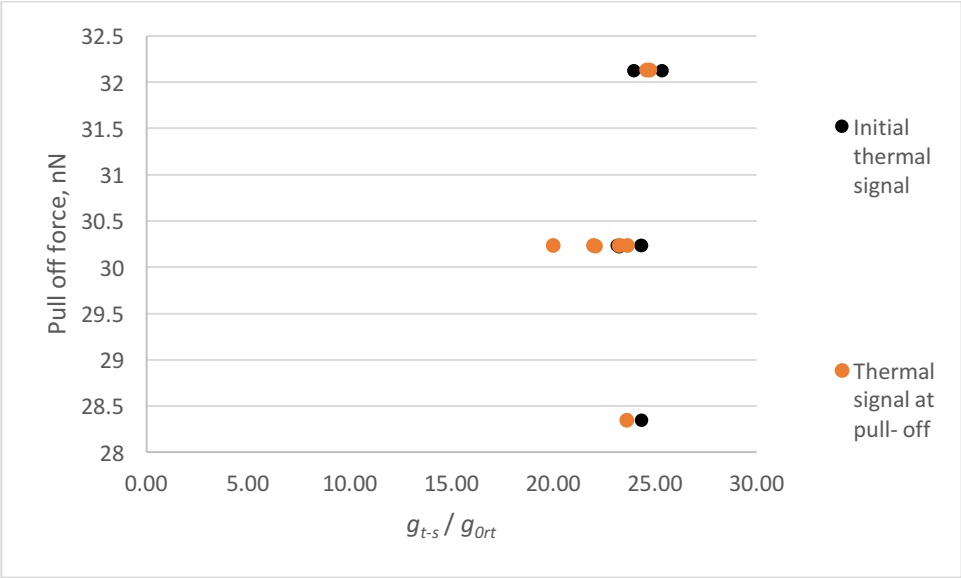

Figure 114 Correlation of pull of force with thermal signal

In contrast, covering the full area of thermally isolated membrane (Figure 115) gives a higher value of thermal conductance. First of all, when comparing the clean membranes, the membrane with 8 supported arms has higher value for thermal conductance than 4 arms and secondly covering the membrane area fully with gold affects the value of tip-sample thermal conductance as the contact resistance changes.

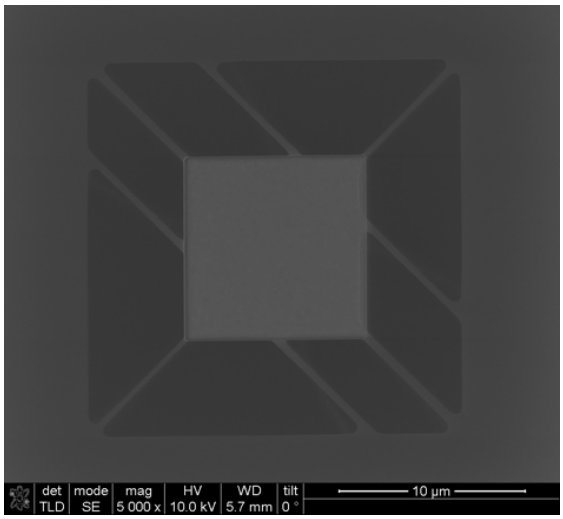

Figure 115 Device B4 membrane covered with gold and 8 supported arms left free of metal

The heated nulling SThM probe tip and device B4 were contacted and the results are shown in Figure 116 and Table 12. The mean for first contacts in thermal conduction was about $41.18 \pm 0.91\ g_{0rt}$. The step change for each contact is relatively similar for all contact. There is a presence of a small pull-off force value of 29.09±4.04 nN.

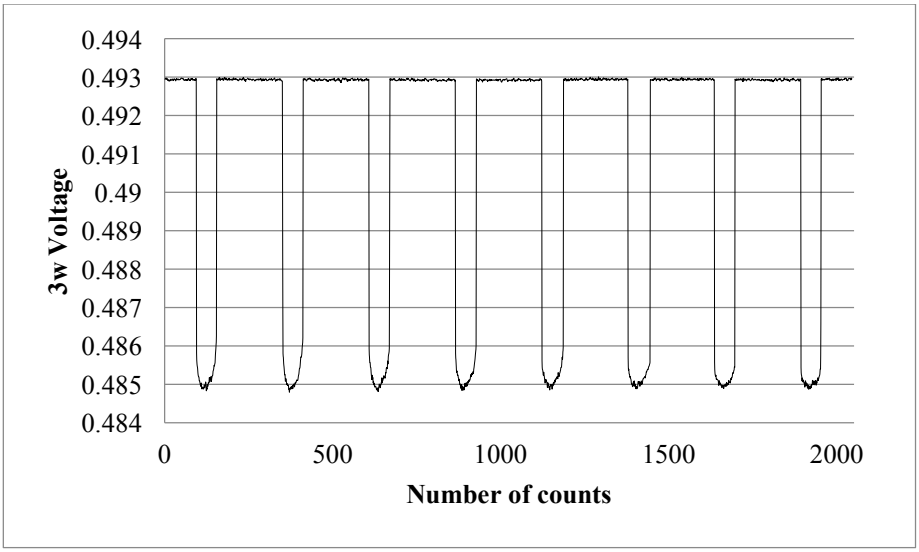

Figure 116 Device B4 in contact with SThM probe tip

Table 12 Device B4 heat transport summary

g_{T-S}, W/K	g_{t-s}/g_{0rt}	F, pull off, nN
$1.16 \cdot 10^{-8}$	40.62	30.24
$1.15 \cdot 10^{-9}$	40.46	28.35
$1.14 \cdot 10^{-8}$	40.05	30.24
$1.16 \cdot 10^{-8}$	40.64	30.23
$1.18 \cdot 10^{-8}$	41.53	34.02
$1.18 \cdot 10^{-8}$	41.31	34.02
$1.20 \cdot 10^{-8}$	41.99	24.57
$1.22 \cdot 10^{-8}$	42.84	22.68

When plotting separately the one approach and zooming in contact area it can be seen that there are no big jumps when in contact. The first stage is when the probe made first contact and second is probe in contact with sample. (Figure 117)

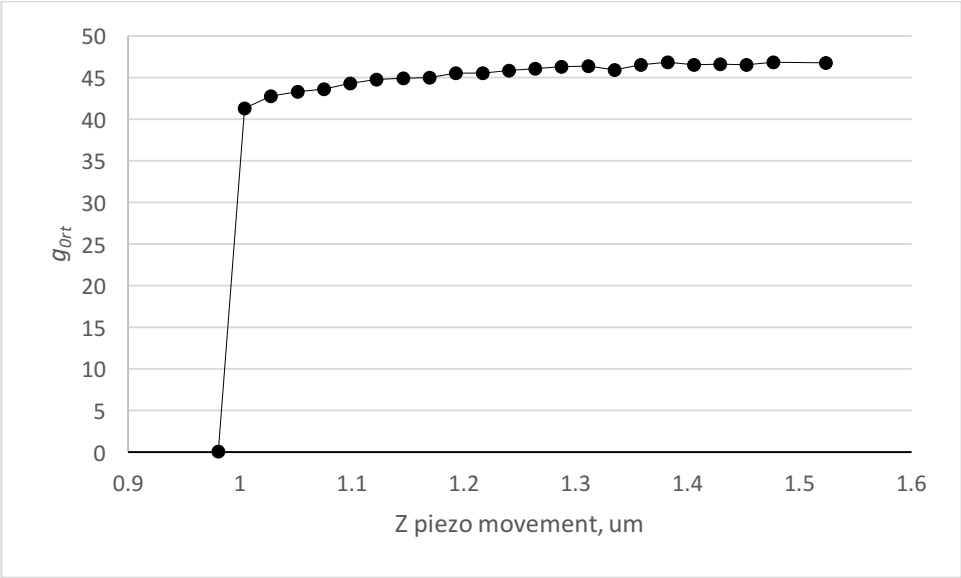

Figure 117 The step of thermal conductance signal when tip is approaching and retracting from device B4

According to values for tip sample thermal conductance when in contact it can be noticed that the $g_{t\text{-}s}$ / g_{0rt} gradually changes with force applied. Plotting the pull-off force with thermal signal: (Figure 118)

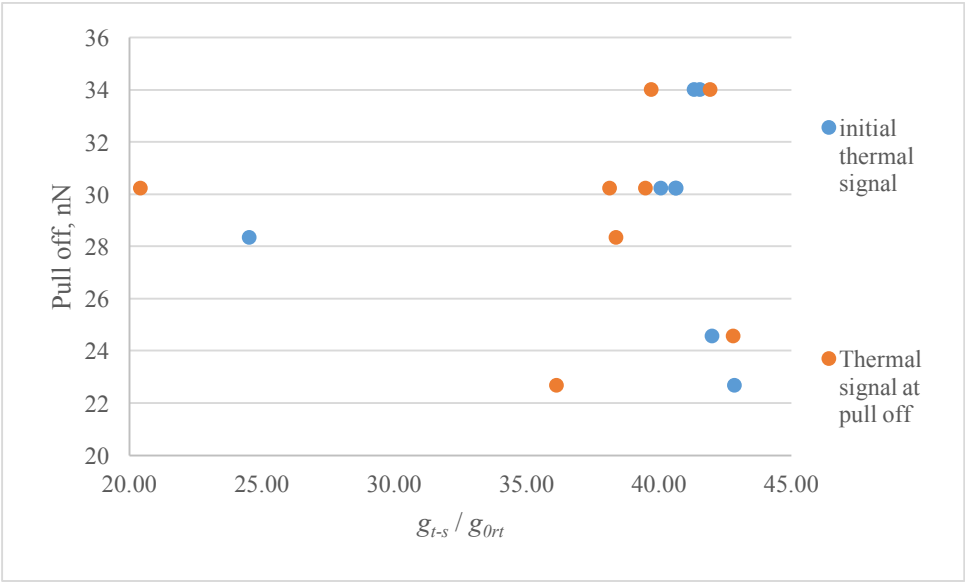

Figure 118 Correlation of pull of force with thermal signal

From plot in Figure 118 it can be seen that there is no obvious correlation between first contact and pulling off force. When looking at thermal signal at pull off there is no correlation with thermal signal.

Another option which was explored for changing the thermal conductance of the membrane was to make wider supporting arms, doubling the size of 700 nm width to 1.4 µm. And as predicted by simulation the value of thermal conductance should be close to device B1

where instead of making wires wider, the number of them was doubled. The device C1 is shown in Figure 119

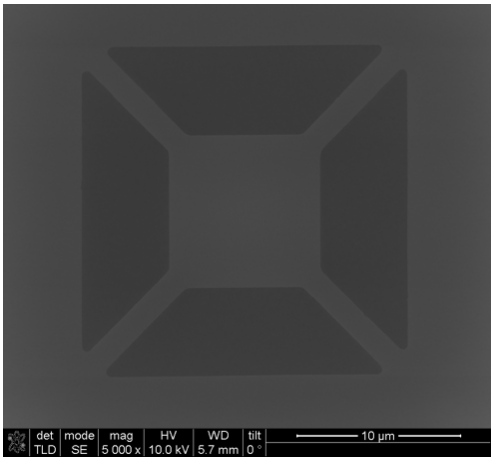

Figure 119 Device C1 clean SiO_2 membrane with wider supported arms

The heated nulling SThM probe tip and device C1 were contacted and the results are shown in **Figure 120** and

Table 13 The mean for first contacts in thermal conduction was about 21.41 ± 0.33. The step change for each contact is relatively similar for all contact. There is a presence of a small pull-off force value of 20.26 ± 0.44 nN.

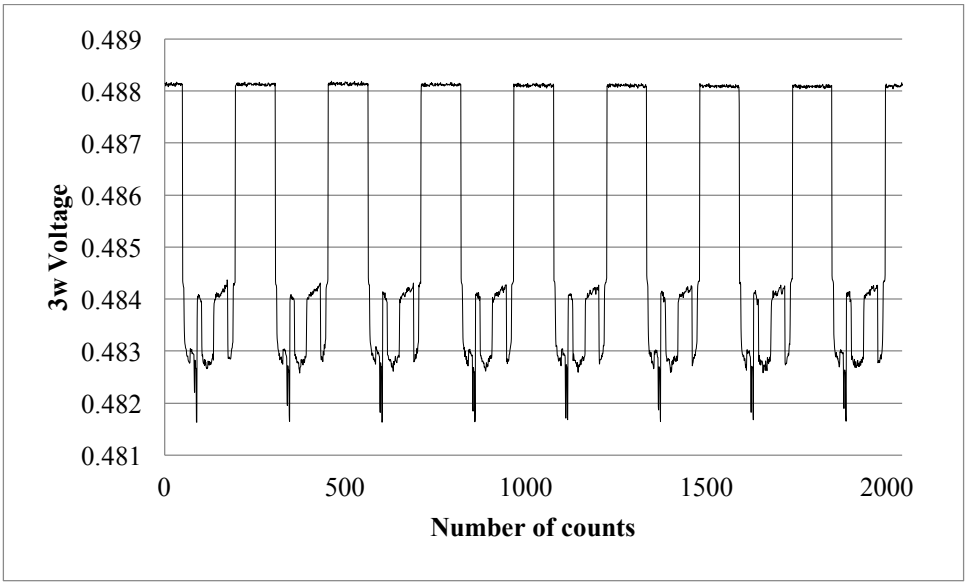

Figure 120 Device C1 in contact with SThM probe tip

As can be seen from the Figure 120 and

Table 13 the value for heat conductance at the initial contact and shape of the curve when in contact are similar and and is a clear case of multi-asperity contact.

Table 13 Device C1 heat transport summary

g_{T-S}, W/K	$g_{t\text{-}s}$ / g_{0rt}	F, pull off, nN
$6.20 \cdot 10^{-9}$	21.76	19.65
$6.24 \cdot 10^{-9}$	21.88	19.65
$6.11 \cdot 10^{-9}$	21.43	21.29
$6.09 \cdot 10^{-9}$	21.38	19.65
$6.15 \cdot 10^{-9}$	21.59	21.29
$5.59 \cdot 10^{-9}$	20.89	21.29
$6.08 \cdot 10^{-9}$	21.35	19.65
$5.99 \cdot 10^{-9}$	21.02	19.65

In order to investigate whether the contact type is multi-asperity the in contact area was zoomed in for all approaches and plotted at the same graph. (Figure 121) When looking at conductance values for each jump they are same for all 8 approaches which means that same part of the tip contacted the sample each time. However, it has some minor shifts with time.

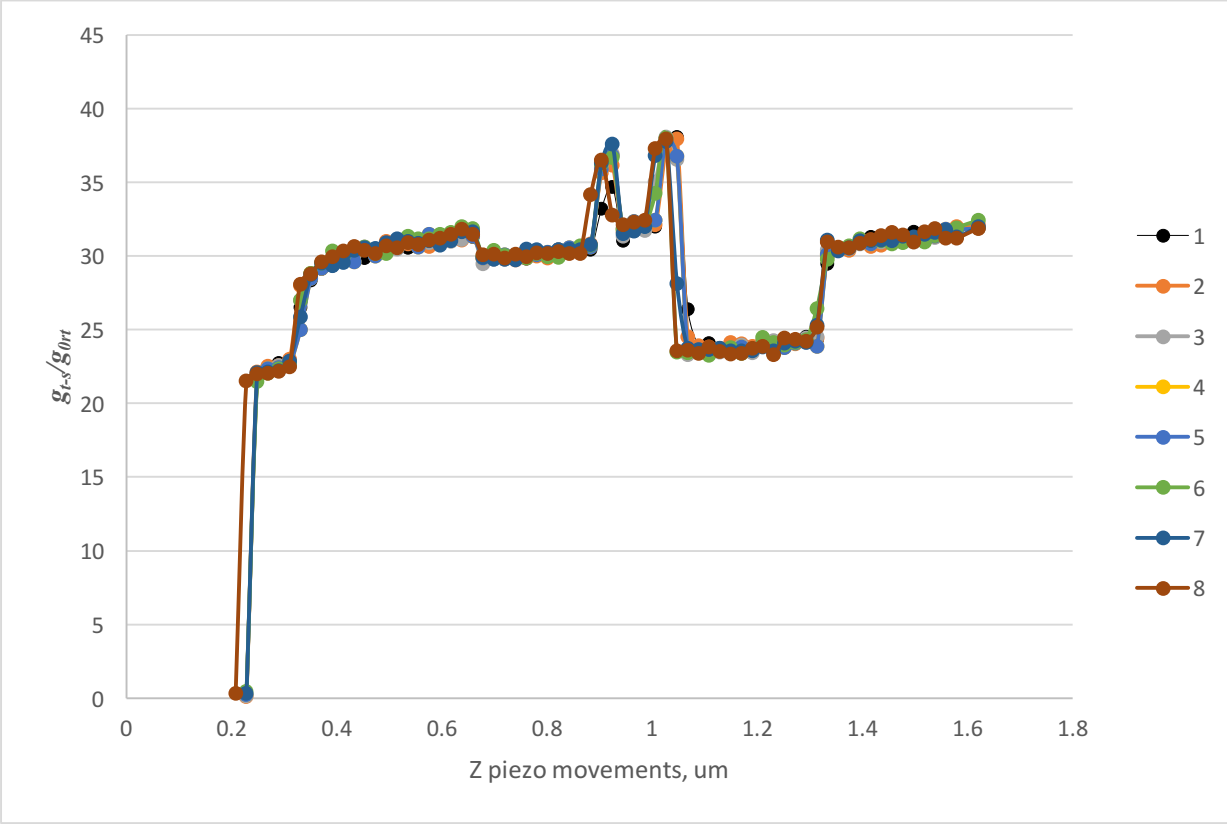

Figure 121 The step of thermal conductance signal when tip is approaching and retracting from device C1

As the jumps are similar for all 8 contacts, it is multi-asperity contact by values for the whole in-contact time. (Figure 122)

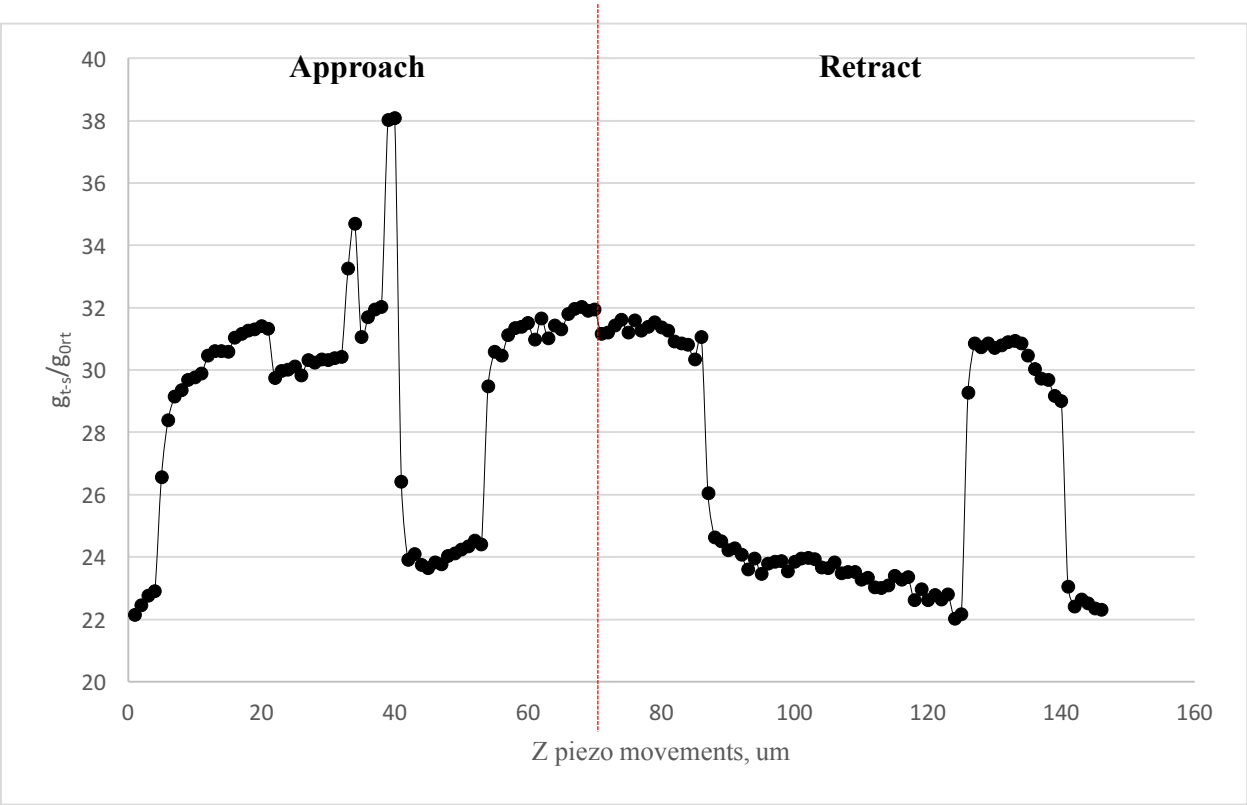

Figure 122 In contact area for device C1.

There are 3 obvious jumps with average value about $5g_0$, $6g_0$ and $8g_0$ was happening while probe in contact. This was assumed for in contact area when considering only obvious thermal jumps and not taking into account small mechanical noise. When considering this jumps, and not taking into account the spikes near count ~35-40, it looks like Pt tip is making another contact of silicon dioxide in 3 step, since the value for 3 jumps is comparable to each other and in sum is comparable to value of first step when tip made first contact (Figure 121).

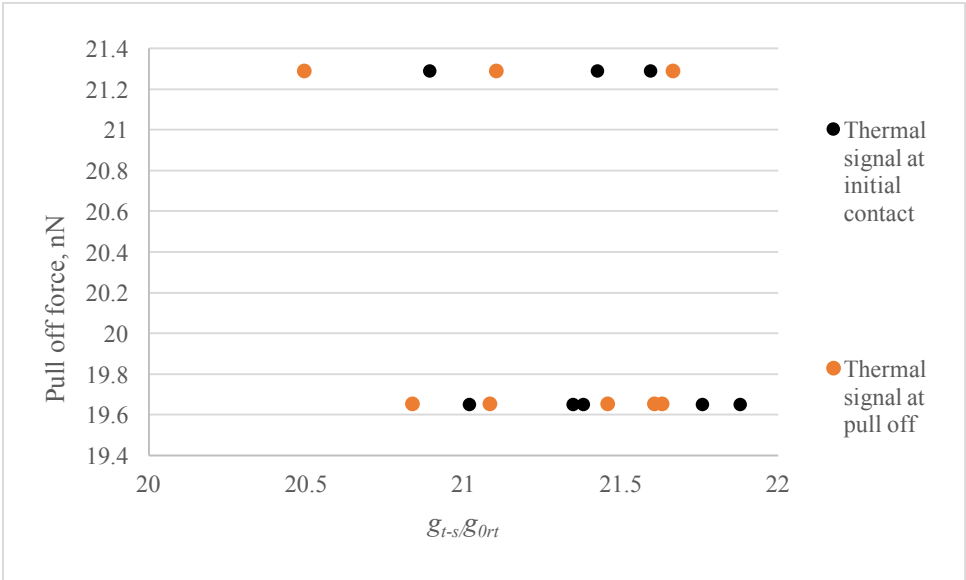

Figure 123 Correlation of pull of force with thermal signal

When plotting the plotting the pulling force with thermal signal there are no obvious correlation. Although the multi-asperity contact has been confirmed.

Covering the whole surface of the membrane and supported arms with layer of gold (Figure 124) was done in the case of device C2.

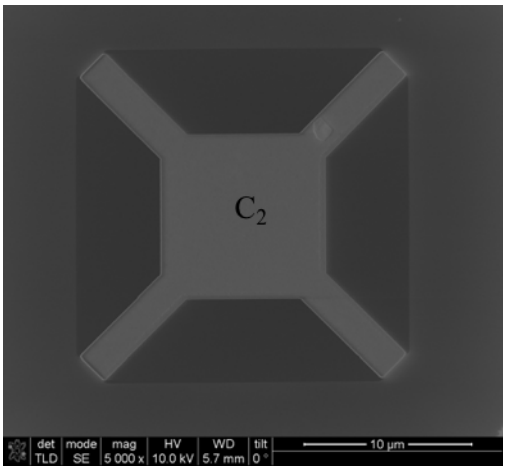

Figure 124 Device C2 fully covered with gold

The heated nulling SThM probe tip and device B4 were contacted and the results are shown in **Figure 125** and

Table 14. The mean for first contacts in thermal conduction was about 85.23 ± 0.94. The step change for each contact is relatively similar for all contacts. There is a presence of a small pull-off force value of 28.45 ± 1.21 nN.

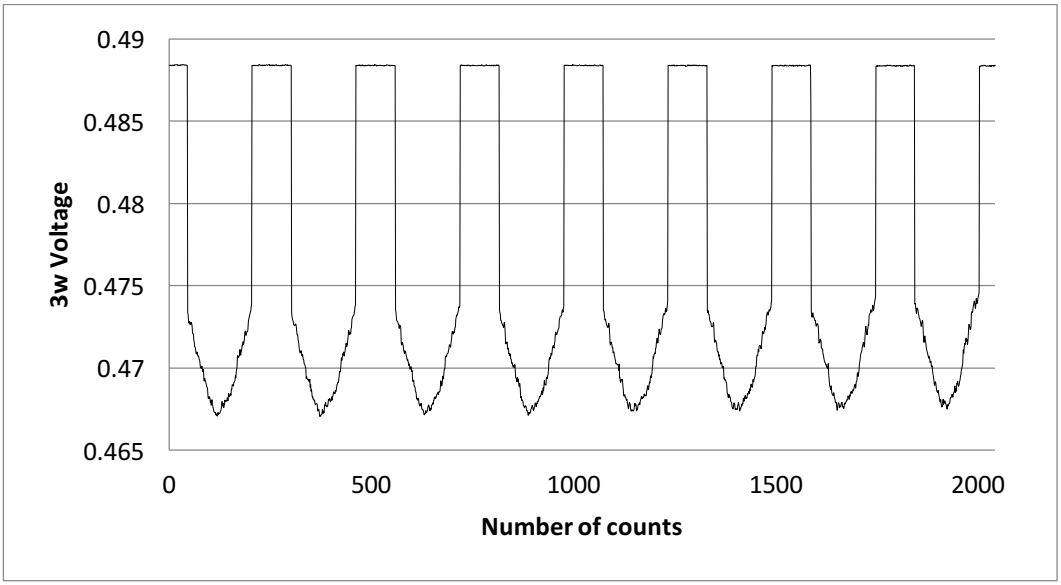

Figure 125 Device C2 in contact with SThM probe tip

Table 14 Thermal transport summary of device C2

g_{T-S}, W/K	$g_{t\text{-}s}$ / g_{0rt}	F, pull off, nN
$2.45 \cdot 10^{-8}$	85.99	27.84
$2.44 \cdot 10^{-8}$	85.90	27.84
$2.41 \cdot 10^{-8}$	84.83	29.48
$2.42 \cdot 10^{-8}$	85.25	29.48
$2.43 \cdot 10^{-8}$	85.58	29.48
$2.43 \cdot 10^{-8}$	85.44	29.48
$2.44 \cdot 10^{-8}$	85.71	27.84
$2.36 \cdot 10^{-8}$	83.06	26.20

As was mentioned in the discussion about device A2, according to the resistance network model, the tip-sample thermal conduction becomes dominant as the contact is being made between two materials with high thermal conductivities. However, due to metal flakes at the tip of the probe, there were two different parts of the tip touching the surface. Device B2 being made with 4 supported arms left free of metal to show dependence of the thermal resistance in supported arms made of silicon dioxide.

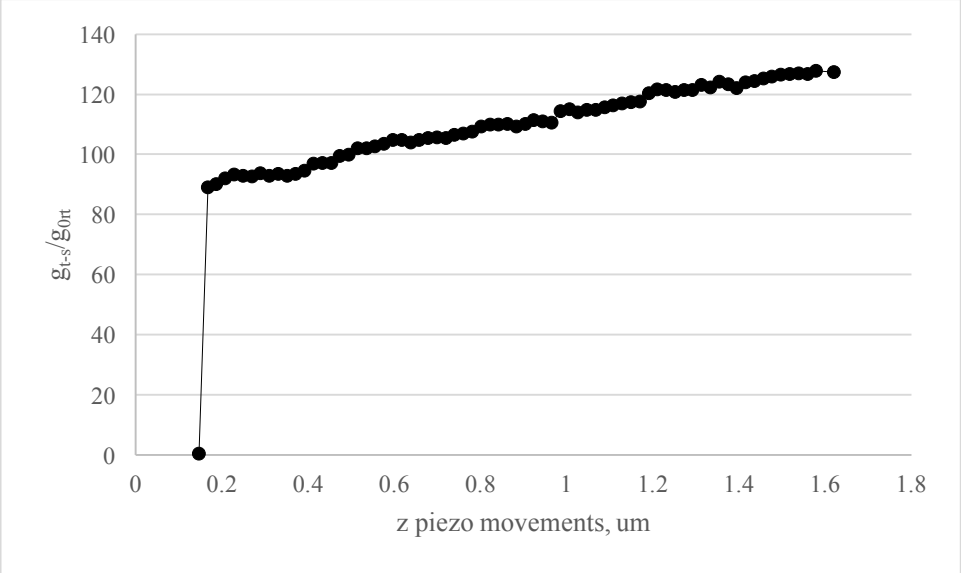

Figure 126 The step of thermal conductance signal when tip is approaching and retracting from device C2

The same as with previous devices no correlation between pulling force and thermal signal was found (Figure 127).

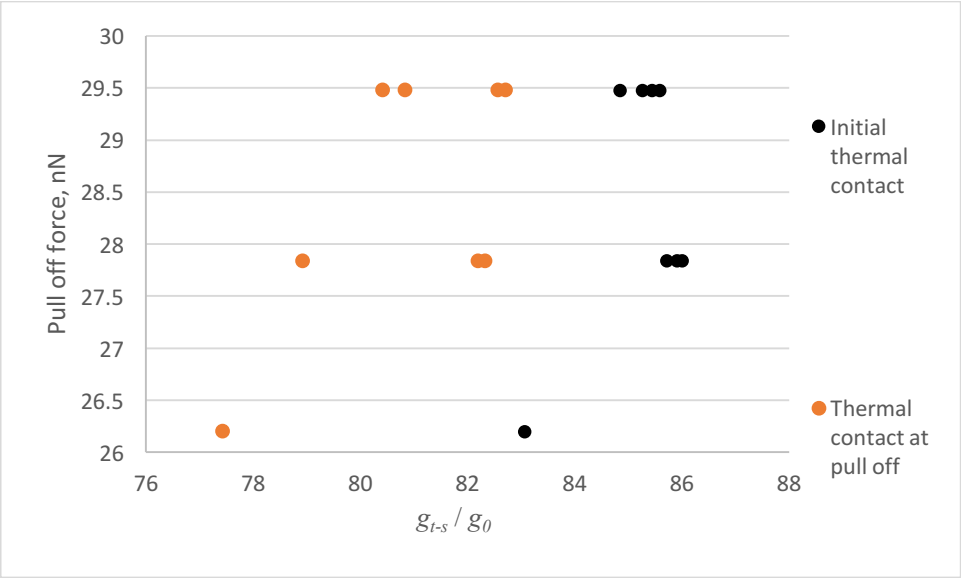

Figure 127 Correlation of pull of force with thermal signal

In the case of device C2 the $g_{t\text{-}s}$ was evaluated as it has very stable thermal signal (Figure 126), apart from some mechanical vibrations which are typical for the membrane. The $g_{t\text{-}s}$ value for device C2 is $2.4 \cdot 10^{-8} \pm 2.7 \cdot 10^{-10} W/K$ which corresponds to the value for a bulk Si substrate.

An attempt to touch a gold dot placed in the centre of the by a heated tip was again made in device C3

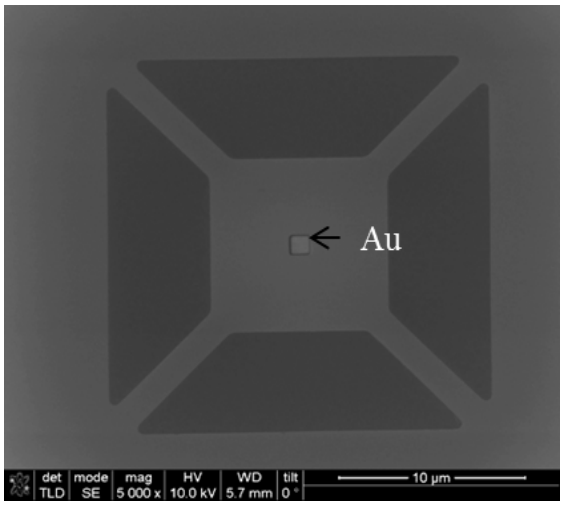

Figure 128 Device C3

The heated nulling SThM probe tip and device C3 were contacted and the results are shown in Figure 129 and Table 15. The mean for first contacts in thermal conduction was about 39.22 ± 3.06 . The step change for each contact is relatively similar for all contacts. There is a presence of a small pull-off force value of 14.54 ± 0.58 nN. There are similar structures of the

repeated contacts. There look to be two jumps and a sloped region which are the same in approach and retract

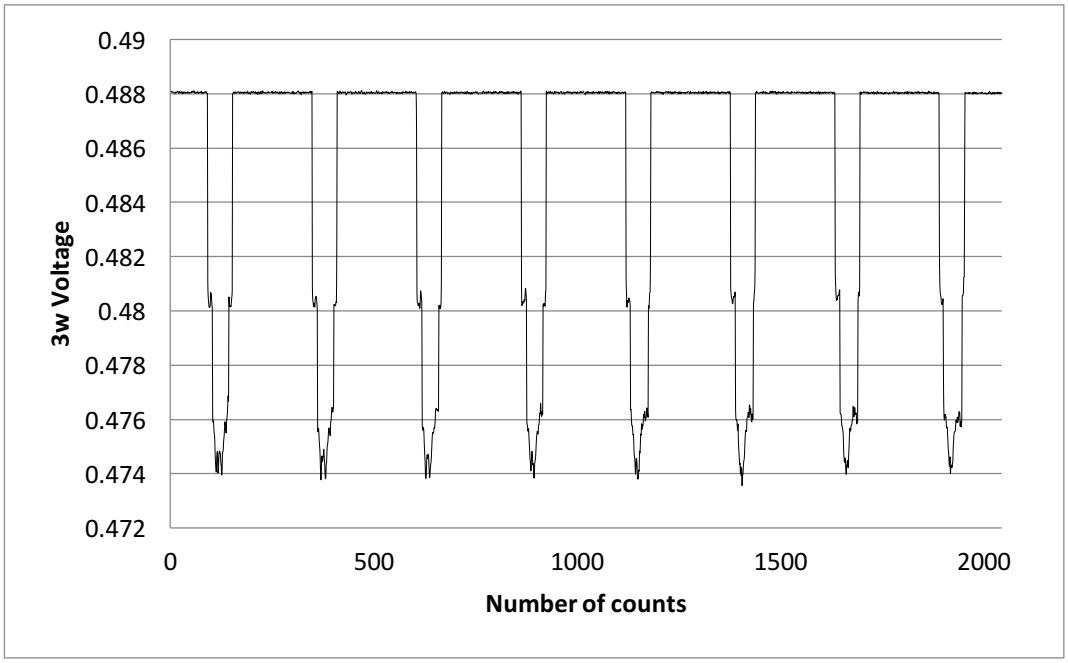

Figure 129 Device C3 in contact with SThM probe tip

According to Figure 129 and Table 15 the initial thermal contact with value about *40* g_0 was made on top of gold dot as the value was suggested by modeling in section 4.1 should be close to device B4 and C4 since the tip –sample thermal conductance dominated by thermal resistance of supported legs.

Table 15 Thermal transport summary of device C3

g_{T-S}, W/K	$g_{t\text{-}s} / g_{0rt}$	F, pull off, nN
$1.15 \cdot 10^{-8}$	40.18	14.74
$1.18 \cdot 10^{-8}$	41.46	14.74
$1.13 \cdot 10^{-8}$	39.60	13.10
$1.19 \cdot 10^{-8}$	41.70	14.74
$1.13 \cdot 10^{-8}$	39.60	14.74
$1.17 \cdot 10^{-8}$	41.18	14.74
$1.08 \cdot 10^{-8}$	37.74	14.74
$9.22 \cdot 10^{-9}$	32.35	14.74

Figure 130 Approaching the sample surface of device C

By 2 jumps on Figure 129 and evaluating the thermal conductance in Figure 130 it might be the Pt contacts first and then the Si_3N_4 slides into the side of the dot as shown in diagram in **Figure 131**.

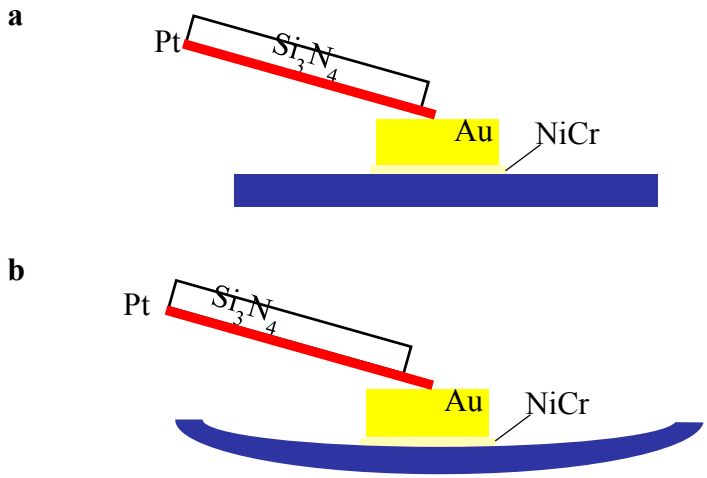

Figure 131 Diagram of tip - sample contact for device C3

The 10X10 μm^2 of gold layer on top of the silicon dioxide (Device C4, Figure 132) can be easily touched by the tip.

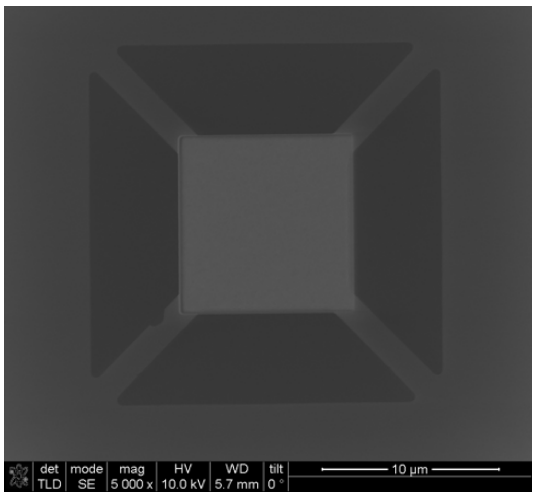

Figure 132 Device C4 membrane covered with gold and supported arms left free of metal

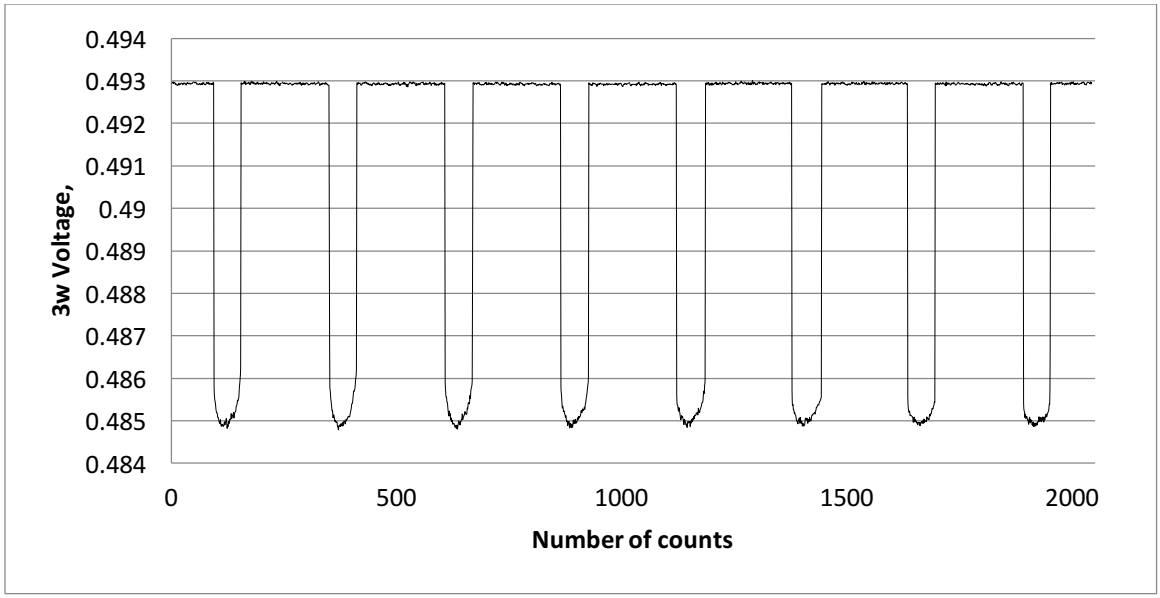

Figure 133 Device C4 in contact with SThM probe tip

The heated nulling SThM probe tip and device C4 were contacted and the results are shown in **Figure 133** and

Table 16. The mean for first contacts in thermal conduction was about $41.23 \pm 0.89 g_{0rt}$ The step change for each contact is relatively similar for all contacts. There is the presence of a small pull-off force value of 24.98±3.98 nN.

Table 16 Thermal transport summary of device C4

g_{T-S}, W/K	$g_{t\text{-}s}$ / g_{0rt}	F, pull off, nN
1.16E-08	40.62	26.20
1.16E-08	40.82	26.20
1.14E-08	40.05	22.93
1.16E-08	40.64	26.20
1.18E-08	41.53	29.48
1.18E-08	41.31	29.48
1.20E-08	41.99	21.29
1.22E-08	42.84	18.02

When zooming in one of the approach curve in Figure 134 it is clear that thermal signal is stable and the possible contact being made is single point with noise of about $0.5g_0$ which is similar to other devices such as A1, B2,B4.

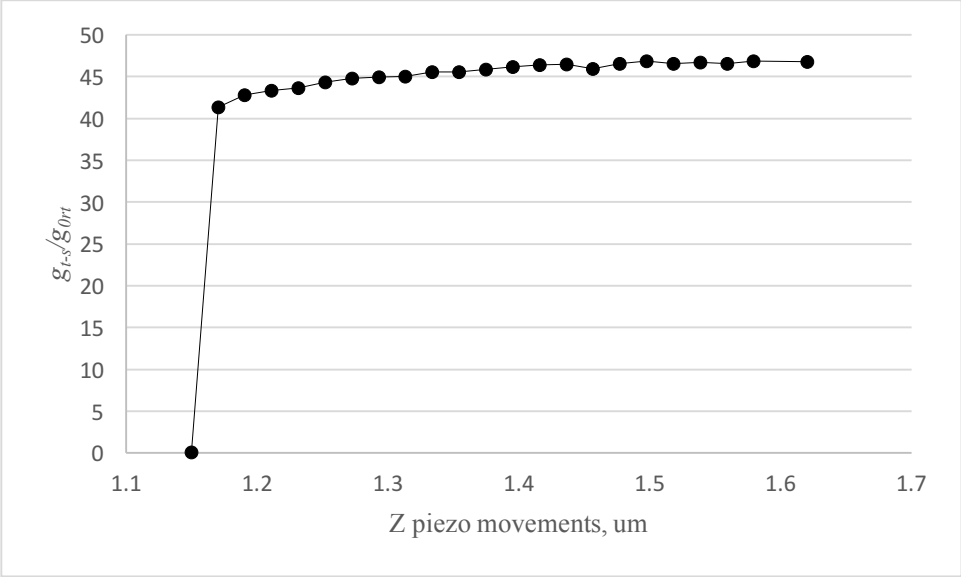

Figure 134 Approaching the sample surface of device C4

The value for initial contact, as was shown by simulation, is close to devices B4 and C3, as the gold dot was missed in cases for devices A3 and B3, these can not be compared.

4.3 Error analysis

When analysing the data for all devices is important to take into account two types of error. The first is the measurement limit which already discussed in the measurements set up part. Thus any change in the 3ω signal higher then $0.27 \pm 0.09 g_0 rt$ when the probe is out of contact is real and characteristic of the nature of the contact.

Another important factor is an estimate of centring errors which shows how well the tip is positioned to the centre of the membrane and represents a random experimental error in the absolute value of the tip-to-sample thermal contact but does not affect the estimated reproducibility of the measurements from contact to contact. This error is only important for the sample with small gold dot in the centre, because, as was suggested by modelling, thermal (

4.1 Passive device modelling Figure 75) spreading resistance and thus tip-sample thermal conductance is not affected by the location within the membrane where contact being made.

The reproducibility of contact, which consists of systematic changes with time and random contact to contact variation, constitutes an error in measurements by SThM. In this case, this is the quantity which is being measured, rather than an error in itself.

To analyse reproducibility of contact the very first 8 contacts for 12 different samples were considered. Reproducibility of contact in terms of contact-to-contact variation for device A1, A2, A3, A4 which can be considered as an intrinsic random «error» in the thermal contact for SThM is shown in Figure 135.

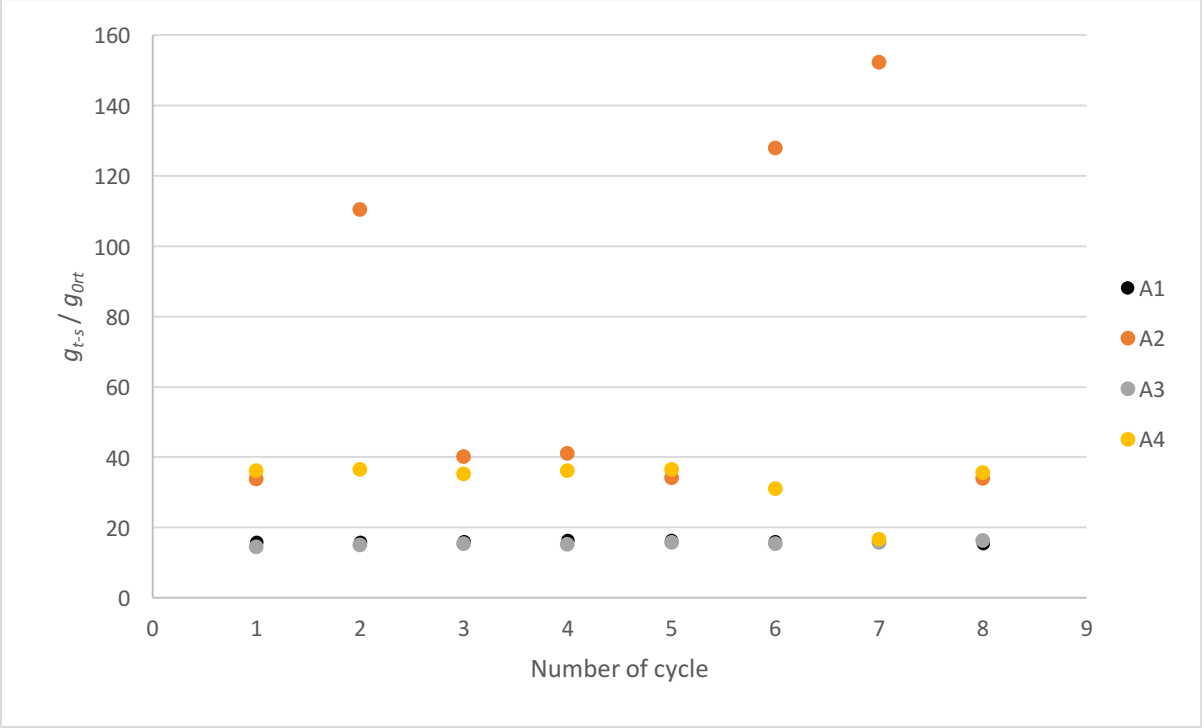

Figure 135 Contact to contact variation of A type devices Dashed lines represent the average contact conductance

The average thermal conductance value device A1 (clean SiO2 membrane with 700nm supported arms) is 16.10 ± 0.29 . When the same device is fully covered with gold (sample A2) that value is changed to 71.79 ± 49.77 . As was discussed earlier in the chapter, a multi-asperity contact happened for device A2. In some cases, Silicon nitride was touching the sample, and other cases it was peeled off metal touching. This was the reason for the big scatter in thermal conductance values. The difference in conduction due to material contrast of the sample is therefore not very clear due to the large scatter resulting from variations of the tip. When the probe tip touches the 1X1 um gold dot (sample A3) the value of tip-sample thermal conductance is 15.35 ± 0.55. This value corresponds to device A1 plane membrane, which means that gold dot was missed. Making a larger metal square increased the probability of tip contacting the gold

area as is seen from the value of the tip-sample thermal conductance which changed to 33.10 ± 6.80 (sample A4)

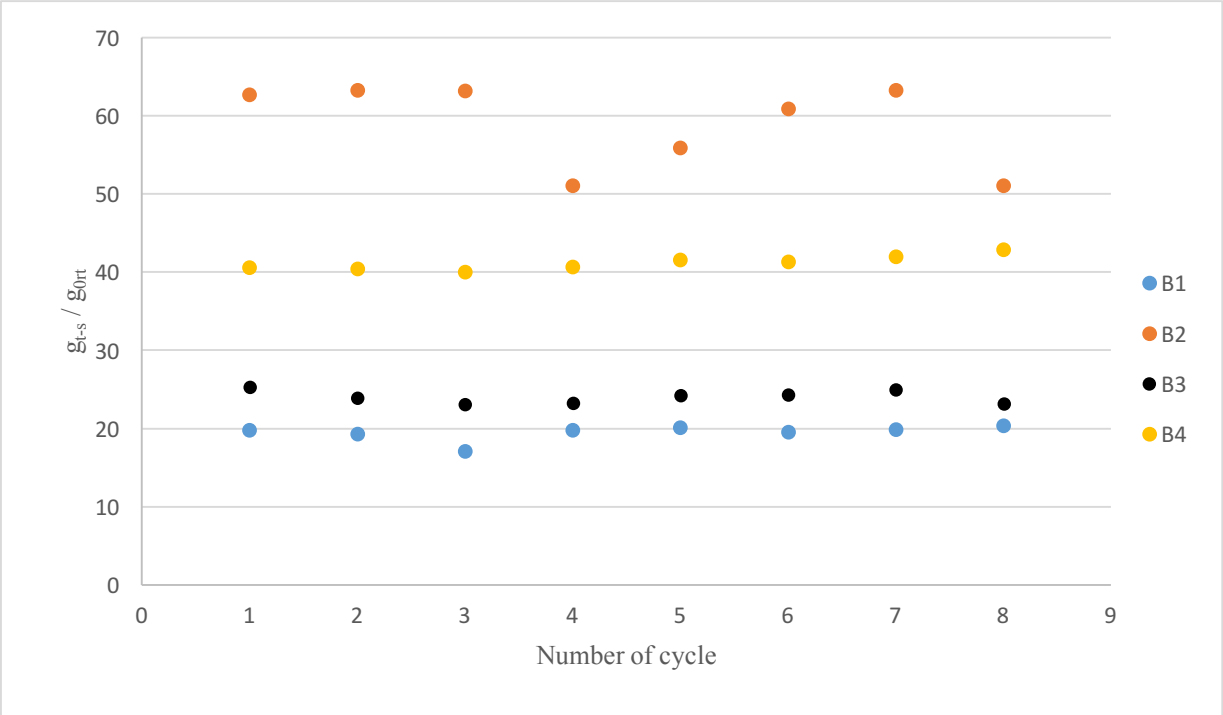

Figure 136 Contact to contact variation of B type devices

For the B series of samples the number of supported arms was increased two times (Figure 136) The average thermal conductance value device B1, a clean SiO2 membrane with eight 700nm width supported arms is 19.49 ± 0.33 . When fully covered with gold that value changed to 58.90 ± 5.46 . The difference in conduction is again believed to be due to material contrast. When the probe tip was supposed to touch the 1X1 um gold dot the value of tip-sample thermal conductance is 24.06 ± 0.82 The probe might be touching the gold square in this case as the number is slightly higher then plane membrane as was suggested by modelling. Approaching the bigger gold square the value tip-sample thermal conductance changed to 41.18 ± 0.92 which suggests that the probe is obviously touching the gold area as the value of thermal conductance is higher than plain membrane and lower than device B2 where membrane and 4 supported legs covered with gold and another 4 left free of metal.

Another option for changing the geometry of the device is making the supporting arms two times wider (series "C"). (Figure 137) The average thermal conductance value device C1 device with four 1.4um width supported arms is 21.46 ± 0.34 which is similar to device B1 with value 19.49 ± 0.33 . Fully covered with gold the device has value of thermal conductance much higher 85.53 ± 0.95 compare with device B2 as it fully covered with gold. When touching the 1X1 um gold dot the value of tip-sample thermal conductance is 39.45 ± 3.32 which might be a

realistic value. Approaching the bigger gold square the value tip-sample thermal conductance is changed to 40.99 ± 0.89. Thus, when the thermal resistance of the arms is decreased the dominant effect is the material of the sample.

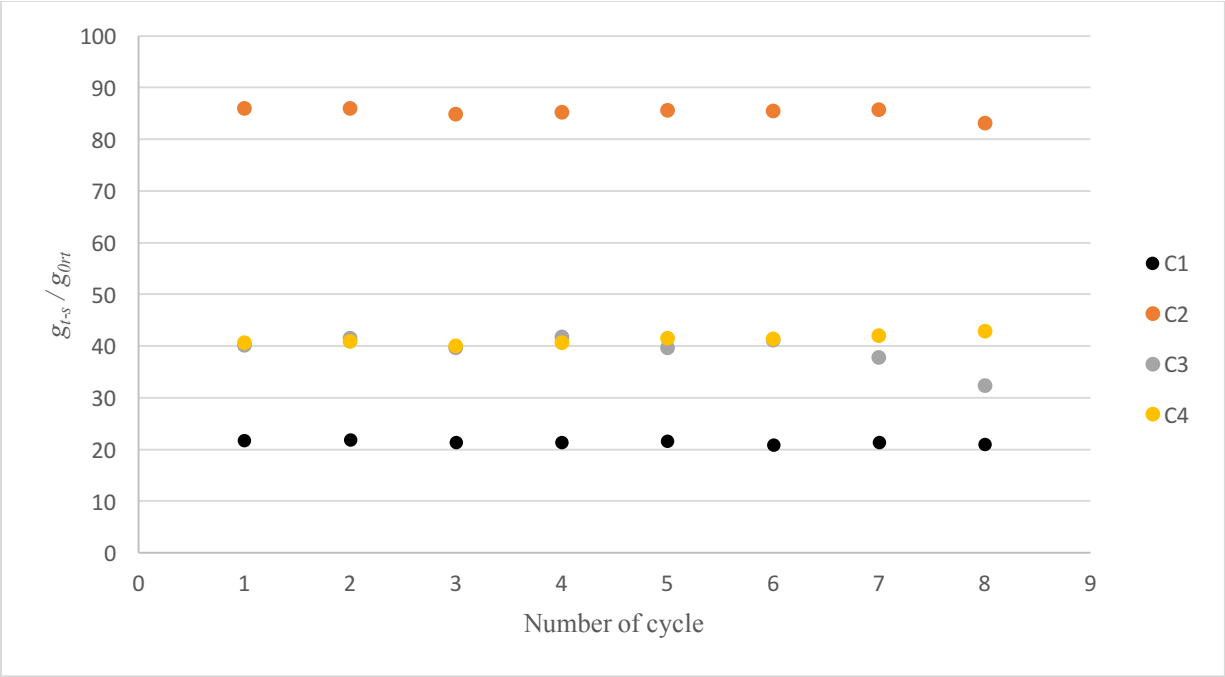

Figure 137 Contact to contact variation of C type devices

A possible key difference between the gold films and SiO_2 membrane is that the latter is almost perfectly smooth, whereas the gold film has significant grain roughness. An improvement in the reproducibility of the calibrations made might be achievable by the development of a completely flat metallic film [162] but this was not attempted during this work.

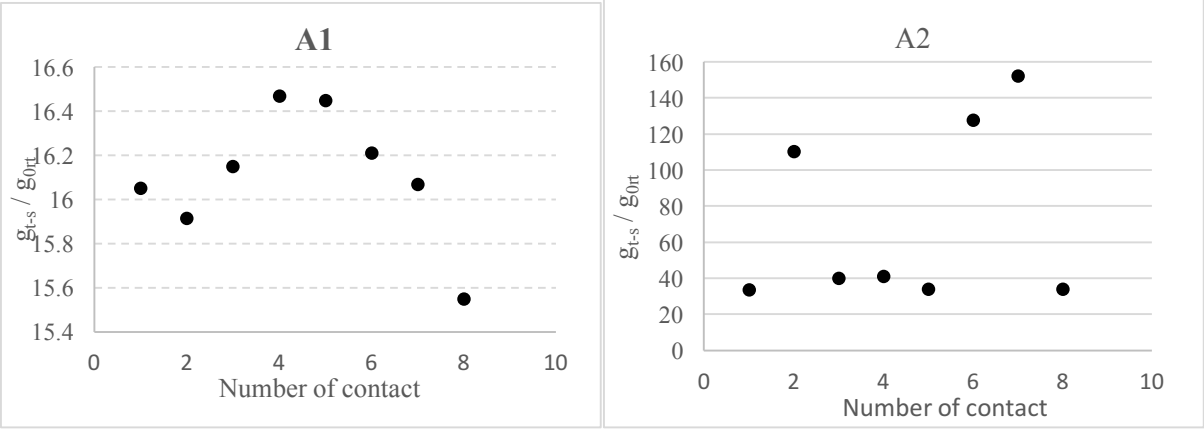

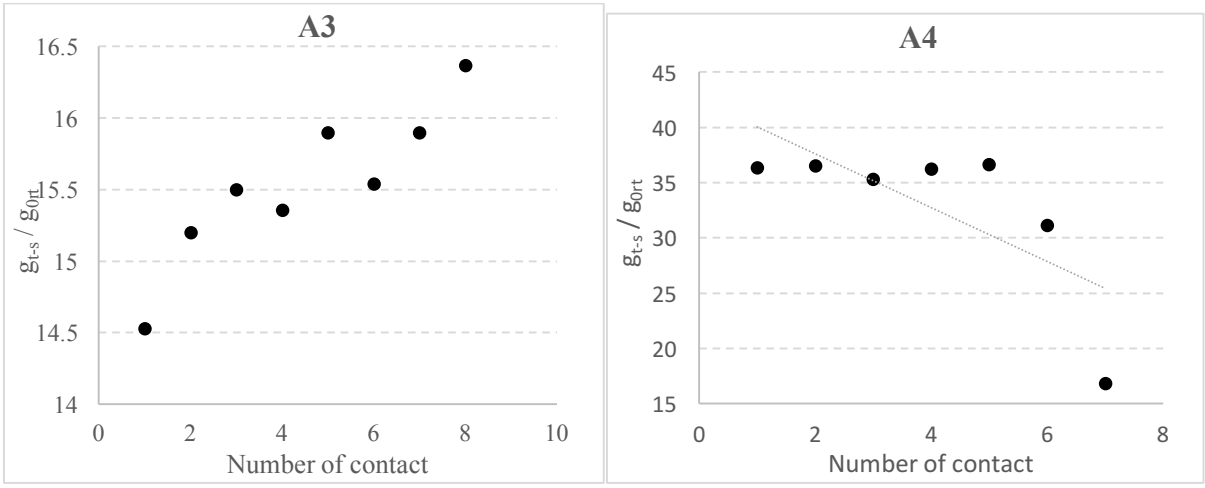

Figure 138 Systematic errors for device A1,A2, A3, A4

Reproducibility of thermal contact for devices A1, A2, A4 are more random rather than systematic as can be seen from Figure 138. Device A3 with small gold dot is increasing thermal conductance with time. The gold dot missed for that device as was discussed earlier in the chapter, however, the tip landed on the corner of silicon dioxide and NiCr, and the thermal conductance touching the corner of two materials was increasing with increasing the force. Randomness for A2 and A4 is associated with a significant change in the nature of the tip-sample contact.

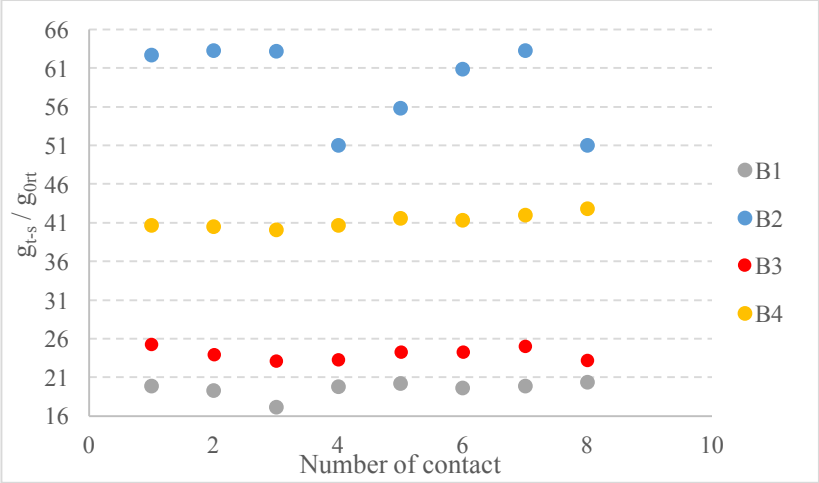

Figure 139 Systematic errors for device B1,B2, B3, B4

The membranes with increased number of supported arms (Figure 139) also have randomly variable thermal contact signal with time. Significant variations of resistance characteristic of changes in the tip are seen for sample B2

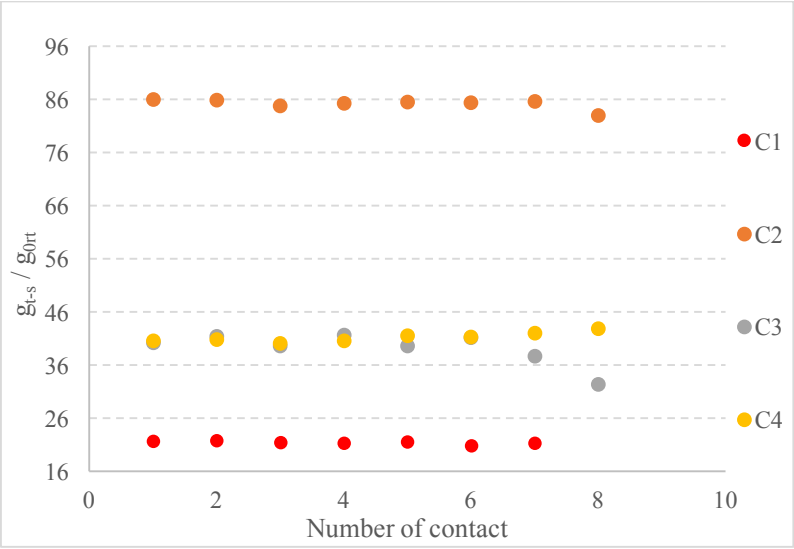

Figure 140 Systematic errors for device C1, C2, C3, C4

Some weak evidence of systematic variation with time in the contact to contact variation occurred when the heated tip was in contact with membranes with wider supported arms. (Figure 140). The variation occurring during the scan still appears to be more random then systematic. Nevertheless, due to the complicated nature of the contact between probe tip and sample a systematic evolution of the multiple contacts between tips and grains might be expected to occur due to lateral stage drift with time, as evidenced by the relative flatness of the traces for uncoated membranes. It is not believed that there is any significant evidence for changes in the nature of the probe tip itself during the measurements.

To sum up thermal characteristics for all devices the mean of thermal conductance values of 12 devices and standard deviation of 8 measurements performed for one device tabulated in table 17

Table 17 the thermal conductance result in vacuum

device	g_{T-S} / g_{0rt}	Stdev
A1	16.02	0.35
A2	71.80	49.77
A3	15.54	0.55
A4	33.10	0.55
B1	21.16	4.97
B2	58.90	5.46
B3	19.50	0.64
B4	41.18	0.91
C1	21.44	0.33
C2	85.23	0.94
C3	39.22	3.06
C4	41.23	0.89

One of the main reasons of fabricating these types of samples is for calibration purposes in SThM materials measurement. Instead of using number of different bulk samples with different materials one sample with number of different thermal conduction defined by geometry might be an attractive option.

Adding an extra gold dot to a thermally isolated membrane as shown from the experiments can change the tip-sample thermal resistance/ conductance; however, the size of the deposited gold film needs to be large enough to give a large probability of the tip contacting the desired area. As is seen with devices A3 and B3 where the gold dot was missed and possible contact being made in the corner of SiO_2 and NiCr which was used as a sticky layer. It is believed that initial contact was made on the silicon dioxide surface since the values of $g_{t\text{-}s}$ correspond to devices A1 and B1. Because the thermal resistance is dominated by the supporting arms as shown in case of device C3 where the contact was made on the gold dot, there is no reason to use small dots as this might cause practical difficulties. The range of available thermal conductance is not significantly increased as was suggested by modelling. Devices A3, B3 and C3 show a two step contact. The first step is contact of the silicon dioxide surface for devices and gold dot for device C3. The second step is contacting the NiCr for devices A3 and B3, and contacting the edge of the gold dot again for device C3.

Devices A1, A4, B1, B2, B4, C2, C4 might be a case of single point contact.

Covering the whole surface with metal giving a high chance of quantifying the tip-sample thermal conductance value. 3 different options of covering the 3 types of devices were explored. Device A2 is like device A1 fully covered with gold, as the geometry of device B1 and C1 are relatively similar, to investigate the influence of the thermal resistance of supported arms, in case of device B2 4 legs are left free of metal and another 4 covered with gold, and device C2 fully

covered with gold which makes device C2 conduct heat for about 25% better than device B2. Device C2 corresponds to the conductivity of bulk Si and should be a suitable device to study tip-sample thermal conductance. However, it was not possible to compare the values for device A2 with devices B2 and C2 since there were big variations in values for first contact thermal conductance. Device A2 might be an example of multi-asperity contact, giving a big variation in conduction values. Some values of initial contact correspond to contact of silicon nitride to the devices and some to a piece of metal to the membrane. Multi-asperity contact was difficult to study in detail due to a lot of scatter.

It is interesting that three distinct groups of thermal conductance (Figure 141) corresponding to clean membrane, membrane covered with gold and fully covered with gold can be obtained. This would suggest that the use of the samples for calibration might be possible. The modelling being made just for spreading resistance to have an idea of thermal resistance of different fabricated samples and gives a constant impedance calibration. Thus the variation does not correspond well to the modelled values.

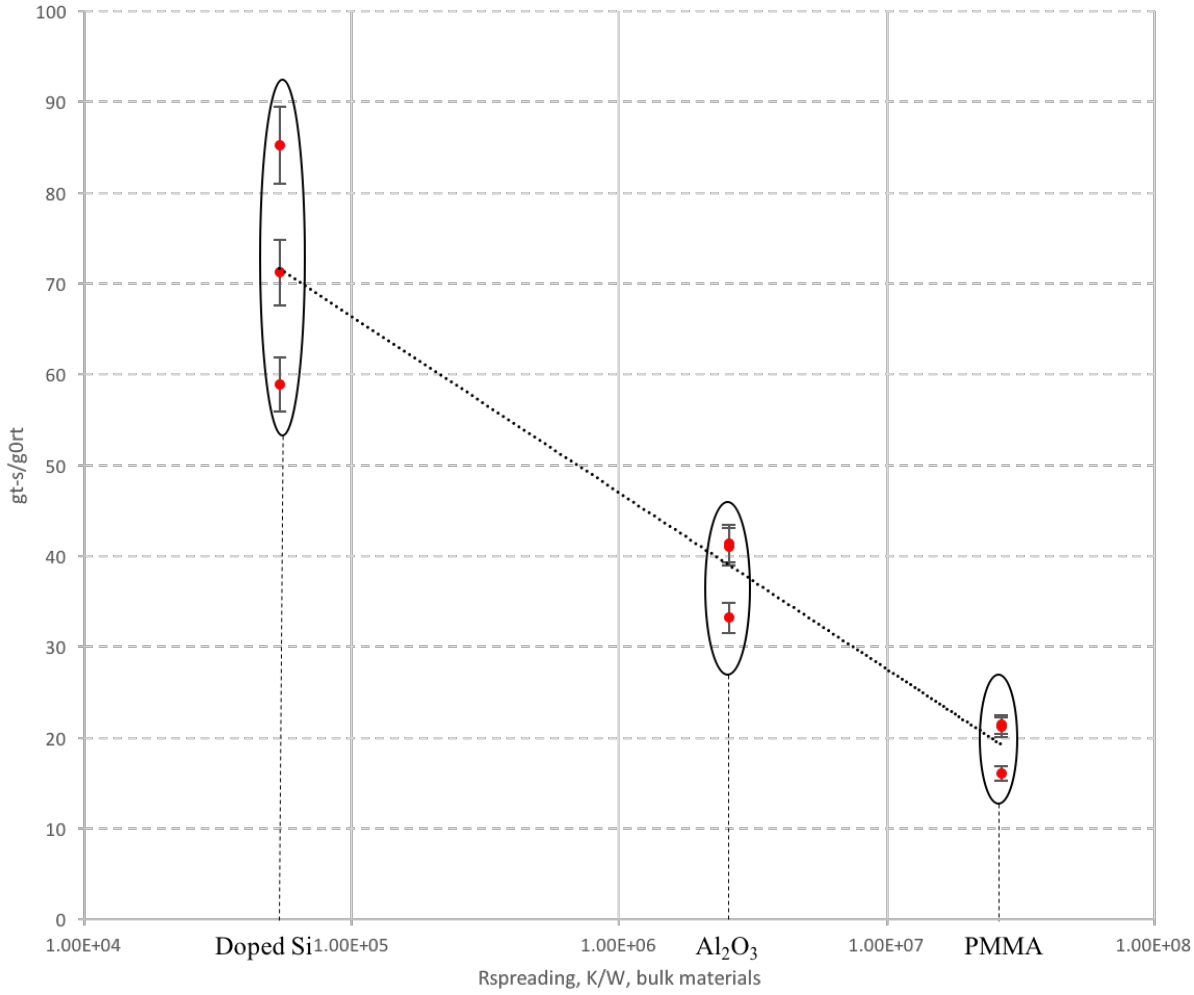

Figure 141 Three groups of thermal conductance values which correpond to different bulk material thermal characteristics. This demonstrates the potential for the "passive" samples to serve as a microfabricated standard for the calibration of measurements of bulk thermal conduction

In future for these type of measurements, it will be better to do real-time observation of the shape and size of the tip, and of the sample surface during the thermal measurements and scan by using combined scanning thermal microscopy and scanning electron microscopy equipment (SThM-SEM). [23]

[23] QUANTIHEAT European project, CNRS_Centre d'Energétique et de Thermique de Lyon

Chapter 5. Active device and passive probe measurements

In this chapter thermal measurements have been obtained using passive AFM probes, where the thermal coupling between a passive probe making contact with an active device was measured.

5.1 Self heating modelling

Heat transfer of the active device in vacuum was simulated in COMSOL. The modelling of temperature distribution and heat transfer boundary conditions has been discussed in chapter 4.1. Here is presented the modelling of the self heating of the device which is useful for getting an idea of the sensitivity of the active device.

Figure 142 shows a simulation in which the membrane is simulated as a thin film membrane attaching to the bulk Silicon which is a heat sink. The temperature boundary conditions were set up at room temperature on the edges of the silicon. As can be seen from the colour on the figure that there is no significant heating of the silicon due to the high thermal conductivity of a bulk silicon relative to the membrane on the edges. To get an accurate estimate of the temperature change in the membrane a very fine mesh was chosen. One of the pads connected to the Pt heater/thermometer was set up as ground with 0V. An input voltage of 0.1 V (about 89 μW) was applied to one of the Au pads leading to the Pt heater/thermometer. The membrane heated by 133 K . This varied by ± 3 when finer or coarser mesh was applied or the membrane thickness was varied by $\pm 10\ nm$ as was measured from the simulation. (Figure 142) The sensitivity of the membrane in vacuum as measured by simulation is $1.49 \cdot 10^6 \pm 3.3 \cdot 10^3$ K/W.

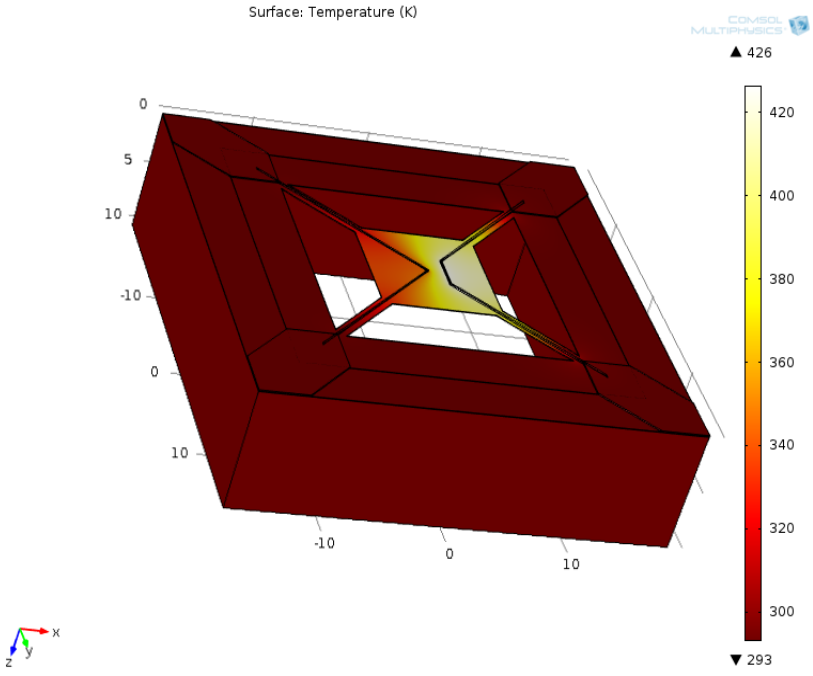

Figure 142 Self heating of active device simulation in COMSOL

5.2 Passive mode measurements

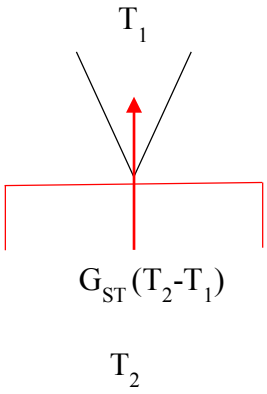

Figure 143 Passive mode measurements

During passive mode measurements (heated sample) the sample membrane was heated by passing alternating current (AC) signal through to the Pt thermal sensor, which is used both as a resistance heater and a resistance thermometer detector (RTD), and the 3ω signal (Voltage) change across the sensor was measured as an unheated tip was brought into contact with it.

Thermal sensors integrated on top of the thermally isolated membrane as described in Chapter 3 allow measurement of the thermal conductance between AFM probes and sample with very high precision thanks to the extreme sensitivity of the active device.

To gain understanding of the tip-sample contact the area and nature of the contact were important variables. The probes were therefore inspected using a scanning electron microscope before and after measurements. SEM measurements were made using a "Helix" detector and reduced vacuum to avoid surface charging and contamination as described in methodology chapter[150]

Passive AFM probes with different materials were used with the same device to investigate the dominant factors influencing the nature of the tip – sample heat transfer mechanism. The four type of probes used are the commercially available FESP probe [24] and Olympus probe[25], the KNT SThM probe[26], and a bare Si_3N_4 KNT probe of the same type as the previous one but without any metallization. These were chosen to correspond to commonly used SThM probe types.

SEM images of the FESP Si probe taken before measurements are shown in (Figure 145). It is a sharp silicon tip, just like the doped silicon SThM probes,[52][53] so it can be used as a

[24] Bruker AFM probe, Bruker AFM Probes, 3601 Calle Tecate, Suite C, Camarillo, CA 93012, FESP V-2
[25] Olympus Corporation, Shinjuku, Tokyo, Japan, Part number: OMCL-AC160TS-C2
[26] Kelvin Nanotechnology, 70 Oakfield Avenue, Glasgow, UK, G12 8LT, KNT-SThM-1an-5

way to investigate the thermal character of the tip sample contact of those probes. The advantage of this probe is that it is very sharp.

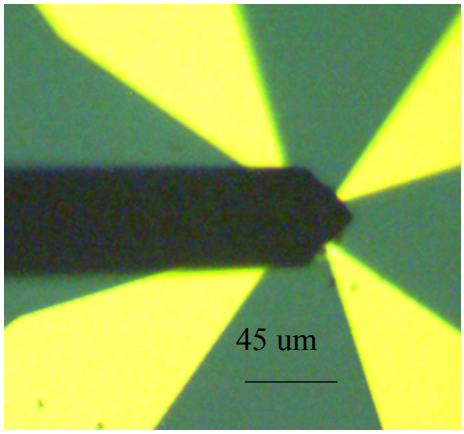

Figure 144 Optical image of FESP probe

However, the tip is not located in the end of the cantilever which makes it difficult to approach the center of the membrane using the optical microscope of the Nanonics AFM. (Figure 144). The cantilever is 2.75 μm thick, 45 μm width and 225 μm long so that it completely obscures the 10X10 μm membrane. So an attempt was made to place the 3 corners of the cantilever ends in the center position of the membrane leads so that the tip was positioned in the middle of device.

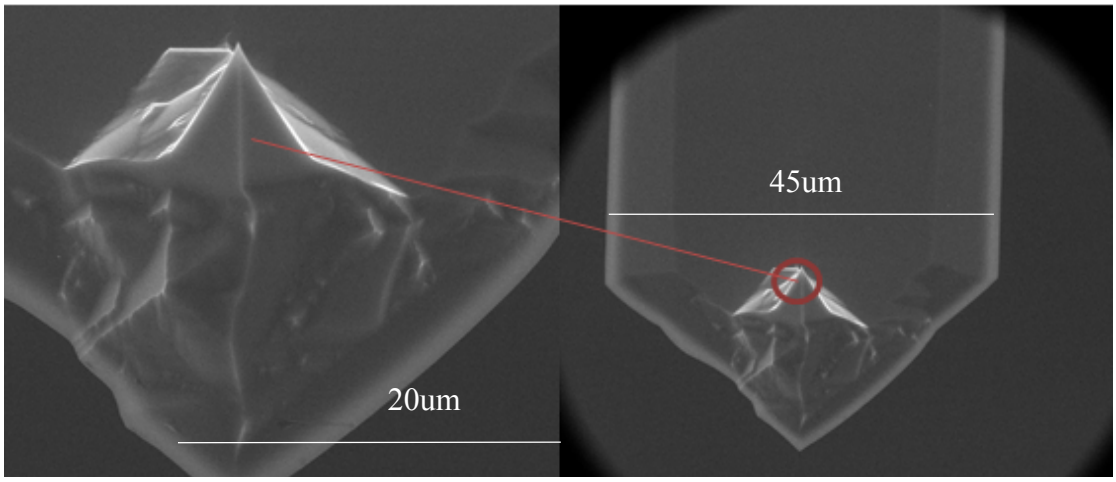

Figure 145 FESP probe before measurements

The FESP probe and heated active membrane device were contacted and the results are shown in Figure 146. The mean of first contacts step change in thermal conduction was 433.95 ± 33.03. The error was happening due to tip became blunt. The step change for first contact is smaller compared to other contacts. This happened due to tip sharpness before measurements as can be seen from Figure 145. There is a presence of a small pull-off force value

of 15.22±2.04 nN. By repeating the same measurement for several cycles we can observe changes in the nature of the contact and tip sharpness.

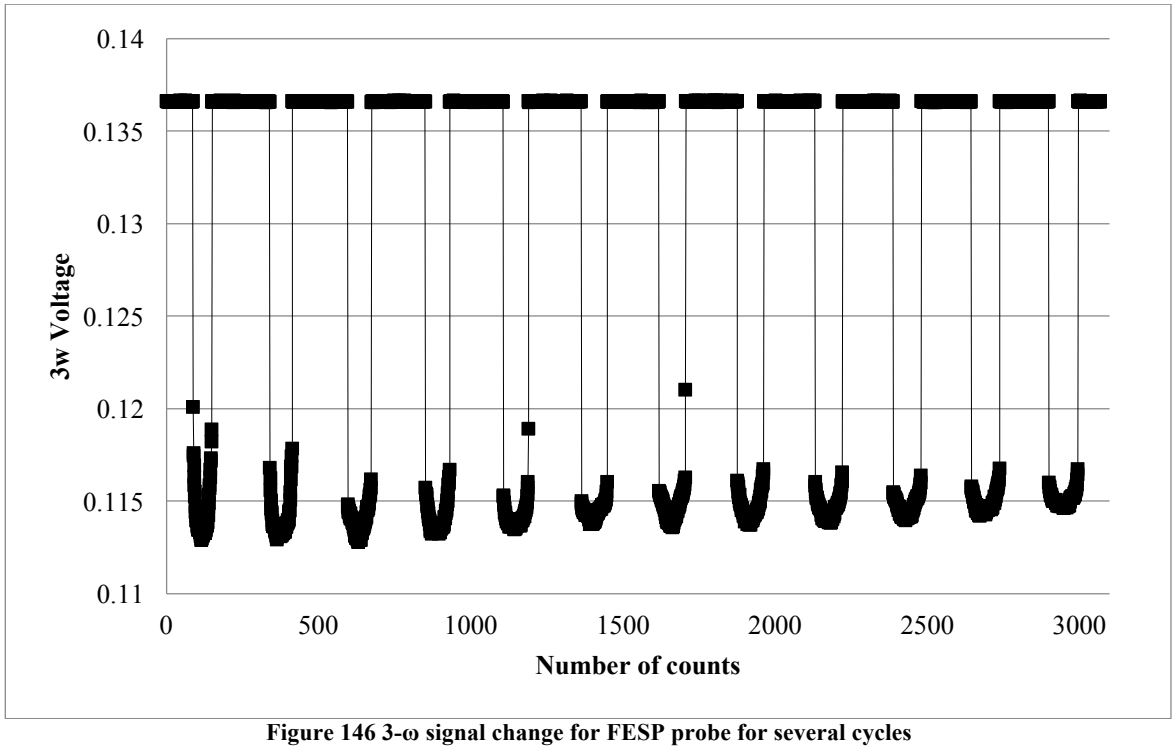

Figure 146 3-ω signal change for FESP probe for several cycles

The repeated process of approaching and retracting the sample surface is shown in Figure 146.

Initial contact is smaller at first, and then gets stronger. Rate of change with force is initially large then gets smaller after first contact. The next point is consistent with similar pull-off force for all measurements and as such is believed to represent a good measure of initial thermal contact. Later curves share the flat shape of measurements made using the cleaved silicon tips.

Thermal conduction at maximum force decreases with number of contact events. The change of the shape of the curve due to the pulling force might be because of the blunting of the tip which can be seen from the SEM images taken after the measurements. (Figure 147). When comparing with the SEM image made of the tip before measurements it is obvious that cleaving happened after the first approach of the tip –sample contact. It can be seen that the pull off force increases as the tip become blunter. From the shape of the in contact and out of contact plot it can be seen that the errors in contact are more random than systematic

The summary of heat transport between FESP probe and heated sample is shown in Table 18.

Table 18 FESP probe and sample heat transport summary

g_{T-S}, W/K	$g_{s\text{-}t}$ / g_{0rt}	F, pull off, nN
$9.58 \cdot 10^{-8}$	335.51	10.08
$1.18 \cdot 10^{-7}$	413.41	13.86
$1.32 \cdot 10^{-7}$	462.03	13.86
$1.25 \cdot 10^{-7}$	439.71	15.12
$1.28 \cdot 10^{-7}$	450.02	15.12
$1.30 \cdot 10^{-7}$	457.64	16.38
$1.27 \cdot 10^{-7}$	444.92	16.38
$1.23 \cdot 10^{-7}$	430.29	16.38
$1.23 \cdot 10^{-7}$	432.54	15.12
$1.27 \cdot 10^{-7}$	445.91	15.12
$1.25 \cdot 10^{-7}$	438.60	17.64
$1.23 \cdot 10^{-7}$	432.80	17.64

Table **18** there are two group of thermal conductance. The first corresponds to a very sharp tip in the start of the measurements. The second group of values is for the probe after being cleaved. Thus, the in contact area of the thermal conduction curve is plotted for the first and last approach in order to compare the tip-sample thermal conductance and evaluate the change of tip shape.

From the SEM image in Figure 147 it is seen that the probe after measurements became blunt. And from the data in table it might be seen that this happening after the first contact.

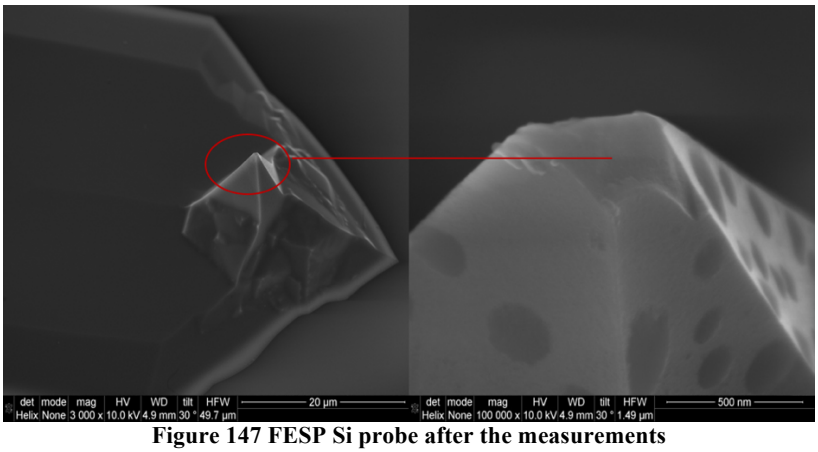

Figure 147 FESP Si probe after the measurements

When looking at the first and last approach curve closer (Figure 148) it is obvious that tip became blunt. The small jumps of 4 when tip in contact happening for first and last contact shown that it might be a case of small of multi-asperity contact happening.

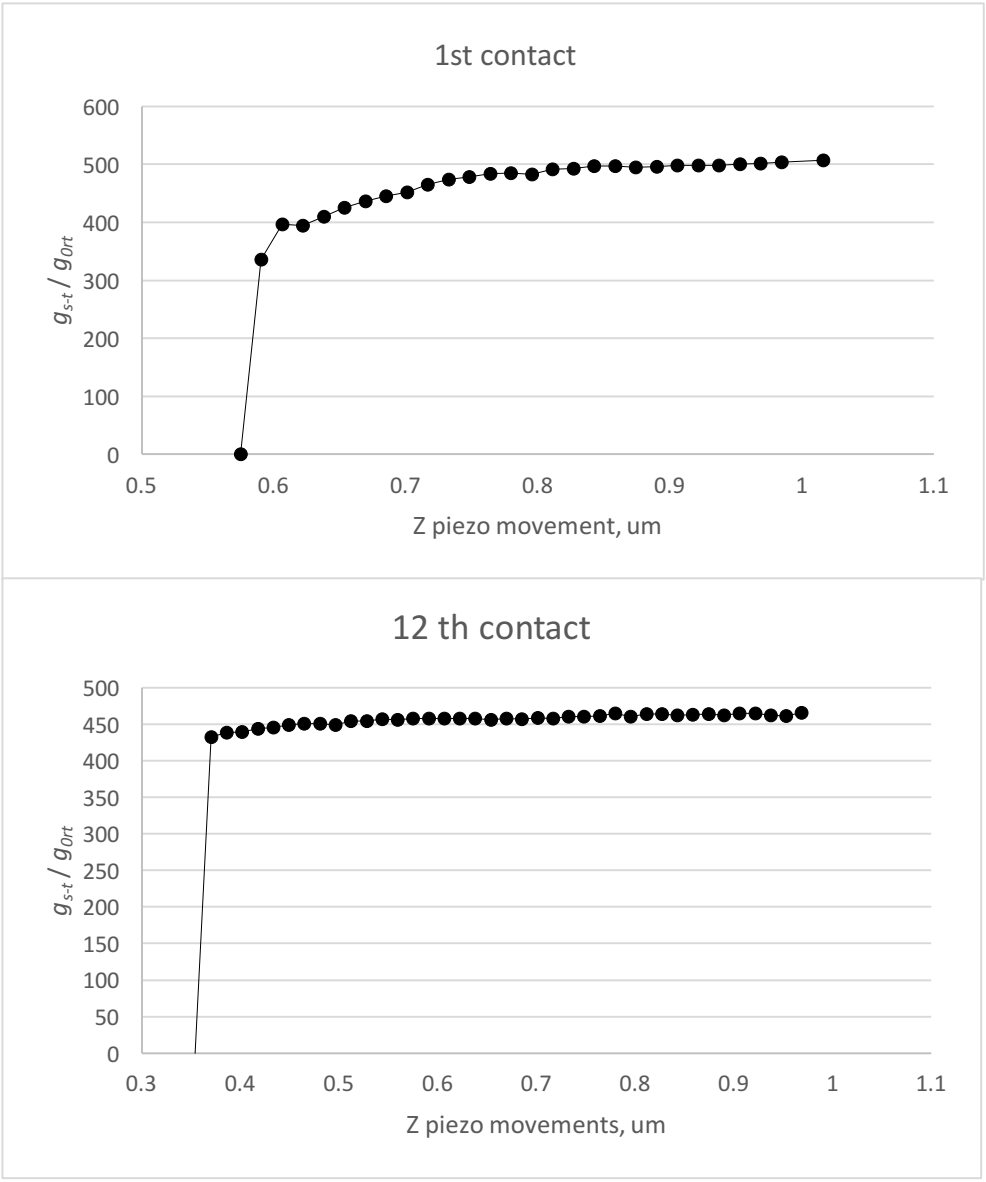

Figure 148. Approaching the heated sample by FESP Si probe in first and last contact

The noise happening in contact area is assumed to be due to mechanical vibrations. Looking for a correlation between pull-off force and thermal signal: (Figure 149)

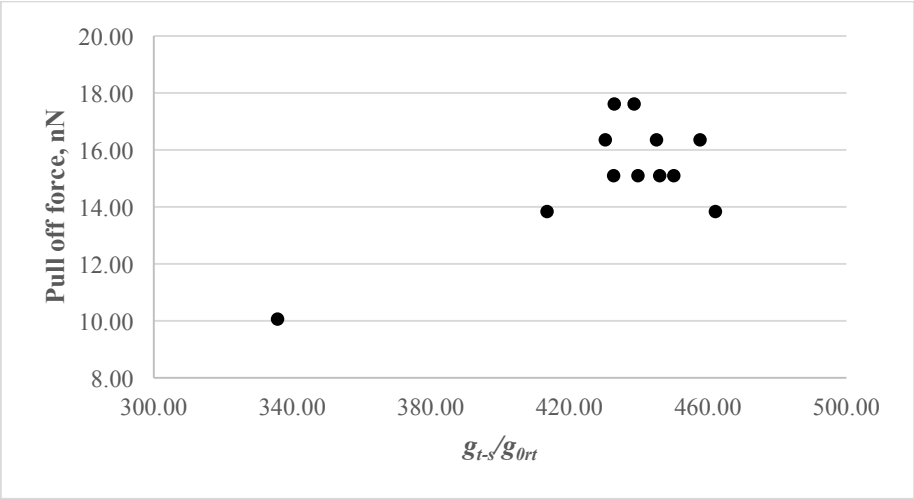

Figure 149 Correlation of pull of force with thermal signal

There is a strong correlation between thermal conduction and pull-off force for the first contact only.(Figure 149) Since the first contact took place before the tip was blunted by damage, this occured when the area of the tip-sample contact corresponded to the initial sharp tip size which is of order 10nm. Further contacts give a larger thermal contact which varies from contact to contact. The pull-off force and thermal conduction on initial contact are not correlated in this case. This may be due to the thermal contact between tip and sample being large enough so that the total change is dominated by the resistance of the sample, hence leading to a saturation of the signal, or else because the pull-off force corresponds to a different part of the tip to that which was making the initial contact. This data serves to emphasise the importance of achieving a stable and smooth tip shape in probes used for thermal conduction measurement

The next choice of probe is an “Olympus probe”. The “Olympus probe” has a tetrahedral tip located at the very end of the cantilever.

The Olympus probe is same material and sharpness as FESP but easier to centre on the membrane as the sample is visible under the tip. (Figure 150)

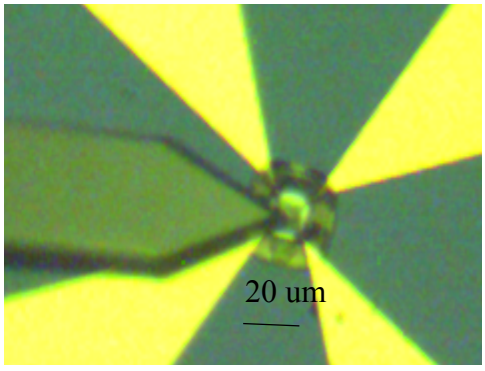

Figure 150 Optical image of Olympus probe and sample

This allows us to sit over a particular point of interest on the sample and to precisely align the tip using the optical microscope. The largest contact happens first and it then decreases with number of contacts. In the case of the FESP the contact starts small and gets bigger (Figure 151).

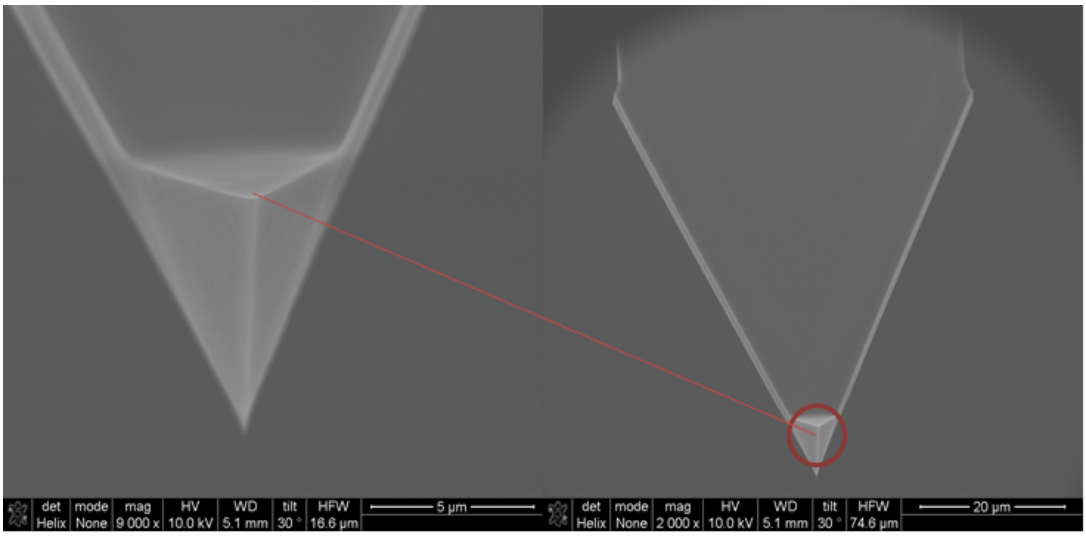

Figure 151 Olympus probe before measurements

The Olympus probe and heated active membrane device were contacted and the results are shown in Figure 152. The mean of first contacts step change in thermal conduction was 219.10 ± 42.14. The step change for first contact is larger compared to other contacts and then gradually decreases. The probe was retracted after contact number 9 and approached again for another 3 contacts. There is a presence of a small pull-off force value of 10.91 ± 0.98 nN. By repeating the same measurement for several cycles we can observe changes in the nature of the contact and tip sharpness.

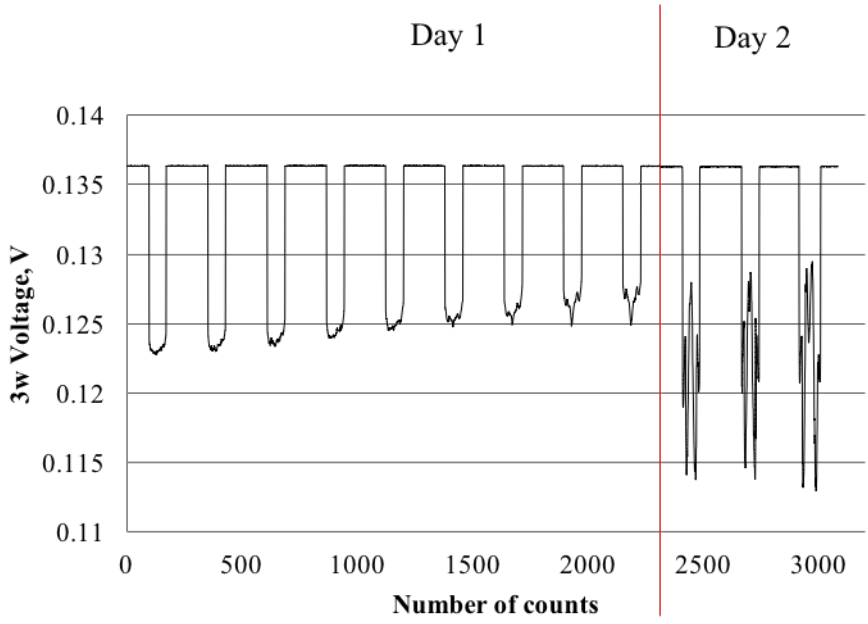

Figure 152 3-ω signal change for Olympus probe

The summary of heat transport between Olympus probe and heated active device is placed in Table 19.

Table 19 Olympus probe and sample heat transport summary

g_{T-S}, W/K	$g_{s\text{-}t}$ / g_{0rt}	F, pull off, nN
$7.01 \cdot 10^{-8}$	245.81	12.60
$6.37 \cdot 10^{-8}$	236.06	10.08
$6.60 \cdot 10^{-8}$	231.46	11.34
$6.24 \cdot 10^{-8}$	218.90	11.34
$5.73 \cdot 10^{-8}$	201.11	10.08
$5.46 \cdot 10^{-8}$	191.75	10.08
$5.28 \cdot 10^{-8}$	185.23	11.34
$4.89 \cdot 10^{-8}$	171.68	11.34
$4.60 \cdot 10^{-8}$	161.49	10.08
$8.51 \cdot 10^{-8}$	298.56	10.08
$8.06 \cdot 10^{-8}$	282.85	10.08
$5.28 \cdot 10^{-8}$	204.32	12.60

The approaching of Olympus probe has been done in two steps. The first step includes 9 approaches and retracts. The second step was done next day in 3 approaches and retracts.

When looking in contact area when probe is approaching the sample surface it looks that tip started with single point contact and changed to multi-asperity by the end of the scan. The first contact has higher value of thermal conductance as the measurements started with sharp tip. And then the blunting of the tip was happening and the contact was made by the corner of blunted edge which is even sharper then initial tip sharpness. By the end of the scan the value of thermal conductance is decreased (Figure 153)

In the first approach single point contact occurred with noise level of about $2g_{0.}$ After first contact the value of thermal conductance decreases and the nature of in contact area is changing gradually to multi-asperity. Starting from contact 2 until contact 9 the Si tip might be touching the heated sample surface with blunter tip. The value of thermal conductance jump when in contact is about 20 ± 2. The error may be happening due to mechanical vibrations.

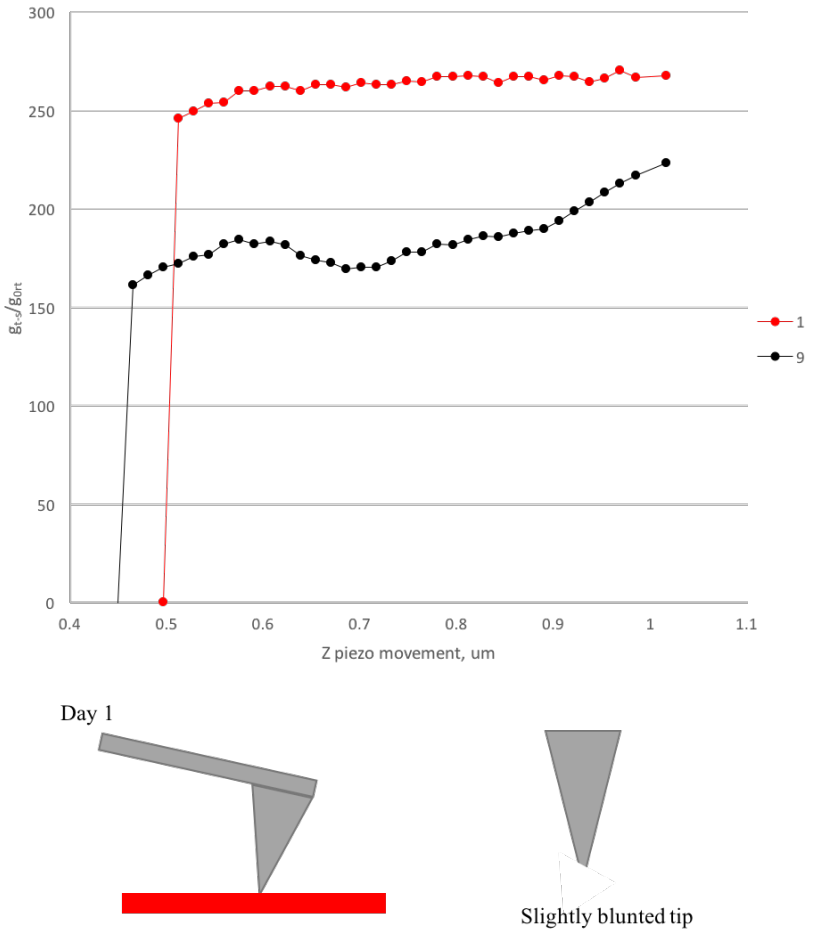

Figure 153 Approaching the active device by Olympus probe stage 1. Not in scale

After probe being completely retracted a second step of approaching the sample was made next day. Contacts 10-12 are shown in Figure 154. By zooming in contact for contact 10 and 12 (Figure 154) we can observe that the tip might be completely broken and crunched as can be seen from Figure 155 that is not a case of slight blunting of the tip. As was suggested by Killgore et.al [163] the Si AFM tip, which has the advantage of a very sharp tip, tends to be blunted and broken during a scan. The increase in tip radius leads to a change of contact area. This dramatic change in the tip happened as the z-piezo was moved down by 0.015 V after the first scan. On approaching the probe stage had slightly drifted and wasn't at the same position. After approaching the sample by the same distance the tip end was broken as it came to close to the sample surface. By comparing the width of z piezo distance when tip in contact when the for first day and second day, it was found that sample was 0.015 V closer to the probe. So when looking at the plot in Figure 154 there is a large multi-asperity contact happening as the broken tip has more complicated geometry and the jumps when in contact corresponds to value of tip-sample thermal conductance of about $200 \pm 30\ g_{0rt}$. The error was estimated by change in jump when in contact due to uncertainty of contact region and complicated geometry of crunched tip.

We conclude that another part of the Si tip made contact with sample on the second time of approach.

The error is due to mechanical vibrations which is higher compared to the previous stage. The next contact within the multi-asperity contact might be again Si.

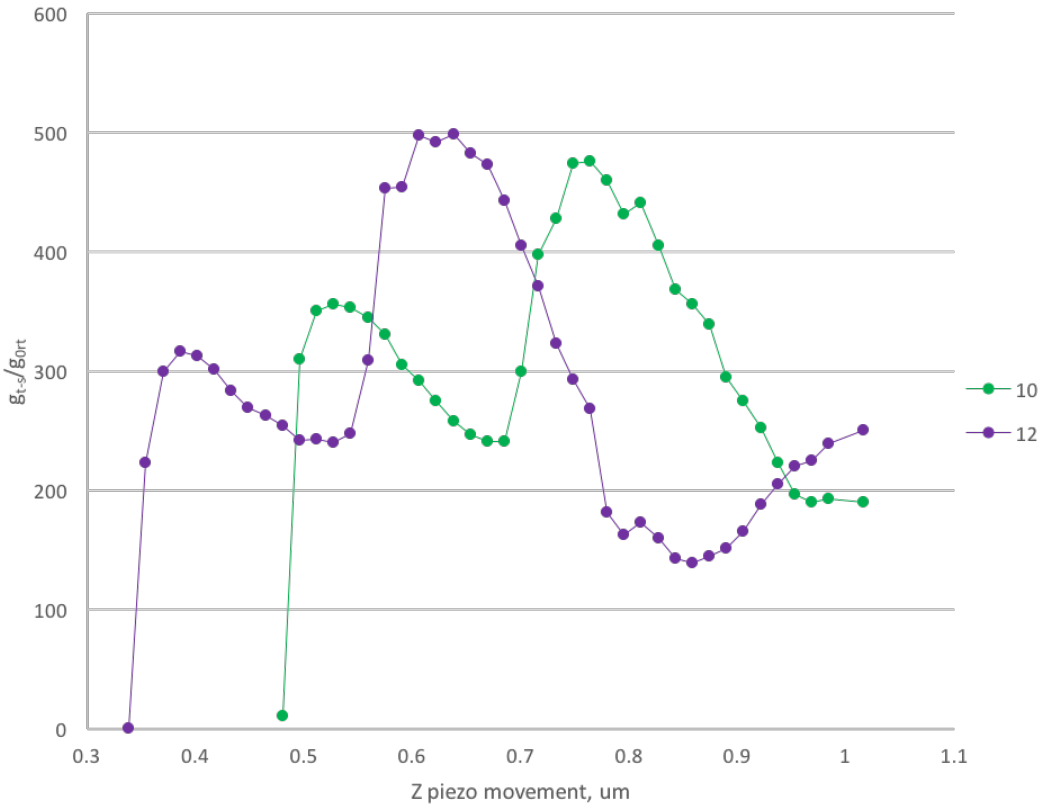

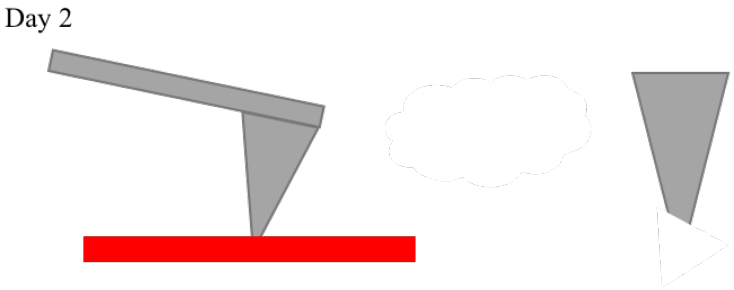

Figure 154 Approaching the active device by Olympus probe stage 2

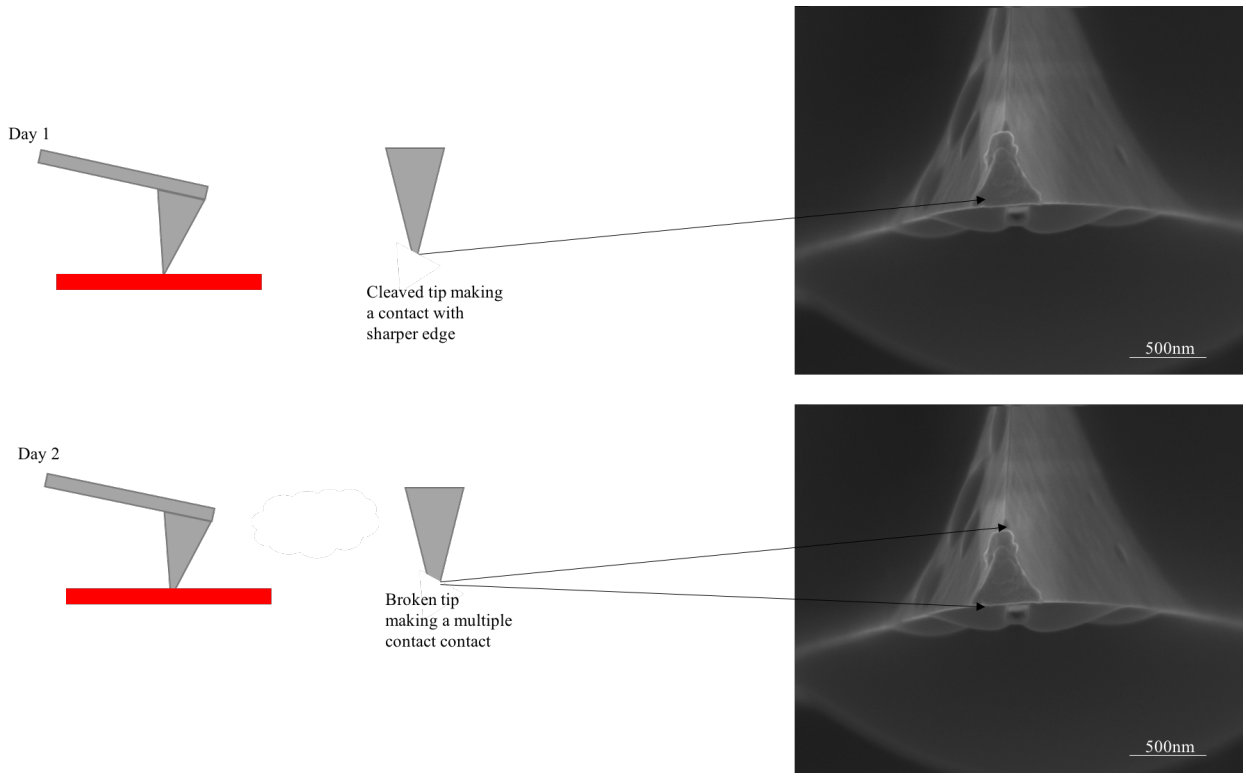

Figure 155 Olympus probe tip after the measurements

There are two circumstances which might be influencing the Olympus tip-heated active sample contact. The first of all is tip blunting. The second is that the tip end might be completely broken. All these factors appeared to cause multi-asperity contacts. The first contact is corresponding to Si tip-sample, then heavily blunted Si tip-sample, and then again Si tip with complicated geometry-sample.

The sharp FESP and Olympus Si tips have the main advantage of very fine tip-sample contact area. Silicon probes start off sharp, but then blunt immediately, so analysis of SThM contrast is hard because the tip sharpness is changing. Moreover, an opaque cantilever can make it difficult to focus on the desired area of the membrane. This is impossible with the FESP, but possible with Olympus.

The next probe to be examined was the KNT probe with a 400 nm thick silicon nitride transparent cantilever and blunter tip. Resistive tip coating of 5 nm NiCr and 40 nm palladium. Tip side and pads are coated with 5 nm NiCr and 140 nm Au and a series resistor is made of 33nm NiCr. These are the tips mostly used for SThM so such measurements of tip-sample thermal conduction are of great practical importance. These tips are relatively simple to align to the device.

An example optical image is shown in Figure 156 with a KNT probe aligned to the device during the measurements. The optical micrograph does not have high enough resolution to accurately find the very middle of the device.

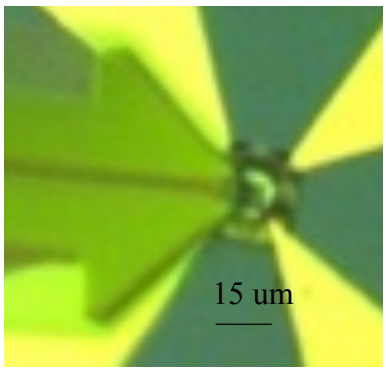

Figure 156. Optical micrograph of KNT probe and device during the scan.

The slightly rounded KNT probe presented in Figure 157 is taken before measurements. And as can be seen there is no additional metal peeling from the end of the tip.

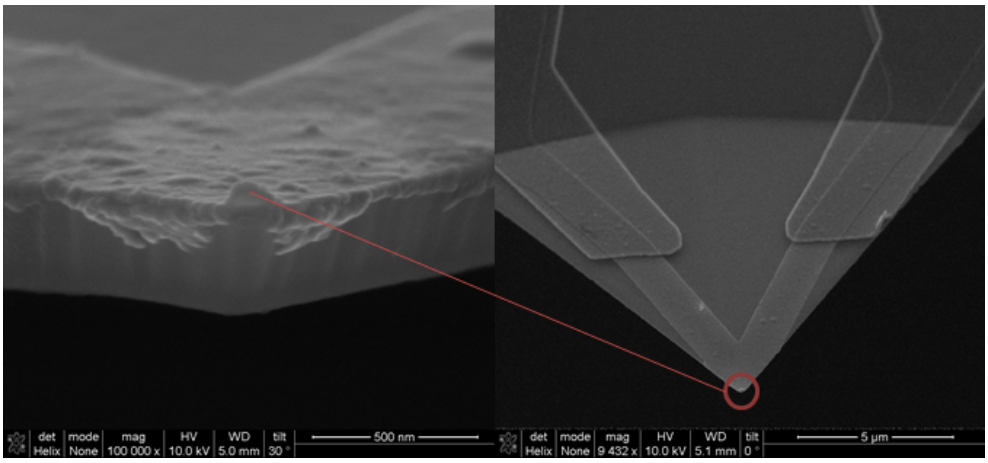

Figure 157 KNT probe before measurements

The KNT probe and heated active membrane device were contacted and the results are shown in Figure158. The mean of first contacts step change in thermal conduction was 87.58 ± 8.85. The step change for the first 12 contacts are similar in value and correspond approximately to device C2 (Figure 125) discussed in previous chapter 4. It might be due to Pt and palladium having same thermal conductivity (71.6 and 71.8 W/m/K) and the metal coating of the tip and sample are similar in both cases. The probe was retracted after contact number 12 and approached again for another 5 contacts on the next day. As can be seen from the plot the step change is increased and didn't reach the same value as with previous scan. There is a presence of a small pull-off force value of 39.80±3.48 nN. By repeating the same measurement for several cycles changes in thermal conductance are seen which may possibly be caused by metal flaking off from the tip (see Figure 161).

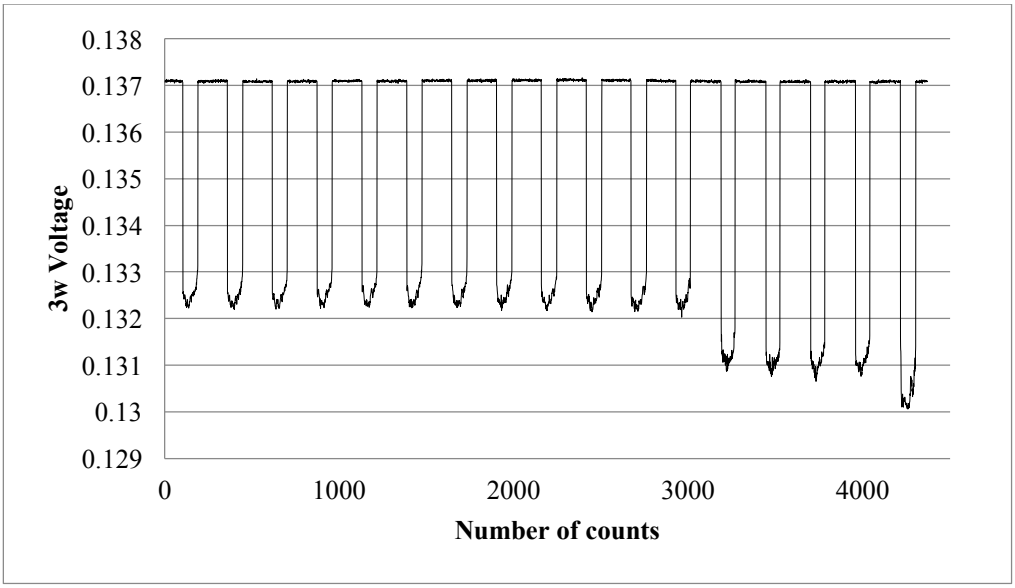

Figure158. 3-ω signal change for KNT probe

The values of thermal conductance and pull-off force calculated for each cycle are presented in Table 20

Table 20 Heat transport summary for KNT probe

	g_{T-S}, W/K	$g_{s\text{-}t}$ / g_{0rt}	F, pull off, nN
	$2.37 \cdot 10^{-8}$	83.17	42.83
	$2.38 \cdot 10^{-8}$	83.74	42.83
	$2.37 \cdot 10^{-8}$	83.32	40.31
	$2.38 \cdot 10^{-8}$	83.57	40.31
1st	$2.35 \cdot 10^{-8}$	82.37	40.31
measurements	$2.32 \cdot 10^{-8}$	81.37	41.57
	$2.24 \cdot 10^{-8}$	78.58	42.83
	$2.28 \cdot 10^{-8}$	80.11	42.83
	$2.29 \cdot 10^{-8}$	80.53	41.57
	$2.38 \cdot 10^{-8}$	83.56	42.83
	$2.40 \cdot 10^{-8}$	84.23	41.57
	$2.43 \cdot 10^{-8}$	84.04	34.02
2nd	$2.40 \cdot 10^{-8}$	91.99	35.28
measurements	$2.88 \cdot 10^{-8}$	101.17	35.28
	$3.00 \cdot 10^{-8}$	105.26	34.02
	$2.97 \cdot 10^{-8}$	104.11	35.28
	$2.79 \cdot 10^{-8}$	97.81	42.83

And plotted in figure 160.

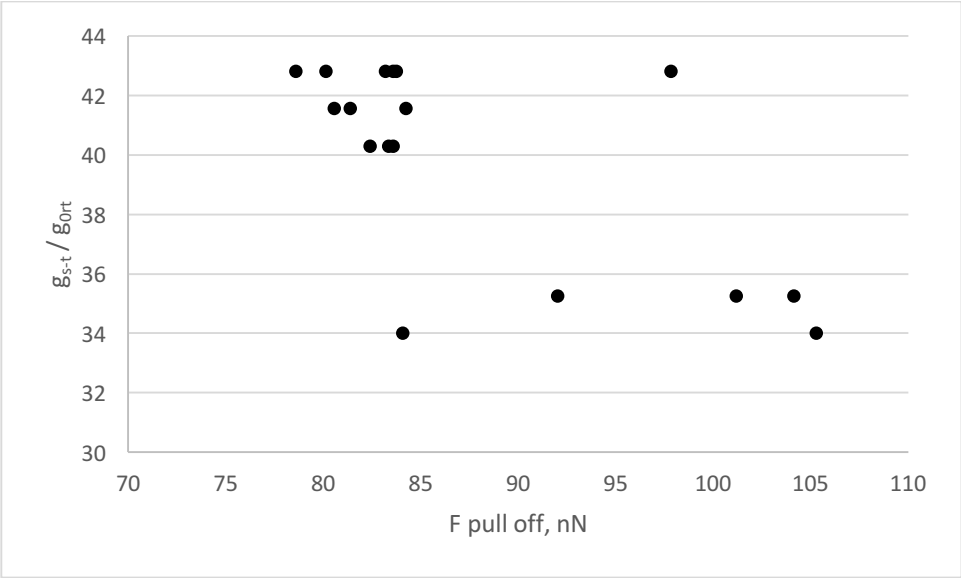

Figure 159 Correlation of pull of force with thermal signal

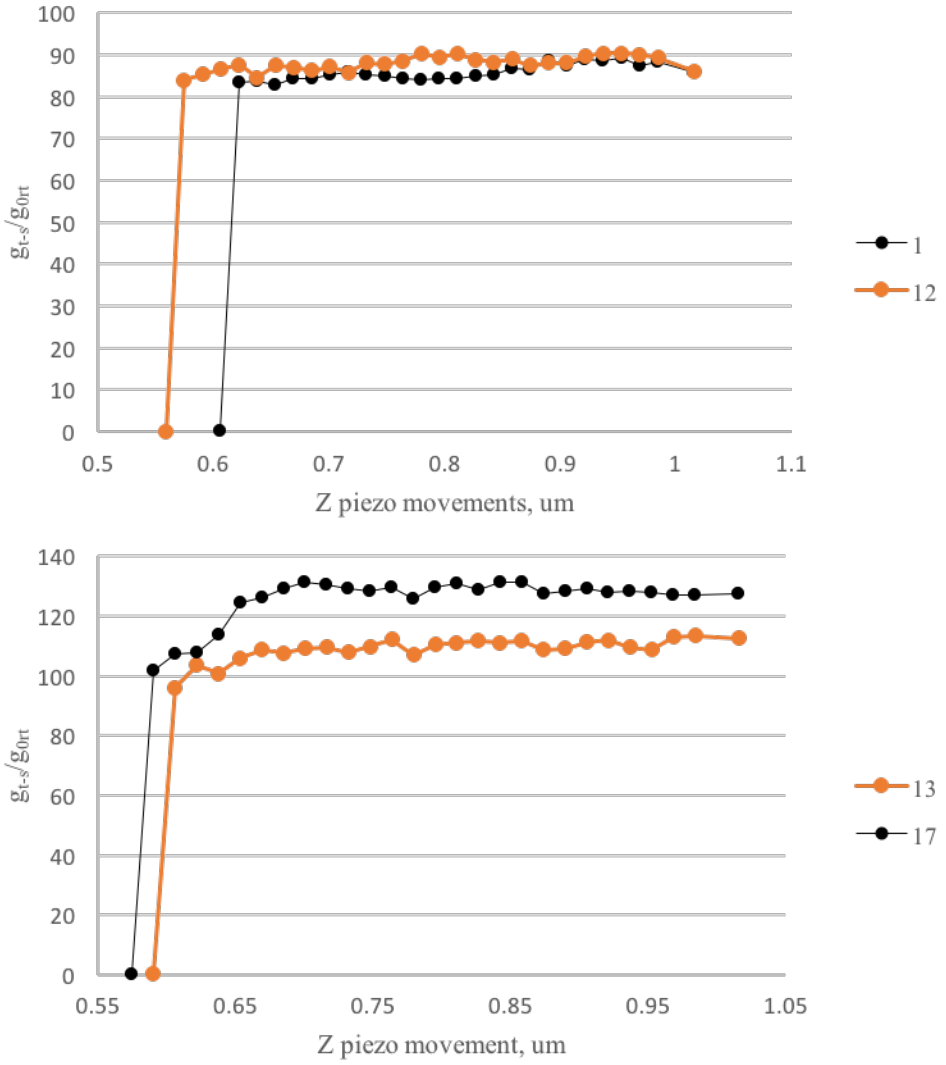

Figure 160 Approaching the heated sample by KNT probe first day for plot number 1 and 12 and second day for plots number 13 and 17.

When looking closer at the plot in the contact region it will be interesting to compare the signal on first and last approaches. The are no big changes for thermal conductance values for approaches number 1 and 12. The in contact region is more stable for first approach with presence of mechanical noise of $0.5g_{0rt}$. It possibly the multi-asperity contact is happening from first approach with jumps in contact of $2g_{0rt}$ which is higher than the noise limit and possibly the silicon nitride is making another contact after contact being made by metal sensor. The signal became noisier when in contact with value of mechanical noise of $1g_{0rt}$ which is believed to be happening due to mechanical vibrations.

After completely retracting the probe from sample, another attempt was made to contact the heated active sample. As can be seen from Table 20 and Figure158 lines 13 and 17 from the plot, the first signal for tip-sample thermal signal conductance is increasing. The approaching curve has some jumps with value of $5g_0$ it looks that the contact is multi-asperity. Increases in the noise and bigger jumps when contacting might be happening because metal was peeling off after the scan. Instability of the metal on the end of the probe is a possible explanation for the noise in the in-contact measurements as well as mechanical vibrations.

The process of flaking was captured before the fragment of metal was wiped away in use when the probe was examined after the experiment. (Figure 161)

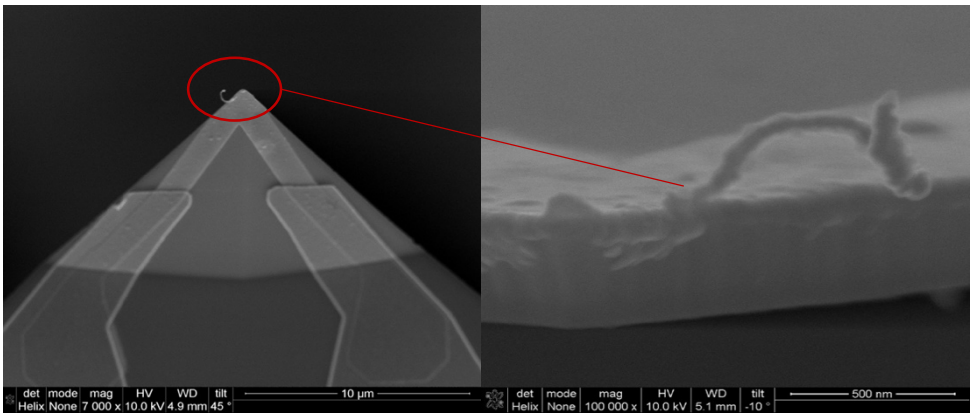

Figure 161 KNT probe after the measurements

KNT SThM tips have been observed to be unreliable in thermal measurement, for example being sensitive to thermal conductivity of the sample one day and then not the next.[164] This has been interpreted as being due to the metal on the end of the probe flaking off so that the nature of the portion of the tip in contact with the sample might sometimes by metallic and sometimes insulating. This is visible in the SEM pictures of the KNT probe taken after scanning. One important difference in this experiment is that the probe was used for a very short time, and not scanned laterally.

The effect of the tip-metal was investigated further by scanning an identical KNT probe in which the metal had been deliberately removed, leaving a plain blunt Silicon Nitride tip. (Figure 162)

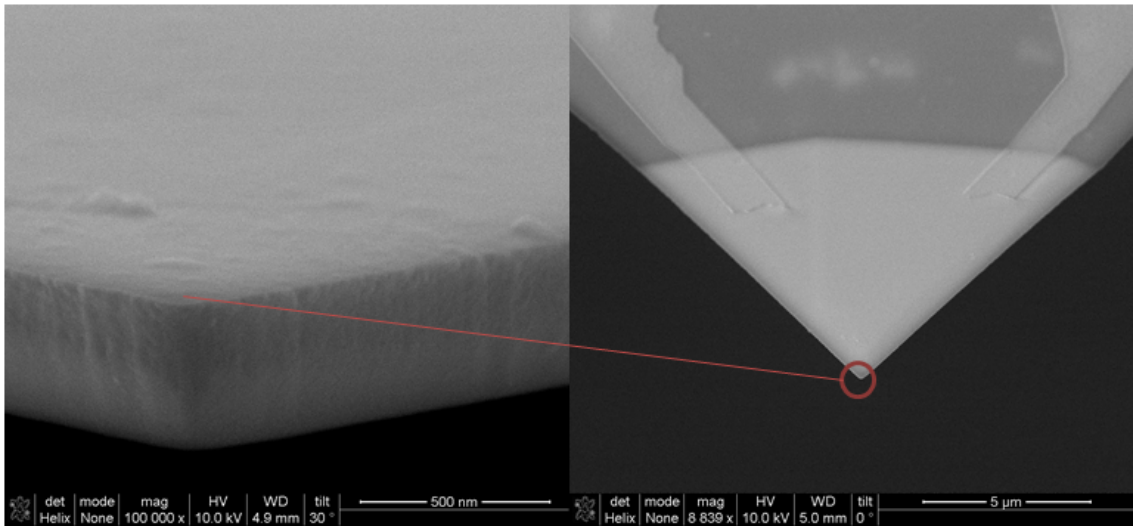

Figure 162 Si3N4 KNT probe with no metal

The bare nitride KNT probe and heated active membrane device were contacted and the results are shown in Figure 165. The mean of first contacts step change in thermal conduction was 43.89 ± 3.09. The step change for first contact is smaller compared to other step changes and gradually increases. There appear to be multi-asperity contact first contacts and then stabilising by the last approach. There is a presence of a small pull-off force value of 26.88 ± 6.16 nN. The tip has a consistent change in signal with number of contacts.

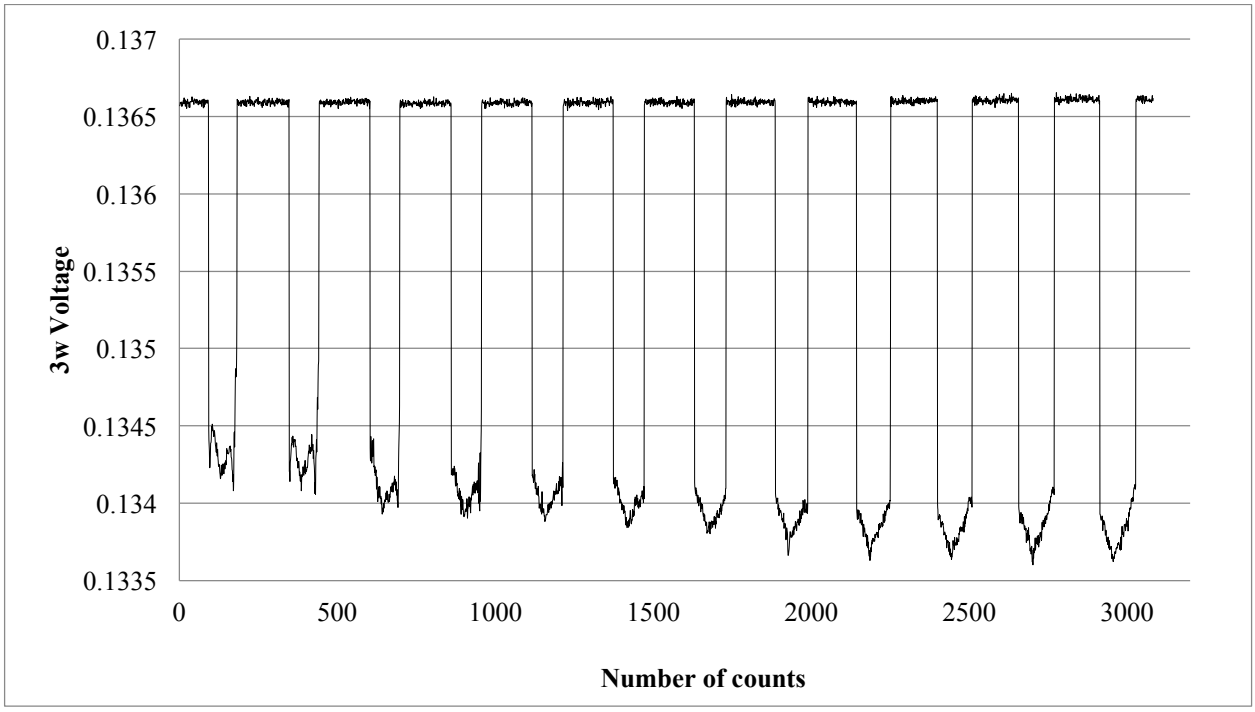

Figure 163 3-ω signal change for KNT probe

The values for thermal conductance at initial contacts and pull off force values are given in Table 21.

Table 21 The heat transport summary for bare nitride KNT probe

g_{T-S}, W/K	$g_{s\text{-}t} / g_{0rt}$	F, pull off, nN
$1.06 \cdot 10^{-8}$	37.31	21.42
$1.22 \cdot 10^{-8}$	42.91	22.68
$1.14 \cdot 10^{-8}$	40.01	20.16
$1.22 \cdot 10^{-8}$	42.71	22.68
$1.23 \cdot 10^{-8}$	43.05	22.68
$1.24 \cdot 10^{-8}$	43.49	22.68
$1.25 \cdot 10^{-8}$	43.87	25.20
$1.28 \cdot 10^{-8}$	44.82	26.46
$1.34 \cdot 10^{-8}$	47.02	31.50
$1.33 \cdot 10^{-8}$	46.69	32.76
$1.34 \cdot 10^{-8}$	47.14	36.54
$1.36 \cdot 10^{-8}$	47.70	37.80

As was assumed based on the analysis for previous probes changes in thermal conductance happen due to contamination, increasing force and tip blunting. It was necessary to zoom in to the in contact area and quantify the value of noise level and jumps and check the SEM image after the scan to determine what is happening. (Figure 164 and Figure 165)

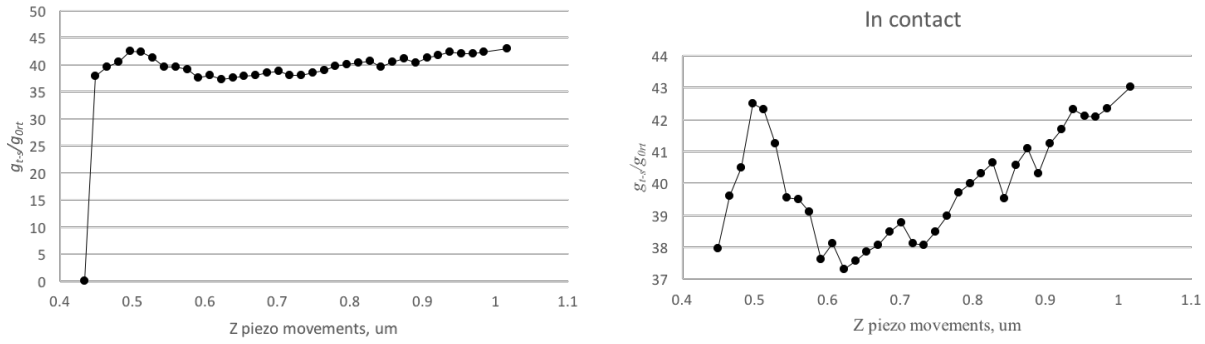

Figure 164 First approaching the heated sample surface

The first approach of the heated sample gives a thermal conductance value of $37.31 \pm 0.75 g_{0rt.}$ The error taken into account is noise happening due to mechanical vibrations.

There are jumps happening in the in contact area of about $5\pm0.75g_{0rt}$ which are possibly due to slightly rounded silicon nitride making a contact.

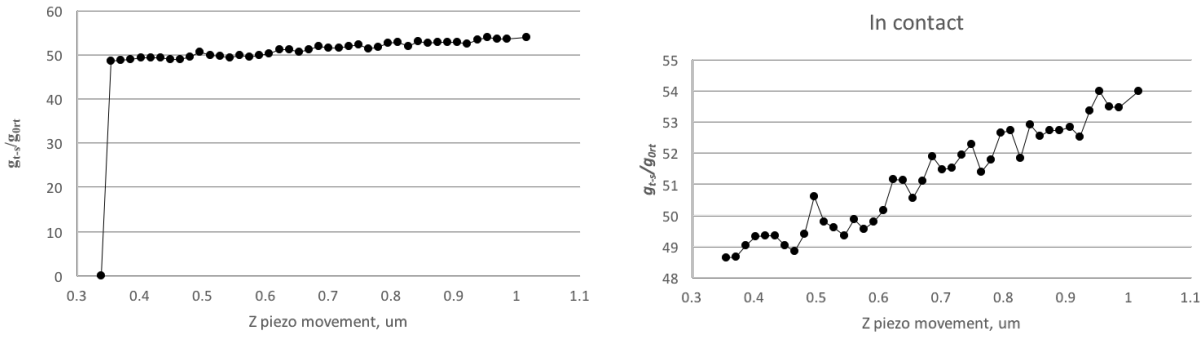

Figure 165 Last approaching the heated sample surface

In the last approach the thermal conductance value increased to 47.77 ± 0.75. There is no evidence of multi-asperity contact happening in the last approach with no obvious jumps when probe is in contact. The noise happening due to mechanical vibration is still present with value of $0.75g_{0.}$

The bare Silicon nitride probe after the measurements is shown in Figure 166. Some contamination occurred during the measurements compared to Figure 162.

Based on the SEM images of the probe taken after the measurements there is no obvious tip blunting, however, tip has more contamination compared to the SEM image before thermal scan. (Figure 162). However, the contaminated area is further away from tip so wouldn't affect tip-sample thermal conductance.

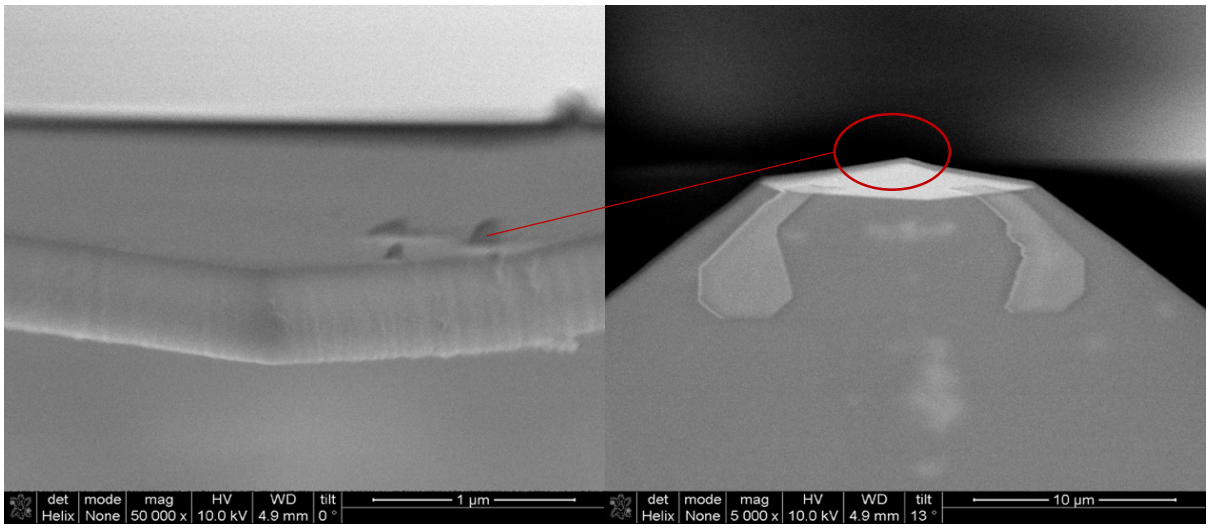

Figure 166 KNT probe with no metal after the measurements

When plotting the initial thermal signal with pull – off force it can be seen that there is some correlation. (Figure 167)

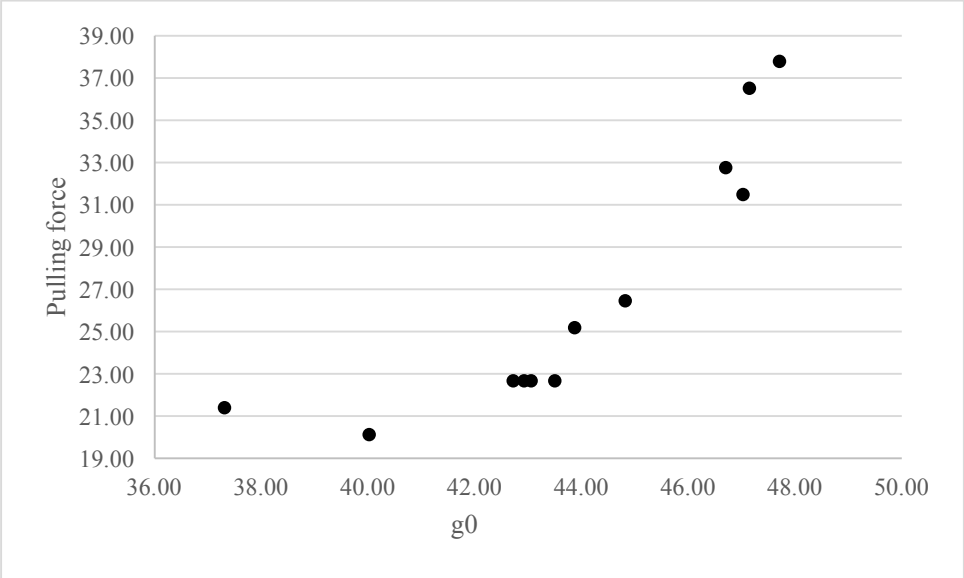

Figure 167 Correlation of thermal signal with force

After first approach some jumps occurred when tip was in contact. The in contact area was stabilized with increasing the pressure as can be seen from Figure 167 that there is a correlation of thermal signal with pull off force.

5.3 Error analysis

Four probes with different material contrast and geometry were chosen for the measurements. Two commercial silicon probes were examined as proxies for the “doped silicon” style thermal microscope probes and two silicon nitride commercial KNT probes, one with metal and one bare silicon nitride.

When analysing the data for all probes is important to take into account 3 types of errors. The first is the measurement limit which already discussed in the measurements set up part. Thus any change in the 3ω signal higher then $0.36 \pm 0.16 g_0$ is real characteristic of the nature of the contact.

The thermal gradient across the membrane changed, but signal didn’t depend from gradient when the heated point moved from the centre as was suggested by modelling. (

4.1 Passive device modelling) Thus the centring error wasn't taken into account.

Another type of error is the reproducibility of contact, which consists of systematic changes with time and random contact to contact variation. This leads to an "error" in SThM measurement which is characteristic of the probe itself and is the thing which is being measured here.

To analyze reproducibility of contact the very first contacts for all new probes were considered. Reproducibility of contact in terms of contact-to-contact variation which can be considered as an intrinsic random error in the thermal contact is shown in Figure 168. The average thermal conductance value for the FESP probe was $431.94 \pm 33.03\, g_0$ and for the Olympus probe *219.10*$\pm$*42.14* g_0. Both were large but varied rapidly with contacting. The FESP started very sharp and blunted after first contact. Thus the value of first contact differs from all other contacts. As after blunting the tip reaches the maximum strength and doesn't break with next contact. The Olympus probe was used over 2 days. On the first day it was sharp and blunting, with small and slight change of the tip end due to blunting. On the second day the tip end was broken and making a contact with complicated geometry which caused the variation in contact with time. The differences in conduction for probes made of same materials might be due to the sharpness and random nature of the tip smashing of the FESP probe compared to Olympus probe. The thermal conduction of the KNT silicon nitride probe with metal is equal to $87.58 \pm 8.85 g_0$ and with no metal has value of $43.89 \pm 3.09\ g_0$. The stable KNT probe tip contact had smooth change with time and increasing the pressure. However, during the measurements a detached metal flake was making a contact, which can be seen from the plot and very clear from SEM image (Figure 161). The KNT probe with no metal made the most stable contact. The random errors in terms of contact-to contact variation are 8% for FESP probe, 19% for Olympus probe, 10% for KNT probe with metal and 7% for KNT probe with no metal.

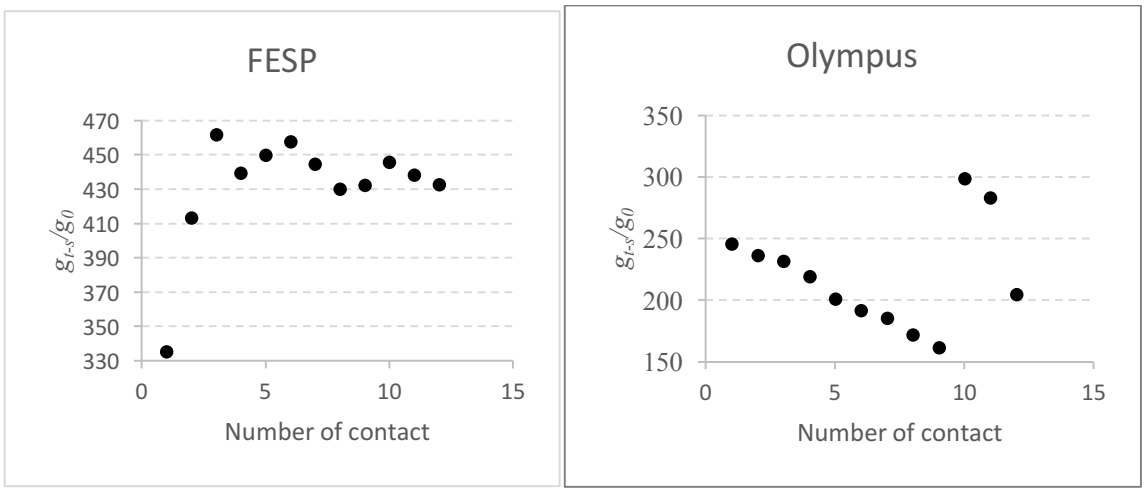

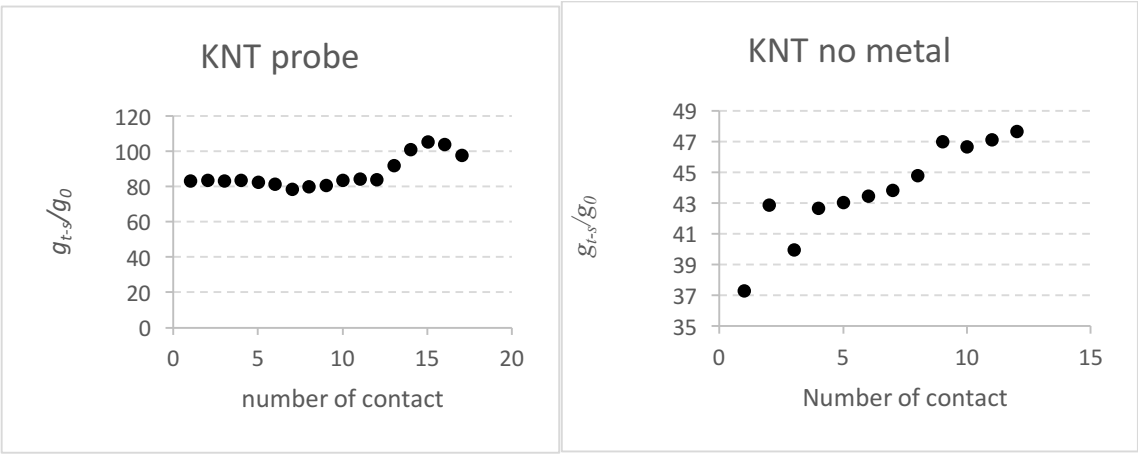

Figure 168 Tip -sample contact –to – contact variation

From the plots above it can be seen that the thermal conductance value changes with time systematically. So when plotting the value sample-tip thermal conductance value there is an obvious linear change with time for the KNT probe with no metal. (Figure 169).

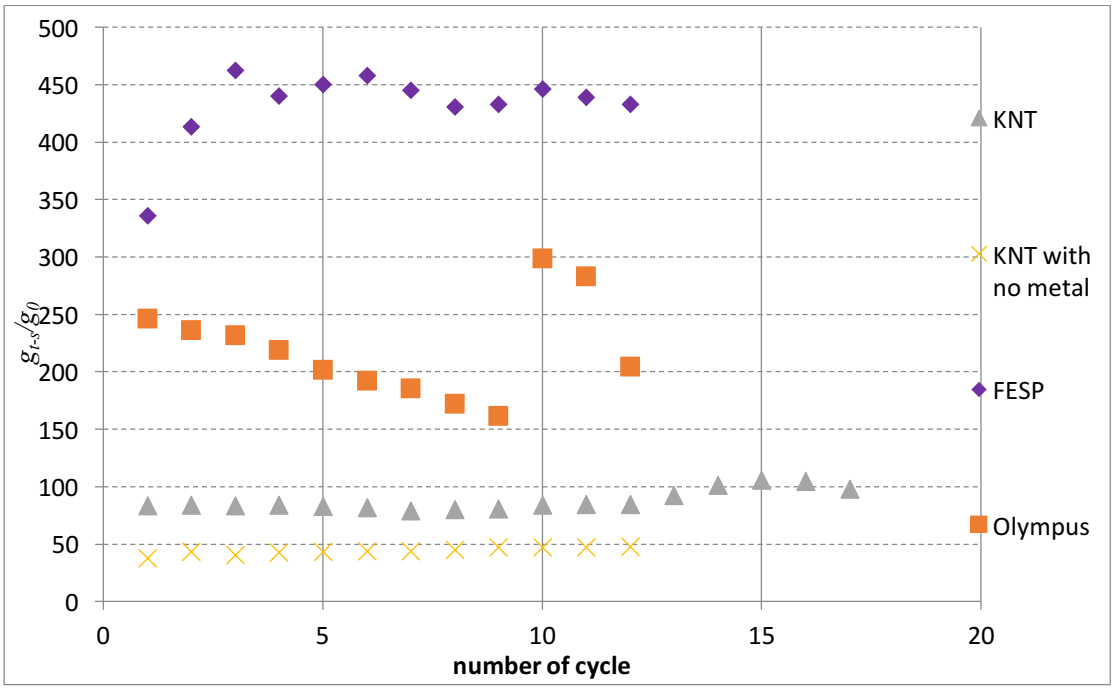

Figure 169 Change in contact with time

The thermal conductivity value for Si is higher than Silicon nitride however lower than thin platinum film. The reason that the thermal conduction between the KNT probe with the sample is still not higher than for Si probes might be due to the small contact area of the platinum flake or the poor thermal conduction from the platinum film to the silicon nitride cantilever. The role of Si tip blunting can be seen from the plot as the conductance value decreases with the number of tip-sample contact as the tip.

After all measurements done by four different probes it can be concluded that the sharp Si probes are attractive to use however, due to its sharpness it tends blunt from very first contact and analysing the data without taking SEM image after each approach would be difficult which

will cause additional complications when using vacuum system. On the hand, the measurements performed with FESP probe shown that after first contact the tip blunted and reached its maximum strength. Thus designing and fabrication of a silicon probe with a smooth blunt tip like a sphere would be a possible solution. Measurements accomplished with commercially available commonly used KNT probe didn't have obvious problem of tip blunting. However, the self aligned metal on the tip was peeled off during the measurements thus using the probe which didn't use self –alignment would be an option.

6. Summary and future work

The main advantage of SThM over other thermal measurement techniques is that it can measure heat transport at the nanoscale. As well as temperature measurements, determination of the thermal properties such as thermal conductivity and thermal conductance are possible with the technique. This is of extreme importance since thermal effects are a key limitation in modern devices and systems and the materials used in modern devices are unavailable as bulk samples. In order to make such measurements the SThM system needs to be developed into a quantitative measurement technique in both active and passive SThM modes. By far the most important problem in using the SThM in this way is the lack of reproducibility of the contact between the sample surface and probe tip. This is the subject of this work.

The goals of the thesis were

- To quantify the variation in tip-sample thermal contact with a sensitivity of better than one thermal conductance quantum.
- To investigate the physical sources of the variation in tip-sample thermal conduction with a view to informing the design of future SThM probes
- To develop a set of microfabricated calibration artefacts for active-mode SThM to eliminate the need for the use of a range of bulk materials as standards of thermal conduction

In order to achieve the necessary precision of measurement a number of nanofabricated devices were fabricated to allow the measurement of the extremely small (a few thermal conductance quanta) conduction between the apex of the SThM tip and the sample. Due to the extreme sensitivity of the devices (which is necessary given their purpose) the development of suitable electrical testing procedures for device calibration was a significant achievement. The SThM was used under high vacuum conditions (10^{-6} mbar) to simplify the heat path between the probe and the sample, since thermal conduction through the air or through the water meniscus between probe and sample is a complicating factor which may easily be avoided.

The importance of measuring the tip-sample conduction is that it permits quantification of the main source of variability in the results obtained using SThM.

Based on the results and data presented in chapters of this thesis, the following summary and conclusions can be made:

1) After all measurements were done using four different probes it can be concluded that the sharp Si SThM tips, modelled in this case by standard FESP and Olympus AFM probes, suffer from extreme changes in geometry in use. Due to their sharpness and brittleness they tend to blunt from the very first contact. The blunting of the probes

occurs by a brittle fracture, leading to a complex tip shape. Interpreting the data without taking an SEM image after each approach would be difficult, but such measurements would represent an unreasonable complication of the technique, even when using a vacuum system. On the hand, the measurements performed with FESP probe show that after the first contact the tip blunted and reached its maximum strength: The process of tip modification appears to be self-limiting. Thus the design and fabrication of a silicon probe with a smooth blunt tip like a sphere with a radius of a few hundred nanometres would be a possible solution to the variability of tip-sample contact using silicon probes.

2) The commercial SiNx SThM probe (named as KNT-SThM-01a) is not ideal as by the end of the scan it was found that sensor metal part-peeled off the tip, detaching as a metal flake. As well as changing the sensor calibration the changes in the shape and composition of the tip cause significant variation in contact. The contact which was made for devices such as the clean silicon dioxide membrane with wider supported arms and the device with 4 narrow supported arms fully covered with gold show a case of multi-asperity contact for these devices. This led to big variation in the values of tip-sample conduction obtained with the same sample and tip. Some values of initial contact conduction correspond to contact of silicon nitride to the device and some to a chunk of metal to the membrane. Such defects led to multi-asperity contact which was difficult to quantify even in this ideal system due to a lot of scatter. This is a known problem with SThM. In contrast, the same type of probe without metallization proved to give a stable contact with no significant change in geometry during scanning. Accordingly it is proposed that a change in the fabrication of SThM probes such that the sensor metal is defined to be some distance from the end of the tip (i.e. without the use of self-alignment) should result in a much more stable and quantifiable probe.

Future work

From the set of data measured, it can be seen that samples modelled and fabricated for calibration purposes might be used to quantify tip-sample conductance value. Further work to develop the materials used will be necessary to reduce scatter and improve the range of accessible values of conduction. The accuracy and reproducibility of such a calibration will still be limited by the instability of the SThM tips themselves.

For active mode measurements several improvements in future will be essential. The shape of the sample is easily variable by lithography and future samples may be developed which are designed around the specific microscope used. These can be made on the same wafer at the same time and with the same processes as other samples and will allow for differences in scan size, coarse positioning and optical microscope resolution of specific instruments. Thus, in future it will be possible to vary a square of covered metal for all devices within the membrane. Also instead of using an evaporation technique to deposit metal, another technique such an ALD would be an option, eliminating grain roughness of evaporated metal films.

To improve passive SThM mode measurement with fabricated sample several changes might be made.

One possibility is on getting more controlled materials and shapes at the end of probes.

Another option will be adding new materials to the end of bare silicon nitride KNT probe such as CNT, [168]or ALD to avoid metal flaking off. Additionally, instead of using self-aligned sensor definition on the KNT probe, it would be better to use a sensor aligned back from the tip of the cantilever.

As suggested earlier, using a Si tip with rounded end as a sphere will be better to avoid the problem of uncontrolled tip blunting

In future for these type of measurements, it would be better to do real-time observation of the shape and size of the tip, and of the sample surface during the thermal measurements and scan by using combined scanning thermal microscopy and scanning electron microscopy equipment (SThM-SEM). [27]

[27] QUANTIHEAT European project, CNRS_Centre d'Energétique et de Thermique de Lyon

Bibliography

[1] U. Grigull, “Fahrenheit, a Pioneer of Exact Thermometry,” *Proceedings Of The Workshop On The Second Law of Thermodynamics*, vol. 1. pp. 11–13, 1966.

[2] H. Struchtrup, *Thermodynamics and Energy Relations*, vol. 38, no. C. 1988.

[3] J. Holman, *Heat Transfer*. 2010.

[4] A. Majumdar, “Microscale Heat Conduction in Dielectric Thin Films,” *J. Heat Transfer*, vol. 115, no. 1, p. 7, 1993.

[5] J. Fourier, “The Analytical Theory of Heat,” *Cambridge Univ. Press*, pp. 1–489, 1878.

[6] a. a. Joshi and a. Majumdar, “Transient ballistic and diffusive phonon heat transport in thin films,” *J. Appl. Phys.*, vol. 74, no. 1993, pp. 31–39, 1993.

[7] E. T. Swartz and R. O. Pohl, “Thermal boundary resistance,” *Rev. Mod. Phys.*, vol. 61, no. 3, pp. 605–668, 1989.

[8] G. Electrostatic, K. Schwab, E. A. Henriksen, J. M. Worlock, and M. L. Roukes, “Measurement of the quantum of thermal conductance,” *Nat. Mater.*, vol. 1275, no. 1997, pp. 1997–2000, 2000.

[9] B. Gotsmann and M. a. Lantz, “Quantized thermal transport across contacts of rough surfaces,” *Nat. Mater.*, vol. 12, no. 1, pp. 59–65, 2012.

[10] Aritra Banerjee, Sudipta Pal1, E Rozenbergand B K Chaudhuri1, “Adiabatic and non-adiabatic small-polaron hopping conduction in La1−xPbxMnO3+δ ($0.0 \leq x \leq 0.5$)-type oxides above the metal–semiconductor transition,” *J. Phys. Condens. Matter*, vol. 13, Feb. 2001.

[11] D. G. Cahill, “Analysis of heat flow in layered structures for time-domain thermoreflectance,” *J. Appl. Phys.*, vol. 31, no. 74, 1993.

[12] D. G. Cahill, “Thermal conductivity measurement from 30 to 750 K: The 3omega method,” *Rev. Sci. Instrum.*, vol. 61, no. 2, pp. 802–808, 1990.

[13] Y. Q. Liu, D. Tainoff, M. Boukhari, J. Richard, a Barski, P. Bayle-Guillemaud, E. Hadji, and O. Bourgeois, “Sensitive 3-omega measurements on epitaxial thermoelectric thin films,” *IOP Conf. Ser. Mater. Sci. Eng.*, vol. 68, p. 12005, 2014.

[14] S. Karg, P. Mensch, B. Gotsmann, and H. Schmid, “Measurement of Thermoelectric Properties of Single Semiconductor Nanowires,” vol. 42, no. 7, pp. 2409–2414, 2013.

[15] D. Li, S. T. Huxtable, and A. R. Abramson, “Thermal Transport in Nanostructured Solid-State Cooling Devices,” vol. 127, no. January 2005, 2017.

[16] E. Lemaire, T. P. Nguyen, A. Bontempi, L. Thiery, D. Teyssieux, P. Vairac, H. Shea, and D. Briand, “Micromachined calibration chip with heat source and temperature sensors for

Scanning Thermal Metrology (SThM)," *Procedia Eng.*, vol. 120, pp. 130–133, 2015.

[17] A. Majumdar, "Scanning Thermal microscopy," *Annu. Rev. Mater. Sci.*, vol. 25, pp. 505–585, 1999.

[18] B. Bonello, B. Perrin, and C. Rossignol, "Photothermal properties of bulk and layered materials by the picosecond acoustics technique," *J. Appl. Phys.*, vol. 83, no. 6, 1998.

[19] D. G. Cahill, "Analysis of heat flow in layered structures for time-domain thermoreflectance," *Rev. Sci. Instrum.*, vol. 75, no. 12, pp. 5119–5122, 2004.

[20] J.-C. Z. Zheng, X, D.G. Cahill, P. Krasnochtchekov, R.S. Averback, "High-throughput thermal conductivity measurements of nickel solid solutions and the applicability of the Wiedemann – Franz law," *Acta Mater.*, vol. 55, pp. 5177–5185, 2007.

[21] L. W. Christian Monachon, "Thermal boundary conductance of transition metals on diamond," *Acta Mater.*, vol. 55, pp. 5177–5185, 2007.

[22] D. G. Cahill, P. V Braun, G. Chen, D. R. Clarke, S. Fan, K. E. Goodson, P. Keblinski, W. P. King, G. D. Mahan, A. Majumdar, H. J. Maris, S. R. Phillpot, E. Pop, and L. Shi, "Nanoscale thermal transport . II . 2003 – 2012," *Rev. Sci. Instrum.*, vol. 80, 2009.

[23] A. J. Schmidt, R. Cheaito, and M. Chiesa, "A frequency-domain thermoreflectance method for the characterization of thermal properties," *Rev. Sci. Instrum.*, vol. 80, pp. 3–8, 2009.

[24] J. R. K. Marland, C. Dunare, A. Tsiamis, E. González-Fernandez, E. O. Blair, S. Smith, J. G. Terry, A. F. Murray, and A. J. Walton, "Test structures for optimizing polymer electrolyte performance in a microfabricated electrochemical oxygen sensor," *IEEE Int. Conf. Microelectron. Test Struct.*, 2017.

[25] P. Reviews, "Opportunities of CMOS-MEMS integration through LSI foundry and open facility," *Jpn. J. Appl. Phys.*, vol. 56, 2017.

[26] P. S. Dobson, G. Mills, and J. M. R. Weaver, "Microfabricated temperature standard based on Johnson noise measurement for the calibration of micro- and nano-thermometers," *Rev. Sci. Instrum.*, vol. 76, no. 5, 2005.

[27] M. Denoual, M. Pouliquen, and D. Robbes, "Microfabricated test structures for thermal gas sensor," *IEEE*, pp. 28–31, 2016.

[28] L. Lu, W. Yi, and D. Zhang, "3Ω Method for Specific Heat and Thermal Conductivity Measurements," *Rev. Sci. Instrum.*, vol. 72, pp. 2996–3003, 2001.

[29] L. Shi and A. Majumdar, "Thermal Transport Mechanisms at Nanoscale Point Contacts," *J. Heat Transfer*, vol. 124, no. April, p. 329, 2002.

[30] N. Sabaté, J. Santander, I. Gràcia, L. Fonseca, E. Figueras, E. Cabruja, and C. Cané, "Characterization of thermal conductivity in thin film multilayered membranes," *Thin*

Solid Films, vol. 484, no. 1–2, pp. 328–333, 2005.

[31] J. Tersoff and D. Hamann, "Theory and application for the scanning tunneling microscope," *Phys. Rev. Lett.*, vol. 50, no. 25, p. 1998, 1983.

[32] G. Binnig, H. Rohrer, C. Gerber, and E. Weibel, "Surface studies by scanning tunneling microscopy," *Phys. Rev. Lett.*, vol. 49, no. 1, pp. 57–61, 1982.

[33] G. Binnig and H. Rohrer, "Scanning tunneling microscopy," *Surf. Sci.*, vol. 126, no. 1–3, pp. 236–244, 1983.

[34] E. . S. D. Eigler, "Positioning single atom with scanning tunneling microscope," *Nature*, vol. 344, 1990.

[35] A. Majumdar, "Thermoelectricity in Molecular Junctions," *Science (80-.).*, vol. 315, no. March, pp. 1568–1571, 2004.

[36] L. E. C. van de Leemput and H. van Kempen, "Scanning Tunneling Microscopy," *Reports Prog. Phys.*, vol. 55, no. 8, pp. 1165–1240, 1992.

[37] G. Binnig, C. Quate, and C. Gerber, "Atomic Force Microscope," *Physical Review Letters*, vol. 56, no. 9. pp. 930–933, 1986.

[38] J. Otero and M. Puig-vidal, "Low-noise Instrumentation for," in *IEEE Instrumentation and Measurement technology conference*, 2008, pp. 9–13.

[39] Y. Martin C. C. Williams and H. K. Wickramasinghe, "Atomic force microscope-force mapping and profmng on a sub 100A scale," *J. Appl. Phys. 61, 4723 ; (7 pages)*, vol. 61, no. 1987, p. 4723, 1987.

[40] D. Baird and a Shew, "Probing the history of scanning tunneling microscopy," *Discov. Nanoscale*, pp. 145–156, 2004.

[41] J. M. R. Weaver, "High resolution atomic force microscopy potentiometry," *J. Vac. Sci. Technol. B Microelectron. Nanom. Struct.*, vol. 9, no. 3, p. 1559, 1991.

[42] Y. Martin and H. K. Wickramasinghe, "Magnetic imaging by ``force microscopy'' with 1000 [Å-ring] resolution," *Appl. Phys. Lett.*, vol. 50, no. 20, pp. 1455–1457, 1987.

[43] C. D. Bugg and P. J. King, "Scanning capacitance microscopy," *J. Phys. E*, vol. 21, no. 1985, p. 147, 1988.

[44] B. K. Chong, H. Zhou, G. Mills, L. Donaldson, and J. M. R. Weaver, "Scanning Hall probe microscopy on an atomic force microscope tip," *J. Vac. Sci. Technol. A Vacuum, Surfaces, Film.*, vol. 19, no. 4, p. 1769, 2001.

[45] H. K. Wickramasinghe, "Scannhlg thermal profile!," vol. 10598, no. September, pp. 1587–1589, 1986.

[46] M. Nonnenmacher and H. K. Wickramasinghe, "Scanning probe microscopy of thermal conductivity and subsurface properties," *Appl. Phys. Lett.*, vol. 61, no. 2, pp. 168–170,

1992.

[47] A. Hammiche and H. M. Pollock, “THERMAL CONDUCTIVITY IMAGING USING THE ATOMIC FORCE MICROSCOPE,” in *PROCEEDINGS OF THE TWENTY-EIGTH CONFERENCE OF THE NORTH AMERICAN THERMAL ANALYSIS SOCIETY*, 2000.

[48] A. Majumdar, J. Lai, M. Chandrachood, O. Nakabeppu, Y. Wu, and Z. Shi, “Thermal imaging by atomic force microscopy using thermocouple cantilever probes,” *Rev. Sci. Instrum.*, vol. 66, no. 6, pp. 3584–3592, 1995.

[49] T. Leinhos, M. Stopka, and E. Oesterschulze, “Micromachined fabrication of Si cantilevers with Schottky diodes integrated in the tip,” *Appl. Phys. A Mater. Sci. Process.*, vol. 66, no. SUPPL. 1, pp. 65–69, 1998.

[50] A. I. Buzin, P. Kamasa, M. Pyda, and B. Wunderlich, “Application of a Wollaston wire probe for quantitative thermal analysis,” *Thermochim. Acta*, vol. 381, no. 1, pp. 9–18, 2002.

[51] G. B. M. Fiege, A. Altes, R. Heiderhoff, and L. J. Balk, “Quantitative thermal conductivity measurements with nanometre resolution,” *J.Phys.D:Appl.Phys.*, vol. 32, pp. 13–17, 1999.

[52] W. P. King, B. Bhatia, J. R. Felts, H. J. Kim, B. Kwon, B. Lee, S. Somnath, and M. Rosenberger, “Heated Atomic Force Microscope Cantilevers and Their Applications,” *Annu. Rev. Heat Transf.*, vol. 16, no. 1, pp. 287–326, 2013.

[53] J. Lee, T. Beechem, T. Wright, B. Nelson, S. Graham, and W. King, “Electrical, Thermal, and Mechanical Characterization of Silicon Microcantilever Heaters,” *J. Microelectromechanical Syst.*, vol. 15, no. 6, pp. 1644–1655, 2006.

[54] B. W. Chui, T. D. Stowe, T. W. Kenny, H. J. Mamin, B. D. Terris, and D. Rugar, “Low-stiffness silicon cantilevers for thermal writing and piezoresistive readback with the atomic force microscope,” *Appl. Phys. Lett.*, vol. 69, no. 18, pp. 2767–2769, 1996.

[55] S. Sadat, A. Tan, Y. J. Chua, and P. Reddy, “Nanoscale thermometry using point contact thermocouples,” *Nano Lett.*, vol. 10, no. 7, pp. 2613–2617, 2010.

[56] W. H. Weaver JMR, Walpita LM, “Optical absortion microscopy and spectroscopy with nanometre resolution,” *Lett. to Nat.*, vol. 342, 1989.

[57] A. Majumdar, J. P. Carrejo, and J. Lai, “Thermal imaging using the atomic force microscope,” *Appl. Phys. Lett.*, vol. 62, no. 20, pp. 2501–2503, 1993.

[58] H. Zhou, “Generic scanned-probe microscope sensors by combined micromachining and electron-beam lithography,” *J. Vac. Sci. Technol. B Microelectron. Nanom. Struct.*, vol. 16, no. 1, p. 54, 1998.

[59] A. Buck, B. K. Jones, and H. M. Pollock, “Temperature and thermal conductivity modes

of scanning probe microscopy for electromigration studies," *Microelectron. Reliab.*, vol. 37, no. 10–11, pp. 1495–1498, 1997.

[60] G. Hwang, J. Chung, O. Kwon, G. Hwang, J. Chung, and O. Kwon, "Enabling low-noise null-point scanning thermal microscopy by the optimization of scanning thermal microscope probe through a rigorous theory of quantitative measurement," *Rev. Sci. Instrum.*, vol. 85, 2014.

[61] G. Mills, H. Zhou, a. Midha, L. Donaldson, and J. M. R. Weaver, "Scanning thermal microscopy using batch fabricated thermocouple probes," *Appl. Phys. Lett.*, vol. 72, no. 22, pp. 2900–2902, 1998.

[62] G. Binnig, M. Despont, U. Drechsler, W. Häberle, M. Lutwyche, P. Vettiger, H. J. Mamin, B. W. Chui, and T. W. Kenny, "Ultrahigh-density atomic force microscopy data storage with erase capability," *Appl. Phys. Lett.*, vol. 74, no. 9, p. 1329, 1999.

[63] B. P. Ng, Y. Zhang, S. Wei Kok, and Y. Chai Soh, "Improve performance of scanning probe microscopy by balancing tuning fork prongs," *Ultramicroscopy*, vol. 109, no. 4, pp. 291–295, 2009.

[64] H. M. Pollock and A. Hammiche, "Micro-thermal analysis: Techniques and applications," *J. Phys. D. Appl. Phys.*, vol. 34, no. 9, pp. 23–53, 2001.

[65] "The Fabrication of Ultrafine Platinum Wire," *Platin. Met. Rev.*, vol. 30, no. 1, p. 1986, 1986.

[66] A. Kittel, W. Müller-Hirsch, J. Parisi, S. A. Biehs, D. Reddig, and M. Holthaus, "Near-field heat transfer in a scanning thermal microscope," *Phys. Rev. Lett.*, vol. 95, no. 22, pp. 1–4, 2005.

[67] A. Hammiche, H. M. Pollock, M. Song, and D. J. Hourston, "Sub-surface imaging by scanning thermal microscopy," *Meas. Sci. Tech.*, vol. 7, no. 2, pp. 142–150, 1996.

[68] R. Pylkki, P. Moyer, and P. West, "Scanning near-field optical microscopy and scanning thermal microscopy," *Japanese J. Appl. ...*, vol. 3785, pp. 895–899, 1994.

[69] H M Pollock and A Hammiche, "Micro-thermal analysis : techniques and," *J. Phys. D. Appl. Phys.*, 2001.

[70] P. S. Dobson, J. M. R. Weaver, and G. Mills, "New methods for calibrated Scanning Thermal Microscopy (SThM)," *Proc. IEEE Sensors*, pp. 708–711, 2007.

[71] Y. Ge, Y. Zhang, J. A. Booth, J. M. R. Weaver, and P. S. Dobson, "Quantification of probe–sample interactions of a scanning thermal microscope using a nanofabricated calibration sample having programmable size," *Nanotechnology*, vol. 27, no. 32, p. 325503, 2016.

[72] J. . (2011) Zhang , Y ., Dobson , P . , and Weaver, "Batch fabricated dual cantilever

resistive probe for scanning thermal," *Microelectron. Eng.*, vol. 88, no. September, pp. 2435–2438, 2012.

[73] Y. Zhang, P. S. Dobson, and J. M. R. Weaver, "High temperature imaging using a thermally compensated cantilever resistive probe for scanning thermal microscopy," *J. Vac. Sci. Technol. B Microelectron. Nanom. Struct.*, vol. 30, no. 1, p. 10601, 2012.

[74] B. Samson and L. Aigouy, "Recent improvements on micro-thermocouple based SThM," *J. Phys. Conf. Ser.*, vol. 755, p. 11001, 2016.

[75] E. Farshidi and A. V. Wheatstone, "A Low-Voltage Current-Mode Wheatstone Bridge using CMOS Transistors," *Int. J. Electr. Electron. Eng.*, vol. 8313, pp. 767–771, 2011.

[76] L. Ramiandrisoa, A. Allard, Y. Joumani, B. Hay, and S. Gomés, "A dark mode in scanning thermal microscopy," *Rev. Sci. Instrum.*, vol. 88, no. 12, 2017.

[77] A. Assy, S. Lefèvre, P.-O. Chapuis, and S. Gomès, "Analysis of heat transfer in the water meniscus at the tip-sample contact in scanning thermal microscopy," *J. Phys. D. Appl. Phys.*, vol. 47, no. 44, p. 442001, 2014.

[78] F. Menges, H. Riel, A. Stemmer, and B. Gotsmann, "Quantitative thermometry of nanoscale hot spots," *Nano Lett.*, vol. 12, no. 2, pp. 596–601, 2012.

[79] S. G. Assy, Ali, "Heat transfer at nanoscale contacts investigated with scanning thermal microscopy," *J. Appl. Phys.*, vol. 107, no. 43105, 2015.

[80] P.-O. Chapuis, E. Rousseau, A. Assy, S. Gomès, S. Lefèvre, and S. Volz, "Heat transfer between a hot AFM tip and a cold sample: impact of the air pressure," *MRS Proc.*, vol. 1543, pp. 159–164, 2013.

[81] S. Gomès, A. Assy, and P. O. Chapuis, "Scanning thermal microscopy: A review," *Phys. Status Solidi Appl. Mater. Sci.*, vol. 212, no. 3, pp. 477–494, 2015.

[82] A. Hammiche, "Scanning thermal microscopy: Subsurface imaging, thermal mapping of polymer blends, and localized calorimetry," *J. Vac. Sci. Technol. B Microelectron. Nanom. Struct.*, vol. 14, no. 2, p. 1486, 1996.

[83] Z. Dai, E. a Corbin, and W. P. King, "With Improved Thermal Resistance for Nanotopography Measurements," *IEEE Int. Conf. Microelectron. Test Struct.*, pp. 460–463, 2010.

[84] E. Brown, L. Hao, D. C. Cox, and J. C. Gallop, "Scanning thermal microscopy probe capable of simultaneous electrical imaging and the addition of a diamond tip," *J. Phys. Conf. Ser.*, vol. 100, no. PART 5, 2008.

[85] R. Aubry, J. C. Jacquet, J. Weaver, O. Durand, P. Dobson, G. Mills, M. A. di Forte-Poisson, S. Cassette, and S. L. Delage, "SThM temperature mapping and nonlinear thermal resistance evolution with bias on AlGaN/GaN HEMT devices," *IEEE Trans.*

Electron Devices, vol. 54, no. 3, pp. 385–390, 2007.

[86] G. Wielgoszewski, M. Babij, R. F. Szeloch, and T. Gotszalk, "Standard-based direct calibration method for scanning thermal microscopy nanoprobes," *Sensors Actuators, A Phys.*, vol. 214, pp. 1–6, 2014.

[87] D. I. Florescu, L. G. Mourokh, F. H. Pollak, D. C. Look, G. Cantwell, and X. Li, "High spatial resolution thermal conductivity of bulk ZnO (0001)," *J. Appl. Phys.*, vol. 91, no. 2, pp. 890–892, 2002.

[88] S. Grauby and J. Rampnoux, "Fabrication of Bi 2 Te 3 nanowire arrays and thermal conductivity measurement by 3 omega-scanning thermal microscopy," *J. Appl. Phys.*, vol. 54308, no. 113, 2013.

[89] G. B. M. Fiege, A. Altes, R. Heiderhoff, and L. J. Balk, "Quantitative thermal conductivity measurements with nanometre resolution," *J. Phys. D. Appl. Phys.*, vol. 32, no. 5, 1999.

[90] A. Assy and S. Gomès, "Heat transfer at nanoscale contacts investigated with scanning thermal microscopy Heat transfer at nanoscale contacts investigated with scanning thermal microscopy," *Appl. Phys. Lett.*, vol. 107, no. 2015, p. 43105, 2015.

[91] B. Cretin, "Scanning Thermal Microscopy," *Europhys. News*, vol. 28, no. 1, pp. 29–29, 1997.

[92] M. Pumarol, M. C. Rosamond, P. D. Tovee, M. C. Petty, D. A. Zeze, V. I. Falko, and O. V Kolosov, "Direct nanoscale imaging of ballistic and diffusive thermal transport in graphene nanostructures Direct nanoscale imaging of ballistic and diffusive thermal transport in graphene nanostructures," *Metrologia*, vol. 52, 2015.

[93] A. F. Robertson and D. Gross, "An Electrical-Analog Method for Transient Heat-Flow Analysis," *J. Res. Natl. Bur. Stand. (1934).*, vol. 61, no. 2, pp. 105–115, 1958.

[94] A. Assy and S. Gomès, "Heat transfer at nanoscale contacts investigated with scanning thermal microscopy Heat transfer at nanoscale contacts investigated with scanning thermal microscopy," *Appl. Phys. Lett.*, vol. 107, p. 43105, 2015.

[95] J.-O. Carlsson and U. Jansson, "Progress in chemical vapor deposition," *Prog. Solid State Chem.*, vol. 22, no. 4, pp. 237–292, 1993.

[96] A. Stoffel, A. Kov??cs, W. Kronast, and B. M??ller, "LPCVD against PECVD for micromechanical applications," *J. Micromechanics Microengineering*, vol. 6, no. 1, pp. 1–13, 1996.

[97] S.M. Sze, *VLSI Techology*. 1988.

[98] B. E. Deal and a. S. Grove, "General relationship for the thermal oxidation of silicon," *J. Appl. Phys.*, vol. 36, no. 12, pp. 3770–3778, 1965.

[99] H. Z. Massoud, “Thermal Oxidation of Silicon in Dry Oxygen: Growth-Rate Enhancement in the Thin Regime,” *J. Electrochem. Soc.*, vol. 132, no. 11, p. 2693, 1985.

[100] E. P. Eernisse, “Stress in thermal SiO2 during growth,” *Appl. Phys. Lett.*, vol. 35, no. 8, pp. 6–9, 1979.

[101] a Stoffel, a Kovács, W. Kronast, and B. Müller, “LPCVD against PECVD for micromechanical applications,” *J. Micromechanics Microengineering*, vol. 6, no. 1, pp. 1–13, 1999.

[102] S. S. N. Diaphragms, J. Yang, J. Gaspar, and O. Paul, “Fracture Properties of LPCVD Silicon Nitride and Thermally Grown Silicon Oxide Thin Films From the Load-Deflection of Long Si 3 N 4,” *J. MICROELECTROMECHANICAL Syst.*, vol. 17, no. 5, pp. 1120–1134, 2008.

[103] L.F. Thompson, “A n Introduction to L i t h o g r a p h y,” *Am. Chem. Soc.*, 1983.

[104] J. T. M. Stevenson and a M. Gundlach, “The application of photolithography to the fabrication of microcircuits,” *J. Phys. E.*, vol. 19, pp. 654–667, 2000.

[105] B. S. Rao and U. Hashim, “Pattern transfer of 1μm sized microgap and microbridge electrode for application in biomedical nano-diagnostics,” *Adv. Mater. Res.*, vol. 925, pp. 533–537, 2014.

[106] S. Thoms and D. S. Macintyre, “Linewidth metrology for sub-10-nm lithography,” *J. Vac. Sci. Technol. B Microelectron. Nanom. Struct.*, vol. 28, no. 6, p. C6H6, 2010.

[107] A. A. Tseng, K. Chen, C. D. Chen, and K. J. Ma, “Electron beam lithography in nanoscale fabrication: Recent development,” *IEEE Trans. Electron. Packag. Manuf.*, vol. 26, no. 2, pp. 141–149, 2003.

[108] C. G. Chen, P. T. Konkola, J. Ferrera, R. K. Heilmann, and M. L. Schattenburg, “Analyses of vector Gaussian beam propagation and the validity of paraxial and spherical approximations.,” *J. Opt. Soc. Am. A. Opt. Image Sci. Vis.*, vol. 19, no. 2, pp. 404–412, 2002.

[109] S. P. Steven S Henning, “CAD system interface for a stand-alone ebeam tester,” *Micro Nano Eng. Conf. 1996 (MNE 96)*, vol. 7, pp. 317–325, 1987.

[110] C. Vieu, F. Carcenac, A. Pepin, Y. Chen, M. Mejias, A. Lebib, L. Manin-Ferlazzo, L. Couraud, and H. Launois, “Electron beam lithography - Resolution limits and applications,” *Appl. Surf. Sci.*, vol. 164, pp. 111–117, 2000.

[111] F. Yaghmaie, J. Fleck, A. Gusman, and R. Prohaska, “Improvement of PMMA electron-beam lithography performance in metal liftoff through a poly-imide bi-layer system,” *Microelectron. Eng.*, vol. 87, no. 12, pp. 2629–2632, 2010.

[112] Q. Wang, Y. F. Chen, S. B. Long, J. B. Niu, C. S. Wang, R. Jia, B. Q. Chen, M. Liu, and

T. C. Ye, “Fabrication and characterization of single electron transistor on SOI,” *Microelectron. Eng.*, vol. 84, no. 5–8, pp. 1647–1651, 2007.

[113] H. Namatsu, T. Yamaguchi, M. Nagase, K. Yamazaki, and K. Kurihara, “Nano-patterning of a hydrogen silsesquioxane resist with reduced linewidth fluctuations,” *Microelectron. Eng.*, vol. 41–42, pp. 331–334, 1998.

[114] P. K. Dey, B. Pramanick, A. Ravi Shankar, P. Ganguly, and S. Das, “Microstructuring of su-8 resist for mems and bio-applications,” *Int. J. Smart Sens. Intell. Syst.*, vol. 3, no. 1, pp. 118–129, 2010.

[115] D. Tu, M. Liu, L. Shang, C. Xie, and X. Zhu, “A ZEP520-LOR bilayer resist lift-off process by E-beam lithography for nanometer pattern transfer,” *2007 7th IEEE Int. Conf. Nanotechnol. - IEEE-NANO 2007, Proc.*, no. c, pp. 624–627, 2007.

[116] J. M. Rocque, C. J. Brooks, R. W. Henry, D. E. Benoit, and P. J. S. Mangat, “UVIII-positive chemically amplified resist optimization,” in *23rd Annual International Symposium on Microlithography*, 1998, no. June 1998, p. 487.

[117] J. M. Rocque, C. J. Brooks, R. W. Henry, D. E. Benoit, and P. J. S. Mangat, “UVIII-positive chemically amplified resist optimization,” in *PROCEEDINGS OF SPIE*, 1998, no. June 1998, p. 487.

[118] Y. Chen, D. Macintyre, and S. Thoms, “Electron beam lithography process for T- and Γ-shaped gate fabrication using chemically amplified DUV resists and PMMA,” *J. Vac. Sci. Technol. B Microelectron. Nanom. Struct.*, vol. 17, no. 6, p. 2507, 1999.

[119] J. Golden, H. Miller, D. Nawrocki, and J. Ross, “Optimization of Bi-layer Lift-Off Resist Process,” *Transition*, no. 617, 2009.

[120] S. Thoms and D. S. Macintyre, “Investigation of CSAR 62, a new resist for electron beam lithography,” *J. Vac. Sci. Technol. B, Nanotechnol. Microelectron. Mater. Process. Meas. Phenom.*, vol. 32, no. 6, p. 06FJ01, 2014.

[121] J. O’Brien, P. J. Hughes, M. Brunet, B. O’Neill, J. Alderman, B. Lane, A. O’Riordan, and C. O’Driscoll, “Advanced photoresist technologies for microsystems,” *J. Micromechanics Microengineering*, vol. 11, no. 4, pp. 353–358, 2001.

[122] M. Qi, E. Lidorikis, P. T. Rakich, S. G. Johnson, J. D. Joannopoulos, E. P. Ippen, and H. I. Smith, “A three-dimensional optical photonic crystal with designed point defects,” *Nature*, vol. 429, no. 6991, pp. 538–542, 2004.

[123] S. Thoms, Y. Zhang, and J. M. R. Weaver, “Improved alignment algorithm for electron beam lithography,” *J. Vac. Sci. Technol. B*, vol. 32, no. 6, p. 06F509, 2014.

[124] J. Safarian and T. A. Engh, “Vacuum Evaporation of Pure Metals,” *Metall. Mater. Trans. A*, vol. 44, no. 2, pp. 747–753, 2013.

[125] J. Chlumská, V. Kolařík, S. Krátký, M. Matějka, M. Urbánek, and M. Horáček, “Lift-Off Technique Using Different E-Beam Writers,” *Nanocon*, vol. 10, no. 13, pp. 2–6, 2013.

[126] A.-P. Blanchard-Dionne and M. Meunier, “Electron beam lithography using a PMMA/P(MMA 8.5 MAA) bilayer for negative tone lift-off process,” *J. Vac. Sci. Technol. B, Nanotechnol. Microelectron. Mater. Process. Meas. Phenom.*, vol. 33, no. 6, p. 61602, 2015.

[127] P. Cardoso and J. P. Davim, “A BRIEF REVIEW ON MICROMACHINING OF MATERIALS,” *Rev. Adv. Mater. Sci.*, vol. 30, pp. 98–102, 2012.

[128] G. T. A. Kovacs, N. I. Maluf, and K. E. Petersen, “Bulk Micromachining of Silicon,” in *Micromachined Devices and Components*, 1998, vol. 86, no. 8.

[129] O. Powell and H. B. Harrison, “N e w shapes in (100) Si using KOH and EDP etches,” *J. Micromechanics Microengineering*, vol. 2, no. 75, pp. 1–6, 1992.

[130] M. Science-poland, “Study on etching anisotropy of Si (hkl) planes in solutions with different KOH and isopropyl alcohol concentrations,” *Sensors Actuators A*, vol. 29, no. 4, pp. 278–284, 2011.

[131] H. Seidel, “Anisotropic Etching of Crystalline Silicon in Alkaline Solutions,” *J. Electrochem. Soc.*, vol. 137, no. 11, p. 3626, 1990.

[132] P. Vasco and E. Herriko, “An improved anisotropic wet etching process for the fabrication of silicon MEMS structures using a single etching mask,” no. July 2017, 2008.

[133] O. Powell and H. B. Harrison, “Anisotropic etching of {100} and {100} planes in (100) silicon,” *J. Micromechanics Microengineering*, vol. 11, no. 100, pp. 217–220, 2001.

[134] M. Shikida, K. Sato, K. Tokoro, and D. Uchikawa, “Differences in anisotropic etching properties of KOH and TMAH solutions,” *Sensors Actuators, A Phys.*, vol. 80, no. 2, pp. 179–188, 2000.

[135] J. Albero, L. Nieradko, C. Gorecki, H. Ottevaere, H. Thienpont, J. Pietarinen, B. Päivänranta, and N. Passilly, “Fabrication of spherical microlenses by a combination of isotropic wet etching of silicon and molding techniques,” vol. 17, no. 8, pp. 6283–6292, 2009.

[136] N. Ahmad, J. Manaf, and K. H. Park, “Charactrerization of RObust Alignment Mark to Improve Alignment performance,” *Int. Electron. Manuf. Technol.*, pp. 518–523, 2006.

[137] P. M. Dunlap and S. R. Faris, “Surface Tension of Aqueous Solutions of Potassium Hydroxide,” *Nature*, vol. 196, pp. 1312–1313, 1962.

[138] “To the introduction to research in nanoscience and nanotechnology By Dr . Haiping Zhou Room 601 in Rankine building Plasma Processing,” 2014.

[139] A. Samarelli, L. Ferre Llin, S. Cecchi, J. Frigerio, T. Etzelstorfer, E. M??ller, Y. Zhang, J.

R. Watling, D. Chrastina, G. Isella, J. Stangl, J. P. Hague, J. M. R. Weaver, P. Dobson, and D. J. Paul, “The thermoelectric properties of Ge/SiGe modulation doped superlattices,” *J. Appl. Phys.*, vol. 113, no. 23, 2013.

[140] X. Zhu, D. W. Greve, and G. K. Fedder, “Characterization of Silicon Isotropic Etch by Inductively Coupled Plasma Etch in Post-CMOS Processing,” in *IEEE*, 2000, vol. 4.

[141] P. Kaspar, S. Holzapfel, E. J. Windhab, S. Kim, H. Chong, R. M. D. La Rue, J. H. Marsh, and A. C. Bryce, “Electron-beam writing of photonic crystal patterns using a large beam-spot diameter,” *Nanotechnology*, vol. 14, pp. 1004–1008, 2003.

[142] J. Kim, D. C. Joy, and S. Lee, “Controlling resist thickness and etch depth for fabrication of 3D structures in electron-beam grayscale lithography,” 2007.

[143] O. Nalamasu, E. Reichmanis, J. E. Hanson, R. S. Kanga, L. A. Heimbrook, A. B. Emerson, F. A. Baiocchi, and S. Vaidya, “Effect of post-exposure delay in positive acting chemically amplified resists: An analytical study,” *Polym. Eng. Sci.*, vol. 32, no. 21, pp. 1565–1570, 1992.

[144] D. Paul and A. Samarelli, “Prospects for SiGe thermoelectric generators,” *... Integration on Silicon ...*. pp. 5–8, 2013.

[145] P. Numbers, “Crystalbond ^{TM} Adhesives,” pp. 3–4.

[146] S. S. Narkhede and S. S. Dudam, “VLSI IMPLEMENTATION OF TERNARY GATES USING TANNER TOOL,” in *International Conference on Devices, Circuits and Systems (ICDCS)*, 2014, pp. 1–5.

[147] M. Feil and W. Mader, “Investigation of the Adhesion Mechanism of NiCr Layers on Al2O3 and AlN Substrates,” *Proc. Electron. Components Technol. Conf.*, vol. 41, no., pp. 134–140, 1991.

[148] T. A. Green, “Gold etching for microfabrication,” *Gold Bull.*, vol. 47, no. 3, pp. 205–216, 2014.

[149] K. H. Kim, Z. Akase, T. Suzuki, and D. Shindo, “Charging Effects on SEM/SIM Contrast of Metal/Insulator System in Various Metallic Coating Conditions,” *Mater. Trans.*, vol. 51, no. 6, pp. 1080–1083, 2010.

[150] B. L. Thiel, M. Toth, R. P. M. Schroemges, J. J. Scholtz, G. Van Veen, and W. R. Knowles, “Two-stage gas amplifier for ultrahigh resolution low vacuum scanning electron microscopy,” *Rev. Sci. Instrum.*, vol. 77, no. 33705, pp. 1–7, 2006.

[151] D. G. Pierce and P. G. Brusius, “Electromigration: A review,” *Microelectron. Reliab.*, vol. 37, no. 7, pp. 1053–1072, 1997.

[152] E. Pop, “Energy dissipation and transport in nanoscale devices,” *Nano Res.*, vol. 3, no. 3, pp. 147–169, 2010.

[153] A. I. Luis De Los Santos V, Angel Bustamante, Lizbet Leon F., Thanos Mitrelias, "Journal of Materials Science and Engineering Crystallization and Morphology of Gold Thin Films on Unpolished Si (100) Substrates after Furnace and Flame Annealing," vol. 4, 2010.

[154] D. G. Cahill and R. O. Pohl, "Thermal conductivity of amorphous solids above the plateau," *Phys. Rev. B*, vol. 35, no. 8, pp. 4067–4073, 1987.

[155] S. E. Gustafsson, "Transient Hot Strip Techniques for Measuring Thermal Conductivity and Thermal Diffusivity," *Rigaku J.*, vol. 4, no. 1, 1987.

[156] G. R. M. Changkun Dong, Parixit Mehrotra, "Several Technical Measures to Improve Ultra-High and Extreme-High Vacuum," *Off. Sci. Tech. Inf. Tech. Reports*, 2002.

[157] C. L. Neft and C. D. Schauder, "Theory and Design of Getter -Ion pump," *J. Sci. Instrum.*, vol. 36, no. 105, pp. 105–116, 1959.

[158] J. Chung, K. Kim, G. Hwang, O. Kwon, S. Jung, J. Lee, J. W. Lee, and G. T. Kim, "Quantitative temperature measurement of an electrically heated carbon nanotube using the null-point method," *Rev. Sci. Instrum.*, vol. 81, no. 11, 2010.

[159] A. Termehyouse, S. Bagheri, S. Shahnazar, H. Rahman, and N. Adib, "Computational local stiffness analysis of biological cell : High aspect ratio single wall carbon nanotube tip," *Mater. Sci. Eng. C*, vol. 59, pp. 636–642, 2016.

[160] P. D. A.Szekers, "Mechanical stress in SiO 2 / Si structures formed by thermal oxidation of amorphous and crystalline silicon," *Semicond. Sci. Technol.*, vol. 11, no. 1225, 1996.

[161] J. Bodzenta, J. Juszczyk, A. Kazmierczak-Balata, P. Firek, A. Fleming, and M. Chirtoc, "Quantitative Thermal Microscopy Measurement with Thermal Probe Driven by dc+ac Current," *Int. J. Thermophys.*, vol. 37, no. 7, 2016.

[162] Y. Ge, Y. Zhang, J. M. R. Weaver, H. Zhou, and P. S. Dobson, "Topography-free sample for thermal spatial response measurement of scanning thermal microscopy," *J. Vac. Sci. Technol. B, Nanotechnol. Microelectron. Mater. Process. Meas. Phenom.*, vol. 33, no. 6, p. 06FA03, 2015.

[163] J. P. Killgore, R. H. Geiss, and D. C. Hurley, "Continuous measurement of atomic force microscope tip wear by contact resonance force microscopy," *Small*, vol. 7, no. 8, pp. 1018–1022, 2011.

[164] S. Poon ; J. Spièce ; A. Robson ; O.V. Kolosov ; S. Thompson, "Probing thermal transport and layering in disk media using scanning thermal microscopy," *IEEE*, 2017.

[165] S. Thoms, Y. Zhang, J. M. R. Weaver, S. Thoms, Y. Zhang, and J. M. R. Weaver, "Improved alignment algorithm for electron beam lithography Improved alignment algorithm for electron beam lithography," *J. Vac. Sci. Technol. A Vacuum, Surfaces,*

Film., vol. 509, no. 2014, 2016.

[166] N. Mosso, U. Drechsler, F. Menges, P. Nirmalraj, S. Karg, H. Riel, and B. Gotsmann, "Heat transport through atomic contacts," *Nat. Nanotechnol.*, vol. 12, no. 5, pp. 430–433, 2017.

[167] E. R. and B. K. C. Aritra Banerjee, Sudipta Pal, "Adiabatic and non-adiabatic small-polaron hopping oxides above the metal – semiconductor transition," *J. Phys. Condens. Matter*, vol. 13, pp. 9489–9504, 2001.

[168] P. D. Tovee, M. E. Pumarol, M. C. Rosamond, R. Jones, M. C. Petty, D. a. Zeze, and O. V. Kolosov, "Ultra High Thermal Resolution Scanning Probe Microscopy via Carbon Nanotube Tipped Thermal Probes," *Mesoscale Nanoscale Phys.*, pp. 1–21, 2013.

Appendices A

Table 22 Photolithography process for cleave lines and markers for back side alignment

Photolithography. Cleave lines for wet etch and etch markers
Primer 80/20 spin at 4000rpm
S1818 spin at 4000rpm for 30s
Baking in 90°C oven for 30min
MA6 hard contact for 5sec
MicroDeveloper : RO water 1:1 for 75s
RO water rinse for 30s and blow dry
Postbake in 120°C oven for 20min
Dry etch for stripping SiO2/Si3N4 : BP80 RIE C2F6 100W, 15mT, 20sccm for 5min
Acetone, and IPA clean for 5min each with ultrasonic for resist cleanness
Barrel ash 200W for 5min using Gala asher tool in Oxygen plasma.
De-oxidise wafer in 20:1 RO water :48% HF for 3min
Silicon Fast Etching for membrane and cleaving Molar + 5% KOH solution at 105^{0} C for 70 minutes (No stirrer; KOH solution: 618.9g KOH +1.5L RO water, take 1.6L)
1 minute in 4:1(RO water : H_2SO_4), thorough water rinse(several beakers of water prepared to rinse the wafer), transfer to IPA, blow dry
Stripping the oxinitride from entire wafer: 5:1 buffered HF soaking for 3 hours - 40/60 LPCVD has been stripped thoroughly from the top and back side, RO water rinse for 15min.

Appendices B

Table 23 Back side to top side alignment

Photolithography. Alignment back side to top side. Pattern global markers for ebeam
dehydration 200C on hot plate for 5min
LOR 3A 100% spin @3000rpm for 60s: CD26 clean backside
Baking on 190C hot plate for 5min
S1818 spin at 4000rpm for 30s
Baking on 118C hot plate for 75s
Barrel ash at 40W for 30s
Hardbake on hot plate @129C for 5min
Undercut by CD26 for 90s, then RO water rinse for 30s
Barrel ash @40W for 30s
Metallization: NiCr/Au 5nm/145nm by Plassys II
Liftoff in warm SVC14 for 30 min., then clean by SVC14, rinse in IPA for 1min, blow dry

Appendices C

Table 24 Active device fabrication stage

Level 1 of ebeam: Au pads, leads and wires (10nm NiCr/33nm Pt/50 nm Au)
Spinning resist 8 % 2010 PMMA resist 5000 rpm 60 sec (thickness about 200nm)
Bake 180^0 C oven -1 hour, or hot plate 160^0 C 7 min.
Spinning the resist 4% 2041 PMMA 5000 rpm, 60sec (thickness about 100nm)
Bake 180^0 C oven -1 hour, or hot plate 160^0 C 7 min.
Exposure
Develop 30 sec 23^0 C/ IPA -15 sec then blow dry
Ash (80W 30 sec)
Plassys 2 deposit Nicr/Pt/Au (10/33/50nm)
Fill beaker with acetone, put sample in, put in the bath, cover and leave for 2 hours.
Lift-off
Level 2 of ebeam Pt window for heater/ Gold etch
Spinning resist 12 % 2010 PMMA resist 5000 rpm 60 sec
Bake 180^0 C oven -1 hour, or hot plate 160^0 C 7 min.
Exposure
Develop 30 sec 230 1:1 MIBK developer/ 15 sec IPA
Ash (80 W 30 s)
Gold etching in KI/I2 solution for 8 s.
Level 3 of ebeam: Au wires: big and small (33 nm Nicr/ 90nm Au)
Spinning resist 8 % 2010 PMMA resist 5000 rpm 60 sec (thickness about 200nm)
Bake 180^0 C oven -1 hour, or hot plate 160^0 C 7 min.
Spinning the resist 4% 2041 PMMA 5000 rpm, 60 sec (thickness about 100nm)
Bake 180^0 C oven -1 hour, or hot plate 160^0 C 7 min.
Exposure
Develop 30 sec 23 ^{0} C/ IPA -15 sec then blow dry
Ash (80W 30 sec)
Plassys 4 deposit Nicr/Au wires (33/90nm)
Fill beaker with acetone, put sample in, put in the bath, cover and leave for 2 hours.

Appendices D

Table 25 Releasing the membrane

Releasing the membrane
Dehydration bake at 180°C for 1 hour
Spin HMDS (MCC 80:20) leave on the sample for 10s
Spin at 3000 rpm for 30 seconds
Spin UVIII 3000rpm
Soft bake on vacuum hotplate at 137 °C for 1 minute
Spin another layer of UVIII 3000 RPM
Exposure
Post exposure bake 137 °C for 1 minute on vacuum hotplate
Development must be immediately after PEB. CD26 for 1 minute at room temperature
Rinse well in water and blow dry
Hard bake for dry etch process. 145 °C for 3 minutes.
Wet etch for stripping the SiO_2 from opened windows
Put sample into buffered 5:1 HF solution for 1.5 minutes.
Rinse well and blow dry
Dry etch for releasing the membrane and stripping the resist
Dry etch 3 minutes STS tool to release the membrane *Recipe:* KNTNL03 SF6 = 130sccm; Coil/Platen 800/15W; Pressure: 45mT
The stripping the resist RIE 80 plus Gas: O2 50 sccm; Power: 100 W; Pressure: 50 mT

Appendices E

Table 26 Modelled thermal resistance values

Device	a, K/W	b, K/W	r_{th}, K/W	Comments
A1	2.32E+07	7.27E+07	9.60E+07	The thermal resistance in the legs is dominant
A2	9.39E+04	3.16E+05	4.10E+05	By fully covering with metal it possible to change the overall resistance by 2 orders of magnitude.
A3	1.15E+07	7.18E+07	8.33E+07	Small dots dropped the overall resistance but might cause difficulties in experiment
A4	9.38E+04	6.22E+07	6.23E+07	Bigger area of gold might be easier to find with probe during the experiment and also reduces the resistance
B1	2.17E+07	3.37E+07	5.55E+07	Increasing the number of arms make the resistance roughly equal in both parts of the sample.
B2	8.65E+04	1.47E+05	2.33E+05	Big change in overall resistance with gold coating by a similar feature to Al:A2.
B3	9.96E+06	3.40E+07	4.40E+07	Similar effect as with device A3
B4	8.73E+04	3.11E+07	3.12E+07	Similar effect as with device A4
C1	2.25E+07	3.83E+07	6.08E+07	Increasing the width of supported arms changes the conductance value but is about the same as with device B1, with proportion of b/a equal to 1.7

C2	9.37E+04	1.67E+05	2.61E+05	Similar effect as with devices A2 and B2
C3	1.14E+07	3.75E+07	4.91E+07	Similar effect as with devices A3 and B3
C4	9.34E+04	3.11E+07	3.12E+07	Similar effect as with devices A4 and B4